DIELECTRIC NANOCOMPOSITES FOR HIGH PERFORMANCE EMBEDDED CAPACITORS IN ORGANIC PRINTED CIRCUIT BOARDS

A Dissertation
Presented to
The Academic Faculty

by

Jianwen Xu

In Partial Fulfillment
of the Requirements for the Degree
Doctor of Philosophy in the
School of Materials Science and Engineering

Georgia Institute of Technology
August 2006

DIELECTRIC NANOCOMPOSITES FOR HIGH PERFORMANCE EMBEDDED CAPACITORS IN ORGANIC PRINTED CIRCUIT BOARDS

Approved by:

Dr. C.P. Wong, Advisor
School of Materials Science and Engineering
Georgia Institute of Technology

Dr. Christopher Summers
School of Materials Science and Engineering
Georgia Institute of Technology

Dr. Rosario A. Gerhardt
School of Materials Science and Engineering
Georgia Institute of Technology

Dr. Dennis W. Hess
School of Chemical and Biomolecular Engineering
Georgia Institute of Technology

Dr. Meilin Liu
School of Materials Science and Engineering
Georgia Institute of Technology

Date Approved: June 12, 2006

This dissertation is dedicated to my parents, my wife, and my son for their love, support, and encouragement during my entire PhD studies.

ACKNOWLEDGEMENTS

First, I am deeply indebted to my advisor Professor C.P. Wong for his motivation, guidance, support, and encouragement throughout the course of this research. He has been and will continue to be my best sources of inspiration and support. I would like to extend my gratitude to Professor Rosario A. Gerhardt, Professor Meilin Liu, Professor Christopher Summers, and Professor Dennis W. Hess for serving on my Ph.D. committee as well as providing invaluable discussions and insights.

I would like to thank the faculty and staff members in the National Science Foundation Microsystems Packaging Research Center and the School of Materials Science and Engineering. They are Professor Rao R. Tummala, Professor Zhong Lin Wang, Professor Mo Li, Dr. Swapan Bhattarcharya, Dr. Leyla Conrad, Dr. Fuhan Liu, Dr. Isaac Robin Abothu, Dr. Raj Pulugurtha, Dr. Lilly Tsai, Dr. Zurong Dai, Mr. Dean Sutter, Mr. Seth Johnson, Ms. Yolande Berta, Ms. Susan Bowman, Ms. Vicki Speights, Ms. Mechelle Kitchings, Ms. Karen Hutcheson, Mr. James Cagle, and Mr. Tim Banks.

My special thanks go to my fellow co-workers in Dr. Wong's group, for all the discussions and helps I received from Dr. Lianhua Fan, Dr. Kyoun-Sik Moon, Dr. Yang Rao, Dr. Shijian Luo, Dr. Haiying Li, Dr. Zhuqing Zhang, Dr. Silvia Liong, Dr. Fei Xiao, Dr. Hai Dong, Dr. Brian Englert, Mr. Jireh J. Yue, Mr. Ramakrishna S. Cherukuri, Mr. Suresh Pothukuchi, Ms. Lara Martin, Ms. Yangyang Sun, Ms. Yi Li, Mr. Hongjin Jiang, Ms. Jiongxin Lu, Mr. Lingbo Zhu, Mr. Yonghao Xiu, Ms. Jessica Burger, Ms. Guseul Yun. I would also like to acknowledge my undergraduate research assistants who worked

with me during the course of my PhD research. They are Mr. Christopher Tison, Ms. Michelle Wong, Mr. Sunil Smith, Mr. Jason R. Fodstad, and Mr. William Florkowski.

I would like to acknowledge the cleanroom staff at the Microelectronic Research Center for their assistance with the equipment. They are Dr. Zhiping Zhou, Mr. Gary Spinner, Mr. Charlie Suh, Mr. Tran-Vinh Nguyen, and Mr. Brandon Harrington.

This work was financially supported by the National Science Foundation through grant ECS-0203412 and grant ECS-0501405. Special thanks to Hitachi Chemical Co., Ltd., Sumitomo Bakelite Co., Ltd., ALPS Electric, Inc., nGimat Co., Korean Institute of Science and Technology, and Oak-Mitsui Technologies for their interests and support of this work.

Finally, I would like to thank my parents, my parents-in-law, and my wife for their continuous support and encouragement. Without them, this dissertation would not be possible.

TABLE OF CONTENTS

LIST OF TABLES

LIST OF FIGURES

SUMMARY

Conventionally discrete passive components like capacitors, resistors, and inductors are surface-mounted on top of the printed circuit boards (PCBs). To match the ever increasing demands of miniaturization, cost reduction, and high performance in microelectronic industry, a promising approach is to integrate passive components into the board during PCB manufacture. Because they are embedded inside multilayer PCBs, such components are called embedded passives.

This work focuses on the materials design, development and processing of polymer-based dielectric nanocomposites for embedded capacitor applications. The methodology of this approach is to combine the advantages of the polymer and the filler to satisfy the electric, dielectric, mechanical, fabrication, and reliability requirements for embedded capacitors. Restrained by poor adhesion and poor thermal stress reliability at high filler loadings, currently polymer-ceramic composites can only achieve a dielectric constant of less than 50. In order to increase the dielectric constant to above 50, effects of high-κ polymer matrix, bimodal fillers, and dispersing agent are systematically investigated. Surface functionalization of nanofiller particles and modification of epoxy matrix with a secondary rubberized epoxy to form sea-island structure are proposed to enhance the dielectric constant, adhesion and high-temperature thermal stress reliability of high-κ composites. To obtain photodefinable high-κ composites, fundamental understanding of the photopolymerization of the novel epoxy-ceramic composite photoresist is addressed. While the properties of high-κ composites largely depend on the polymer matrix, the fillers can also drastically affect the material properties. Carbon black- and carbon nanotubes-filled ultrahigh-κ polymer composites are investigated as

the candidate materials for embedded capacitors. Dielectric composites based on percolation typically show a high dielectric constant, and a high dielectric loss which is not desirable for high frequency applications. To achieve a reproducible low-loss percolative composite, a novel low-cost core-shell particle filled high-κ percolative composite is developed. The nanoscale insulating shells allow the electrons in the metallic core to tunnel through it, and thereby the composites exhibit a high dielectric constant as a percolation system; on the other hand, the insulating oxide layer restricts the electron transfer between filler particles, thus leading to a low loss as in a polymer-ceramic system.

CHAPTER 1

INTRODUCTION

1.1 Evolution of Electronic Packaging

Electronic packaging, beyond being simply considered as a passive container, has been viewed as an important factor that determines the ultimate performance limits of an integrated circuit (IC) in recent years. As a matter of fact, packaging technology, which makes IC chips suitable for applications in various environments such as in computers, consumer electronics, light and heavy motor automobiles, aerospace, medical devices, magnet and optical storage, and etc., is one of the key drivers that has had great economic and technological impact on the semiconductor industry. Currently the electronic packaging industry is a $125 billion worldwide market encompassing such technology industries such as personal computers, cellular phones, digital cameras, and etc. [1].

Electronic packaging technology is an art of interconnection and essentially involves the design and manufacture of the structure surrounding ICs in order to miniaturize the electronic system and maximize its performance. The four main functions of an electronic packaging are power distribution, thermal dissipation, mechanical protection, and signal distribution. Electronic packaging includes a multi-level hierarchy, as shown in Figure 1.1 [2]. The first level package involves the process of establishing interconnection between an IC chip and a module. It must provide the required number of contacts for power and signal transmission, provide thermal expansion compatibility between the chip and the second level package, and provide a thermal path for heat removal, while minimizing transmission delay and electrical noise. Three major techniques are flip-chip, wire bonding and tape automated bonding (TAB). The second-level packaging is the process of joining a module with a card such as a printed circuit

board (PCB). The card contains the necessary power and signal lines to handle the communications between the chips and the third level package. The current second-level packaging technologies include pin through hole (PTH), peripheral surface mount technology (SMT), and surface-mount-array (SMA) technology. The third-level packaging is the process of placing the PCB onto a motherboard. However, the emerging of new technology has blurred the distinction between different levels of packaging. For example, the chip-on-board (COB) technology, where an IC is directly attached onto a PCB, may be considered a level 1.5 package.

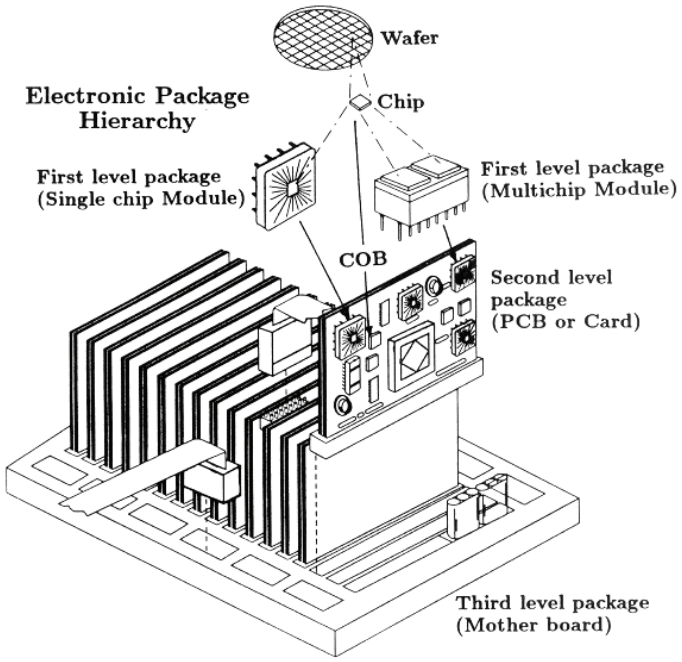

Figure 1.1 Schematic of electronic package hierarchy.

The packaging concepts and technologies in all packaging level are under quick evolution because of the dramatic changes in the computer, telecommunications, automotive, and consumer electronics industries for low-cost, portability, high performance, diverse functions, and environment- and user-friendliness. Figure 1.2 shows the evolution of packaging technology in the past four decades. The shift from traditional through-hole packages began sometime in the 1980s when dual in line package (DIP) began to be displaced in select applications by surface-mount packages such as quad flat

packages (QFP), and area array packages like pin-grid array (PGA) and ball-grid array (BGA). Chip scale packaging (CSP) is the second generation packaging technologies emerged in the mid-1990s, which can increase the IC silicon efficiency 30-40%. The most advanced technology in packaging is called wafer-level packaging (WLP) or wafer-level chip scale package (WLCSP), which involves building power and signal redistributions and packaging protections onto the wafer, representing the convergence of front-end and back-end processes in packaging. The next generation packaging technology will be a system-level integrated package. An example is the system-on-a-package (SOP), proposed by the NSF Packaging Research Center (PRC) at the Georgia Institute of Technology. SOP, as shown in Figure 1.3, employs a low cost large area organic substrate to define a multiple level metal-polymer dielectric structure that provides power, ground, and controlled impedance interconnection functions together with a full range of integral passives. The convergence of RF, digital, optoelectronic, and sensing multi-functionalities in a single package is an ideal way of achieving very high packaging efficiency. In the SOP structure, the passive components (capacitors, inductors, resistors, and etc.) are embedded in the organic substrate, as illustrated in Figure 1.3.

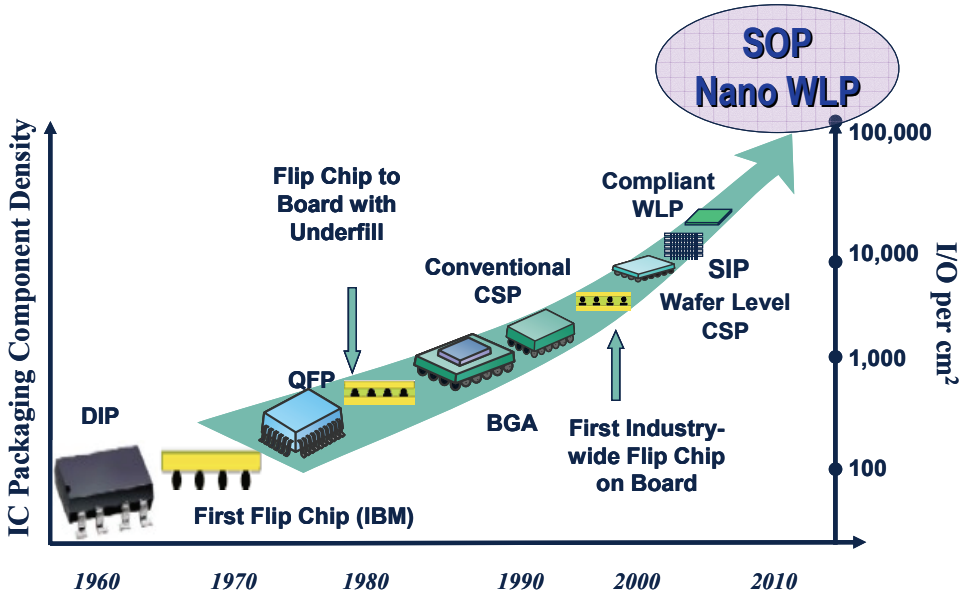

Figure 1.2 Evolution of packaging technology in last four decades.

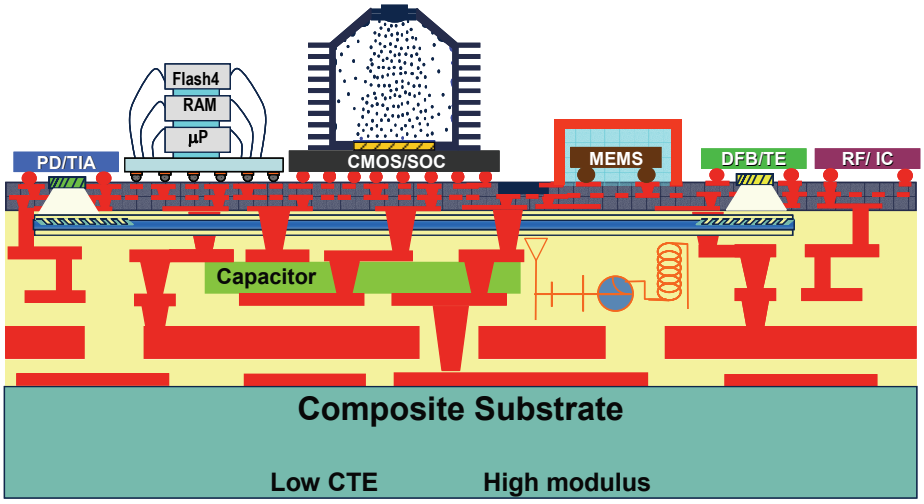

Figure 1.3 Schematic showing SOP structure (courtesy of PRC).

1.2 Dielectric Films for Electronic Packaging

Because of the advancements in electronic packaging technology, dielectric films with both low dielectric constant (low-κ) and high dielectric constant (high-κ) are in great demand.

1.2.1 Low-κ Dielectric Films for Electronic Packaging

A low-κ film can be used as an interlayer dielectric (ILD) or a substrate.

Signal distribution and propagation is one of the most important aspects of electronic packaging. As the IC pitch size migrates from 90 nm to 65 nm, the dielectric constant of ILD will play a more crucial role in determining the parasitic capacitance and thus the ultimate performance of a device. The term τ, defined as $\tau = RC$, is called the *RC* time delay of the signals, where *R* is the line resistance and *C* is the capacitance of the structure. Assuming that the minimal pitch equals twice the metal line width and assuming the dielectric thickness equals the thickness of the metal line, the RC delay can be estimated as follows [3]:

$$\tau = RC = 2\rho\varepsilon\varepsilon_0\left(\frac{4L^2}{P^2} + \frac{L^2}{T^2}\right) \qquad \text{Equation 1.1}$$

where R is total line resistance, C is the total line capacitance, ρ is the metal resistivity, ε is the dielectric constant, ε_0 is the permittivity of free space, L is line length, P is the interconnect pitch, and T is the metal thickness. Therefore, the signal delay is a direct function of the dielectric constant of the interlayer dielectrics.

In the case of ceramic packages, the signal propagation delay is governed by the dielectric constant of the ceramic substrate where metal lines are deposited or embedded, as shown in the following equation [4]:

$$t_d = \frac{l\sqrt{\varepsilon_r}}{C} \qquad \text{Equation 1.2}$$

where t_d is the signal propagation delay, l is the line length, ε_r is the relative dielectric constant of the substrate, and C is the speed of light.

From Equation 1.1 and 1.2, it can be seen that the interlayer dielectrics and substrates with low dielectric constant are required to minimize the signal propagation delay.

1.2.2 High-κ Dielectric Films for Electronic Packaging

On the other hand, high dielectric constant films are typically used as capacitors, e.g. dynamic random access memory (DRAM) capacitors, decoupling capacitors, and etc., because of their capability to store electric charge. In the next generation packaging technology, as shown in Figure 1.3, the passive components such as capacitors (C), resistors (R), and inductors (L), will be integrated into the SOP substrate as a layer of thin film instead of being surface mounted on the top of the substrates as discrete components. The passive components buried inside the substrate are called integral passives or embedded passives. For embedded capacitors, high-κ dielectric films are required in order to achieve small form factor devices.

1.3 Overview of Embedded Passives

1.3.1 Passive Components

Passive components are the majority of electronic components in a typical microelectronic product today and they typically take up 40% of the printed circuit board (PCB) surface area, 30% of the solder joints, and up to 90% of the placement time for an average electronic assembly. In 2003, about a trillion passive components were placed in electronic systems, leading to worldwide sales of 125 billion US dollars [5]. Figure 1.4 shows the image of a printed circuit board. An IC chip is in the center, but there are numerous passive components with various sizes surrounding it. Table 1.1 shows the number of passive components being used in cellular phones, consumer portable, and other communication systems [6]. The number of passive components is much more than that of the ICs, and the ratio of passives/ICs can be as much as 47:1. It is evident that the passive components used to support the ICs are dominant in numbers. Therefore, the influences that passive components have on microelectronic system size, cost, and reliability are substantial. In order to provide smaller, lighter, faster, cheaper, and more reliable devices in the next generation electronic systems, alternatives to discrete passives are imperative.

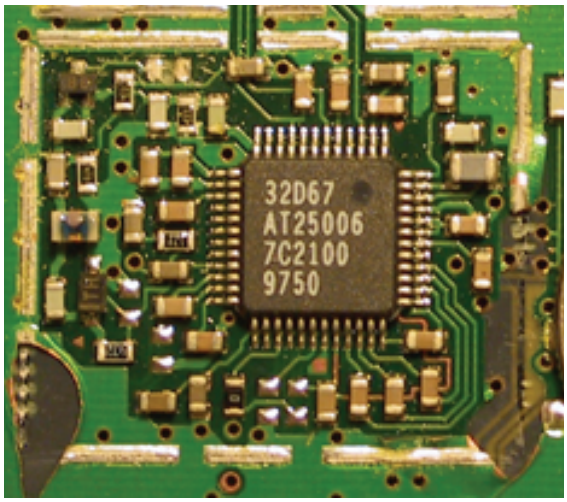

Figure 1.4 Image of a printed circuit board.

Table 1.1 Passives in electronic systems

System	Passives	ICs	Ratio
CELLULAR PHONES			
Ericsson DH338 Digital	359	25	14 : 1
Ericsson E237 Analog	243	14	17 : 1
Philips PR93 Analog	283	11	25 : 1
Nokia 2110 Digital	432	21	20 : 1
Motorola Mrl 1.8 GHz	389	27	14 : 1
Casio PH-250	373	29	13 : 1
Motorola StarTAC	993	45	22 : 1
Matsushita NTT DoCoMo	492	30	16 : 1
CONSUMER PORTABLE			
Motorola Tango Pager	437	15	29 : 1
Casio QV10 Digital Camera	489	17	29 : 1
1990 Sony Camcorder	1226	14	33 : 1
Sony Handy Cam DCR-PC7	1329	43	31 : 1
OTHER COMMUNICATION			
Motorola Pen Pager	142	3	47 : 1
Infotac Radio Modem	585	24	24 : 1
Data Race Fax-Modem	101	8	13 : 1

1.3.2 Advantages of Embedded Passives

Embedded passives have been recognized as the most promising alternative to replace discrete passives, and this technology may have similar impact on the current electronic packaging industry as integrated circuits had done to the microelectronics industry half of a century before. Embedded passives provide many advantages over discrete components. Currently passive components take up more than 40% of the substrate surface area in a typical electronic system, and by embedding them into the board this large amount of area will be saved. Figure 1.5 shows the schematics of discrete and embedded passives; the size reduction from replacing discrete passives with embedded passives can be easily observed. Besides size reduction, embedded passives can enhance electrical performance of an electronic system as well, because the shorter interconnects from using embedded passives can effectively reduce the electromagnetic interference, reduce the electrical delay, and suppress electrical parasitic signals. These advantages are particularly desirable for capacitors, as discrete capacitors always suffer

from the parasitic inductance from the long conduction lines. For instance, for high-end products, discrete passives used for functions such as bus-line decoupling, strip-line termination, and initialization are speed limiting factors because of their size, configuration and distance from the active circuit they serve. Embedding passive components into the board can remove such speed barriers, because they can be placed much closer to the integrated circuits. Moreover, placement time for discrete components are one of the major factors that determine the cost of passive components; by using embedded passives, mass production by monolithic batch fabrication can be used, which can substantially reduce the assembly time and cost. Due to the elimination of solder joints, the reliability of electronic systems using embedded passives can be significantly improved as well, as the solder joint failure is one of the major failure modes for electronic systems with discrete components.

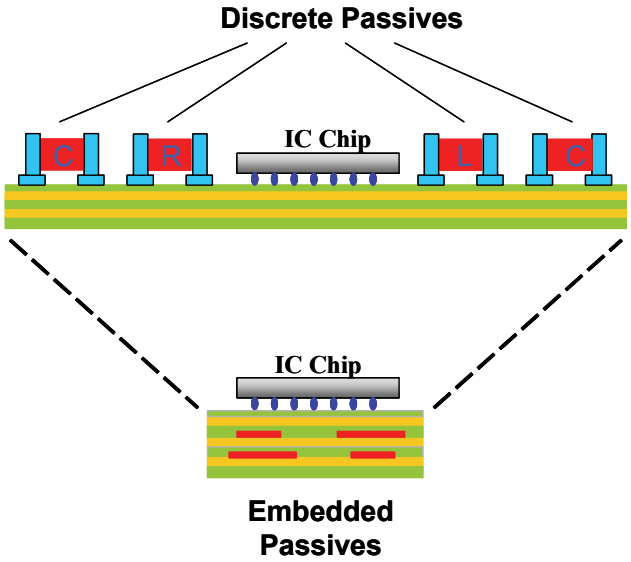

Figure 1.5 Schematics of discrete passives and embedded passives.

1.3.3 Capacitors and Decoupling Capacitors

Among all passive components, capacitors call for special attention. Capacitors are more than any other type of passive component. Figure 1.6 shows the market shares of capacitors, resistors, and inductors in the United States, according to the 2004

International Electronic Manufacturing Initiative (iNEMI) Roadmap [7]. Capacitors account for a 15.26 billion dollars market, which is much more than 1.0 billion dollars for inductors and 4.0 billion dollars for capacitors. Because of the large amount of capacitors employed in electronic systems, integration of capacitors is of much importance.

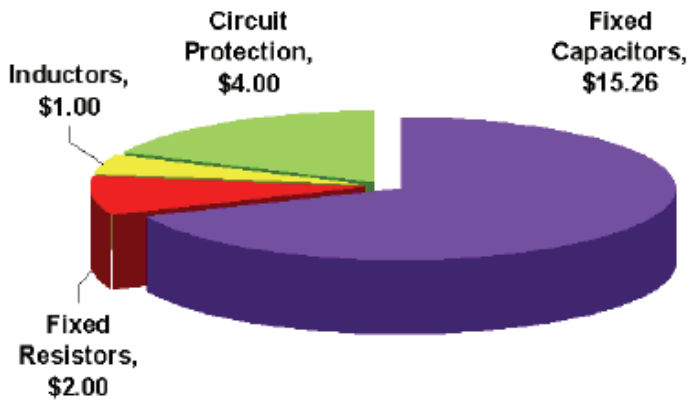

Figure 1.6 Market shares of capacitors, resistors, and inductors (billion dollars).

Capacitors have many applications, as shown in Table 1.2. They can be used for filtering, timing, A/D conversion, termination, decoupling, and energy storage. Particularly, the development of microelectronics requires decoupling capacitors with higher capacitance and shorter distance from its serving devices. Decoupling capacitors typically have a capacitance of about 1-100 nF. The capacitance range of capacitors in a typical electronic systems is shown in Figure 1.7 [8].

Decoupling capacitors are used as a rescue charge tank in electronic circuits to support the instantaneous current needed for simultaneous switching. There are basically two sources of noise in electronic packages: 1) the noise on the power supply caused by the inductance of the supplying networks, which increases with cycle frequency and the number of switching drivers and 2) the noise induced by the crosstalk between adjacent signal paths. Such noises can cause voltage fluctuations. Remedies for such voltage fluctuations include reducing the separation distance between power and ground planes and using high dielectric constant dielectric materials for decoupling capacitors.

Figure 1.8 is the schematics showing the function of decoupling capacitors [9]. For a real circuit, the non-zero impedance leads to a non-ideal power distribution; but with the decoupling capacitor, an ideal power distribution can be achieved as in an ideal zero-impedance circuit. Figure 1.9 is an example showing the decoupling capacitors embedded in the PCB substrate. Because embedded decoupling capacitors can be placed very close to the IC chips in the PCB substrate, the parasitic resistance and inductance associated with the conduction lines can be further reduced. Dielectric materials with a relative dielectric constant in the range of 25-170 is required to satisfy various decoupling capacitance needs [10].

Table 1.2 Applications and properties of capacitors

Application	**Value Range**	**Tolerance Required**	**Stability Required**
Filtering, Timing	1 pF – 100 pF	Moderate	Moderate
A/D Conversion	1 pF – 10nF	Very High	Very High
Termination	50 – 200 pF	Low	Low
Decoupling	1nF – 100 nF	Low	Low
Engergy Storage	1 μF and up	Low	Low

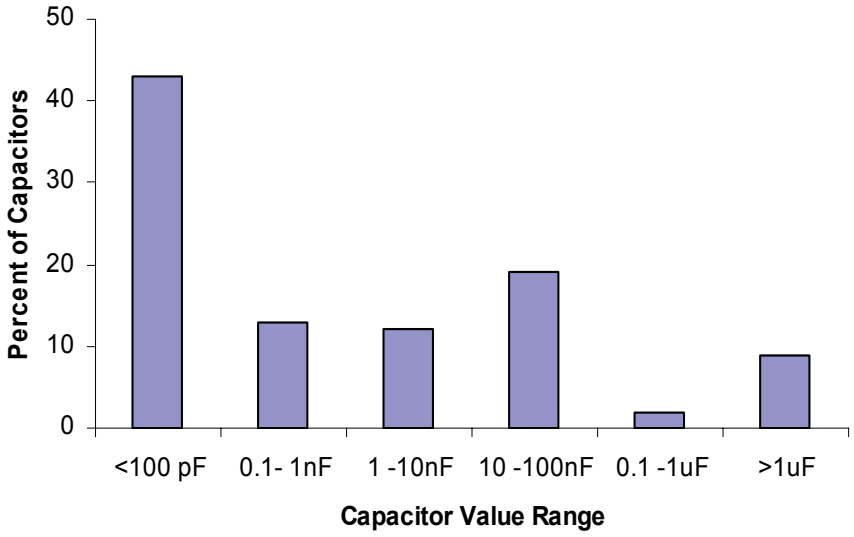

Figure 1.7 Distribution of capacitor values in typical portable consumer systems.

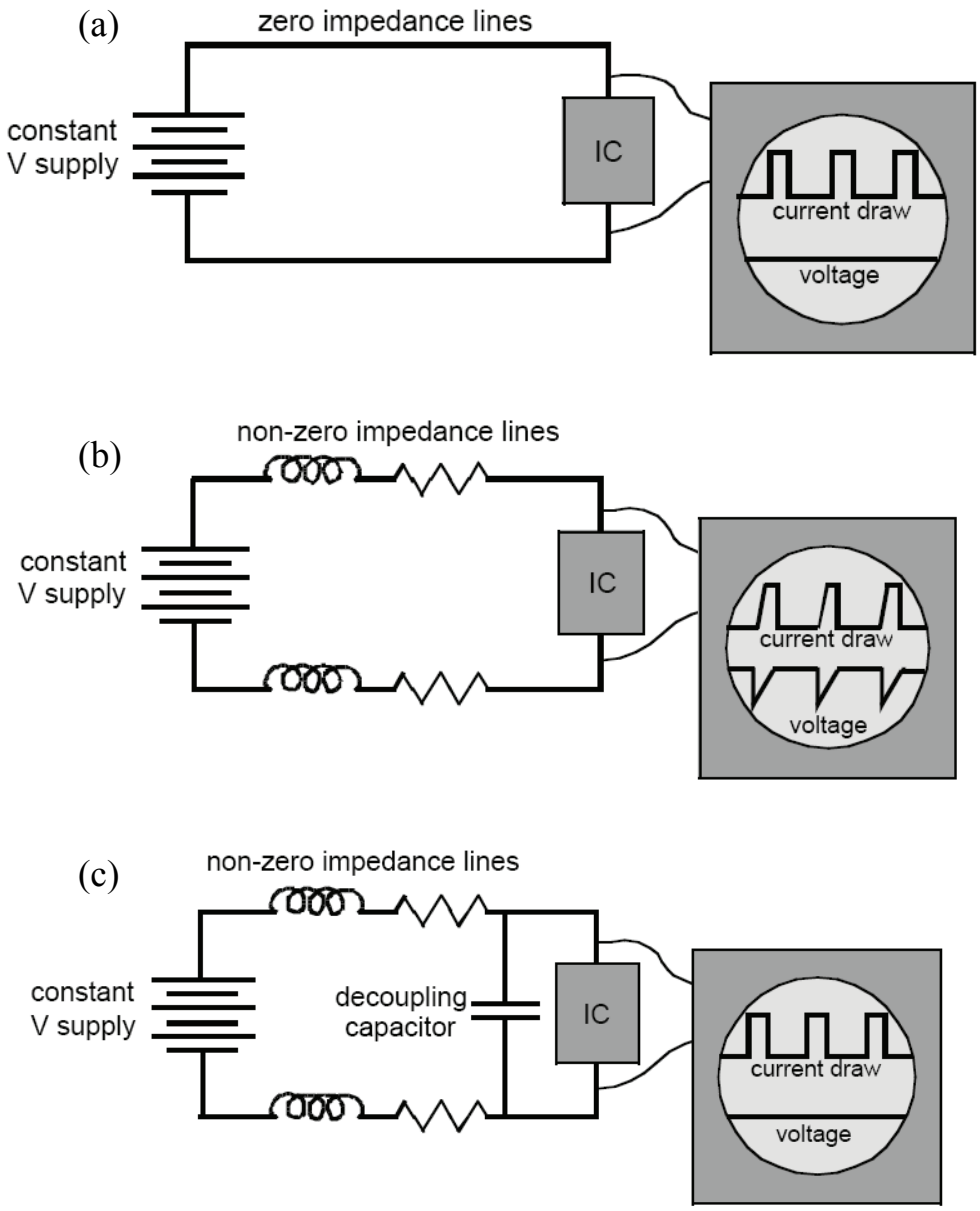

Figure 1.8 Schematics showing the function of embedded capacitors. (a) An ideal circuit with zero impedance and ideal power distribution, (b) a real circuit with non-zero impedance and non-ideal power distribution, and (c) a real circuit with non-zero impedance but ideal power distribution because of the decoupling capacitor.

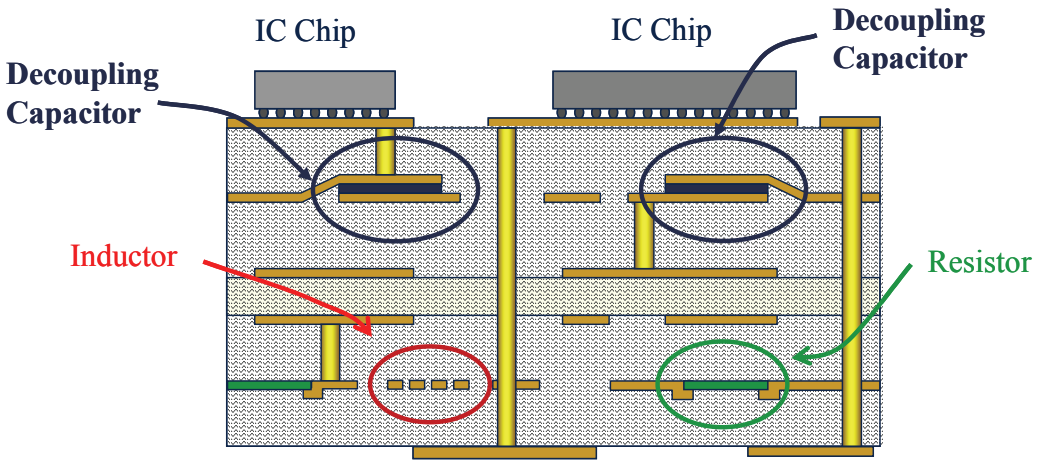

Figure 1.9 Example showing the decoupling capacitors embedded in the PCB substrate.

1.4 Dielectric Polarization Mechanisms

For a capacitor, capacitance (C) is used as the measure of how much electric charge can be stored in a capacitor. It is defined as the ratio of the electric charge (Q) and the applied voltage (V):

$$C = \frac{Q}{V} \qquad \text{Equation 1.3}$$

The unit of capacitance is farad (F), but most capacitors used in electronic circuits have a capacitance in the order of 10^{-6} farad (μF) or even 10^{-12} farad (pF).

Dielectric constant (κ or ε_r) represents the capability of storing electric charge by the dielectric material. The relationship between capacitance C and dielectric constant ε_r is given by the following equation:

$$C = \frac{\varepsilon_0 \varepsilon_r A}{t} \qquad \text{Equation 1.4}$$

where ε_0 is dielectric constant of the free space (8.854 x 10^{-12} F/m), A is the area of the electrical conductor, t is the thickness of the insulator layer, and ε_r is the dielectric constant of the insulator layer.

From Equation 1.4, it can be seen that with a given geometry, a larger dielectric constant leads to a larger capacitance. Therefore, dielectric materials with higher dielectric constant are desirable in order to achieve a small form factor.

When under an alternate electric field, the dielectric constant of materials can be expressed by complex permitivities:

$$\varepsilon^* = \varepsilon' - j\varepsilon'' = \varepsilon_0\varepsilon_r - j\varepsilon'' \qquad \text{Equation 1.5}$$

where ε′ is real permittivity and ε″ is the imaginary permittivity.

The term tan δ, defined as the ratio of imaginary permittivity and real permittivity (ε″/ε′'), is called the dielectric loss or dissipation factor of a material. The dielectric loss is a material property and does not depend on the geometry of a capacitor. The energy loss (*W*) due to consumption of a dielectric material can be determined by the following equation:

$$W \approx \pi\varepsilon'\xi^2 f \tan\delta \qquad \text{Equation 1.6}$$

where ξ is the electric field strength and *f* is the frequency [11]. Therefore, the energy dissipated is proportional to the dielectric loss. As such, a low dielectric loss is preferred in order to reduce the energy dissipated by a dielectric material, particularly for high frequency applications.

The value of dielectric constant depends on the polarizability of a material. Generally speaking, polarization occurs when the centers of the negative and positive charge do not coincide spatially. There are four major types of polarization that occur at specific frequency ranges: electronic polarization, ionic polarization, molecular or dipolar or orientation polarization, and interfacial polarization.

Electronic polarization is due to an applied electric field that shifts the electron cloud of the atom from its original center position, as shown in Figure 1.10(a). This type of polarization is not permanent; once the applied electric field is removed the

polarization will dissipate. This polarization mechanism is common to all dielectric materials.

The second mechanism of polarization is ionic polarization, also called atomic polarization, which is the displacement of anions and cations in the presence of an electric field, as shown in Figure 1.10(b). The cations are attracted towards the negative electrode and the anions are directed towards the positive electrode.

The third mechanism of polarization is molecular or dipolar or orientation polarization, as shown in Figure 1.10(c). Orientation polarization is present in certain types of polymers and ceramics, and is associated with the presence of permanent electric dipoles that exists even without an electric field. This particular type of polarization is similar to electronic polarization except that the polarization is retained after the removal of the electric field.

The fourth polarization mechanism is interfacial polarization or space charge polarization, as shown in Figure 1.10(d). Interfacial polarization is due to the movement of mobile charge carriers like electrons under an applied electric field. The charge carriers become piled up at a physical barrier such as grain or phase boundaries, defects, or free surfaces.

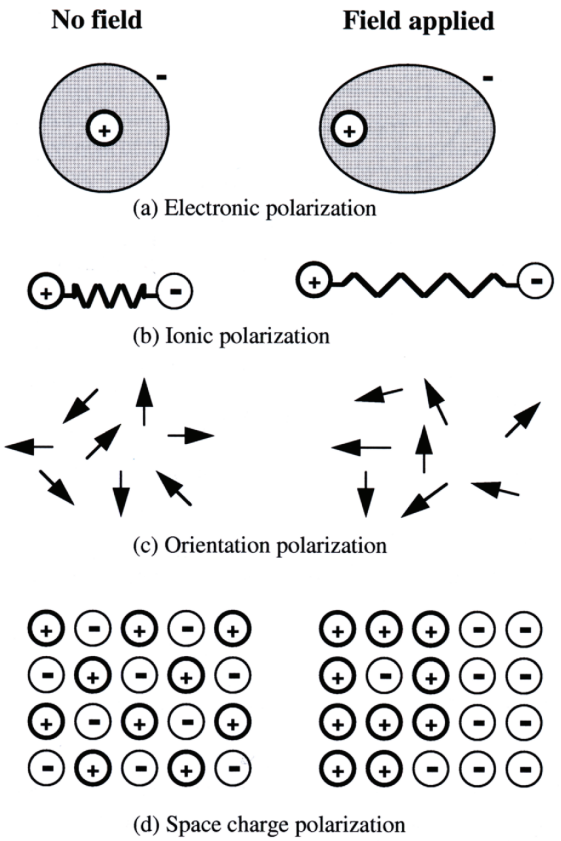

Figure 1.10 Schematic representation of four polarization mechanisms [12].

The total polarizability of a dielectric material is represented as the sum of these individual polarizations, as shown in Equation 1.7 [13]:

$$\alpha = \alpha_e + \alpha_i + \alpha_0 + \alpha_f \qquad \text{Equation 1.7}$$

where α_e, α_i, α_o, and α_f are the electronic, ionic, orientation, and interfacial polarizations, respectively.

The relationship of dielectric constant to the polarizability is given by the Claussius-Mosotti equation [14]:

$$\varepsilon = \frac{3}{1 - N\alpha / 3\varepsilon_0} - 2 \qquad (0 < \alpha < 3\varepsilon_0/N) \qquad \text{Equation 1.8}$$

where ε is the realative dielectric constant, N is the number of molecules per unit volume, α is the polarizability of each molecule. According to this equation, the dielectric constant increases with the increased polarizability.

1.5 Factors that Affect Dielectric Constant

1.5.1 Frequency Responses of Dielectric Constant

Frequency can dramatically affect the dielectric behavior of a material by acting through the relevant polarization mechanisms, as shown in Figure 1.11 [12]. There is a relaxation time associated with each of the polarization mechanisms that is caused by the inertia-to-charge or electron movement. For a material to exhibit a constant polarizability with frequency, the dipole must reverse direction at the same rate as that of the electric field for the polarization to remain in phase with the field. However, as the frequency increases, a particular dipole may not be able to follow the reversal rate of electric field, which results in a decrease in dielectric constant with frequency. Electronic polarization is the only process sufficiently rapid to occur in the alternative electric fields up to the range of visible spectrum (10^{15} Hz). Ionic polarization can follow an applied electric field up to the frequency range of infrared spectrum (10^{12}-10^{13} Hz) and still make contribution to the dielectric constant. Dipolar polarization occurs in the frequency range up to subinfrared range (10^{11}-10^{12} Hz). Dipolar polarization is one of the major polarization mechanisms in most polymers and some types of ceramics. Compared to electronic, ionic, and dipolar polarization, space charge polarization has a much lower relaxation frequency, i.e., usually up to 10^{3} Hz.

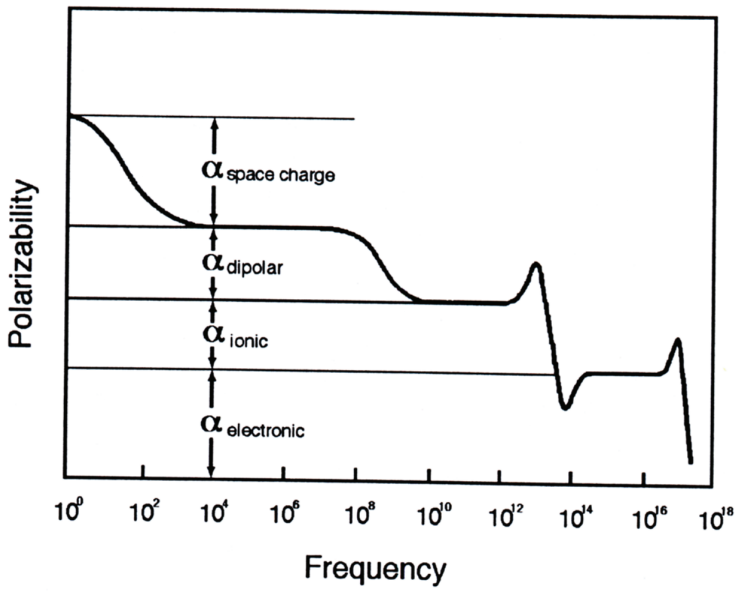

Figure 1.11 Frequency dependency of polarizability.

The change of dielectric constant at very high frequency due only to electronic polarization can be expressed by the following equation [15]:

$$\varepsilon = 1 + \frac{Nze^2 / \varepsilon_0 m_e}{\varpi_0^2 - \omega^2} \qquad \text{Equation 1.9}$$

where N is the number of atoms per unit volume, z is the number of electrons per atom, m_e is the mass of the electron, ω is the frequency, and ω_0 is the resonance frequency. Therefore, dielectric constant can be decreased by the decreased number of electrons per atom z. A decrease in the size and the effective number density of electrons can also lower the dielectric constant.

1.5.2 Temperature Responses of Dielectric Constant

Temperature is another important factor that has significant affects on the dielectric behavior of materials. The temperature coefficient of capacitance (TCC) is often used to describe the change of dielectric constant or capacitance with temperature. TCC is expressed in ppm/°C and can be defined by the following equation:

$$TCC = \frac{dC}{CdT} = \frac{\Delta C}{C\Delta T} \qquad \text{Equation 1.10}$$

where C is the capacitance and T is the temperature.

TCC tends to be positive. As the temperature increases, most materials will expand, which results in a larger dipole moment when the materials is under an electric field. Figure 1.12 shows the temperature responses of paraelectric and ferroelectric materials [9]. For paraelectric Ta_2O_5, the TCC is monotonically positive. And the temperature shows a more complicated effect on ferroelectrics because of the temperature dependence of their crystal structure. For instance, at Curie temperature the dielectric constant of a barium titanate film could change more than 50%, as shown in Figure 1.12.

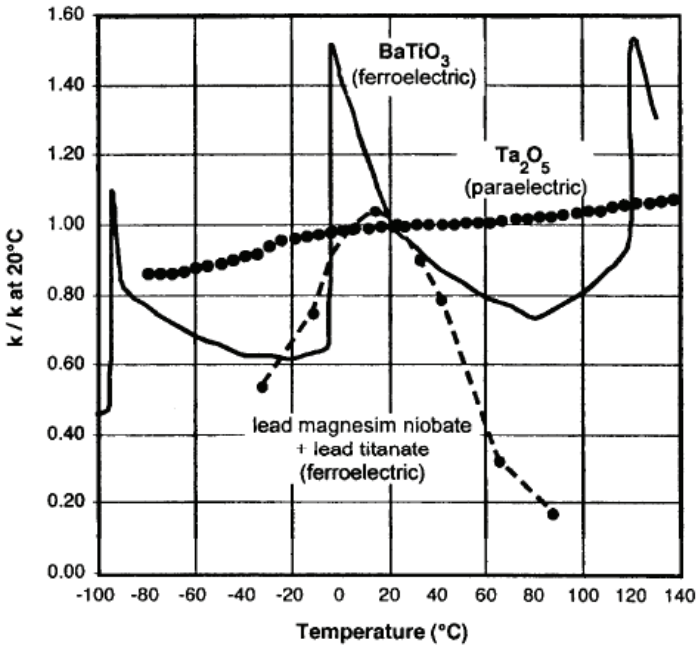

Figure 1.12 Temperature responses of paraelectric and ferroelectric materials.

1.6 Overview of High-κ Dielectric Films for Embedded Capacitors

To enable embedded capacitors, high-κ dielectric materials that satisfy the requirements of fabrication, electrical performance, and mechanical performance need to be developed. The general requirements for embedded capacitor dielectrics include high

dielectric constant, low dissipation factor, low processing temperature, low leakage current, high breakdown voltage, and etc. Due to the limited area and space in the PCB board, a dielectric material with much higher dielectric constant is required to reach similar capacitance as in discrete capacitors. And the dielectric material is preferably to have a low processing temperature compatible with PCB fabrication, because the PCB board, where the capacitors will be incorporated into, typically has a low processing temperature less than 250 °C. To realize the above-mentioned materials requirements for embedded capacitors, a number of materials and approaches have been investigated and evaluated.

1.6.1 Ceramics

Ceramics have long time been used as the dielectrics for capacitors. According to their crystal structure and dielectric constant, ceramic dielectrics can be classified in two different categories: paraelectrics and ferroelectrics. Paraelectrics have a relatively low dielectric constant, and their dielectric behavior is more stable and less affected by the change of temperature or frequency of electric field. Ferroelectrics are characterized by their asymmetric or polar structures. A ferroelectric is a spontaneously polarized material with reversible polarization, which is the cause of large dielectric constants. In this section, we will discuss ceramic materials and corresponding processes for thin film dielectric deposition that may be suitable for embedded capacitor applications.

1.6.1.1 Sputtered Ceramic High-κ Materials

Sputtering is a plasma assisted process where materials on a target are sputtered and deposited on a substrate by ion or neutral species bombardment, as a result of the momentum transfer from the incoming particle to the target atoms. Dielectric films from tens of nanometers to several microns may be deposited by sputtering. Unlike many other vapor phase techniques there is no melting of the material. Sputtering is used to deposit

high-κ materials for embedded capacitor applications, because it can be performed near room temperature. Ta_2O_5 can be sputtered to form a 2000 Å dielectric film with a relative dielectric constant of 23 or a capacitance density of 100 nF/cm^2 [16]. Annealing the film at 550 °C gives orthorhombic polycrystalline Ta_2O_5 film which has a higher dielectric constant of 50. Alers et al. [17] studied the sputtering of amorphous Zr-Sn-Ti-O (aZTT) as the embedded capacitor dielectric film at 200 °C. The best composition was found to be $Zr_2Sn_2Ti_6O_x$, which showed a dielectric constant of 62. Tsukada et al. [18] developed $BaZrTiO_3$ thin films with a dielectric constant of about 145 by sputtering. Takken and Tckerman [19] and Clearfield et al. [20] investigated the sputtering of Al_2O_3 films and obtained a high capacitance density of about 50 nF/cm^2. Almost all paraelectrics can be sputtered to form dielectric thin film without further processing, however, for a ferroelectric thin film, it must be annealed at high temperature after sputtering in order to obtain desirable asymmetric crystal structure. The major disadvantages of sputtering are high cost and the difficulties in fabricating capacitors over a large-area substrate.

1.6.1.2 Chemical Vapor Deposition of High-κ Materials

Chemical vapor deposition (CVD) and metal-organic chemical vapor deposition (MOCVD) are also used for fabricating high dielectric constant embedded capacitors. These methods require that the precursors be fed into an evacuated low-pressure chamber as gases. The precursors can be dissociated at a sufficiently low temperature by the energy provided by plasma, which is compatible with PCB manufacture. CVD has been used to produce ferroelectric thin films such as $SrTiO_3$ and $Ba(Sr)TiO_3$ [21, 22]. A plasma-enhanced MOCVD method has been applied to deposit and pattern $PbTiO_3$ and $Pb_xLa_{1-x}TiO_3$ films for high value capacitors, and feasibility of incorporating a low temperature MOCVD process in large area packaging is being studied [23, 24]. Recently, thin TiO_2 film with a dielectric constant of 34 and a capacitance density larger than 110 nF/cm^2 has been deposited on PWB substrates at temperatures below 180 °C [23, 24].

Misman [24] and Park [25] used MOCVD to deposit Ta_2O_5 film for embedded capacitor. Mixed oxides of Bi_2O_3 and Ta_2O_5 with dielectric constants of 20 to 40 were produced on single-crystal smooth silicon substrate [26, 27]. Because of the high cost of precursors, MOCVD is considered to be the most expensive way to deposit a dielectric thin film. Moreover, these MOCVD-deposited inorganics often exhibit high loss and the dielectric constants in these materials decrease rapidly with increasing frequencies.

1.6.1.3 Sol-Gel Ceramic High-κ Materials

Sol-gel method is another deposition process used in depositing ceramic films with high dielectric constant. At the start of the process, a homogeneous solution (sol) of precursors is formed. The precursors are commonly organometallic compounds that are dissolved in alcohol to create a homogeneous solution. The solution is gelated by reaction with water or exposure to atmosphere, and the gelation forms a polymeric, or colloidal, network. The sol-gel process allow for the deposition of dielectric thin films with a high degree of chemical homogeneity at relatively low temperatures. Sol-gel is a low cost approach for depositing high-κ thin films as compared to CVD and sputtering because no vacuum and no expensive equipment are required. This method has been employed in depositing thin film of PLZT type materials with high dielectric constant. Dimos et al. [28] reported a dielectric constant of 900 in a PLZT system. Heistand [29] developed sol-gel derived PZT materials with capacitance in the range of 1 to 5 nF on a 1 μm thick film, with a nominal dielectric constant of 1000 thus providing a good commercialization opportunity. However, a final cure at 600-700 °C is needed for sol-gel thin film to produce cubic perovskite crystal structure with high dielectric constant. This calcination temperature is much too high for applications in the organic board-compatible multi-chip module-laminate (MCM-L) technology.

1.6.1.4 Hydrothermal Ceramic High-κ Materials

Hydrothermal route is not a new technique and were largely used for the synthesis of minerals in the last century. In recent years, hydrothermal method has been used to produce ferroelectric dielectric thin films because it provides a low temperature and direct route, avoiding the high temperature calcination step required in sol-gel method. Hydrothermal process involves dissolution and reaction of precursors in hot, pressurized water. Hot water is the medium used to transmit pressure and allows the reaction to take place at a low temperature because the free energy of hydrated ions is similar to that of crystalline $BaTiO_3$. This unique characteristic enables the reaction to occur at temperature below 100 °C. Barium titantate hydrothermal syntheses are usually based upon $Ba(OH)_2$ and TiO_2 or titanium hydroxide at a high pH value in an aqueous solution of NaOH [30-35]. Vivekananadan et al. extended the hydrothermal technique to the preparation of barium titanate zirconate (BZT) [36]. Substrate with lattice structures closer to the films can help nucleate and grow defect free dielectric films. Titanium foils, titanium-alkoxide coated substrates, or titanium sputtered substrates can be used to react with $Ba(OH)_2$ solution and form $BaTiO_3$. Films reacted at 90 °C yielded a capacitance of 1.5 microfarad/cm^2 [37, 38]. Hydrothermal process-produced dielectric films are usually porous and have microcracking, as such the yield is poor.

1.6.1.5 Anodized Oxides

Anodization is a method routinely used to produce discrete capacitors such as tantalum capacitors [39, 40] and aluminum capacitors [19, 41, 42]. Besides tantalum and aluminum, other metals such as titanium, zirconium, bismuth, antimony, niobium, tungsten, and hafnium can also be anodized [39]. In recent years the anodization method has been used with vacuum deposited aluminum [43] and tantalum [26, 44] films to form thin dielectric oxide films for embedded capacitors. Sputtered tantalum films are oxidized thermally or electrolytically to make thin Ta_2O_5 capacitor films. Kapadia [44] reported anodized Ta_2O_5 films with capacitance about 200 nF/cm^2. During annodization, the final

film thickness is directly proportional to the final voltage used in the cell, and an lower-conductivity solutions allow thicker films [40]. The anodization technique is quite simple and can grow tens of nanometers thin film without defects. However, it is found that most anodizable materials have low breakdown voltages at temperatures above 100 °C.

1.6.2 Polymers

Polymers such as epoxies, silicones, polystyrenes, parylene, polyolefins, benzocyclobutenes (BCB), and polyimides (PI) can be used as the embedded capacitor dielectrics when only a low capacitance value is required. Generally speaking, polymers have very low dielectric constant, e.g., ~ 2.5 for polystyrene, ~ 2.65 for BCB, ~2.7 for parylene, ~2.72 for silicone, and ~ 3.5 for epoxy and polyimide. Most polymers used in microelectronic industry are available for applications by spin-on or various coating methods, followed by a moderate temperature cure. As such, polymer dielectrics are fully compatible with the organic PCB manufacture. Depending on the viscosity of polymers and rotation speed of spin coater, the polymer dielectric film can be as thin as a few hundreds of nanometers, which can significantly increase their capacitance density. The dissipation factor of polymers is also very low, much lower than ferroelectric ceramics. According to Equation 1.6, the energy dissipated is proportional to the dielectric loss. As such, a low dielectric loss is preferred in order to reduce the energy dissipated by a dielectric material, particularly for high frequency applications.

Epoxies are of particular interests for embedded passive application due to their perfect compatibility with manufacturing process of PCB boards, which are mostly based on epoxies, too. For epoxies, a relatively high dielectric constant can be achieved by tailoring the epoxy system. Basically, epoxy system contains three components, i.e., epoxy resin, hardener, and catalyst. By proper choice of the catalyst such as metal acetylacetonate, the dielectric constant of epoxy system can be increased significantly from 3.2 to 5.0 [45].

Most polymers have dielectric constants in the range of 2-10, however, some electroactive polymers, called ferroelectric polymers, can have a dielectric constant of above 10, because of its polar backbone. Pure polyvinylidene fluoride (PVDF) polymer has a dielectric constant of about 11 at 1 kHz/25 °C, and PVDF exhibits four relaxations at 1 KHz when temperature changes from -80 °C to 160 °C [46, 47]. Polythiourea-formaldehyde (PTUF) polymer, whose ferroelectric properties were first discovered in 1978, has a relatively high dielectric constant of 20-30 at 10 kHz/25 °C [48]. Its dielectric constant can be as high as 320 at 145 °C/10 kHz. Polyvinylidene fluoride–trifluoroethylene [P(VDF-TrFE)] copolymer (50/50) exhibits s a high dielectric constant of about 50 at 1 kHz/25 °C, after 4×10^5 Gy irradiation at 120 °C [49]. The irradiated copolymer shows a large strain under the electric field. As the irradiation process requires expensive and complicated equipment, Petchsuk et al. [50] and Yu et al. [51] synthesized polyvinylidene fluoride–trifluoroethylene-chlorotrifluoroethylene [P(VDF-TrFE-CTrFE)] terpolymers, in order to obtain a similar structure as irradiated P(VDF-TrFE) copolymer by introducing CTrFE block in the polymer. It was found that P(VDF-TrFE-CTrFE) terpolymer with VDF:Tr-FE:CTrFE molar ratio of 65:35:9 exhibits a high dielectric constant of about 60 at 1 kHz/33 °C with a dielectric loss of about 0.1. The above mentioned high-κ polymers have a non-conjugated backbone; for a conductive polymer with conjugated backbone, the dielectric can be even higher. Polymeric phthalocyanines have a large planar structure of predominantly aromatic nature, which allows the π electrons completely delocalized over the entire chain molecule. Polymeric iron phthalocyanine (FePc) shows higher dielectric constant and dielectric loss as compared to monomeric FePc[52]. KOH-treated poly-CuPc shows a dielectric constant of 800 and the dielectric loss is about 6 at 1 kHz/25 °C [53]. In the case of poly-CoPc with carboxylic end group, a high dielectric constant of about 7,500 was obtained at 100 Hz/30°C. However, the polymeric phthalocyanines usually have a high frequency dependence, e.g.

the dielectric constant of poly-CoPc decreases from 7,500 to about 86 when the frequencies increase from 100 Hz to 1 MHz [54-57].

1.6.3 High-κ Composite Dielectric Films

The approaches (sputtering, CVD, sol-gel, hydrothermal, anodization) used to deposit ceramic high-κ dielectrics can produce high capacitance density films for embedded capacitors; however, these processes also have many prominent disadvantages. They either require expensive tools or cannot be easily implemented over large PCB substrate area. Moreover, high temperature annealing or sintering (>500 °C) are often needed to improve the quality of deposited ceramic dielectric films. Such high temperature annealing process will destroy the organic PCB board, as the organic board needs to be processed under 250 °C. On the other hand, polymers have low cost and can be easily and compatibly processed, but the dielectric constant of a polymer typically is low. However, polymer-ceramic nanocomposites may have the potential to introduce high dielectric constant with low temperature thick-film fabrication process, because they can combine the advantages of high dielectric constant from the ceramic part and good processibility from the polymer part. Figure 1.13 shows the advantages and disadvantages of using polymer, ceramic filler, and polymer composites for embedded capacitors, respectively. Because of the combined advantages of polymer-ceramic composites, they have been subjected to extensive research and been selected as a major material candidate for the development of embedded capacitors inside organic substrates.

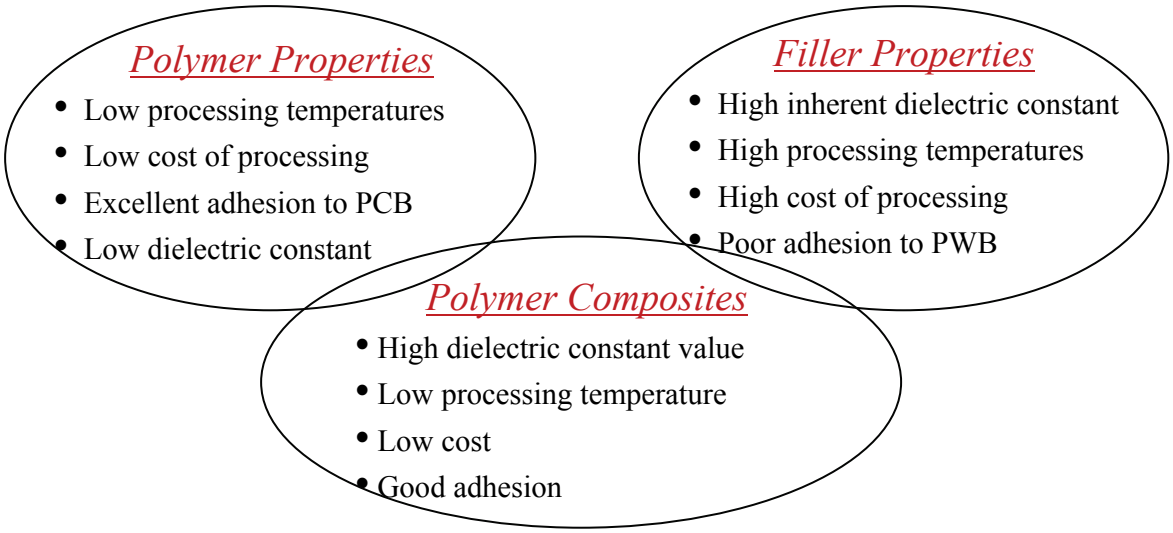

Figure 1.13 Schematic showing the advantages of polymer composites for embedded capacitors.

Das-Gupta et al. [58] first reported the study of polymer-ceramic composites as high dielectric constant material. Dielectric constant of about 100 (at 1KHz) was obtained for composite materials with different volume percentages of lead zirconate titanate (PZT) ceramic filler in polyvinylidene difluoride (PVDF) polymer matrix. Sinha and Pillai [59, 60] studied the dielectric properties of composites of PZT with polymethylmethacrylate (PMMA), polystyrene (PS), polyvinylchloride (PC) and PVDF in the weight ratio of 90:10. The dielectric constant of PVDV sample was found to have excellent temperature and frequency stability. This type of dielectric behavior is desirable for capacitor applications. These materials demonstrated the feasibility of obtaining high dielectric constant with polymer-ceramic composites, although they were not best suitable for embedded capacitors in the organic PCB board.

The NSF Microsystems Packaging Research Center at Georgia Tech was among the first to employ polymer-ceramic composites for embedded capacitors. To ensure good compatibility with organic PCB boards, which are typically made of epoxy or polyimide, epoxy and polyimide based composites have been mostly studied. Chahal et al [10] first

achieved a high dielectric constant of 65 with 58 vol% of lead magnesium niobate – lead titanate (PMN-PT) in polyimide composite. Later, Ogitani et al [61] increased the dielectric constant to 70 in an epoxy filled with 71 vol% of PMN-PT, and a dielectric constant of 74 was obtained by Agarwal et al [62] by adding bimodal barium titanate (BT) fillers into epoxy. With the combination of high-κ epoxy and bimodal filler PMN-PT/BT, Rao et al [63] achieved a dielectric of 110 at 70 vol% filler loading. Subsequently, Windlass et al [64] increased the dielectric constant to 135 by surface treatment of PMN-PT prior to the mixing of ceramic filler with epoxy. So far the highest dielectric constant of polymer-ceramic composites was reported to be 150 by Rao et al [45], with addition of 85 vol% of PMN-PT/BT in high-κ epoxy formula.

For polymer-ceramic composites, the connectivity, i.e., the microstructure arrangement of the component phases in the composite is an important parameter. Each component phase in a composite can be self-connected in zero, one, two, or three dimensions. For a diphasic system, there are ten connectivities, which can be denoted as 0-0, 0-1, 0-2, 0-3, 1-1, 1-2, 1-3, 2-2, 2-3, and 3-3, as shown in Figure 1.14 [65, 66]. A typical connectivity of polymer-ceramic composite is 0-3 composite, which indicates that ceramic fillers are dispersed without continuity in a three-dimensionally connected continuous polymer matrix. For a 0-3 composite, the dielectric constant of the material is dependent on the relative permitivitty and the volume fraction of both the polymer (ε_1, v_1) and the ceramic (ε_2, v_2). In the simplest case, the dielectric constant of a system that consists of two different homogeneous dielectrics connected in parallel (n = 1) or in series (n = -1) can be predicted by the following equation [67]:

$$\varepsilon^n = v_1\varepsilon_1^n + v_2\varepsilon_2^n \qquad \text{Equation 1.11}$$

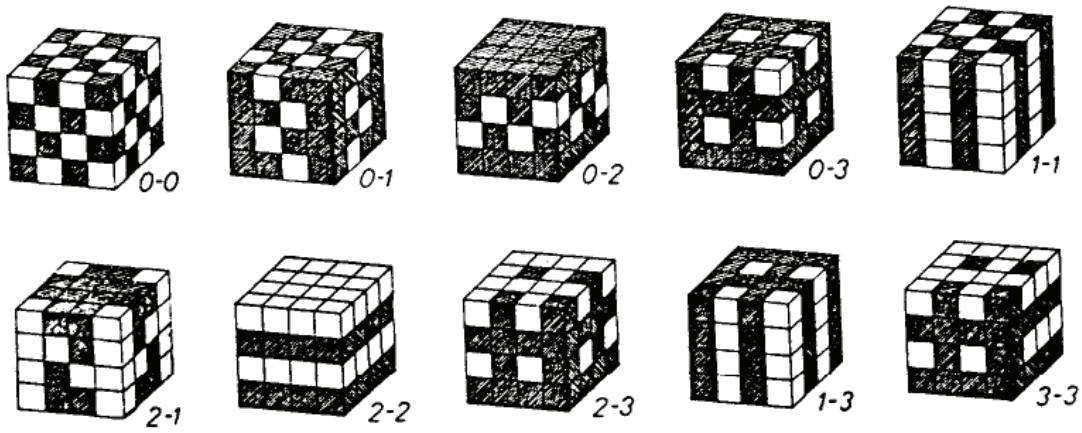

Figure 1.14 Connectivity patterns for a diphasic solid.

A commonly used equation for the prediction of permittivity of randomly dispersed 0-3 composite is Maxwell equation [68]. Maxwell expressed the effective dielectric constant (ε) for a composite system consisting of a continuous polymer phase and ellipsoidal ceramic particles as:

$$\varepsilon = \varepsilon_1[1 + \frac{nv_2(\varepsilon_2 - \varepsilon_1)}{n\varepsilon_1 + (\varepsilon_2 - \varepsilon_1)v_1}] \qquad \text{Equation 1.12}$$

where n is the aspect ratio of the ceramic particles.

Besides Maxwell equation, there are many other dielectric mixture models and formulas developed for dielectric spheres dispersed in continuous medium [69-74]. However, these proposed equations are only suitable for composites with limited ceramic filler loading level ($v_2 < 0.5$) because of the assumption of isolated spheres. When an electric field is applied to the composite, the dielectric spheres are polarized by the applied field and an individual sphere can be represented by a dipole moment. In turn, this dipole moment can locally modify the applied field in the surrounding medium. In cases of small volume fractions of spheres, the influence of this dipole field on neighboring spheres is negligible, and therefore, the prediction of dielectric properties by using the isolated sphere theory is reasonable. However, as v_2 further increases, the

interaction between the fields of the neighboring spheres must be taken into account when one estimates the effective dielectric constant of the composite.

Lichteneker [75] used a fitting factor *k* to represent this interactive effect between neighboring spheres, in order to estimate the dielectric constant of composites that have high volume fraction of ceramic loading.

$$\log \varepsilon = \log \varepsilon_1 + v_2(1-k)\log(\frac{\varepsilon_2}{\varepsilon_1}) \qquad \text{Equation 1.13}$$

where *k* is typically 0.3 for well dispersed suspensions.

Jayasundere and Smith [76] modified the Kerner model [71] to include field interactions between neighboring spheres for the case of high volume fraction of the ceramic phase, which is presented in the following equation.

$$\varepsilon_{eff} = \frac{\varepsilon_1 v_1 + \varepsilon_2 v_2[3\varepsilon_1/(\varepsilon_2+2\varepsilon_1)][1+3v_2(\varepsilon_2-\varepsilon_1)/(\varepsilon_2+2\varepsilon_1)]}{v_1 + v_2[3\varepsilon_1/(\varepsilon_2+2\varepsilon_1)][1+3v_2(\varepsilon_2-\varepsilon_1)/(\varepsilon_2+2\varepsilon_1)]} \qquad \text{Equation 1.14}$$

In order to achieve high-κ in the polymer-ceramic composites, ferroelectric ceramics are used as the filler. Titanates are well known for their ferroelectricity and extremely high dielectric constant. For example, lead magnesium niobate – lead titanate (PMN-PT) has a dielectric constant of 17, 800, and barium titanate (BT) has a dielectric constant of 2,000 - 4,500. However, there's always an environmental concern for using lead containing PMN-PT. And it should be noted that beyond a critical point, the increase of dielectric constant of ceramic filler may not necessarily increase the dielectric constant of the composites [77].

The size of ceramic particles is also a critical parameter. Finer particle size is required to obtain a thin dielectric film and to increase the capacitance density. However, extremely fine ceramic particles may leads to the change of their crystal structure and hence the loss of high permittivity [78-81]. Overall, the tetragonality of the nano-sized particles, which results in the high permittivity of ceramic powder, decreases with the

decrease of the particle size. Therefore, a trade-off must be made between the dielectric constant and film thickness by proper choosing of the filler particle size.

Generally speaking, the dielectric constant of polymer-ceramic composites increases with the filler loading. However, this may not necessarily be true due to the increase of porosity and the change of connectivity in the film at high filler loading level. Presence of agglomerates or regions where ceramic particles connect each other can greatly affect the dielectric constant of the composites. In addition to the intrinsic dielectric properties of the filler and polymer, processing methods become extremely important at high filler loading, since it will determine the distribution and packing efficiency of the composite system. A better dispersion of ceramic filler leads to a more homogeneous packing and more uniform properties of the dielectric film. And it's expected that an efficient packing gives a higher dielectric constant. Agarwal's work [62] suggests that a better packing efficiency and thus a higher dielectric constant may be obtained by using of bimodal filler and proper choice of surfactant. And the latest development of high-κ polymer-ceramic composite is based on these two methods [45, 64, 82].

1.7 Challenges and Research Objectives

1.7.1 Challenges

Polymer composite has been recognized as a promising candidate dielectric for embedded capacitors. However, despite all those advantages with polymer composites, embedded passives have not yet been extensively commercialized because material design and processing are still critical barriers to realize the embedded passive components.

To achieve dielectric constants above 50, high filler loadings above 60 vol% have to be used, which drastically deteriorates the peel adhesion strength and thermal stress reliability of the high-κ composites, inhibiting their real application as an embedded capacitor dielectric. To make the high-κ composites useful, a lower volume filler loading (≤50 vol%) has to be used, but this in turn will reduce the dielectric constant of the composites. So far the commercially available polymer-ceramic composites can only achieve a maximum dielectric constant of about 30, due to the stringent requirements of adhesion strength and thermal stress reliability. However, a much higher dielectric constant of 50-200 is required to make layout area small enough for embedded capacitors in many cases such as for decoupling. Therefore, fundamental understanding of the adhesion and thermal stress reliability of dielectric films needs to be addressed in order to obtain high dielectric constant ($\kappa>50$) embedded capacitor dielectrics that can successfully pass the adhesion and thermal stress reliability tests.

Conventional polymer-ceramic composites are not photosensitive, which requires additional processing steps and thereby increases cost in order to pattern it into desired geometry. On the other hand, a photodefinable high-k composite can be easily patterned into desired geometry so that it can save the substrate area and save the time needed for laser drilling of via holes as in conventional high-κ composites. Because ceramic nanoparticles can absorb and reflect UV light, the photodefinition capability of polymer-ceramic composites has a large difference from the pure photodefinable polymer matrix. Therefore, the photosensitivity of polymer-ceramic composites needs to be investigated and the processing conditions of photodefinable high-κ composite also need to be optimized.

While polymer-ceramic composites have shown some successful commercial applications, the dielectric constant of polymer-ceramic composites is not sufficiently high ($\kappa<100$) for many applications in the next generation electronics. To address this

issue, disruptive innovation on polymer high-κ composites needs to be explored. An approach showing good potential is the high-κ polymer-conductive filler composites based on percolation mechanism. According to scaling theory, high dielectric constant can be obtained when the actual filler loading is very close to the percolation threshold. Because the filler loading used in the percolative composites is lower than polymer-ceramic composites, a better material processibility and adhesion strength can be expected. However, due to its percolation nature, the electric and dielectric properties of a percolative composite are very sensitive to the composition. A slight change in the composition will lead to a significant change of materials properties, which impose serious challenge of producing materials with reproducible properties. In addition, the dielectric loss (tan δ) of a percolative composite usually is high, which is not desirable for high frequency applications. Fundamental understanding of the dielectric loss of the polymer-conductive filler composites needs to be obtained, and a viable method to obtain a percolative composite with reproducible high dielectric constant and low dielectric loss needs to be developed.

1.7.2 Research Objectives

This work focuses on the materials design, development, processing and optimization of polymer-based dielectric nanocomposites for high performance embedded capacitor applications. The methodology of this approach is to combine the advantages of the polymer and the filler to satisfy the fabrication (low-temperature processability), dielectric (high dielectric constant, low dielectric loss), electrical (low leakage and high breakdown), and mechanical (good adhesion and thermal stress reliability) requirements for embedded capacitors. Polymer-based dielectric materials will be compatible with the sequential buildup processes of organic substrates.

The objectives of this research include the following aspects:

- Improve the dielectric constant of polymer-ceramic nanocomposites at moderate filler loadings by a systematic approach. Effects of the matrix, fillers and dispersing agent on the nanocomposite dielectric constant will be studied in depth and these results will be crucial for the capacitor applications.
- Obtain fundamental understanding of the adhesion and thermal stress behavior of polymer-ceramic composite dielectric films and develop high dielectric constant (κ>50) embedded capacitor dielectrics that can successfully pass the adhesion and high temperature thermal stress tests. Modification of filler particle surface chemistry will be performed in order to enhance the filler-polymer and nanocomposite-substrate interaction. A secondary rubberized epoxy will be introduced into the primary continuous epoxy phase to improve the thermal stress reliability behavior of polymer-ceramic nanocomposites.
- Study the photosensitivity of polymer-ceramic high-κ composites and optimize the processing conditions of photodefinable high-κ composites. The effects of ceramic nanoparticle size, filler loading, and UV irradiation dose on SU8 epoxy photopolymerization will be systematically investigated. Embedded capacitor components using the novel high dielectric constant SU8 composite photoresist will be fabricated on flexible polyimide substrates by UV lithography method.
- Explore the dielectric behavior of polymer-carbon black super high-κ composites based on percolation mechanism and obtain the fundamental understandings of the dielectric loss of the polymer-conductive filler composites. Study the effect of processing conditions and carbon nanotubes

dispersion/orientation state on the electric and dielectric behavior of polymer-carbon nanotubes composites.

- Develop a novel low-loss high-κ percolative composite, which is a polymer hybrid filled with core-shell nanoparticles. The dielectric behavior of this novel percolative composite will be systematically investigated. Fundamental understandings will be obtained for the specific composite system that shows the combined properties of a polymer-ceramic system and a polymer-metal percolative system.

CHAPTER 2

EXPERIMENTAL

2.1 Materials

To ensure low-temperature, low-cost processibility, high-κ dielectric nanocomposites for embedded capacitors were based on polymers. Specifically, epoxy-based composites were the focus of this research because of its good compatibility with the sequential buildup processes of organic substrates. Other polymers used as polymer matrices in this research were polyimide, benzocyclobutene (BCB), silicone, and polynorbornene.

2.1.1 Epoxy

An epoxy generally refers to a molecule containing one or more 1,2-epoxide (or oxirane) groups, which are a three-member ring consisting of a oxygen bonded to two carbon atoms. In the cured resin, all of epoxide groups may have reacted and it no longer contains any epoxy group, but the cured resin is still called epoxy. Because of the strained nature of the three-member ring, epoxies are highly reactive. Epoxies are a fascinating material that has unique chemical and physical properties, which have made them the predominate thermosetting resin for electronic packaging. An epoxy is typically composed of an epoxy resin, a hardener, a catalyst, and some necessary additives.

2.1.1.1 Epoxy resin

The base epoxy resins are very important in that many ultimate material properties such as viscosity, adhesion, toughness, moisture absorption, and electrical properties are mainly determined by the base epoxy resins. The commonly used epoxy resins can be categorized in two groups: diglycidyl ether type and cycloaliphatic type.

The base epoxy resin can be liquid or solid. Liquid epoxy includes low molecular weight bisphenol A type epoxy, bisphenol F type epoxy, cycloaliphatic epoxy, and etc. The chemical structures of liquid epoxy resins used in this research are show in Figure 2.1.

Bisphenol A (Epon 828):

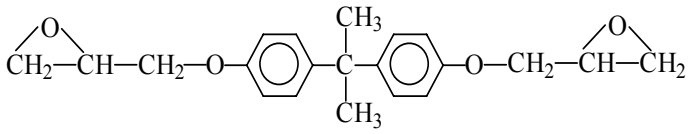

Bisphenol F (Epon862)

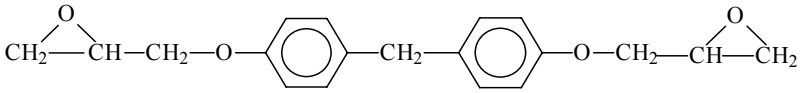

Cycloaliphatic (ERL4221)

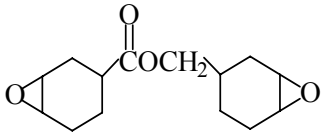

Figure 2.1 Chemical structures of liquid bisphenol A, bisphenol F, and cycloaliphatic epoxy resins.

The bisphenol-A epoxy (EPON828) with an equivalent epoxide weight (EEW) of 187 g was from Aldrich. The bisphenol-F epoxy (EPON 862) with an EEW of 171 g was from Shell Chemicals. The cycloaliphatic epoxy (ERL4221) with an EEW of 134 g was from Union Carbide.

Solid epoxy resins typically require use of solvents. After solvent evaporation, a solid film can be formed, which is desirable for some applications such as in sequential buildup and photoresist. A novolac epoxy (SU8), shown in Figure 2.2, was used in this research. γ-butyrolactone was used as the solvent. The novolac epoxy resin (SU-8) was obtained from Hexion Specialty Chemicals.

Novolac Epoxy (SU8)

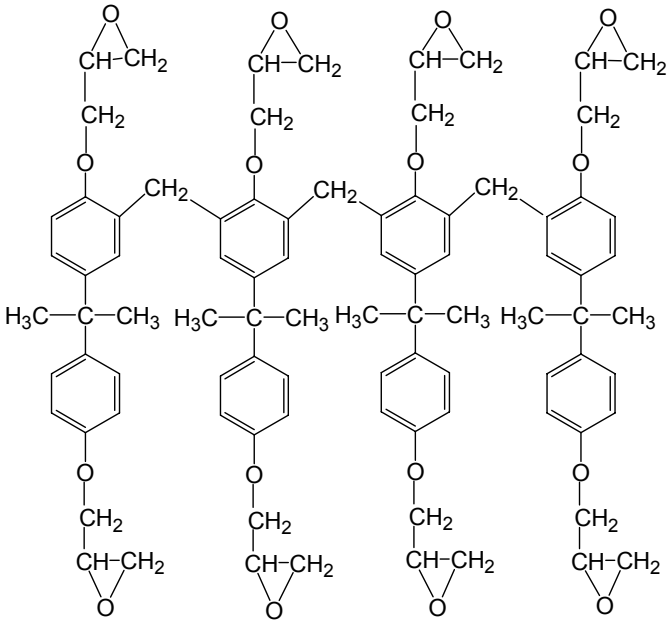

Figure 2.2 Chemical structure of SU8.

For printed circuit board applications, more complicated systems called epoxy varnish have been used. The formulations may have more than one type of epoxy in order to control their processing, thermal, and mechanical properties. The epoxy resin can have higher functionality than the linear bisphenol A or bisphenol F epoxy. For example, the epoxy shown in Figure 2.3 was in the epoxy varnish used in this work. The epoxy varnish was obtained from Oak Mitsui Technologies.

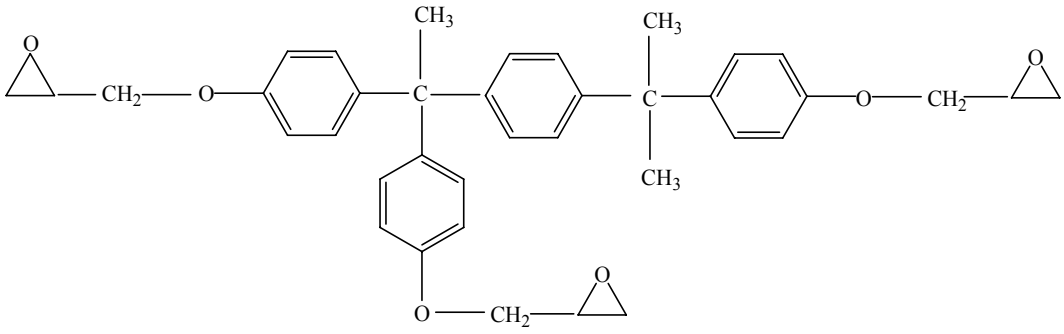

Figure 2.3 High functionality epoxy used in the epoxy varnish.

2.1.1.2 Curing Agent

To form three-dimensional thermoset networks, it is necessary to use curing agent to cure the epoxy resin. Curing can take place by either a polyaddition/copolymerization with a multifunctional curing agent or a homopolymerisation initiated by a catalytic curing agent. The curing agents for epoxy resins can be divided into three categories [83, 84]:

(1) Active hydrogen compounds, which cure an epoxy resin by polyaddition reactions. Active hydrogen compound curing agents include polyamines, carboxylic acids, anhydrides, polymercaptans, and polyphenols.

(2) Ionic initiators, which initiate homopolymerization and cure an epoxy resin through ionic or coordination polymerization. The ionic initiators include anionic initiators (such as metal hydroxides, secondary amines, and tertiary amines) and cationic initiators (such as metal halides, boron-trifluoride complexes, and coordination catalysts, i.e., metal alkoxides, metal chelates, and metal oxides).

(3) Hydroxyl crosslinkers, which cure an epoxy resin through the reaction with the secondary hydroxyls of the epoxy resin. Crosslinker is represented by a broad range of melamine-, phenol-, and urea-formaldehyde resins.

Epoxy resin systems used in electronic application are primarily cured with curing agents of the first and second type.

Depending on the specific applications of the epoxy systems, a carboxylic anhydride (4-methylhexahydrophthalic anhydride, MHHPA), a polyamine (tetraethylenepentaamine, TEPA), and a cationic initiator (triarylsulfonium, TAS) were used as the curing agents in this research. MHHPA, TEPA, and TAS were all from Aldrich Chemicals. Their chemical structures are shown in Figure 2.4.

MHHPA

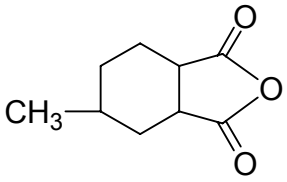

TEPA

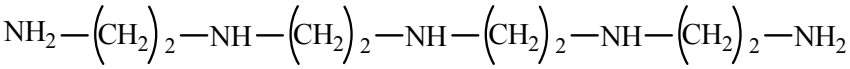

TAS

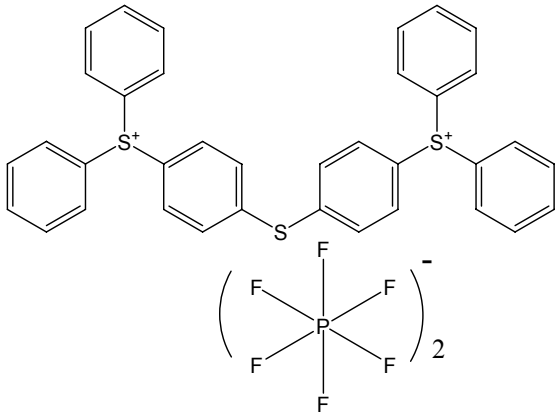

Figure 2.4 Chemical structures of curing agents MHHPA, TEPA, and TAS.

Acid anhydrides such as MHHPA are widely used epoxy resin curing agents. Most of anhydride cured epoxy systems require accelerators. Lewis bases, e.g. tertiary amines and imidazoles are often used as the anhydride accelerators. The reaction mechanism of the tertiary amine-catalyzed epoxy/anhydride reaction is given in Figure 2.5 [85]:

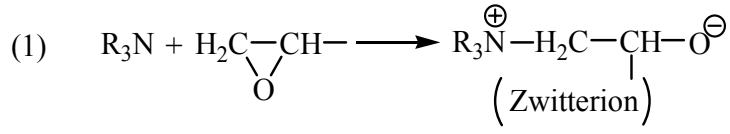

Figure 2.5 Reaction mechanism of tertiary amine-catalyzed epoxy/anhydride reaction.

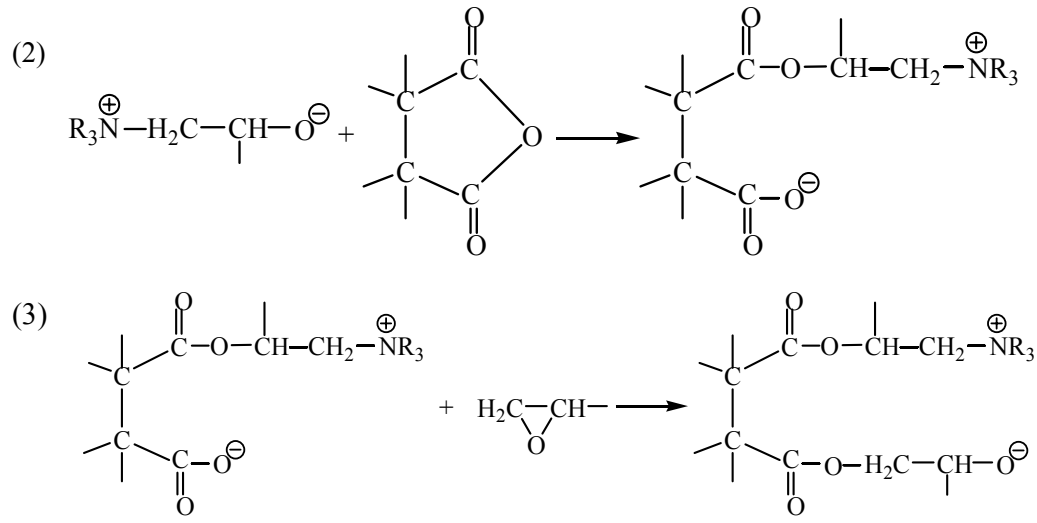

Figure 2.5 Continued.

Amine curing agents have a reactive =N–H group, which forms a chemically resistant C-N bond after curing with an epoxy resin. Epoxy resins cured with an amine have excellent chemical resistance, adhesion, hardness, and abrasion resistance. All amines, including aromatic amines and aliphatic polyamines, react with the epoxide group by addition reaction without producing any by-products. Aromatic amines require elevated temperatures to accelerate reaction, but aliphatic amine curing agent containing primary or secondary aliphatic amine groups (such as TEPA used in this research) can react with epoxide group at room temperature. Figure 2.6 shows the reaction mechanism of a primary amine curing agent with an epoxy.

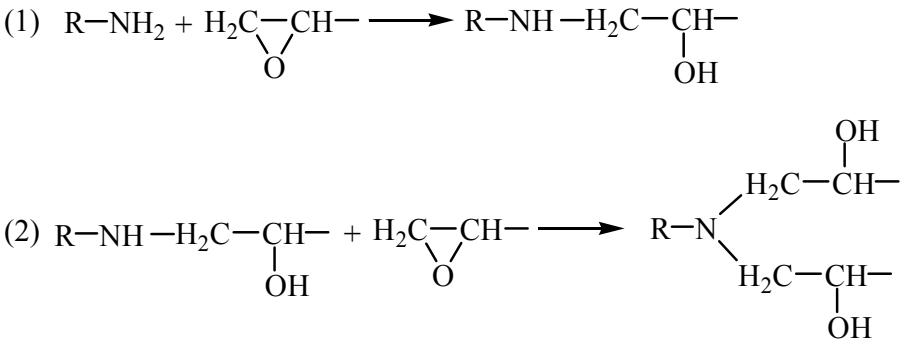

Figure 2.6 Reaction mechanism of a primary amine curing agent with an epoxy.

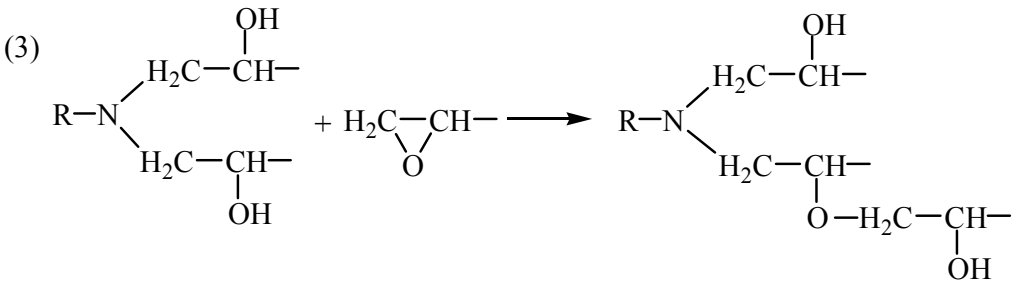

Figure 2.6 Continued.

2.1.1.3 Catalyst

The pot-life, curing temperature and time, and processability of an epoxy system are mainly determined by the curing catalysts. Tertiary amines, imidzaoles, and ureas are the most often used curing catalysts. Tertiary amines can react with epoxy resins at low temperature. As such, they are used catalytically as accelerators in elevated temperature cured system, e.g. anhydride/bisphenol A epoxy system. Imidazoles are efficient accelerators for anhydride/epoxy resin at moderate to high temperatures. The imidazole catalyst used in this research was 1-cyanoethyl-2-ethyl-4-methylimidazole (2E4MZ-CN) from Shikoku Chemicals. The chemical structure is shown in Figure 2.7. The imidazole 2E4MZ-CN reacts with an epoxy ring, forming a highly reactive alkoxide ion, which can initiate rapid anionic polymerization of epoxy resin, as shown in Figure 2.8.

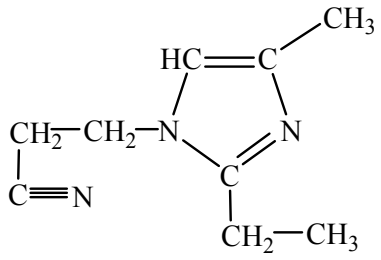

Figure 2.7 Chemical structure of 2E4MZ-CN.

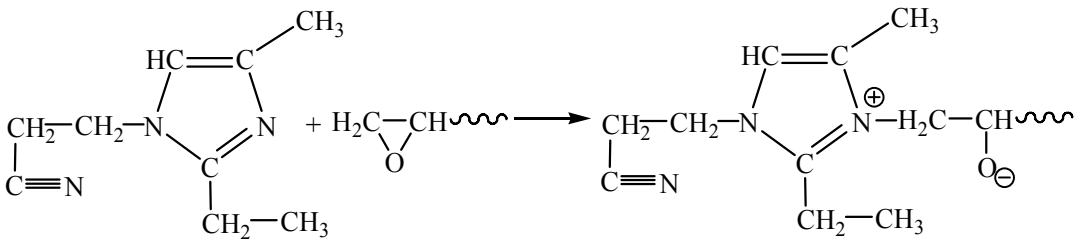

Figure 2.8 Reaction mechanism with imidazole catalyst.

Another catalyst used in this study was cobalt acetylacetonate (CoAcac). CoAcac has a β-diketone structure and has been used as latency curing agent in anhydride/bisphenol A epoxy system [86]. It is also reported that CoAcac can also enhance the dielectric constant of a cycloaliphatic epoxy resin [63]. Figure 2.9 shows the structure of cobalt acetylacetonate. The cobalt acetylacetonate was from Strem Chemicals.

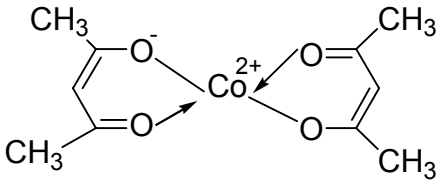

Figure 2.9 Chemical structure of cobalt acetylacetonate.

In the epoxy varnish used for printed circuit board, a urea compound was used as the curing catalyst. The urea compound, shown in Figure 2.10, has outstanding latency at ambient temperatures for more than 1 year and is widely used in one-pack formulations.

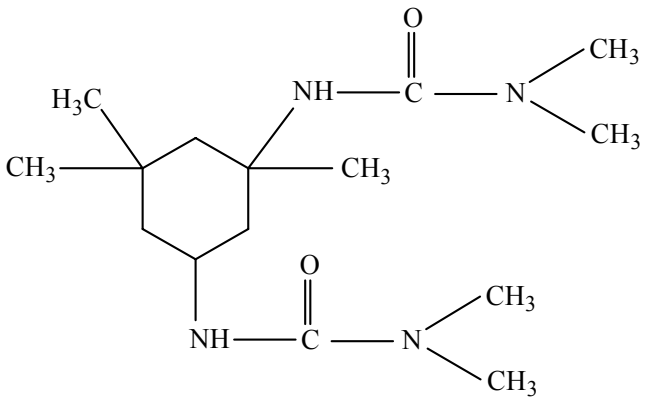

Figure 2.10 Urea curing catalyst.

2.1.1.4. Other additives

For the filled epoxy systems, adhesion promoters are often used to improve the adhesion between epoxy resin and filler, and between cured epoxy and substrates. Organo-silanes, mercaptan compounds, titanate, and aluminum chelates can be used as adhesion promoters, but the most popular ones are organo-silane compounds [87]. Table 2.1 shows the coupling agents that were used in this work to improve the adhesion of high-κ nanocomposites with Cu substrates in this research.

Table 2.1 Coupling agent used to improve the adhesion of high-κ nanocomposites with Cu substrates

Type	Chemical Name/Structure
Mercapto-type silane coupling agent	(3-mercaptopropyl)trimethoxysilane
Mercapto-type silane coupling agent	(3-mercaptopropyl)triethoxysilane
Cyanato-type silane coupling agent	3-isocyanatopropyltriethoxysilane
Amino-type silane coupling agent	3-Aminopropyltrimethoxysilane
Epoxy-type silane coupling agent	γ-glycidoxypropyltrimethoxysilane
Titanate dispersing agent	Tetra-butyl titanate
Titanate dispersing agent	Titanium acetylacetonate
Phosphate dispersing agent	Acidic phosphate ester
Functionalized Copolymer	PVP-epoxidized acrylic copolymer

2.1.2 Other Polymers

Polyimide, benzocyclobutene (BCB), silicone, and polynorbornene (PNB) were also used as polymer matrices for embedded capacitor high-κ dielectric nanocomposites in this research.

Polyimide is a high temperature engineering polymer with excellent mechanical, thermal, and electrical properties. It has been widely used as a stress buffer, passivation layer, chip bonding, and interlayer dielectric in the microelectronic industry. Polyimide

has excellent dielectric properties, with a dielectric constant of about 3.5 and a dissipation factor of about 0.002. Polyimide (PI2729) was from HD Microsystems.

Silicone as a low loss dielectric material has been widely used in the electronic industry because of its good compatibility with most device surfaces. Cured silicone has a dielectric constant of about 2.72 and a dissipation factor of about 0.0007, which is much lower than 0.02 for an epoxy. Silicone (HIPEC® Q1-4939) was from Dow Corning Incorporation. The mixing ratio of part A (resin) to part B (hardener and curing catalyst) was 1:1 for silicone in this work.

Photosensitive BCB has been developed as a thin film dielectric for microelectronics applications. It has a low dissipation factor of 0.0007 and a low dielectric constant of about 2.72. The thermal curing of BCB includes two steps. The first step involves thermally activated ring opening of BCB to form an *o*-quinodimethane, which then reacts with residue alkene in the polymer to form tri-substituted tetrahydronaphthalene. BCB needs to be cured under nitrogen purging in a Lindberg furnace. BCB (Cyclotene 4024) was from Dow Chemical Company.

Polynorbornene is produced through tightly controlled polymerization of bulky and cyclic monomers to form the saturated polymers by a transition metal catalyst. Because of its saturated hydrocarbon non-polar chemical structure, this polymer has a low moisture absorption (<0.1%), a good thermal stability (Tg ~380ºC), a very low dissipation factor of about 0.0008, and a low dielectric constant of about 2.6. PNB (Avatrel 2090P) was obtained from Promerus Electronic Materials.

2.2 Instrumentation and Characterization Procedure

2.2.1. Differential Scanning Calorimeter (DSC)

A modulated differential scanning calorimeter (DSC, Model 2920, from TA Instruments) was used to obtain cure information of the polymer formulations. The DSC can be used to investigate the dynamic curing kinetics and glass transition temperature of polymers as polymer curing and glass transition process involve heat-related events. From DSC thermograph, one can obtain the curing onset temperature, peak temperature, end temperature, heat capacity, curing degree, and glass transition temperature.

In DSC studies, a polymer sample of ~10 mg was placed in a hermetic DSC sample pan. For curing kinetics studies, the sample and a reference were heated in the DSC cell at a rate of 5 °C/min from room temperature to 300 °C under standard mode. Heat was transferred through the disk up into the sample and reference. The difference in the heat between the sample and reference was measured as differential heat flow. The differential heat flow as a function of time and temperature was recorded. For the study of the glass transition temperature of a cured formulation, about 10 mg of cured sample was placed in a hermetic DSC sample pan. The sample and a reference were then heated to 250 °C at a rate of 5 °C/min under modulated mode in order to separate the reversible and non-reversible events. N_2 purging was always applied during all experiments. The purging rate was 40ml/min for DSC cell and 110 ml/min for refrigerated cooling system (RCS).

2.2.2. Thermomechanical Analyzer (TMA)

A thermomechanical analyzer (TMA, Model 2940, from TA Instruments) was used to characterize the thermal and mechanical properties of a polymer and its high-κ composites. For expansion mode measurement, a quartz probe, applied on the top of a sample, was used to determine the dimension change under the applied load at measured temperatures. For film mode measurement, a film sample was attached to the probe by two metal clips. The static force applied on a sample was typically about 0.05 N for both expansion and film modes. N_2 purging was always used for all experiments and the

purging rate was 110 ml/min. In TMA measurement, the sample dimension change as a function of time was recorded. From these data, the coefficient of thermal expansion (CTE) and the glass transition temperature (Tg) of a sample can be obtained. The coefficient of thermal expansion can be calculated from equation 2.1.

$$CTE = K \frac{\Delta L}{L \times \Delta T} \qquad \text{Equation 2.1}$$

where K is the calibrated cell constant, L is the sample length, ΔL is the change of sample length, and ΔT is the change of temperature (°C).

For TMA measurement, a square sample with parallel top and bottom surfaces was placed on the sample stage and heated from room temperature to about 300 °C at a heating rate of 10 °C/min. The coefficient of thermal expansion was obtained according to Equation 2.1. The inflection point of thermal expansion was defined as the glass transition temperature (T_g). The CTE below TMA T_g was defined as α_1, and CTE above T_g was defined as α_2.

2.2.3 Dynamic Mechanical Analyzer (DMA)

A dynamic mechanical analyzer (DMA, Model 2980, from TA Instruments) was used to measure the mechanical properties of materials as a function of time, temperature, and frequency. This DMA can be operated under one of five operation modes to test different types of physical properties of many different materials. Moreover, each operation mode can use one of several types of clamps to meet the samples with different stiffness and geometry.

In this work, multi-frequency mode using single cantilever and film mode were used to measure the mechanical properties of bulk samples and film samples, respectively. For single cantilever measurement, the cured samples were cut into rectangular specimens with uniform dimensions by a diamond saw. The dimension of the prepared specimens was about 20 mm long, 4 mm wide, and 2 mm thick. For film mode

measurement, the sample was about 20 mm long, 4 mm wide, and about 20 μm thick. In a dynamic scan study, the sample was heated from room temperature to 250°C at a rate of 3°C/minute. The sample was under an oscillation mode with a frequency of 1 Hz. Storage modulus (E′), loss modulus (E″), tan delta (tanδ), and glass transition temperatures (Tg) at the frequency of 1 Hz can be obtained. In a frequency sweep study, the oscillation frequencies were varied from 0.1 Hz, 1 Hz, 10 Hz, to 100 Hz at each temperature when the temperature increased from room temperature to 250 °C.

2.2.4 Thermogravimetric Analyzer (TGA)

A thermogravimetric analyzer (TGA, Model 2050 from TA Instruments) was used to characterize the material mass change, either as a function of temperature, or isothermally as a function of time, in a controlled atmosphere. TGA can be used to characterize any material that exhibits a weight change due to decomposition, oxidation, or dehydration. In this work, TGA 2050 was used to investigate the oxidation (weight gain) of filler particles, degradation (weight loss) of materials coated on filler particle surfaces, and thermal stability (weight loss) of cured high-κ composite formulations. In a TGA measurement, the weight of sample, temperature, and time were recorded. The weight change percentage *WC*% can be calculated by Equation 2.2.

$$WC\% = (W_0 - W_t)/W_0 \times 100\% \qquad \text{Equation 2.2}$$

where W_0 is the initial sample mass, W_t is the measured sample mass at a certain time or temperature. A platinum sample pan was used for characterization of non-metal fillers and formulations; and a ceramic sample pan was used for characterization of metal fillers. About 20 mg sample was placed in the TGA sample pan and then heated from room temperature to desired temperature (up to 1000°C) at a rate of 20°C/minute in a nitrogen or air atmosphere. TGA curve showed the sample mass as a function of temperature or time, from which the weight change at a certain temperature can be obtained and the onset temperature of weight change can be defined.

2.2.5 Rheometer

A stress rheometer (Model AR1000, from TA Instruments) was used to characterize the rheology properties, e.g. viscosities of polymer and its high-κ nanocomposite formulations. AR1000 can be run under three operating modes, which are flow, creep and oscillation. Two different geometries were used for testing the rheology properties. The first one was the cone and plate geometry, as shown in Figure 2.11. This geometry was used with neat polymer resin systems without filler. The diameter of the cone geometry was 40 mm and the cone angle is 1.58°. The gap between the cone and plate was set to be 69μm. A continuous shear rate ramp was used in the flow mode. Ten measurements were taken in every decade between the shear rates of 0.02 s^{-1} and 1000.0 s^{-1}. Experiments were conducted at a constant temperature of 25°C. The second geometry used for testing the rheology properties of polymer and its high-κ nanocomposite was the parallel plate, as shown in Figure 2.12. Parallel plates can be used for filled resin systems. The diameter of the plate geometry was 40 mm. The gap distance between parallel plates was 200 μm and a shear rate ramp from 0.02 s^{-1} to 1000.0 s^{-1} was used. Experiments were conducted at a constant temperature of 25°C.

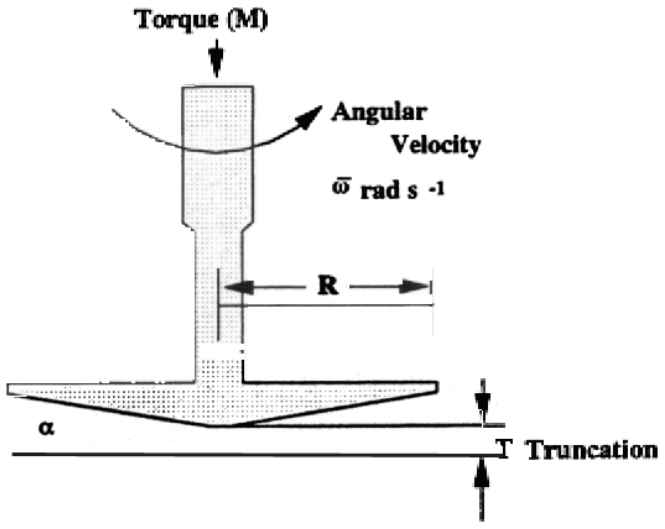

Figure 2.11 Cone and plate geometry of AR1000 rheometer.

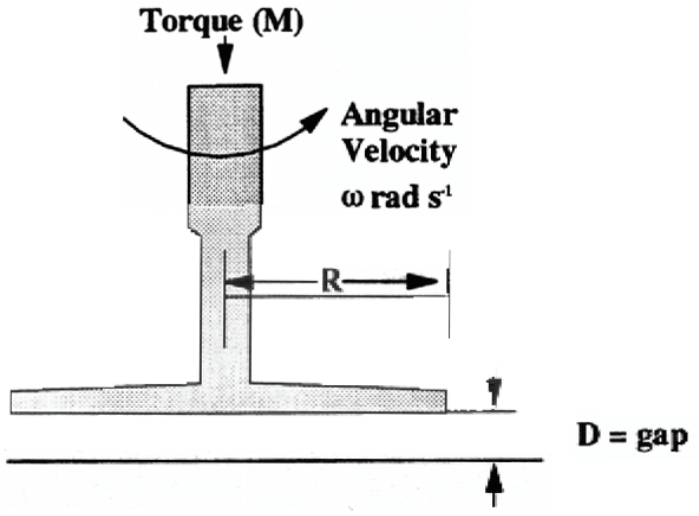

Figure 2.12 Parallel plate geometry of AR1000 rheometer.

2.2.6 Die Shear Adhesion Test

Die shear test by a die shear machine (System 552, from Royce Co.) was used to characterize the adhesion of polymer high-κ nanocomposites with substrates. 3 × 3 mm and 2 × 2 cm passivated silicon dies were cleaned according to the standard procedure mentioned in the reference. The steps were as follows: 5 min soak in terpene; 5 min soak in terpene during ultrasonic cleaning; 5 min soak in isopropyl alcohol; 5 min soak in isopropyl alcohol during ultrasonic cleaning; 3 rinses in deionized water; dry in oven at 120 °C for 30 min under vacuum. Glass beads (0.5% weight of resin) with a diameter of 75 micron were used as spacers to control the gap between the small and large dies. The small 2 × 2 mm die was uniformly coated with a thin layer of high-κ nanocomposites, and then placed on the larger 2 × 2 cm die. The die shear samples were then cured at certain temperatures dependent on the system. Die shear test was performed 12 hours after the curing of the samples. Figure 2.13 shows the diagram of the die shear test setup. The width of the shear tool was 4 mm. The shear tool was aligned to be parallel to the edge of the die, and then moved at a speed of 100 micron/sec until the die was shorn off.

9 dies were tested for each condition and the average die shear strength was reported in MPa.

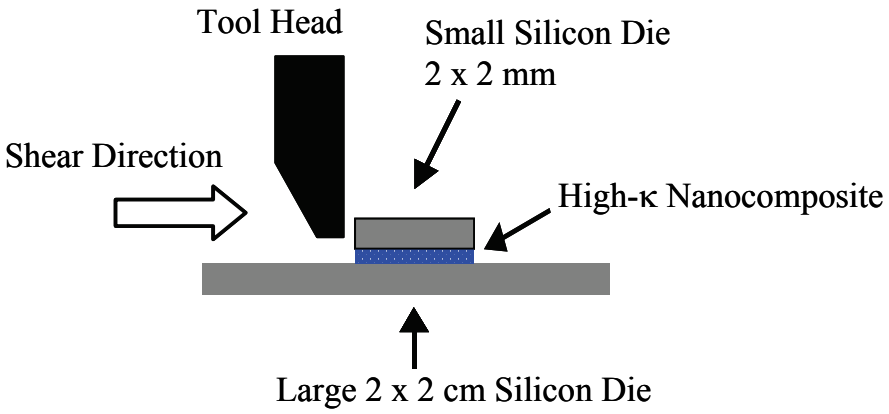

Figure 2.13 Diagram of die shear test setup.

2.2.7 Peel Adhesion Strength Characterization

A motorized 90° peel strength tester (Model MV-220, from Imada, Inc.) was used to measure the peel strength of embedded capacitor components, in order to characterize the adhesion of high-κ nanocomposite with Cu substrate. The peel tester was equipped with a DPS digital force gauge, which provides quick and accurate reading of the applied force. The laminated sample was cut into two different sizes, i.e. 0.25″×6″ and 0.50″×6″, for the peel strength tests. Six samples of each size were tested in order to calculate the peel strength of the nanocomposite with Cu. Figure 2.14 is a schematic showing 90° peel strength testing sample.

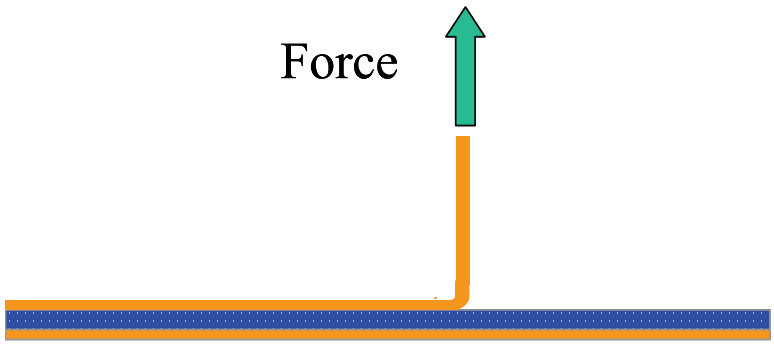

Figure 2.14 Schematic showing 90° peel strength testing sample.

2.2.8 Dielectric Analyzer (DEA)

A dielectric analyzer (DEA, Model 2970, from TA Instruments) was used to measure the dielectric constant (ε'), loss factor (ε"), and dissipation factor (tan δ = ε"/ε') of polymer and its high-κ nanocomposite formulations. In a dielectric analysis experiment, a sample is placed in contact with electrodes and subjected to an applied sinusoidal voltage. This produces polarization within the sample, causing oscillation, which is at the same frequency as the field, but with a phase angle shift (θ). The phase angle shift is measured by comparing the applied voltage to the measured current. The measured current is separated into capacitance and conductance components. Values for these components are calculated by the equations:

$$\text{Capacitance in farads}\,(C) = \frac{I_{measured}}{V_{applied}} \bullet \frac{\sin\theta}{2\pi f} \qquad \text{Equation 2.3}$$

$$\text{Conductance in simens}\left(\frac{1}{R}\right) = \frac{I_{measured}}{V_{applied}} \bullet (\cos\theta) \qquad \text{Equation 2.4}$$

where *f* is the applied frequency (Hz) and *R* is the resistivity (ohms). Dielectric constant measures the alignment of dipoles, while loss factor represents the energy required to align dipoles and move ions.

Ceramic single surface sensors, shown in Figure 2.15, were used to obtain dielectric data for the polymer high-κ formulations. The sensor was based on a co-planar, interdigitated-comb configuration of electrodes. The assembly consisted of a ceramic substrate, metal ground plate, high temperature insulating layer, screen-printed gold electrode arrays, a platinum resistance temperature detector (RTD), and electrical contact pads. In an experiment, the sensor was placed face up at the bottom of the oven. The electrode spacing and sample thickness were predetermined by the sensor. Spring-loaded electrical probes attached to the ram made contact with pads on the sensor, completing the signal circuits. For this study, samples were heated from room temperature to 250°C at a rate of 5°C/min then cooled to room temperature (~30°C).

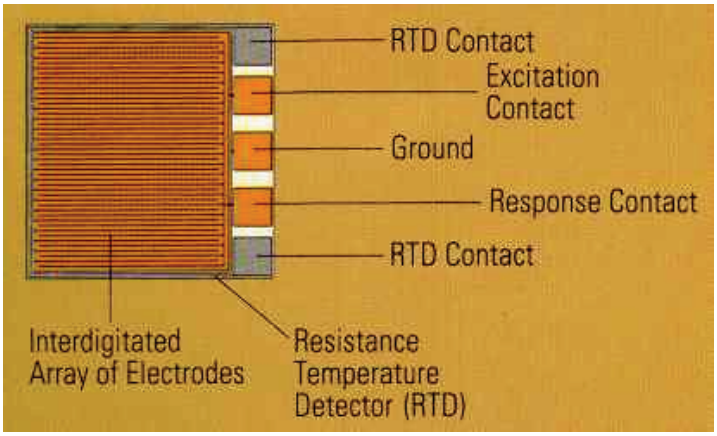

Figure 2.15 Ceramic single surface sensor.

2.2.9 LCR Meter and RF Impedance Analyzer

2.2.9.1 LCR Meter Measurement

The capacitance and conductance of embedded capacitor components was measured by a HP 4275 Multi-Frequency LCR Meter. The measurement was conducted at middle frequency range from 10 KHz to 10 MHz. To make the measurement, embedded capacitors with parallel plate geometry were fabricated. The dielectric constant of the dielectric nanocomposites was calculated from capacitance measurements. After measuring the capacitance and conductance, dielectric constant and dissipation factor (tanδ) can be calculated by Equation 2.5 and Equation 2.6.

$$C = \frac{\varepsilon_0 \varepsilon_r A}{t} \qquad \text{Equation 2.5}$$

$$\tan \delta = \frac{G}{2\pi f C} \qquad \text{Equation 2.6}$$

where C is the capacitance, G is the conductance, f is the frequency, ε_0 is the permitivity of the vacuum, ε_r is the dielectric constant, A is the area of the capacitor and t is the thickness of the capacitor.

2.2.9.2 RF Impedance Analyzer

The dielectric properties of high-κ nanocomposites at high frequencies were measured by an Agilent E4991A RF Impedance Analyzer. The impedance analyzer used the RF I-V approach for highly accurate impedance measurement in the RF frequency range. The measurement frequencies of the impedance analyzer ranged from 1 MHz up to 3 GHz. This technique directly measured voltage and current at the device under test and thereby can achieve higher and wider impedance measurement range. A specific test fixture for dielectric measurement was required. The dielectric measurement employed the parallel plate method for the dielectric constant and dielectric loss characterization. The samples for the measurement had a diameter of about 3.0 mm and a thickness of about 1.0 mm.

2.2.10 Surface Profiler

The thickness of a dielectric material was measured by a KLA-Tencor P-15 profiler. The P-15 profiler is a highly sensitive surface profiler that accurately measures step height. The vertical feature can be up to 326 μm. Measurements were made electromechanically by moving the sample beneath a diamond-tipped stylus. The stage moved the sample beneath the stylus according to the desired scan length, speed, and stylus force. Surface variations caused the stylus to be translated vertically and the instrument detected this motion.

2.2.11 X-Ray Diffractometer

The X-ray diffraction (XRD) patterns of filler particles were characterized by an X-ray powder diffractometer (PW 1800, from Philips Co.). The measurement was conducted at a scanning rate of 0.02°/s in the 2θ range from 10 to 110 with a Cu-Kα radiation (λ~0.154178 nm). XRD was used to investigate the crystal structure of filler particles and to calculate the size of particles.

2.2.12 Scanning Electron Microscope (SEM)

A thermally-assisted field emission (TFE) scanning electron microscope (SEM, Model LEO1530) was used to investigate the microstructure of high-κ nanocomposite materials. LEO 1530 is a state-of-the-art SEM, yielding 1 nm resolution at 20 kV and 3 nm at 1 kV. The SEM was used to study the dispersion uniformity of the filler particles, the size of the agglomerate, and the connectivity between filler particles. The dispersion of nanofiller particles had dramatic affect on the electric and dielectric properties of high-κ nanocomposite. For SEM characterization, the cross section of samples was polished before observation. Since dielectric materials were non-conductive, a thin layer of gold (~20 nm) was sputter coated on the sample surface in order to obtain good images. However, for the study of the dispersion state of CNTs in the composites, no gold coating was applied on the top of observation plane. Instead, a relatively low voltage of 1.5 kV was used in the SEM observations. Because the diameter of the CNTs was very small, a gold coating can make it very difficult to observe the CNTs.

2.2.13 Transmission Electron Microscope (TEM)

Two transmission electron microscopes were used in this work. JEOL 100CX II transmission electron microscope, operating at 100 kV, was used to observe the nanofiller particle size and size distribution. A JOEL 4000EX high-resolution transmission electron microscope (HRTEM), operating at 400 KV, was used to analyze the particle size of core-shell particles and the thickness of the shell layer. The JOEL 4000 EX has a point-to-point image resolution of 0.18 nm, and it uses a top-entry specimen stage for high mechanical stability.

2.2.14 Fourier Transformed Infrared Spectroscopy (FTIR)

The surface chemistry of filler nanoparticles was characterized by an FTIR (Magna IR 560, from Nicolet). The filler particles were first dried in an oven at 100ºC for

2 hours, and then KBr pellets were prepared with the dried particles. The spectrum was collected in the range from 4000 to 400 cm^{-1}.

2.2.15 UV-Vis Spectroscopy Characterization of Nanoparticles

The UV-Vis Spectroscopies of ceramic nanoparticles were characterized by a UV-Vis spectrophotometer (DU520, Beckman), from the wavelength of 300 to 800 nm.

2.2.16 Reliability Test

2.2.16.1 85°C /85RH Aging

For the 85°C/85RH aging test, the embedded capacitor components were placed in an environmental chamber at 85 °C and 85% relative humidity (RH) for 1000 hours. The dielectric properties of embedded capacitor components after 85/85 aging were measured at room temperature.

2.2.16.2 Thermal Cycling

Air to air thermal cycling (AATC) was used to test the reliability of embedded capacitor components. The temperature was from -55°C to 125°C with a dwell time of 10 minutes at each extreme and a ramp time of 10 minutes. The embedded capacitors were subjected to 1000 thermal cycles for the thermal cycling test, and the dielectric properties of the embedded capacitor components were tested at room temperature.

CHAPTER 3

LARGE-AREA PROCESSABLE, EPOXY-BARIUM TITANATE NANOCOMPOSITE-BASED, HIGH-K THIN FILMS FOR HIGH PERFORMANCE EMBEDDED CAPACITORS

3.1 Introduction

Higher performance, lower cost, and smaller size are the major driving forces of the next generation electronic systems. One of the most promising avenues to meet these requirements is the embedded capacitor technology. By combining the low cost, low temperature processability of polymers with the desirable electrical and dielectric properties of ceramic fillers, polymer-ceramic nanocomposites have been identified as the major dielectric materials for embedded capacitors [9, 45, 61-64, 77, 82, 88, 89]. For polymer-ceramic nanocomposite, a common method to increase its dielectric constant (κ) is to increase the ceramic filler loading. Chahal et al [10] first achieved a high dielectric constant of 65 with 58 vol% of lead magnesium niobate – lead titanate (PMN-PT) in polyimide composite. Later, Ogitani et al [61] increased the dielectric constant to 70 in an epoxy filled with 71 vol% of PMN-PT, and a dielectric constant of 74 was obtained by Agarwal et al [62] by adding bimodal barium titanate (BT) fillers into epoxy. With the combination of high-κ epoxy and bimodal filler PMN-PT/BT, Rao et al [63] achieved a dielectric of 110 at 70 vol% filler loading. Subsequently, Windlass et al [64] increased the high dielectric constant to 135 by surface treatment of PMN-PT prior to the mixing of ceramic filler with epoxy. So far the highest dielectric constant of polymer-ceramic composites was reported to be 150 by Rao et al [45], with addition of 85 vol% of PMN-PT/BT in high-κ epoxy formula.

In these studies however, to achieve dielectric constants above 50, high filler loadings about 60 vol% have been used, which deteriorates the processability and leads to a drastic decrease of the adhesion of high-κ nanocomposite to the Cu electrodes. The decrease of adhesion strength at high filler loading subsequently leads to the failure of embedded capacitors during PCB manufacturing and reliability tests, inhibiting their real application as an embedded capacitor dielectric.

Particularly, embedded capacitor components need pass several reflow processes during the course of PCB manufacturing, and high temperature reliability is a crucial parameter of high-κ nanocomposites for embedded capacitors. For a typical multilayer PCB, the reflow can be as many as six times. Reflow processes are used to form interconnects in a PCB board. Figure 3.1 shows a typical reflow temperature profile for Sn/Pb eutectic solder bumps that consists of four temperature zones: preheating zone, soaking zone, reflow zone, and cooling down zone. The peak temperature is typically up to 235 °C for Sn/Pb interconnects.

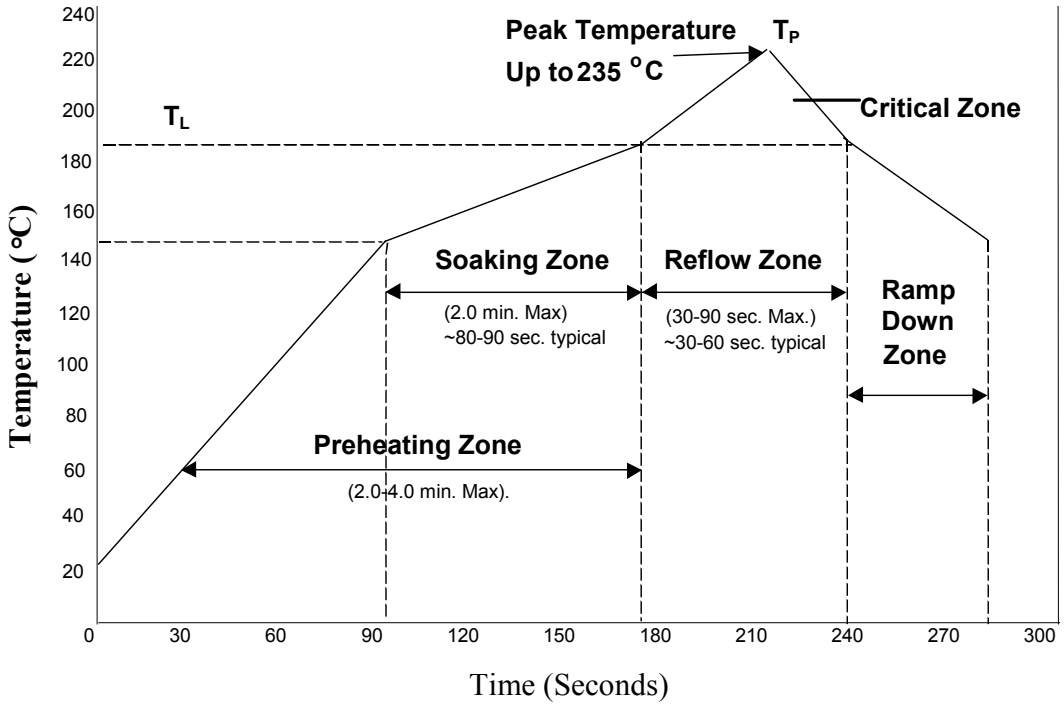

Figure 3.1 Reflow temperature profile for Sn/Pb eutectic solder bumps.

As lead is now banned in Europe and in Japan, lead-free solder is being used, which requires a much higher reflow temperature up to 270 °C. Such a high reflow temperature results in a high thermal stress in the high dielectric constant nanocomposites, which causes failure of embedded capacitor components. To qualify an embedded capacitor component, a high temperature (>280 °C) thermal stress reliability test is often used in the PCB industry to characterize the thermal stress reliability of polymer-ceramic high κ nanocomposites. Such demanding requirements of high temperature reliability of embedded capacitor components restrict the maximum applicable filler loading of nanocomposites and thereby limit their highest dielectric constants. Typically, the ceramic filler loading should be much lower than 50 vol% in order to successfully pass the high temperature thermal stress reliability test. Such a low filler loading consequently leads to a low dielectric constant of polymer-ceramic nanocomposites in the commercial products. Currently, polymer-ceramic high-κ nanocomposites are commercially available from 3M, Dupont, and Oak-Mitsui. The specifications of these materials are summarized in Table 3.1. The highest dielectric constant of these commercial products is only up to 30, even though the reported dielectric constant of polymer-ceramic nanocomposites can be as high as 150 at extremely high filler loadings (~ 85 vol%) [45].

Table 3.1 Specifications of commercially available polymer-ceramic high-κ nanocomposites

	3M (C-Ply™)	**DuPont (HK™)**	**Oak-Mitsui (Faradflex™)**
Capacitance Density	**0.9 – 1.75 nF/cm^2 (@ 1 kHz)**	**0.12-1.75 nF/cm^2 (@ 1MHz)**	**0.15-1.7 nF/cm^2 (@ 1 MHz)**
Thickness	**8μm-16μm**	**8 – 25 μm**	**8-24 μm**
Dielectric constant	**16**	**3.4 - 15**	**4.4-30**

Restrained by poor adhesion and poor thermal stress reliability at high filler loadings, so far the commercially available polymer-ceramic composites only have a maximum dielectric constant of about 30. However, a high dielectric constant of about 50-200 will be needed to make layout area small enough for embedding applications in the next generation electronic systems.

Our objective in this study is to design and develop high dielectric constant ($\kappa>50$) embedded capacitor composite formulations with a moderate volume fraction of ceramic filler that give good adhesion, good thermal stress reliability and good large area processibility at low processing temperature (<200°C). The material formulations were systematically studied, in order to increase the dielectric constant to above 50 at the lowest ceramic filler loading. Effects of high-κ polymer matrix, bimodal fillers, and dispersing agent on the dielectric properties of BT nancomposites were investigated. To improve the adhesion of epoxy-BT nanocomposites whist keeping the high dielectric constant of BT nanocomposites provided by the dispersing agent, the BT nanoparticles were refluxed and functionalized with acidic phosphate ester before being formulated in the epoxy matrix. Thermogravimetric Analyzer (TGA) and Fourier Transformed Infrared Spectroscopy (FTIR) were used to characterize the functionalized particle surfaces. The high dielectric constant nanocomposite with 50 vol% functionalized BT filler was formulated and the adhesion, thermal stress reliability, dielectric properties, and mechanical properties of the nanocomposites were characterized. To further improve the thermal stress reliability of nanocomposites at the filler loading of 50 vol% and pass the high temperature reliability test, the epoxy matrix was modified with a secondary rubberized epoxy, which formed isolated flexible domains (island) in the continuous primary epoxy phase (sea). The effects of sea-island structure on the thermal mechanical properties, adhesion, and thermal stress reliability of embedded capacitors were systematically evaluated. The optimized, rubberized nanocomposite formulations had a high dielectric constant above 50 and successfully passed the stringent thermal stress

reliability test. The leakage current, breakdown voltage, and frequency response of the developed high dielectric polymer-ceramic nanocomposites were characterized.

3.2 Experimental

3.2.1 Materials

A proprietary epoxy varnish for printed circuit boards (PCBs) was used as the polymer matrix for high-κ polymer nanocomposites. The varnish contained two epoxidized copolymers of phenol and aromatic hydrocarbon, a phenolic resin, a polyamide, and a dimethyl urea compound in a solvent mixture of ethanol, acetone, and methyl ethyl ketone. No additional curing agent or catalyst was needed for the varnish and this varnish is room temperature stable for at least 12 months. Use of the epoxy varnish can ensure good compatibility of a high-κ nanocomposite with PCB boards as the embedded capacitors will be buried inside the PCBs. Figure 3.2 DSC shows the curing profile of epoxy varnish. The peak curing temperature was about 169.18 °C. Figure 3.3 shows the DSC heat flow and reversible heat flow of cured epoxy varnish. From the reversible heat flow curve, it was found the cured epoxy varnish had a glass transition temperature of about 161.15 °C. Figure 3.4 shows the DMA characterization of cured epoxy varnish. The DMA characterization was conducted under film mode. The storage modulus of cured epoxy varnish was about 2.7 GPa, and the glass transition temperature from DMA was about 156.62 °C, which was slightly lower than that from DSC characterization.

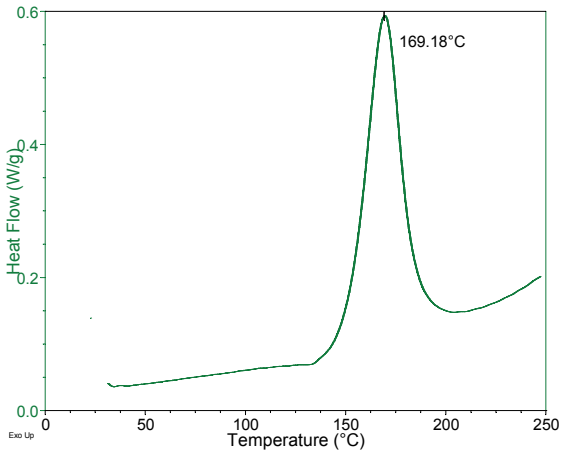

Figure 3.2 DSC curing profile of epoxy varnish.

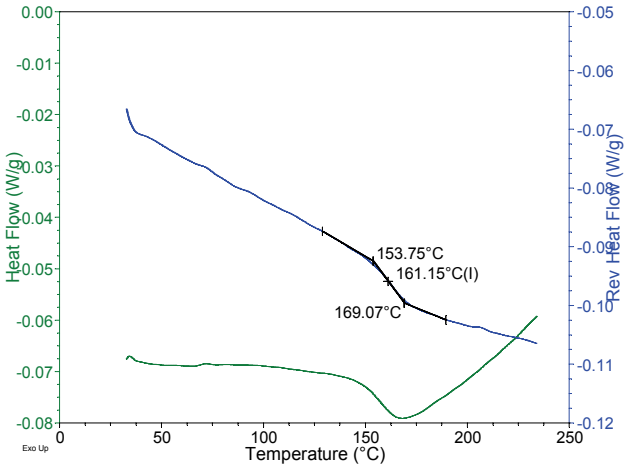

Figure 3.3 DSC heat flow and reversible heat flow of cured epoxy varnish.

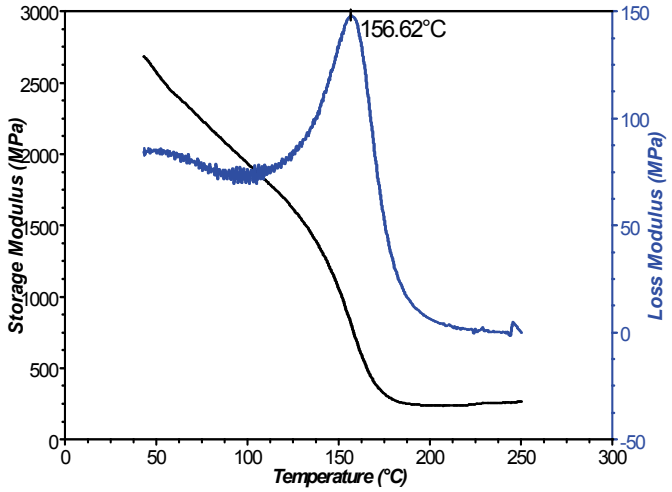

Figure 3.4 DMA characterization of cured epoxy varnish.

The fillers used in the dielectric composites were two spherical barium titanate (BT) powders. One had a nominal particle size of 590 nm, and another 65 nm. The 65 nm BT nanoparticles had a polydispersity of particle size, ranging from 40 nm to 120 nm, as shown in Figure 3.5. The polydispersity of BT particles can increase the packing efficiency of filler in a composite. XRD pattern of the 65 nm BT nanoparticles is shown in Figure 3.6. An acidic phosphate ester was used as the dispersing agent to enhance the dispersion of BT nanoparticles in the epoxy varnish.

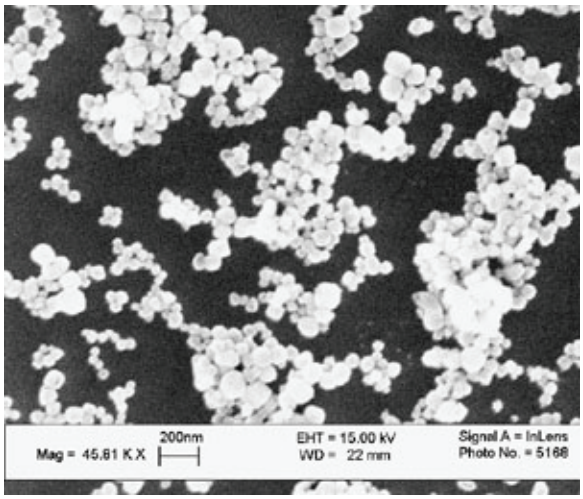

Figure 3.5 SEM images of 65 nm BT nanoparticles.

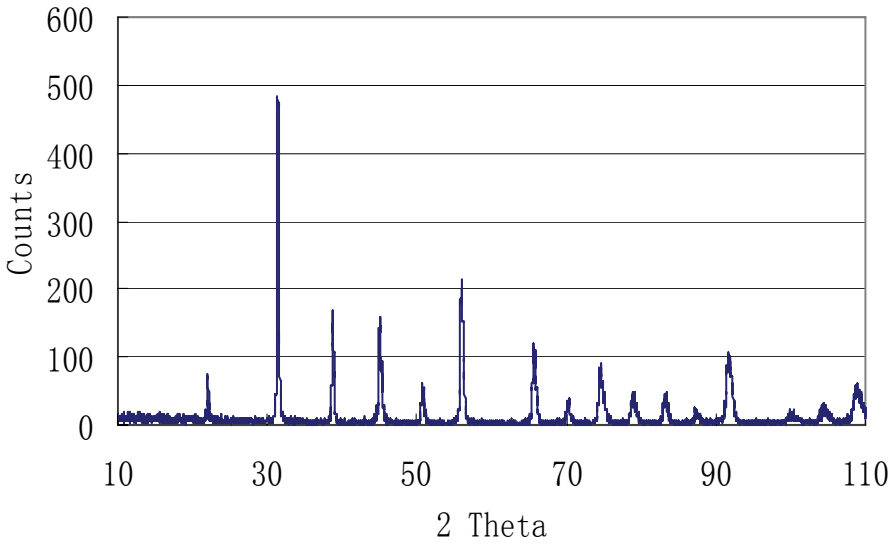

Figure 3.6 XRD pattern of 65 nm BT nanoparticles.

3.2.2 Sample Preparation and Characterization

3.2.2.1 Lamination of Composite-Coated Cu

The epoxy varnish-BT nanocomposites were first ultrasonicated for 1 hour, and then ball milled with zirconia beads at the rate of 220 rpm for 48 hours. Lamination process was used to prepare embedded capacitor components. This process is capable of fabricating capacitor components over a large area (e.g. 12″×12″). First, the ball milled high-κ composites were deposited on 12″×12″ Cu foils by bar coating method. After baking and solvent evaporation, two pieces (cut in 6″×6″ squares for easy handling) of the high-κ nanocomposite coated Cu foils were laminated together at an optimized temperature and pressure for 50 minutes. Figure 3.7 shows the lamination temperature profile for embedded capacitors. The dielectric thickness was mainly determined by the viscosity of high-κ nanocomposite and the size of coating bar. Typically, the laminated dielectric nanocomposite thickness was about 15 μm.

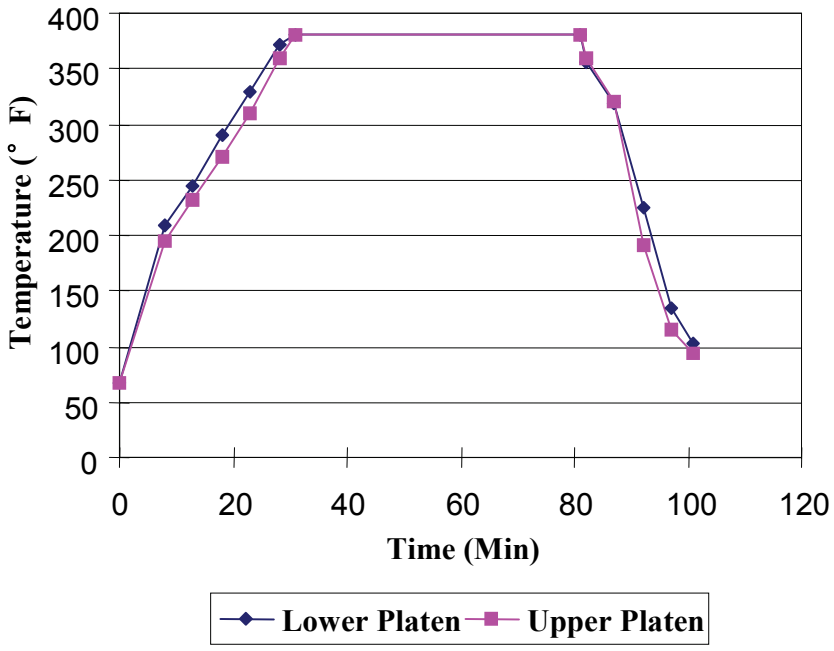

Figure 3.7 Lamination temperature profile.

3.2.2.2 UV Lithography Definition of Embedded Capacitors

To measure the electrical and dielectric properties of capacitor components, the 6″×6″ laminates were patterned by photolithography method. Because the Cu foil was of 1 oz (35 μm) thickness, spin-on resist films, which usually is only a few micron thick, do not have sufficient thickness to well protect the electrode area during the etching of Cu foil. Therefore, we used a 30 μm thick, negative dry resist films instead in the UV lithography. The dry resist films were applied on both sides of the capacitor laminates, and then laminated at 160 °C, 5 atm for 60 s, and 170 °C, 3.5 atm for 30 s. One side of the sample was exposed to 365 nm UV light through a quartz mask for 50 s, by a Karl Suss MA-6 Mask Aligner. The exposed sample was baked at 110 °C for 5 minutes, and then developed in 1 wt% Na_2CO_3 aqueous solution. The unprotected Cu was removed by a saturated $FeCl_3$ etching solution. The sample was rinsed with deionized water for a couple of times, and then the residue photoresist was stripped with 3 wt% NaOH aqueous solution. Figure 3.8 is a schematic showing the process flow for fabricating embedded capacitor components by UV photolithography method. Figure 3.9 shows the image of embedded capacitors patterned by UV lithography method. The top electrodes have a diameter of 0.5″.

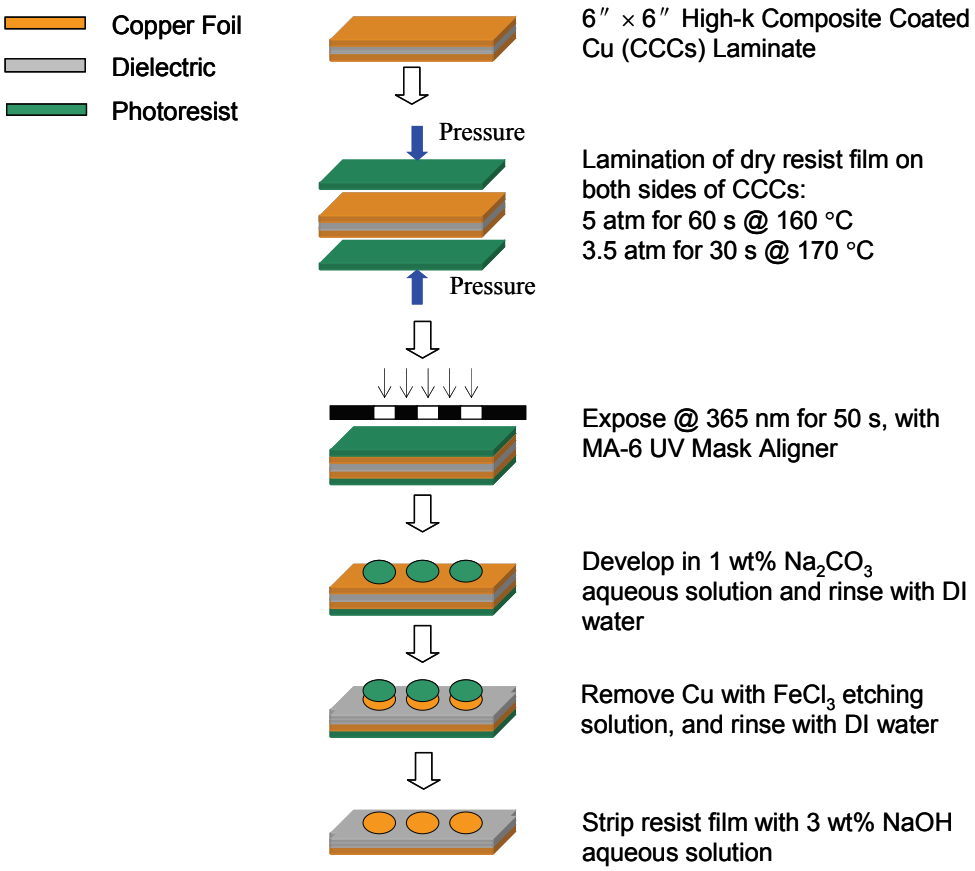

Figure 3.8 Schematic showing the process flow for fabricating embedded capacitor components by UV photolithography method.

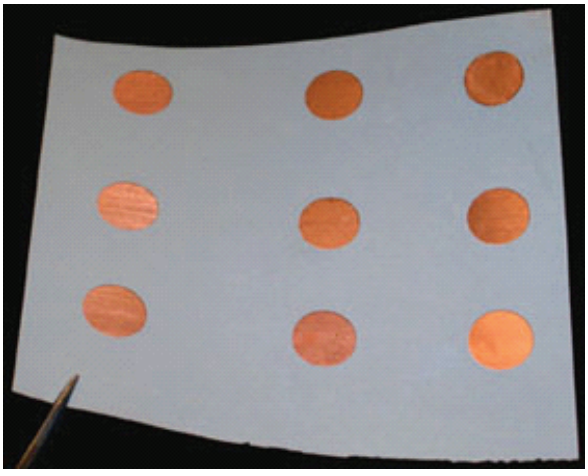

Figure 3.9 Image of an embedded capacitor test vehicle patterned by UV lithography method.

3.2.2.3 Dielectric Properties Measurement

The capacitance and dissipation factor of the capacitor were then measured with an HP 4263A LCR meter, at the frequency from 10 KHz to 10 MHz. However, all data reported were for 10 KHz unless specified.

3.2.2.4 Peel Strength Characterization

The peel strength of embedded capacitor components was measured by a 90° peel strength testing equipment, in order to characterize the adhesion of high-κ nanocomposite with Cu foil. The laminated sample was cut into two different sizes, i.e. 0.25″×6″ and 0.50″×6″, for the peel strength tests. Six samples of each size were tested in order to calculate the peel strength of the nanocomposite with Cu.

3.2.2.5 Thermal Stress Reliability Test

To characterize the thermal stress reliability of embedded capacitor components, the 6″×6″ laminate was cut into 2″×2″ squares, which were than dipped in 288 °C solder bath for 6 times, 20 seconds each time. If the first sample successfully passed the six-time thermal stress test, another sample would be tested with the same procedure. The laminate successfully passed the thermal stress reliability test only when both samples passed the test.

3.2.2.6 Microscope Observation

The morphologies of high-κ composites were observed by a field emission scanning electron microscopy (FESEM, LEO 1530). Cross section of samples was polished before observation.

3.2.2.7 X-Ray Diffractometer

The X-ray diffraction (XRD) patterns of filler particles were characterized by an X-ray powder diffractometer (PW 1800, from Philips Co.). The measurement was

conducted at a scanning rate of 0.02°/s in the 2θ range from 10 to 110 with a Cu-Kα radiation (λ~0.154178 nm).

3.2.2.8 Thermogravimetric Analysis (TGA)

Thermogravimetric analysis was conducted with a TGA 2050 (from TA Instruments) under air atmosphere. The heating rate was 10 ºC/min.

3.2.2.9 DSC Measurement

The curing profiles of selected polymers were studied by a modulated differential scanning calorimeter (DSC, Model 2920, from TA Instruments) at a heating rate of 5 ºC/min under nitrogen atmosphere.

3.2.2.10 Thermomechanical Analysis

The coefficient of thermal expansion (CTE) and the glass transition temperature (Tg) of the laminated dielectric nanocomposites were characterized in film mode using a Thermomechanical Analyzer (TMA, Model 290, from TA Instruments). Thin film sample was prepared by removing Cu from both sides of a laminate with a saturated $FeCl_3$ etching solution. The sample was heated from room temperature to 250 ºC at a rate of 5 ºC/min under a nitrogen atmosphere.

3.2.2.11 Dynamic Mechanical Analysis

A Dynamic Mechanical Aanalyzer (DMA, Model 2980, TA Instruments) was used to study the dynamic moduli and glass transition temperature of laminated dielectric nanocomposites. Thin film sample was prepared with the method as for TMA characterization. The measurement was conducted in a single cantilever mode at 1 Hz sinusoidal strain loading. The sample was heated from room temperature to 250 ºC at a rate of 3 ºC/min in the DMA furnace.

3.2.2.12 Fourier Transformed Infrared Spectroscopy (FTIR)

The surface chemistry of the BT nanoparticles was characterized by an FTIR (Magna IR 560, from Nicolet). The BT particles were first dried in an oven at 100ºC for 2 hours, and then KBr pellets were prepared with the dried BT particles. The spectrum was collected in the range from 4000 to 400 cm^{-1}.

3.3 Results and Discussion

3.3.1 A Systematic Approach to Improve the Dielectric Constant of Polymer-Ceramic Nanocomposites at Moderate Filler Loadings

A high dielectric constant of about 50-200 will be needed to make layout area small enough for embedding applications in the next generation electronic systems. However, restrained by poor adhesion and poor thermal stress reliability at high filler loadings, so far the commercially available polymer-ceramic composites only have a dielectric constant of up to 30. In order to increase the dielectric constant to 50 at moderate filler loadings, we first systematically studied the factors that may affect the dielectric properties of polymer-ceramic nanocomposites.

3.3.1.1 Effect of High-κ Polymer Matrix

The dielectric properties of polymer-ceramic composite are affected by the dielectric constant [63, 88] and the volume fraction [10, 45, 61-64, 77, 88] of the polymer matrix. The polymer used in this study was a proprietary epoxy varnish for printed circuit boards, which has a dielectric constant of about 3.9. To improve the dielectric constant of polymer-ceramic nanocomposites, a β-diketone chelating agent was used to modify the epoxy varnish in order to increase the dielectric constant of the polymer matrix. Figure 3.10 shows the chemical structure of β-diketone chelating agent. β-diketone can be used as a latency catalyst for a bisphenol-A type epoxy system [86], and it can also enhance the dielectric constant of a cycloaliphatic epoxy resin [63]. The addition of β-diketone

can change the curing profile of our epoxy varnish system as well. Figure 3.11 shows that 5 wt% chelating agent reduces the curing peak temperature of epoxy varnish from 176 °C to 169 °C. The exothermic heat also increases slightly from 112 J/g to 128 J/g due to the addition of chelating agent.

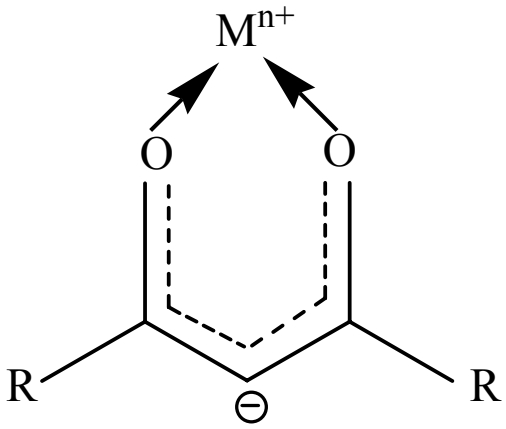

Figure 3.10 Chemical Structure of β-diketone chelating agent.

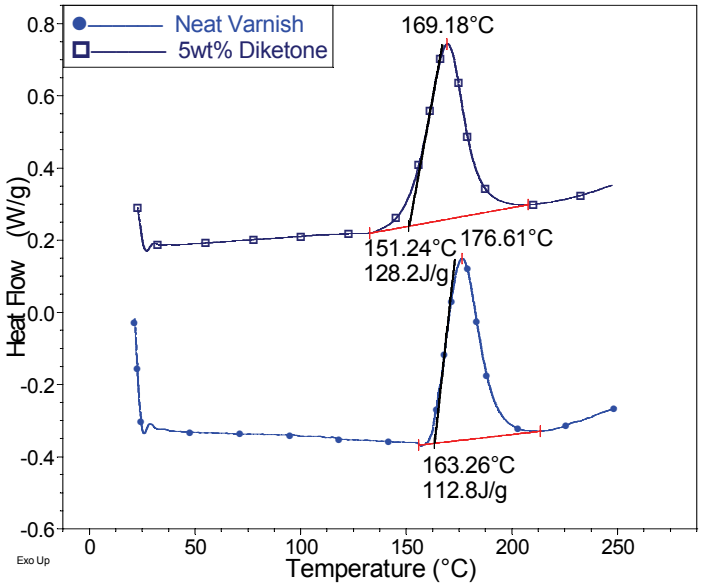

Figure 3.11 Effect of β-diketone chelating agent on the curing behavior of epoxy varnish.

The dielectric properties of β-diketone modified epoxy varnish were studied. Figure 3.12 shows the effect of β-diketone chelating agent on the dielectric constant and dissipation factor of the epoxy varnish. The dielectric constant of modified epoxy varnish

increases with the concentration of the β-diketone chelating agent. Addition of 5 wt% chelating agent can enhance the dielectric constant of the epoxy varnish from 3.9 to 5.0. Because of its highly conjugated structure, the addition of β-diketone in an epoxy can enhance the polarizability and thereby the dielectric constant of the epoxy. The dissipation factor of the modified epoxy varnish slightly increases, but is still at a low level.

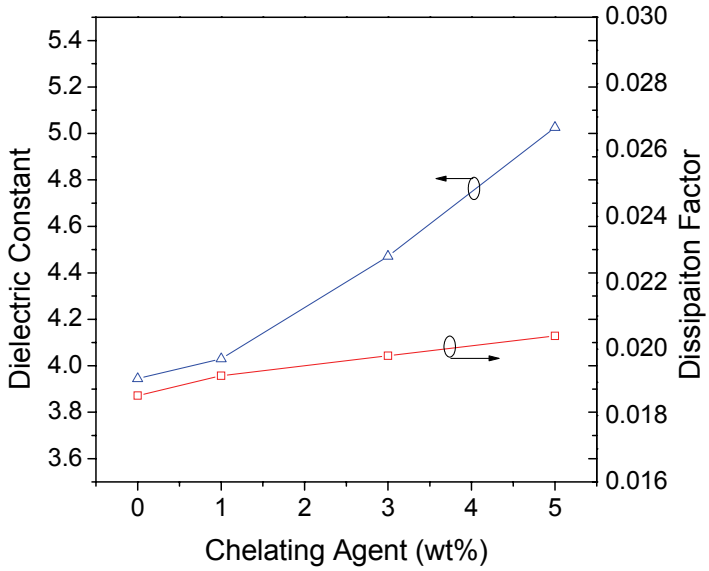

Figure 3.12 Effect of β-diketone chelating agent on the dielectric properties of epoxy varnish.

BT nanocomposites were formulated with modified epoxy varnish, and embedded capacitors based on these formulations were fabricated and characterized. Figure 3.13 shows the effect of β-diketone chelating agent on the dielectric properties of epoxy varnish-BT nanocomposites, which had a loading of 45 vol% 590 nm BT particles as the filler and 1 wt% (to BT) acidic phosphate ester as the dispersing agent. The dielectric constant of epoxy varnish-BT nanocomposites increases with the concentration of chelating agent. 5 wt% chelating agent can enhance the dielectric constant of the BT nanocomposites from 28.5 to about 34.2. Therefore, a higher dielectric constant epoxy

matrix leads to a higher dielectric constant in its BT nanocomposites. The dissipation factor of epoxy varnish-BT nanocomposites is slightly higher than the epoxy varnish.

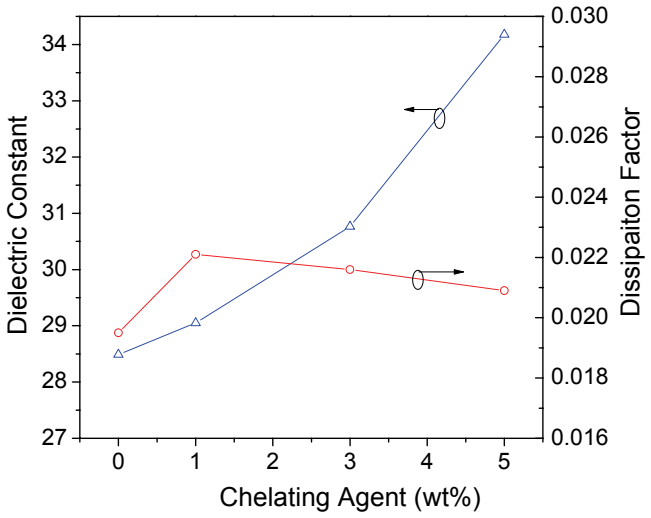

Figure 3.13 Effect of β-diketone chelating agent on the dielectric properties of epoxy varnish-BT nanocomposites.

For 0-3 polymer-ceramic composites, the effective dielectric constant (ε_{eff}) can be correlated to the dielectric constant and the volume fraction of both the polymer (ε_1, v_1) and the ceramic (ε_2, v_2) by the effective medium theory. The Maxwell equation (Equation 3.1) [68], the Lichteneker equation (Equation 3.2) [75], and the Jayasundere and Smith equation (Equation 3.3) [76] are commonly used equations for the prediction of the dielectric constant of 0-3 composites consisting of a continuous polymer phase and spherical ceramic particles.

$$\varepsilon_{eff} = \varepsilon_1[1 + \frac{v_2(\varepsilon_2 - \varepsilon_1)}{\varepsilon_1 + (\varepsilon_2 - \varepsilon_1)v_1}] \qquad \text{Equation 3.1}$$

$$\log\varepsilon_{eff} = v_1 \log\varepsilon_1 + v_2 \log\varepsilon_2 \qquad \text{Equation 3.2}$$

$$\varepsilon_{eff} = \frac{\varepsilon_1 v_1 + \varepsilon_2 v_2[3\varepsilon_1/(\varepsilon_2 + 2\varepsilon_1)][1 + 3v_2(\varepsilon_2 - \varepsilon_1)/(\varepsilon_2 + 2\varepsilon_1)]}{v_1 + v_2[3\varepsilon_1/(\varepsilon_2 + 2\varepsilon_1)][1 + 3v_2(\varepsilon_2 - \varepsilon_1)/(\varepsilon_2 + 2\varepsilon_1)]} \qquad \text{Equation 3.3}$$

The effective dielectric constant of polymer ceramic composites can be calculated based on the above equations. A comparison of the dielectric constant experimental data for 5wt% chelating agent modified epoxy varnish-BT nanocomposites with theoretical predictions is given in Figure 3.14. In the theoretical predictions, the dielectric constant is 5.0 for the polymer matrix (according to the value of 5 wt% β-diketone modified epoxy varnish), and 3000 for the 590 nm BT nanoparticles. The dielectric constant of 3000 for the 590 nm BT nanoparticles is an estimated value according to literature [80], where the authors found that the dielectric constant was 2400 for 0.28 μm BT and 4600 for 0.70 μm BT. In our system, the BT had a particle size of 0.59 μm and should have a dielectric constant between 2400 and 4600. From the experimental data, it can be seen that the dielectric constant of modified epoxy varnish-BT nanocomposites increases with the filler loading. The predicted dielectric constant from Maxwell model is much lower than the experimental data, because this model is too simple and does not consider the interaction between particles. The Lichteneker model is valid for composites in which the dielectric constant of the polymer phase and the filler phase is in close range. Because in high-κ nanocomposites, the dielectric constant of polymer and BT filler has a huge difference, the predicted value is much higher than the experimental data. However, because the Jayasundere and Smith equation includes field interactions between neighboring spheres, the equation can be applied to the case where a high volume fraction of the filler phase is used. Therefore, the experimental data fit this equation rather well.

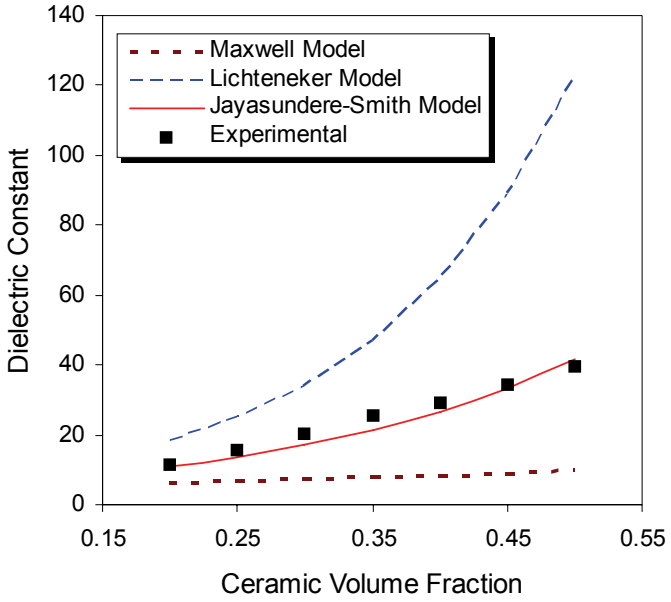

Figure 3.14 Comparison of the dielectric constant data for 5wt% chelating agent modified epoxy varnish-BT nanocomposites with theoretical predictions. In the theoretical predictions, the dielectric constant is 5.0 for the polymer matrix (according to the value of 5 wt% β-diketone modified epoxy varnish), and 3000 for the 590 nm BT nanoparticles.

3.3.1.2 Effect of Bimodal Fillers

The dielectric constant of polymer-ceramic nanocomposites can be affected by the packing efficiency of filler particles. It's well known that polydispersity of filler size can increase the packing efficiency of a filled composite system, because with the increased particle size modality, smaller particles can fill in the gap between large particles [90-92]. Gupta and Seshadriz [92] developed an equation to calculate the maximum packing fraction (MPF, ϕ_m) of polydisperse systems of spheres by taking into consideration of particle size (D_i), size distribution (f_i) and modality. The equation is given as follows:

$$\phi_m = \frac{\sum D_i^3 f_i}{\sum (D_i - \overline{D})^3 + \frac{1}{\overline{n}} \sum \{(D_i - \overline{D})^3 - (D_i \sim \overline{D})^3\} f_i} \qquad \text{Equation 3.4}$$

where $\bar{n} = 1 + \frac{4}{13}(8\phi_m^0 - 1)\bar{D}\frac{\sum (D_i + \bar{D})^2\left\{1 - \frac{3}{8}\left(\frac{\bar{D}}{D_i + \bar{D}}\right)\right\}f_i}{\sum \left\{D_i^3 - (D_i - \bar{D})^3\right\}f_i}$ and $\bar{D} = \sum D_i f_i$.

Theoretical maximum packing fraction can be obtained from calculations of the above equation. For bimodal filler system with particle sizes of 590 nm and 65 nm, respectively, the maximum packing fraction is 84.9% and the corresponding optimal 590nm/65 nm particle ratio is 80%/20%, as shown in Figure 3.15. The optimal particle ratio corresponding to the best packing efficiency was then selected for experimental studies.

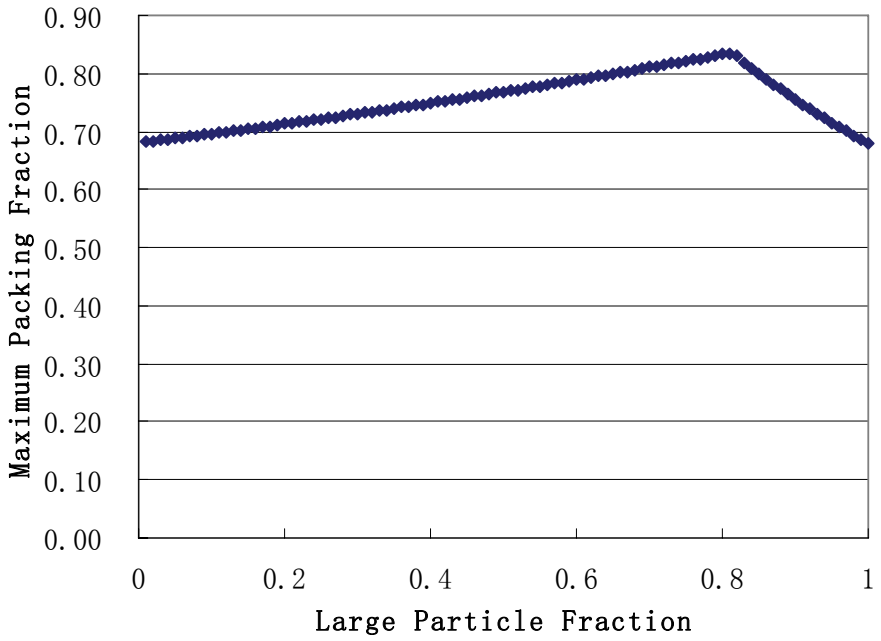

Figure 3.15 Maximum packing fraction (MPF) of bimodal fillers.

Figure 3.16 shows a comparison of the dielectric constant and dissipation factor of epoxy-based uni- and bi-modal BT nanocomposites. Regular epoxy varnish and 1 wt% (to BT) acidic phosphate ester dispersing agent were used in the nanocomposites. In the unimodal BT nanocomposites, 590 nm BT particles were used. With 45 vol% 590 nm BT particles and regular epoxy varnish, the dielectric constant of the unimodal

nanocomposite is about 28.4, and it increases to 35.3 at the loading of 50 vol% 590 nm BT particles. As shown in Figure 3.16, the change of dielectric constant is negligible at 45 vol% filler loading by replacing unimodal filler with bimodal fillers. However, the enhancement of dielectric constant with bimodal fillers is significant at 50 vol% filler loading. The improvement of dielectric constant with the bimodal fillers can be attributed to the better packing efficiency of the filler particles. Voids are inevitable in highly filled nanocomposites, which lead to the decrease of the dielectric constant of the high-κ composites [64]. The amount of voids is expected to be less in the well-packed bimodal filler composites than the unimodal composites, because in bimodal composites small particles can fill in the gaps between large particles. Therefore, bimodal fillers may improve the dielectric constant of BT nanocomposites. However, overall the improvement of the dielectric constant with bimodal fillers is not dramatic, because the actual filler loading (up to 50 vol%) is far below the theoretical maximum packing fraction of 84.9%. The dissipation factor in the bimodal BT nanocomposites is similar as in the unimodal BT composites.

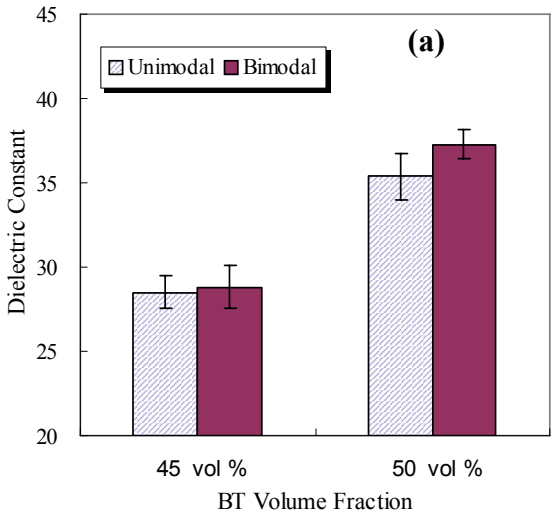

Figure 3.16 Comparison of the (a) dielectric constant and (b) dissipation factor of epoxy-based uni- and bi-modal BT nanocomposites.

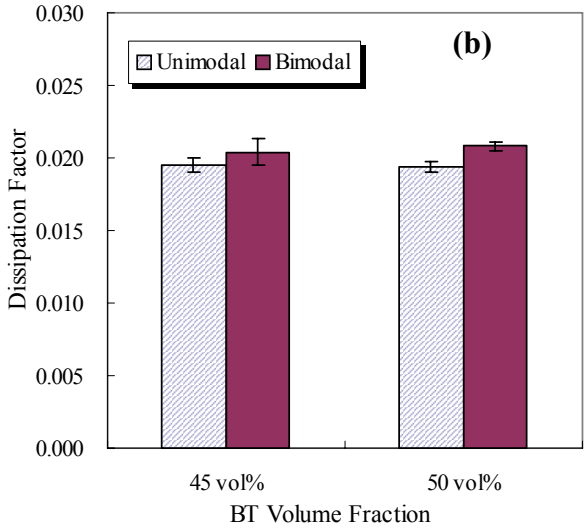

Figure 3.16 Continued.

3.3.1.3 Effect of Dispersing Agent

The dispersion of particles in a polymer matrix has been reported by many researchers to be a critical factor in determining the dielectric behavior of the polymer–ceramic nanocomposites [64]. Many formulation factors and processing methods may affect the particle dispersion, however, the application of dispersing agents in the composites has been found to be one of the most effective approaches. In this study, an acidic phosphate ester was used to improve the dispersion of BT nanoparticles in the epoxy binder. Because β-diketone chelating agent modified epoxy varnish and bimodal fillers can improve the dielectric constant of epoxy varnish-BT nanocomposites, all the formulations for dispersing agent studies contained 5wt% chelating agent and bimodal fillers.

Figure 3.17 shows the effect of acidic phosphate ester dispersing agent on the dielectric properties of 45 vol% BT nanocomposites. Generally, the dielectric constant of BT nanocomposites increases with the concentration of dispersing agent. Particularly,

there is significant improvement of dielectric constant when the dispersing agent concentration increases from nil to 1.0 wt%, indicating the dispersion of BT nanoparticles has been greatly enhanced with 1.0 wt% phosphate ester dispersing agent. The dissipation factor does not change much with the addition of dispersing agent. The acidic phosphate ester dispersing agent contains particle-affinic group (acid group) and polymer resin-like chains (-OR). Therefore, it can assist the wetting, stabilization and thereby the dispersion of BT nanoparticles in the epoxy varnish. Because organic solvent was used in the varnish, the major stabilization mechanism was steric hindrance provided by polymer resin-like chains, instead of electrostatic repulsion for water-based system. The phosphate ester dispersing agent can help BT nanoparticle dispersion and thereby increase the dielectric constant of BT nanocomposites. However, at 45 vol% BT filler loading, the dielectric constant was always less than 50, even if we used 5 wt% β-diketone chelating agent, bimodal fillers, and a large amount (up to 5 wt%) of phosphate ester dispersing agent.

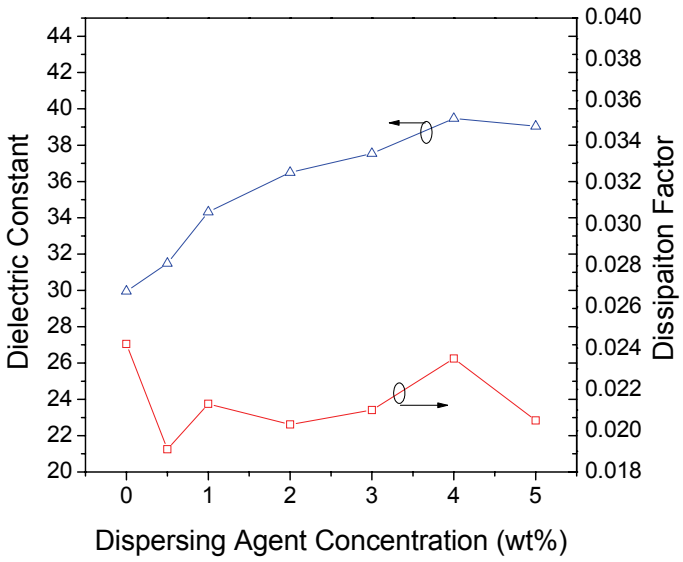

Figure 3.17 Effect of phosphate ester dispersing agent on the dielectric properties of 45 vol% BT nanocomposites.

The effect of phosphate ester dispersing agent on the dielectric properties of 50 vol% BT nanocomposites is given in Figure 3.18. Similar to 45 vol% BT nanocomposites, the dielectric constant increases with the dispersing agent concentration in the 50 vol% BT composites. However, at a higher filler loading of 50 vol%, the effect of dispersing agent is more pronounced, because the fillers are more packed at a higher filler loading and using more dispersing agent leads to better dispersion of the nanoparticles in the epoxy varnish. Dielectric constant of 50 can be achieved when the dispersing agent concentration is above 3 wt%. And with 5 wt% phosphate dispersing agent, a high dielectric constant of about 58 was obtained in the 50 vol% BT nanocomposite, which increases as much as 64% when compared to 35.3 for 50 vol% unimodal 590 nm BT particles in regular epoxy varnish.

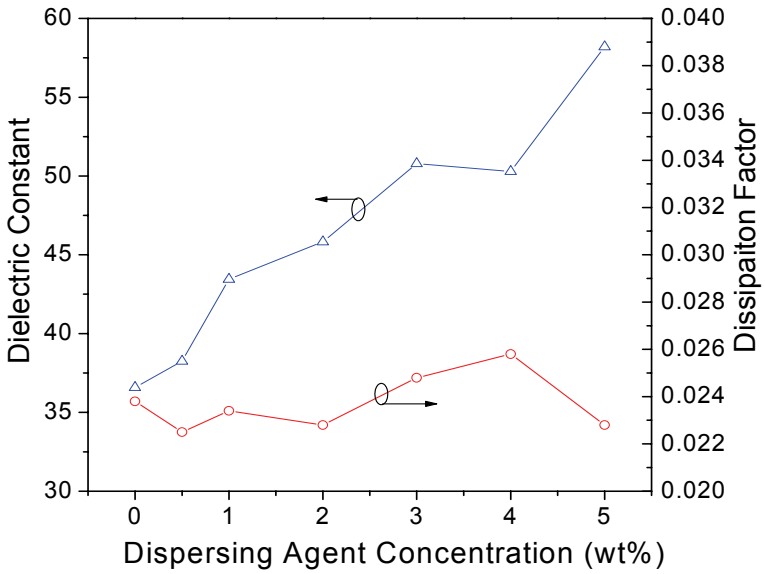

Figure 3.18 Effect of phosphate ester dispersing agent on the dielectric properties of 50 vol% BT nanocomposites.

Figure 3.19 shows the SEM image of 50 vol% bimodal BT nanocomposite dispersed with 1 wt% phosphate ester dispersing agent. It can clearly be observed that in the composite, the smaller particles are filled in between the gap of larger particles, which can improve the packing efficiency of the nanocomposites. The size of larger particles is

about 590 nm and the smaller particle size is mostly in the range of 60-70 nm. The BT nanoparticles were pretty uniformly dispersed in the β-diketone chelating agent modified epoxy.

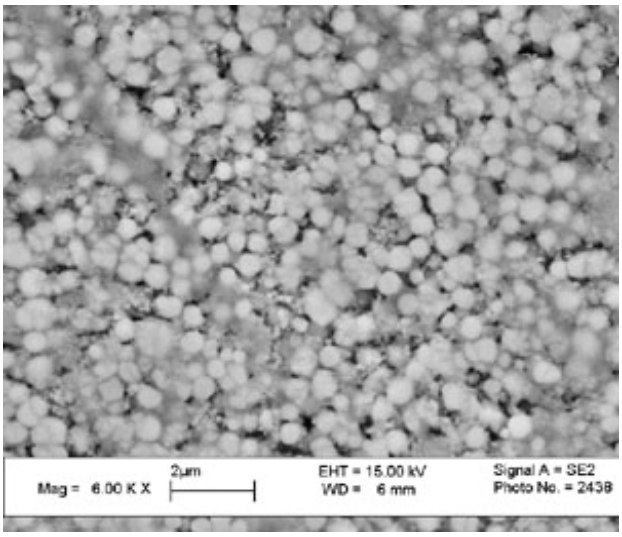

Figure 3.19 SEM image of 50 vol% BT nanocomposite. Magnification: 6.0KX.

3.3.2 Improving the Peel Strength of Polymer-Ceramic Dielectric Nanocomposites to Cu Substrates

3.3.2.1 Effect of Filler Loading on the Peel Strength of High-κ Nanocomposites

From previous discussion, it can be seen that at 45 vol% BT filler loading, the dielectric constant was always less than 50, even if we used 5 wt% β-diketone chelating agent, bimodal fillers, and a large amount (up to 5 wt%) of phosphate ester dispersing agent. However, the dielectric constant can be as high as 58 at 50 vol% BT loading when modified epoxy varnish, bimodal fillers and proper amounts of phosphate ester dispersing agent were used in the BT nanocomposites. Because our objective of this study was to develop high κ (κ>50) nanocomposites with good peel strength and good thermal stress reliability, BT nanocomposites with a filler loading of 50 vol%, which can achieve high dielectric constant of above 50, were used for peel strength studies. All of the 50 vol%

BT nanocomposites for peel strength studies contained 5 wt% β-diketone chelating agent and bimodal fillers.

The adhesion of BT nanocomposites to Cu substrate is strongly dependent on the BT filler loading. At the BT volume fraction of 45%, the peel strength of BT nanocomposite with 1 wt% dispersing agent was about 0.8 KN/m. The peel strength of BT nanocomposite with same amount of dispersing agent drastically decreases to about 0.36 KN/m when the filler loading increases to 50 vol%. The largely decreased peel adhesion strength leads to the failure of capacitor components during high temperature thermal stress reliability test. Figure 3.20 is the image of a 50 vol% BT nanocomposite laminate sample after peel strength test. According to the location where the sample breaks, the failure modes for peeled laminates can be divided in two types: cohesive failure and adhesive failure. It clearly can be seen that the laminate sample failed at the interface between the nanocomposite and the Cu substrate. Therefore, adhesive failure is the failure mode for high dielectric constant 50 vol% BT nanocomposites. The large reduction of peel strength from 0.80 to 0.36 KN/m, when the BT loading increases from 45 vol% to 50 vol%, is related to the weaker interfacial bonding between the BT nanocomposite and the Cu substrate. In the laminate sample, epoxy-Cu bonding provides the adhesion strength at the interface. As the filler loading increases, more filler replaces the epoxy to be in contact with Cu substrate at the interface, and thereby results in the reduction of peel strength. Figure 3.21 shows the SEM image of 50 vol% BT nanocomposites with 1 wt% dispersing agent. At 50 vol%, the filler particles are highly packed. The large amount of filler at the nanocomposite-Cu interface leads to the reduction of peel adhesion strength.

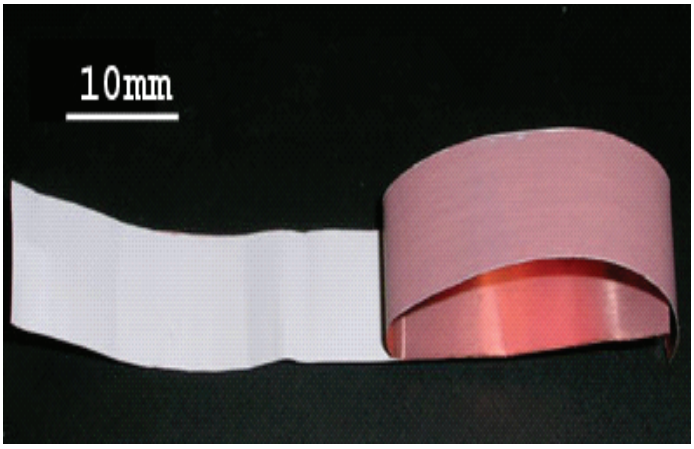

Figure 3.20 50 vol% BT nanocomposite laminate sample after peel strength test.

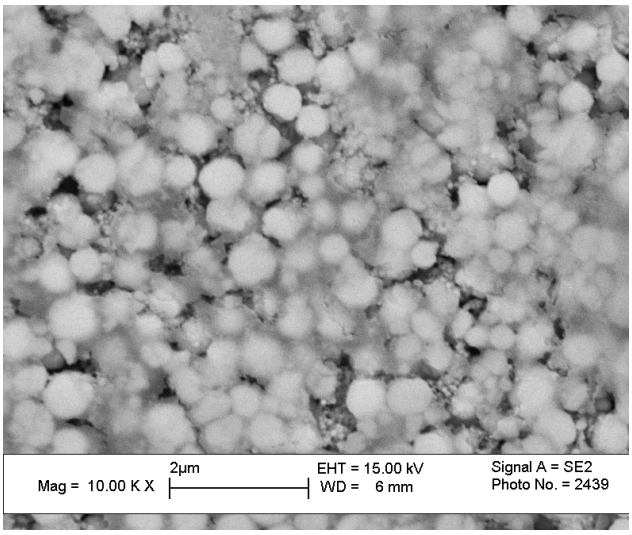

Figure 3.21 SEM image of BT nanocomposites. Magnification: 10.0 KX.

3.3.2.2 Effect of Dispersant on the Peel Strength of High-κ Nanocomposites

Besides filler loadings, the properties of epoxy-BT nanocomposites are also significantly affected by the phosphate ester dispersing agent. Acidic phosphate ester dispersing agent is often used in the polymer-ceramic nanocomposite formulations to improve the dispersion and dielectric constant of nanocomposites. At 50 vol% BT filler loading, the dielectric constant of our nanocomposite is about 37 when no dispersing agent is used. However, the dielectric constant increases to 43.5 when 1 wt% dispersing agent is used, because it can reduce the porosity in the nanocomposite. Dielectric

constant of 50 can be achieved when the dispersing agent concentration is above 3 wt%. The phosphate ester dispersing agent can improve the dielectric constant of epoxy-BT nanocomposites, and it can affect the adhesion as well. Figure 3.22 shows the effect of phosphate ester dispersing agent on the peel strength of 50 vol% BT nanocomposites. When the dispersing agent concentration increases in the 50 vol% BT nanocomposites, the peel strength dramatically decreases. In contrast to the increasing trend of dielectric constant, the addition of dispersing agent overall has adverse effect on the peel strength. This effect is attributable to the interfacial bonding between the nanocomposite and the Cu substrate as well. Because organic solvents were used in the epoxy varnish-BT nanocomposites, the acid groups of phosphate ester cannot feely dissociate and be ionized as in water-based system. Therefore, the acid groups of phosphate ester were physically adsorbed instead of chemically bonded on the particle surfaces, and the interaction between the acid groups of dispersing agent and the hydroxyl groups of BT nanoparticles was not very strong. As the nanocomposites were deposited on the Cu substrate, some dispersing agent may move from the particle surfaces to the Cu substrate surface. The epoxy-Cu bonding at the interface was interfered because of the extra amount of dispersing agent. Therefore, the peel strength in the 50 vol% BT nanocomposite laminate samples decreases with the increase of dispersing agent concentration. Because of the low peel strength at the filler loading of 50 vol%, none of the formulations survived in the harsh thermal stress reliability tests at 288 °C.

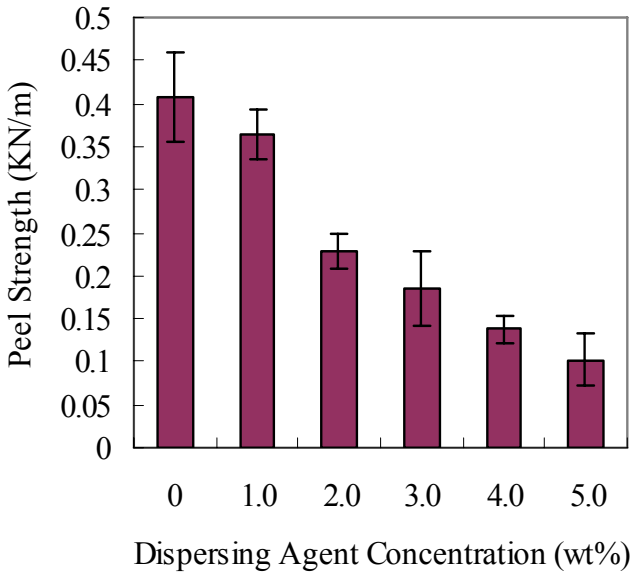

Figure 3.22 Effect of phosphate ester dispersing agent on the peel strength of 50 vol% BT nanocomposites.

3.3.2.3 Effect of Coupling Agent on the Peel Strength of High-κ Nanocomposites

In order to improve the peel adhesion strength of high-κ nanocomposites to Cu substrates, coupling agents were incorporated into the high-κ formulations. Organosilane coupling agent and titanate coupling agent were used in this work. Coupling agent typically has two different types of functional groups on a molecule. One of them can be chemically anchored on the filler particle surfaces, and another can be chemically bonded with the polymer matrix. One of the most studied coupling agents is γ-glycidoxypropyltrimethoxysilane, as shown in Figure 3.23.

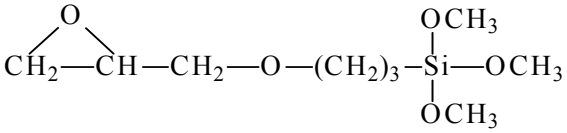

Figure 3.23 Chemical structure of γ-glycidoxypropyltrimethoxysilane.

Because at 50 vol% BT filler loading, the formulation with 1.0 wt% of acidic phosphate ester dispersing agent had a reasonably high dielectric constant (~43.5) and peel adhesion strength (~0.36 KN/m). We then added coupling agent to this formulation in order to increase the peel adhesion strength. Table 3.2 shows the effect of coupling agent (1.0 wt%) on the peel adhesion strength of high-κ nanocomposites to Cu substrates.

Table 3.2 Effect of coupling agent on the peel strength of high-κ nanocomposites

Coupling Agent	Peel (KN/m)	Dielectric Constant
No Coupling Agent	0.36	43.5
(3-mercaptopropyl)trimethoxysilane	0.24	41.2
(3-mercaptopropyl)triethoxysilane	0.21	38.8
(3-isocyanatopropyl)triethoxysilane	0.35	41.3
(3-aminopropyl)trimethoxysilane	0.37	43.4
γ-glycidoxypropyltrimethoxysilane	0.39	46.2
Tetra-butyl Titanate	0.31	41.5
Titanium Acetylacetonate	0.29	42.4

By adding in γ-glycidoxypropyltrimethoxysilane coupling agent, the peel strength and the dielectric constant of high-κ formulations increase from 0.36 KN/m to 0.39 KN/m and from 43.5 to 46.2, respectively. However, because the improvement was not very significant, all the samples failed in the high temperature thermal stress reliability tests.

3.3.2.4 Filler Particle Surface Functionalization and Its Effect on the Peel Strength of High-κ Nanocomposites

The phosphate ester dispersing agent can significantly affect the adhesion of BT nanocomposites. In order to improve the peel strength while keeping the high dielectric constant of BT nanocomposites provided by the dispersing agent, the BT nanoparticles were reflux pretreated with the acidic phosphate ester dispersant, instead of being directly

mixed into the formulations. The particle pretreatment was conducted in the dilute solution of phosphate ester/solvent mixture under reflux condition for 24 hours.

Figure 3.24 shows the TGA analyses of 65 nm and 590 nm BT nanoparticles before and after phosphate ester reflux treatment. The original 65 nm BT particles have about 0.36 wt% weight loss from room temperature to 800 °C, and after reflux treatment, the weight loss increases to 2.13 wt%, indicating the phosphate ester was successfully grafted on the 65 nm BT particle surfaces. For 590 nm BT nanoparticles, the weight loss is about 0.24 wt% for original particles and 0.74 wt% for reflux treated particles. The 65 nm BT particles have larger specific surface area (inversely proportional to the particle size) than 590 nm particles, which provides more reaction sites on the 65 nm particle surfaces, therefore, there are larger amounts of phosphate ester reacted on the 65 nm BT nanoparticles, as suggested by the much larger weight loss in TGA studies.

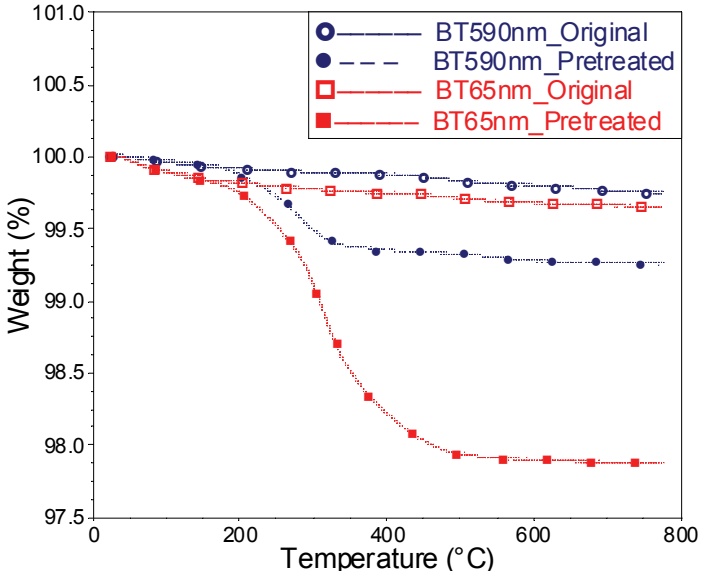

Figure 3.24 TGA analyses of BT nanoparticles.

Figure 3.25 shows the FTIR spectra of (a) 65 nm and (b) 590 nm BT nanoparticles before and after phosphate ester reflux treatment. A subtraction of the FTIR spectrum of reflux treated particles from the spectrum of original particles clearly shows

the effect of phosphate ester treatment. Comparing Figure 3.25 (a) with Figure 3.25 (b), one can find in the subtracted spectra the absorbance of 65 nm particles is stronger than 590 nm particles because of the larger specific surface area, but these following peak positions are the same for both pretreated 65 nm and 590 nm BT nanoparticles: 3452 cm^{-1} (negative peak), 2947 cm^{-1}, 2869 cm^{-1}, 1739 cm^{-1}, and 760 cm^{-1}. The original particles have hydrogen-bonded hydroxyl groups (3452 cm^{-1}) on the particle surface, and after reflux reaction, these hydroxyl groups reacted with the acid groups of the acidic phosphate ester dispersing agent. Therefore, the pretreated BT particles show a negative peak at 3452 cm^{-1}, because of the disappearance of hydroxyl groups. The peaks at 2947 cm^{-1} and 2869 cm^{-1} correspond to the –CH bonds from the polymer resin-like segment (-OR) of the phosphate ester. The strong absorption at 1739 cm^{-1} is attributable to phosphate group (HPO_4^{2-}), and the peak at 760 cm^{-1} corresponds to the P-O bond of the phosphate group. According to the above discussion, it can be seen that the phosphate ester dispersing agent was successfully reacted and chemically bonded on the particle surfaces.

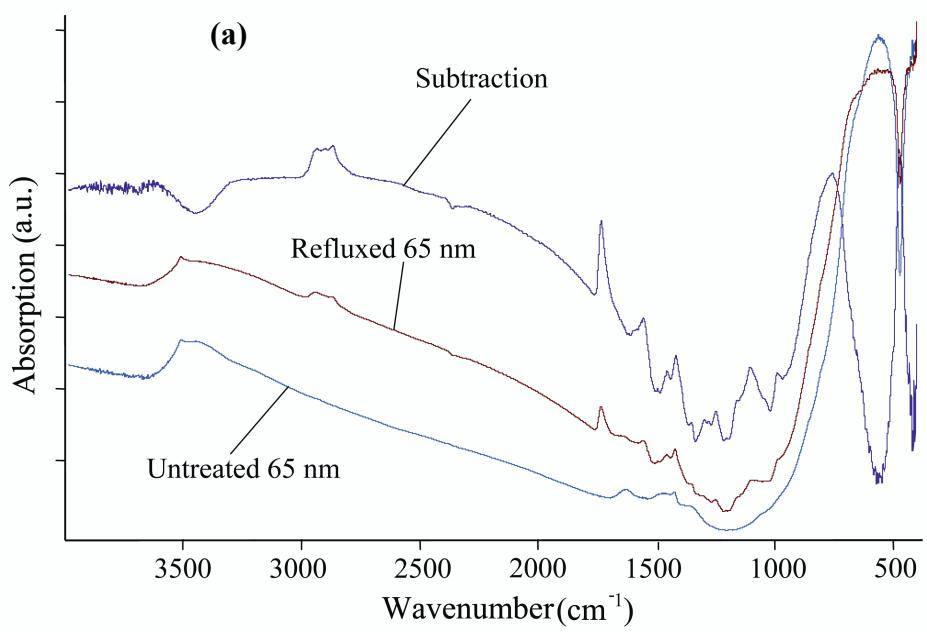

Figure 3.25 FTIR spectra of (a) 65 nm and (b) 590 nm BT nanoparticles.

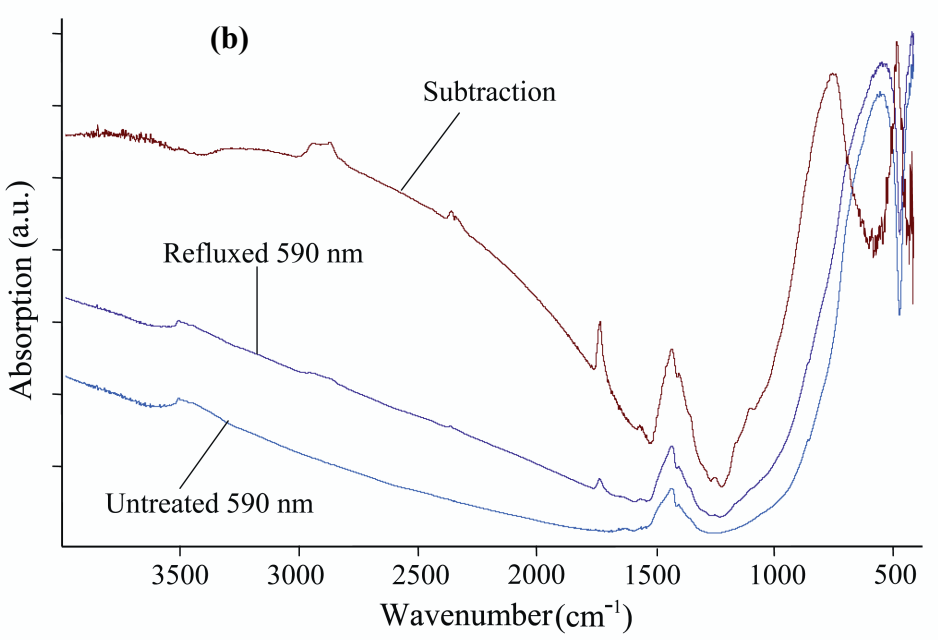

Figure 3.25 Continued.

We formulated epoxy varnish-BT nanocomposite filled with 50 vol% reflux pretreated bimodal BT fillers, and embedded capacitor components based on this formulation were fabricated and characterized. TGA characterization shows that about 0.74 wt% and 2.13 wt% dispersing agent were chemically bonded on the 590 nm and 65 nm BT particles, respectively, and the bimodal filler ratio of 590 nm/65nm particles was 80%/20%. Based on these values, the average amount of phosphate ester dispersing agent reacted on the pretreated bimodal BT particles is calculated to be around 1.0 wt%. Therefore, for nanocomposites directly mixed with dispersing agent, we used 1.0 wt% phosphate ester dispersing agent in the formulations for comparison. Table 3.3 shows a comparison of the peel strength and dielectric properties of epoxy varnish-BT nanocomposites. It is found at the filler loading of 50 vol%, the pretreatment of BT particles lead to a high peel strength of 0.68 KN/m, which increases almost 89% when compared to 0.36 KN/m for the 50 vol% nanocomposite directly mixed with 1 wt% dispersing agent. The embedded capacitor components with pretreated particles

successfully passed the thermal stress reliability test. The dielectric constant of BT nanocomposite with 50 vol% reflux pretreated particles is about 45.6, which is more than 50% higher the best commercially available materials. Therefore, particle pretreatment with the acidic phosphate ester dispersant agent is a critical factor for high dielectric constant nanocomposite in order to obtain high adhesion strength and thereby pass the thermal stress reliability test. The breakdown field (BDV) of nanocomposite with reflux treated particles is also very high, i.e. 111.2 MV/m, which is much higher than the required value for commercial applications. The improvement of peel strength and dielectric properties with pretreated BT particles is due to the chemical bonding of phosphate ester dispersing agent with the BT nanoparticles. Such chemical bonding ensures good dispersion of BT nanoparticles in the epoxy varnish-ceramic nanocomposites and thereby leads to the high dielectric constant. Meanwhile, because of the chemical bonding, the phosphate ester cannot freely move to the interface between the nanocomposites and the Cu substrate to adversely affect the peel strength. Therefore, a high peel strength can be obtained in the composites filled with reflux treated BT nanoparticles.

Table 3.3 Comparison of the peel strength and dielectric properties of epoxy varnish-BT nanocomposites.

	Formulations		
Bimodal BT Fillers	45 vol%	50 vol%	50 vol%
Dispersing Agent	1wt%	1wt%	Pretreated
Peel (KN/m)	0.80	0.36	0.68
Themal Stress (6X)	Pass	Failed	Pass
Dielectric Constant	34.2	43.5	45.6
Dissipation Factor	0.021	0.023	0.018
BDV (MV/m)	99.0	69.9	111.2

BT nanoparticle reflux pretreatment can affect the bulk mechanical properties of BT nanocomposites as well. Figure 3.26 shows the DMA characterization of 50vol% BT nanocomposites. With reflux pretreated BT nanoparticles, the modulus is about 10.41 GPa, which is higher than 9.57 GPa for composite directly mixed with 1 wt% dispersing agent. The glass transition temperature, defined as the peak temperature corresponding to the maximum loss modulus, is about 146.5 °C for 50 vol% nanocomposite with reflux pretreated BT particles. This temperature is about 3.1 °C higher than that of the 50 vol% BT nanocomposite directly mixed with 1 wt% dispersing agent. The higher modulus suggests stronger interaction between the fillers and the epoxy matrix in the nanocomposites with pretreated BT particles, which results in a smaller free volume and thereby a higher glass transition temperature.

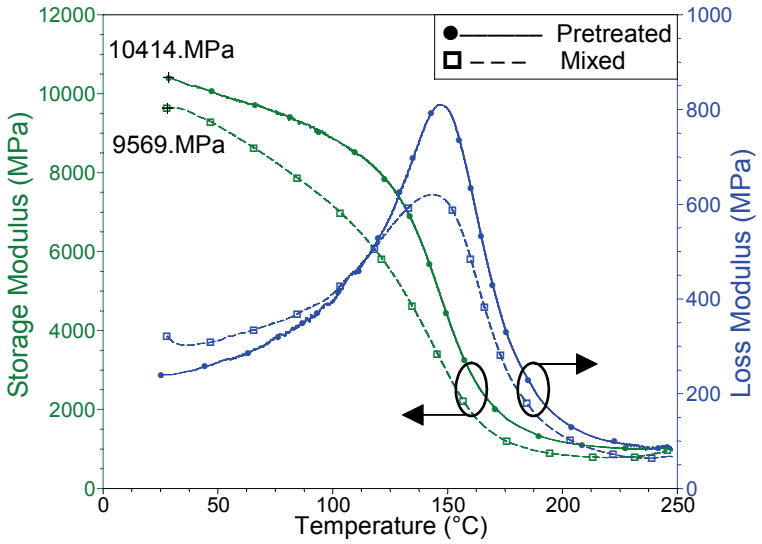

Figure 3.26 DMA characterization of 50vol% BT nanocomposites.

Figure 3.27 shows the frequency responses of the dielectric properties of 50 vol% pretreated BT nanocomposite. The dielectric constant decreases and the dissipation factor increases gradually with the increase of frequency, which is a typical behavior for polymer-ceramic nanocomposites [45].

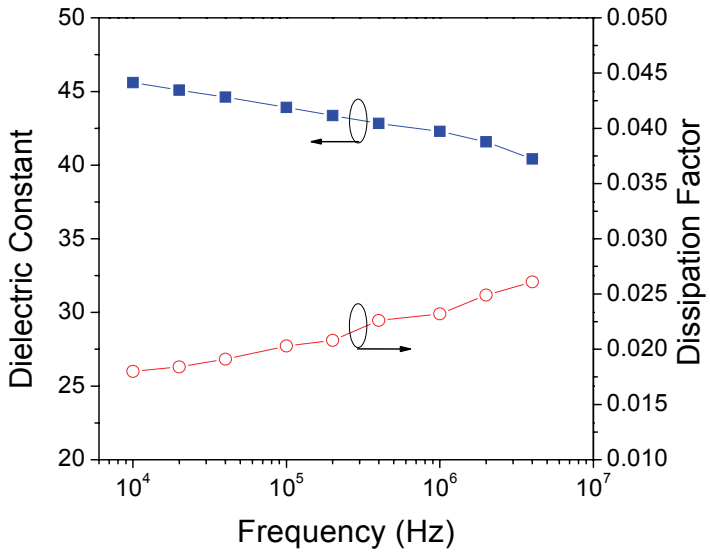

Figure 3.27 Frequency responses of the dielectric properties of 50 vol% pretreated BT nanocomposite.

3.3.3 Enhancing the Thermal Stress Reliability of Polymer-Ceramic Nanocomposites by Introducing Flexible Island Domains in Polymer Matrices

3.3.3.1 Thermal Stress in Embedded Capacitor Components

The high thermal stress in the BT nanocomposites often causes the failure of components during PCB manufacturing and reliability test when the ceramic filler loading reaches 50 vol%. Figure 3.28 shows the image of a failed sample with 50 vol% filler loading after thermal stress test. The bumps on the top part of the image suggest the failure caused by high thermal stress during the test.

During the high temperature thermal stress reliability test, the stress in the capacitor component can be express as follows:

$$Stress = \int_{T1}^{T2} (CTE_{Diel} - CTE_{Cu}) \bullet E \bullet d_T \qquad \text{Equation 3.5}$$

where CTE_{Diel} and CTE_{Cu} are the coefficient of thermal expansion (CTE) of the dielectric material and Cu, respectively; E is the modulus of the dielectric material.

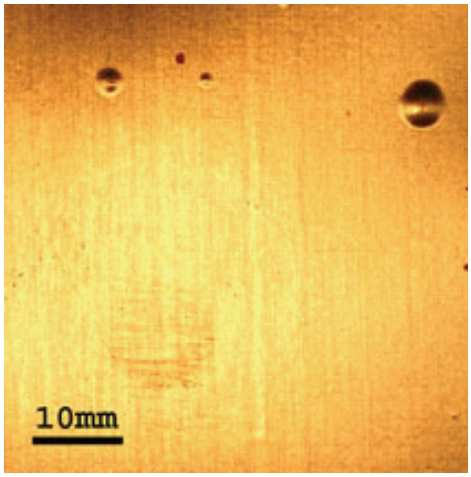

Figure 3.28 Picture of a failed sample after thermal stress test.

From DMA characterization, it was found that the modulus of 50 vol% BT nanocomposite is very high, i.e. 10.41 GPa. The nanocomposte filled with 50 vol% pretreated BT nanoparticles has a CTE of about 44.9 μm/m·°C, which is significantly lower than 82.78 μm/m·°C for the neat epoxy. However, the Cu substrate has a much lower CTE of 17 μm/m·°C. The CTE mismatch between Cu substrate and the BT nanocomposite is about 27.9 μm/m·°C. This large CTE mismatch, together with the large modulus of the nanocomposite, results in a high thermal stress in the embedded capacitor components at high temperature. Such a high thermal stress often causes failure during thermal stress reliability test as shown in Figure 3.28.

3.3.3.2 Effect of Secondary Rubberized Epoxy on the Thermal Stress Reliability of Embedded Capacitor Components

In order to further improve the thermal stress reliability of BT nanocomposites, the large modulus of the high κ nanocomposite was addressed by modifying the epoxy matrix with a rubberized polymer in this study. A carboxyl terminated butadiene-acrylonitrile (CTBN) copolymer modified epoxy functional adduct was used to modify the epoxy varnish. The CTBN rubber segment in the CTBN-epoxy modifier is flexible.

The effects of CTBN-epoxy modifier on the moduli, CTEs, peel strength, and thermal stress reliability of BT nanocomposites were systematically investigated.

Figure 3.29 shows the storage modulus of CTBN-epoxy modified 50 vol% BT nanocomposites. The moduli of 50 vol% pretreated BT nanocomposites decrease drastically from 10.4 GPa to 7.4 GPa by adding 10 phr (per hundred resin) CTBN-epoxy modifier. The reduction of modulus is as much as 29%. Therefore, the rubberized polymer segment CTBN can effectively reduce the modulus of the BT nanocomposite. Further increase of the amount of CTBN-epoxy modifier leads to an even lower modulus. With 20 phr CTBN-epoxy modifier, the modulus of 50 vol% BT nanocomposite is about 6.7 GPa, and the reduction of modulus is about 35%. It's noted the reduction of modulus is not proportional to the amount of rubberized modifier. The portion of rubberized modifier above 10 phr when large amounts (20, 30, 40 phr) were used cannot give as large reduction in modulus as the first 10 phr CTBN-epoxy modifier.

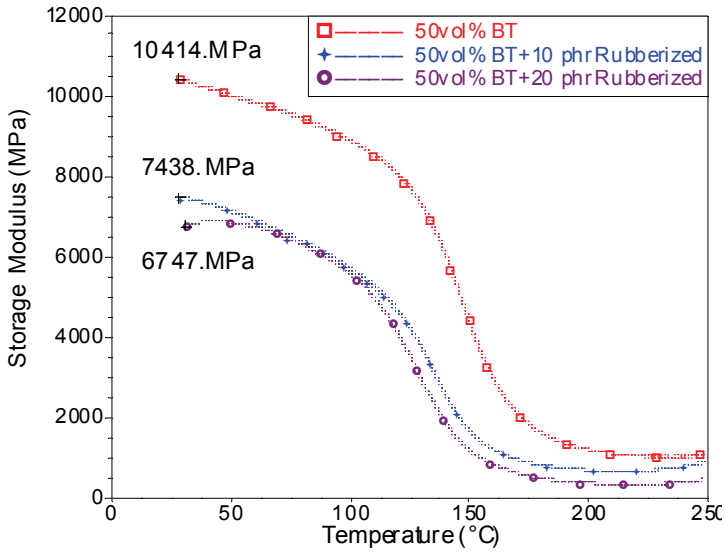

Figure 3.29 Storage modulus of CTBN-epoxy modified 50 vol% BT nanocomposites.

Because the thermal stress in embedded capacitor components is also a function of CTE mismatch between the high-κ nanocomposite and the Cu substrate, the CTEs of the BT nanocomposites were characterized by TMA. Figure 3.30 shows the CTE and Tg

of CTBN-epoxy modified 50 vol% BT nanocomposites. The CTE of 50 vol% BT nanocomposite without rubberized modifier is about 44.9 μm/m·°C, and the CTE mismatch between Cu substrate and the BT nanocomposite is about 27.9 μm/m·°C. Incorporation of CTBN-epoxy modifier in the BT nanocomposites leads to the increase of CTE as well as CTE mismatch. With 10 phr rubberized modifier, the CTE of nanocomposite is 47.9 μm/m·°C, and the CTE mismatch between the nanocomposite and the Cu substrate is about 30.9 μm/m·°C. Therefore, addition of 10 phr rubberized modifier results in the increase of CTE mismatch from 27.9 to 30.9 μm/m·°C, which is about 10% increment. Further increasing the amount of CTBN-epoxy modifier to 20 phr leads to a higher CTE of 49.2 μm/m·°C and a higher CTE mismatch of 32.2 μm/m·°C. Compared to the nanocomposite without rubberized modifier, the increase of CTE mismatch is about 15% with 20 phr CTBN-epoxy modifier in the 50 vol% BT nanocomposite. Figure 4 also shows that the glass transition temperature decreases with the incorporation of rubberized modifier.

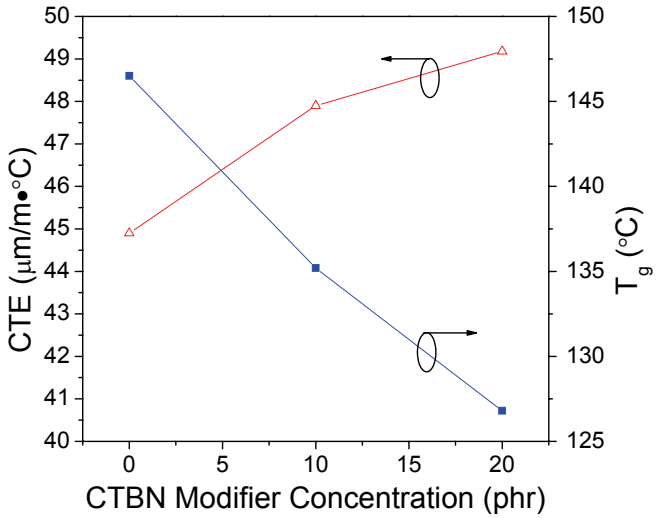

Figure 3.30 CTE and Tg of CTBN-epoxy modified 50 vol% BT nanocomposites.

According to Equation 3.5, the thermal stress in embedded capacitor components is proportional to the product of the modulus of high κ nanocomposite and the CTE

mismatch between the nanocomposite and the Cu substrate. An estimation based on the moduli at room temperature from Figure 3.29 and the CTEs from Figure 3.30 suggests this product is about 78% and 75% of the original value by adding 10 phr and 20 phr CTBN-epoxy modifier in the BT nanocomposites, respectively. Therefore, the thermal stress in embedded capacitor components can be reduced about 22% and 25% with 10 phr and 20 phr rubberized polymer, respectively.

The CTBN-epoxy modifier can effectively reduce the thermal stress in the embedded capacitor components, and the thermal stress reliability of 50 vol% BT nanocomposites modified by 10 phr, 20 phr, 30 phr, and 40 phr CTBN-epoxy was tested. However, contrary to our expectation, only the BT nanocomposite with 10 phr CTBN-epoxy modifier successfully passed the harsh high-temperature reliability test. To understand the thermal stress reliability behavior of the CTBN-epoxy modified BT nanocomposites, the peel strength of the nanocomposites was characterized. As shown in Figure 3.31, the CTBN-epoxy modifier has adverse effect on the peel strength of 50 vol% BT nanocomposites. With 10 phr rubberized polymer modifier, the peel strength decreases from 0.68 KN/m to 0.48 KN/m. The peel strength continuously decreases with further increase of the amount of modifier. With 20 phr rubberized polymer modifier, the peel strength is only about 0.29 KN/m. The decrease of peel strength with 20 phr modifier has already exceeded the benefit of reduced thermal stress from rubberized polymer, which results in the sample failure during the high-temperature thermal stress reliability test.

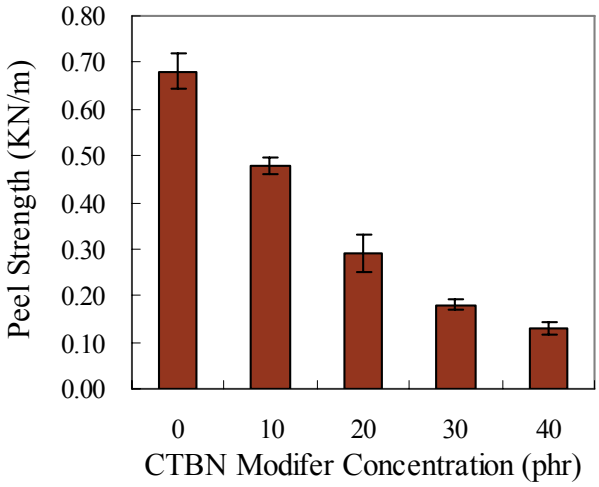

Figure 3.31 Peel strength of CTBN-epoxy modified BT nanocomposites.

Figure 3.32 shows the SEM images of the morphologies of CTBN-epoxy modified epoxy matrix. Figure 3.32a is the image of a control sample, which does not have the rubberized polymer modifier. There is no sea-island structure observed from this control sample. Figure 3.32b is the image for the epoxy matrix with 10 phr CTBN-epoxy modifier. Clearly there is a phase separation in the CTBN-epoxy modified epoxy matrix. The CTBN-epoxy modifier forms island domains in the sea of epoxy matrix. The island domain size of the rubber phase is small, in the range of 200 nm to 500 nm. Such a sea-island structure in the CTBN-epoxy modified epoxy matrix can effectively reduce the modulus of the BT nanocomposites and thereby reduce the thermal stress in the embedded capacitor components. However, such rubber domains cannot provide as good adhesion with the Cu substrate as the original epoxy, which results in the reduction of peel strength. Because the peel strength of BT nanocomposite with 10 phr modifier is still high, the decrease of thermal stress with rubberized polymer can help pass the high temperature thermal stress reliability test. Figure 3.32b, 3.32c, and 3.32d show the morphologies of epoxy matrices with 20 phr, 30 phr, and 40 phr CTBN-epoxy modifier, respectively. At 20 phr, the island domain size of the rubber phase is about 1-2 μm. The island domain sizes continuously increase with the increasing amount of CTBN-epoxy

modifier. The large island domain sizes of rubber phase can significantly reduce the peel strength of the BT nanocomposites. Because the reduction of thermal stress is not significant any more for the portion of modifier above 10 phr, the drastic decrease of the peel strength with large amounts (20, 30, 40 phr) of rubberized polymer leads to the failure of the BT nanocomposites during thermal stress reliability test.

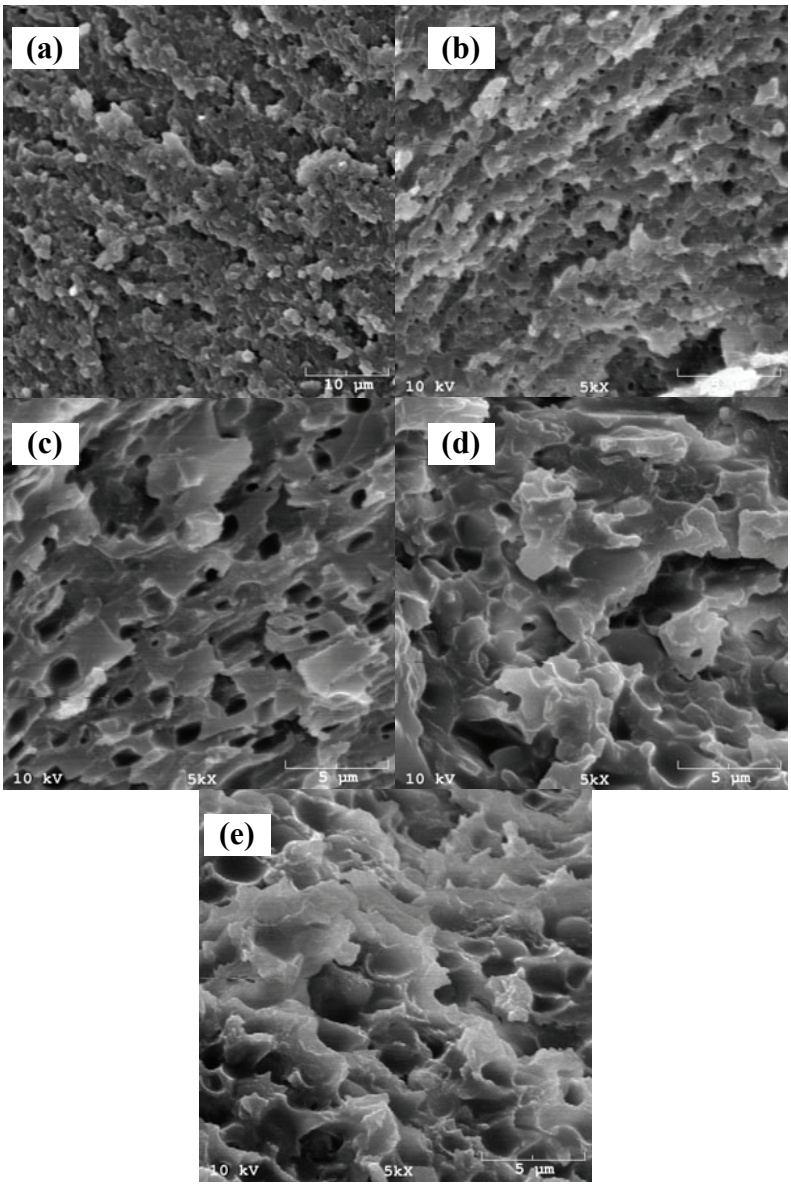

Figure 3.32 SEM characterization of the morphologies of CTBN-epoxy modified epoxy matrix. The CTBN-epoxy modifier concentrations are: (a) 0 phr, (b) 10 phr, (c) 20 phr, (d) 30 phr, and (e) 40 phr.

The dielectric constant of 10 phr CTBN-epoxy modified 50 vol% BT nanocomposite is 50.5, as listed in Table 3.4. The dielectric constant is slightly higher than 46.5 for 50 vol% BT nanocomposite without rubberized modifier. The dissipation factor is low, i.e. about 0.019, and the breakdown voltage is very high, i.e. about 89 MV/m, which is much higher than the required value for embedding applications. The leakage current is very low, about 1.9×10^{-11} A/cm^2 at the applied voltage of 50 V for an 18.4 μm thick dielectric nanocomposite film.

Table 3.4 Characteristics of 10 phr CTBN-epoxy modified BT nanocomposite

BT Fillers	50 vol%
CTBN-Epoxy Modifier	10 phr
Peel (KN/m)	0.48
Themal Stress (6X)	Pass
Dielectric Constant	50.5
Dissipation Factor	0.019
BDV (MV/m)	89.0
Leakage Current (A/cm^2)	1.9×10^{-11}

Figure 3.33 shows the frequency responses of the dielectric properties of 10 phr CTBN-epoxy modified BT nanocomposite. The dielectric constant slightly decreases with the increase of frequency, and the dissipation factor increases with the frequencies but is at a low level in the whole frequency range.

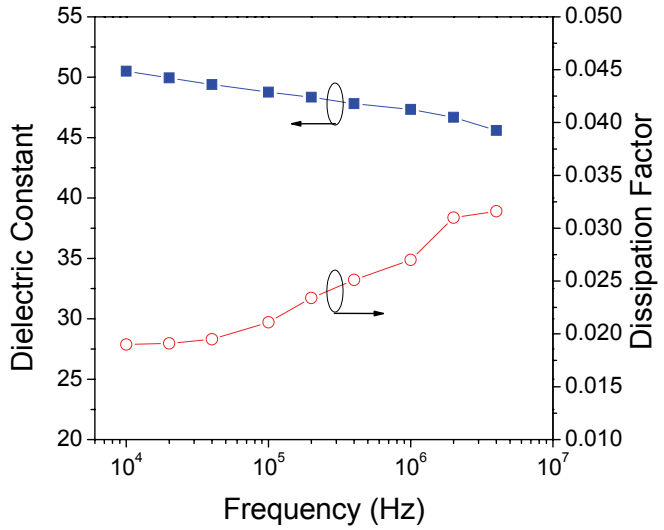

Figure 3.33 Frequency responses of the dielectric properties of 10 phr CTBN-epoxy modified BT nanocomposite.

3.3.3.3 Enhance the Thermal Stress Reliability of Embedded Capacitor Components by a Triazole Compound

To further enhance the peel strength of the CTBN-epoxy modified 50 vol% BT nanocomposite, a triazole compound was introduced into the formulations. This triazole compound contains a thiol group and an amino group. Such triazole compound can be used as the adhesion promoter to improve the adhesion between a nanocomposite and a metal surface such as the Cu substrate. The thiol group of the triazole compound has very strong affinity with the Cu substrate, and the amino group of triazole, on the other hand, can react with the epoxy matrix. Table 3.5 shows the effect of triazole on the peel strength and dielectric properties of BT nanocomposites. With 1.0 wt% triazole, the peel strength of BT nanocomposite increases from 0.48 KN/m to 0.53 KN/m, which is about 10.4% improvement. The dielectric constant also increases, from 50.5 to 53.8. The dissipation factor is 0.024 and the breakdown voltage is still very high, i.e. about 90.6

MV/m. This formulation successfully passed the high-temperature thermal stress reliability test.

Table 3.5 Effect of triazole on the peel strength and dielectric properties of BT nanocomposites

	Formulations	
Pretreated BT Fillers	50 vol%	50 vol%
CTBN-Epoxy Modifier	10 phr	10 phr
Triazole	-	1 wt%
Peel (KN/m)	0.48	0.53
Themal Stress (6X)	Pass	Pass
Dielectric Constant	50.5	53.8
Dissipation Factor	0.019	0.024
BDV (MV/m)	89.0	90.6

The 50 vol% bimodal BT nanocomposite with 10 phr CTBN-epoxy modifier and 1 wt% triazole is the best formulation we obtained so far. We systematically characterized its dielectric properties and electrical properties as embedded capacitor components. Figure 3.34 shows the frequency responses of the dielectric properties of CTBN-epoxy modified 50 vol% BT nanocomposite containing 1 wt% triazole. The dielectric constant decreases with the increase of frequency. In the measurement frequency range, the dielectric constant overall decreases about 10%. The dissipation factor increases with the frequencies, but it is at a low level in the whole frequency range.

Figure 3.35 shows the leakage current of CTBN-epoxy modified nanocomposite containing 1 wt% triazole. As the applied field increases, the leakage current increases. But overall, the leakage current is very low, in the order of 10^{-5} $\mu A/cm^2$. Because the maximum applied filed in the leakage current measurement was 10 MV/m, which was much lower than the breakdown field of the dielectric material (90.6 MV/m), drastic increase of leakage current as in the breakdown region was not observed in the whole measurement range.

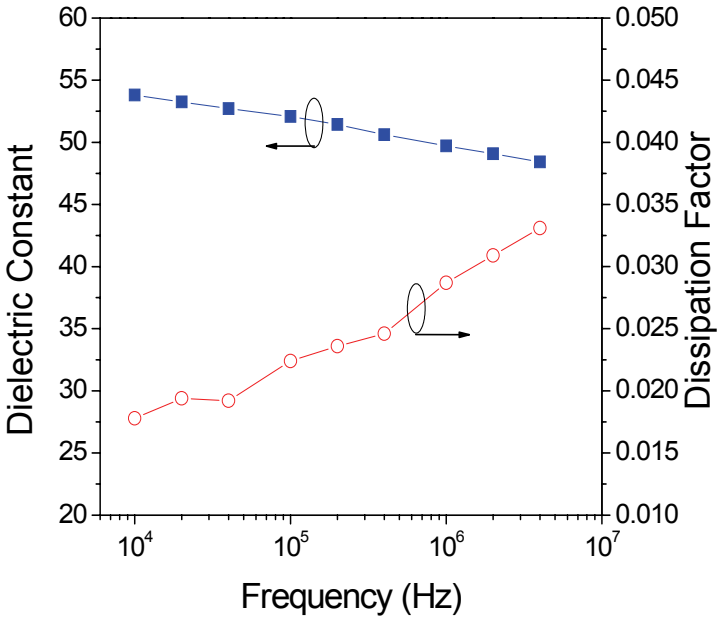

Figure 3.34 Frequency responses of the dielectric properties of CTBN-epoxy modified 50 vol% BT nanocomposite containing 1 wt% triazole.

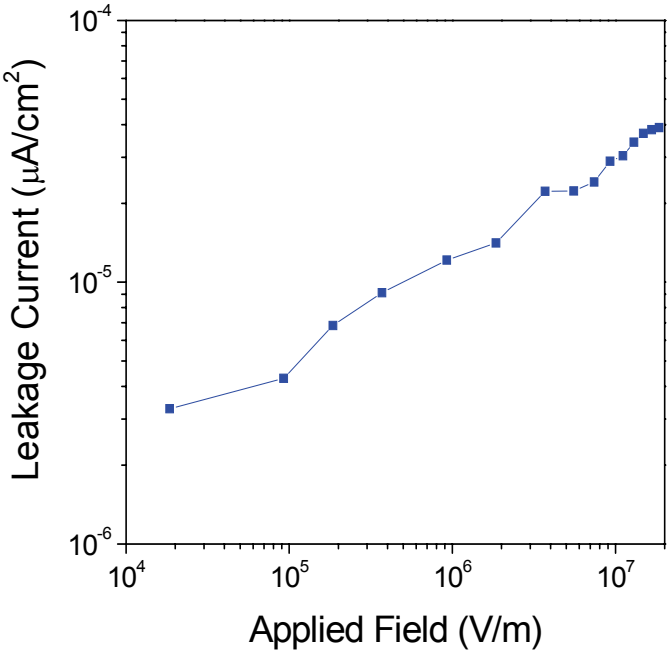

Figure 3.35 Leakage current of CTBN-epoxy modified 50 vol% BT nanocomposite containing 1 wt% triazole.

Figure 3.36 shows the temperature coefficient of dielectric constant and dissipation factor of CTBN-epoxy modified 50 vol% BT nanocomposite containing 1 wt% triazole. A positive temperature coefficient was observed in the nanocomposite for both the dielectric constant and dissipation factor. From room temperature to 150 °C, the dielectric constant increases 11.7%. The dielectric constant first increases linearly with temperature up to about 130 °C, and then levels off at higher temperature. This transition takes place around the glass transition temperature of the nanocomposite. In the initial linear region, the temperature coefficient of dielectric constant (or capacitance) is about 0.16 $°C^{-1}$. In contrast, the dissipation factor first increases gradually, and then increases drastically at temperature around 130 °C, i.e. in the glass transition region.

Figure 3.37 shows the 85°C/85% relative humidity aging reliability of CTBN-epoxy modified 50 vol% BT nanocomposite containing 1 wt% triazole. 85°C/85% relative humidity test for 1000 hours is a standard test for printed circuit board. Because an embedded capacitor component will be buried inside the print circuit board, it must be able to pass this aging test. The embedded capacitor components survived in this test, and the dielectric constant increases with aging time. The dielectric constant increases very fast at the first 24 hours, and then levels off with time. Overall the increase of the dielectric constant during the 1000 hour aging time is about 26% at 10 KHz and about 22% at 1 MHz. The increase of the dielectric constant during aging test is due to the absorption of moisture, because water has a high dielectric constant of about 78.

Air to air thermal cycling was also used to test the reliability of embedded capacitor components. The temperature was from -55°C to 125°C with a dwell time of 10 minutes at each extreme and a ramp time of 10 minutes. The embedded capacitors were subjected to 1000 thermal cycles for the thermal cycling test. No delamination or crack was found in the embedded capacitor components after 1000 temperature cycles. The capacitance of the embedded capacitor components decreased about 8% after thermal

cycling test, which may be attributable to the relaxation of stress in the dielectric film and the corresponding rearrangement of polymer segments in the composites.

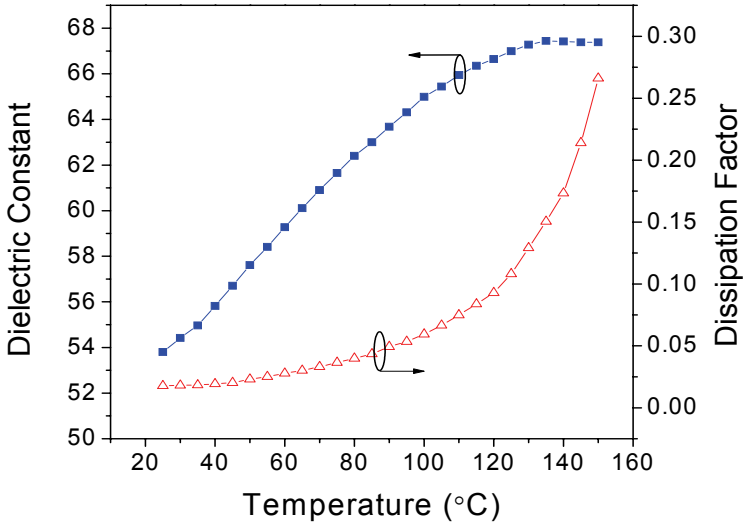

Figure 3.36 Temperature coefficient of dielectric constant and dissipation factor of CTBN-epoxy modified 50 vol% BT nanocomposite containing 1 wt% triazole.

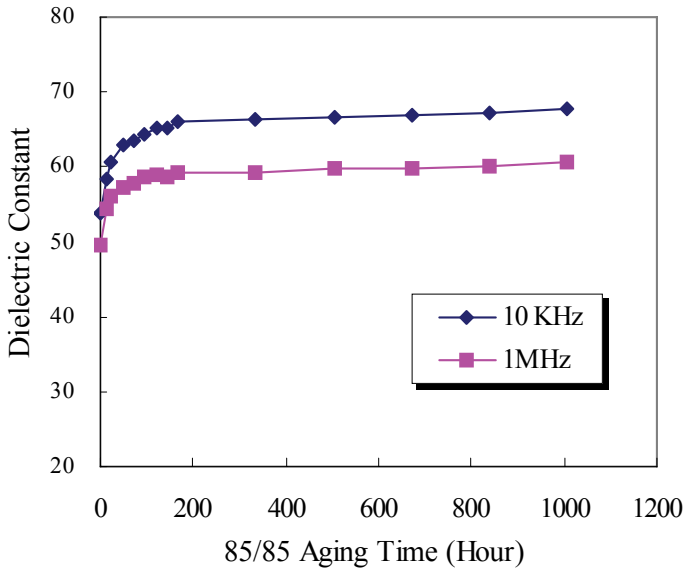

Figure 3.37 85°C/85% relative humidity aging reliability of CTBN-epoxy modified 50 vol% BT nanocomposite containing 1 wt% triazole.

3.4 Conclusions

Polymer-ceramic high-κ nanocomposite formulations were systematically investigated in order to obtain high dielectric constant (κ>50) nanocomposites at the lowest filler loading for embedded capacitor applications. It was found that material design and processing were critical. The addition of chelating agent can effectively improve the dielectric constant of the epoxy varnish, which resulted in the enhancement of the dielectric constant of its BT nanocomposites. Bimodal fillers can increase the dielectric constant of BT nanocomposites by enhancing the packing efficiency of BT nanoparticles. A proper amount of dispersing agent was essential in order to obtain high dielectric constant nanocomposites. With 5 wt% phosphate dispersing agent, a high dielectric constant of about 58 was obtained in the 50 vol% bimodal BT nanocomposite. Acidic phosphate ester dispersing agent can effectively improve the dispersion and dielectric constant of epoxy-barium titanate nanocomposites, however, the incorporation of phosphate ester led to the reduction of adhesion of nanocomposites to Cu substrate. To improve the adhesion of epoxy-BT nanocomposites whist keeping the high dielectric constant of BT nanocomposites provided by the dispersing agent, the BT nanoparticles were refluxed and functionalized with acidic phosphate ester before being formulated in the epoxy matrix. Thermogravimetric Analyzer (TGA) and Fourier Transformed Infrared Spectroscopy (FTIR) showed that the phosphate ester was chemically bonded on the particle surface. It was found the filler surface functionalization can significantly improve the adhesion of nanocomposites to Cu substrate. The nanocomposites with functionalized filler showed a high dielectric constant of 45.6, and successfully passed the high temperature thermal stress reliability test. To further improve the reliability of polymer-ceramic nanocomposites at high filler loadings, the epoxy matrix was modified with a secondary rubberized epoxy, which formed isolated flexible domains (island) in the

continuous primary epoxy phase (sea). The effects of sea-island structure on the thermal mechanical properties, adhesion, and thermal stress reliability of embedded capacitors were systematically evaluated. The optimized, rubberized nanocomposite formulations had a high dielectric constant above 50 and successfully passed the stringent thermal stress reliability test. A high breakdown voltage of 89 MV/m and a low leakage current of 1.9×10^{-11}A/cm^2 were measured in the large area thin film capacitors.

CHAPTER 4

HIGH DIELECTRIC CONSTANT COMPOSITE PHOTORESIST FOR EMBEDDED CAPACITORS

4.1 Introduction

Embedded capacitors require the use of high dielectric constant materials, because of the limited space inside the PCB substrate. Many dielectric materials have been investigated, and particularly polymer-ceramic composites have been extensively studied as the candidate for embedded capacitors because the combination of polymer and filler may give the composites advantages from both components [45, 63, 82, 88, 89]. However, the conventional polymer-ceramic composites are not photosensitive and cannot be directly patterned into desired geometry by the photolithography method, which is a standard process used in PCB board manufacturing. Moreover, via openings in the embedded capacitor layer are often required in order to make interconnects in the PCB board, as shown in Figure 4.1. An expensive and time-consuming laser drilling process has to be used to create via in conventional polymer-ceramic high-κ composites. On the other hand, a photodefinable high-κ composite can be easily patterned into desired geometry so that it can save the substrate area and save the time needed for laser drilling of via openings as in conventional high-κ composites. Therefore, successful development of such photodefinable high-κ polymer composite will lead to embedded capacitors with low cost, great design flexibility as well as great versatility in applications.

A photodefinable high-κ composite requires the use of a UV-radiation curable polymer as the matrix. UV radiation-initiated polymerization can be either free-radical polymerization or cationic polymerization. Free-radical photopolymerization is mostly

based on acrylate and methacrylate monomers. These monomers can be modified at the ester functionality, thus allowing the tailor of final materials properties [93]. Free-radical photopolymerization is typically inhibited by the presence of oxygen and often needs to be conducted in inert atmosphere. In contrast, cationic photopolymerization is not affected by oxygen and does not require extra setup for inert environment. In addition, cationic polymerization continues long after UV irradiation has stopped and therefore can penetrate into the area where the UV light cannot directly irradiate on [94]. Therefore, cationic photopolymerization is more advantageous for filled composite photoresist systems. Cycloaliphatic epoxies and SU8 epoxy are two most often used monomers that can be polymerized by cationic photopolymerization.

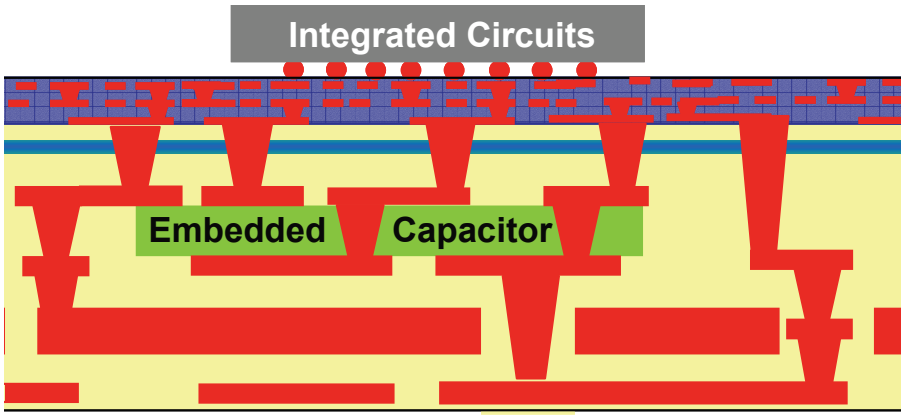

Figure 4.1 Embedded capacitors in the PCB board. Interconnects are required through the embedded capacitor dielectric layers.

In this work, we present a study on the novel, photodefinable, high dielectric constant composite material for embedded capacitor applications. It consists of SU8 epoxy as the polymer matrix and barium titanate (BT) nanoparticles as the filler. UV lithography was used to pattern the SU8 composite photoresist on a variety of substrates, i.e. rigid glass substrate, Cu-coated rigid glass substrate, and polyimide flexible substrate. The UV absorption characteristics of BT nanoparticles were studied with a UV-Vis

spectrophotometer. The effects of BT nanoparticle size, filler loading, and UV irradiation dose on the SU8 photopolymerization were systematically investigated. The dielectric properties of the photodefined SU8 nanocomposites were characterized by a LCR meter.

4.2 Experimental

4.2.1 Materials and Composite Photoresist Formulation

The SU8 (Epon Resin SU-8) was obtained from Hexion Specialty Chemicals. Su8 is an epoxy-type, negative, near UV (365 nm) photoresist that has high optical transparency and is well suited for applications where it is imaged and permanently left in place. The chemical structure of SU8 is shown in Figure 4.2. Because the resist has a high functionality, a high degree of crosslinking can be achieved, resulting in a high aspect ratio and straight sidewall structure in lithographic applications. SU8 has been extensively used to fabricate high-aspect ratio structure such as micro-electro-mechanical systems (MEMS), micro fluidic devices, and etc. [95-99]. Triarylsulfonium (TAS) salt (from Aldrich), with a fixed concentration of 10 wt%, was used as the photosensitive compound to initiate the cationic polymerization of SU8 epoxide ring. γ-butyrolactone (GBL) and propylene glycol monomethylether acetate (PGMEA) were used as the solvent and developer, respectively. Two BT nanopowders, with average particle sizes of 65 nm (denoted as small nanoparticles) and 590 nm (denoted as large nanoparticles), respectively, were used in the SU8 composite photoresist in order to increase its dielectric constant.

The high dielectric constant composite photoresists were obtained by a two-step mixing procedure. The formulations were first ultrasonicated for 1 hour, and then ball milled with yttrium-stabilized zirconia beads at the rate of 220 rpm for 24 hours.

SU8

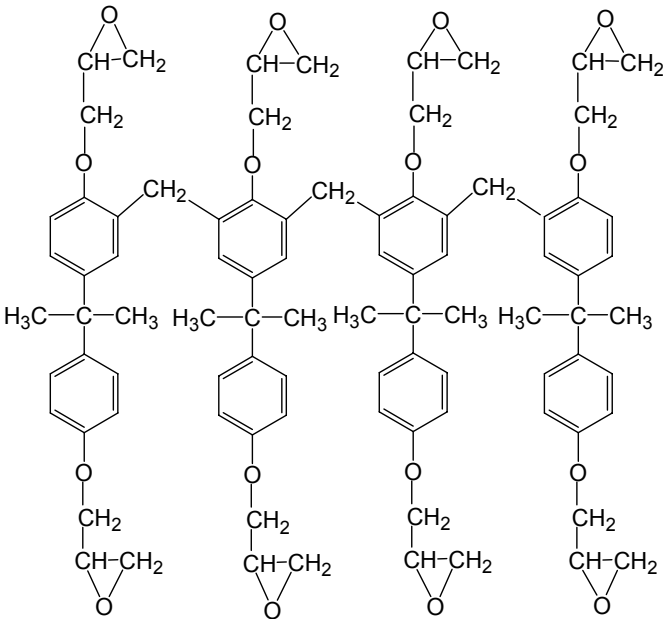

Triarylsulfonium Salt

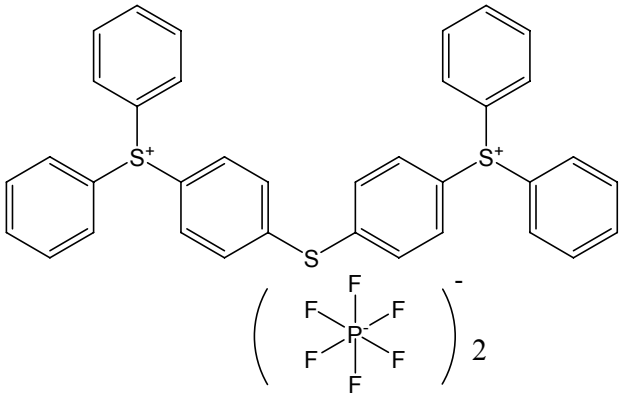

γ-Butyrolactone

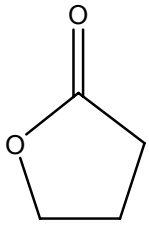

PGMEA

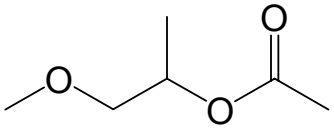

Figure 4.2 Chemical structures of SU8, triarylsulfonium salt, γ-butyrolactone, and propylene glycol monomethylether acetate (PGMEA).

4.2.2 UV-Vis Spectroscopy Characterization of BT Nanoparticles

The UV-Vis Spectroscopies of small and large BT nanoparticles were characterized by a UV-Vis spectrophotometer (DU520, Beckman), from the wavelength of 300 nm to 800 nm. The particles were dispersed in γ-butyrolactone, which almost has no UV absorption in this range.

4.2.3 Microfabrication Process and Characterization

To study the effects of BT nanoparticle size, filler concentration, and UV irradiation dose on the photopolymerization of the composite photoresist, glass substrates were used to fabricate the testing structure. First, the glass substrates were cleaned by oxygen plasma in a reactive ion etcher (RIE, from Plasma Therm). The conditions were as follows: power 300 W, flow rate 30 sccm, pressure 150 mTorr, and time 10 minutes. Oxygen plasma cleaning can effectively improve the adhesion of composite photoresist on glass substrates. Because spin coating cannot produce very thick composite films uniformly, we used bar coating method instead to deposit composite photoresist of about 50 μm thickness. The composite photoresist was then prebaked at 95 °C for 1 hour to evaporate solvent γ-butyrolactone. To study the photopolymerized thicknesses, back-side UV exposure was utilized to initiate the crosslinking of SU8 photoresist, as this can guarantee good adhesion of polymerized structure on the substrate. The back side of composite-coated glass substrate was exposed to UV source through quartz masks by a UV Mask Aligner (MA-6, from Karl Suss). The exposure was at I line, with a wavelength of 365 nm. The exposed composite photoresist was then postbaked at 95 °C for 30 minutes in order to complete the acid-catalyzed cationic polymerization. Then the patterned structure was developed in PGMEA to remove unexposed composite photoresist. Ultrasonication for a few minutes was required to obtain good and clear structure. Isopropyl alcohol (IPA) was used to rinse the developed high dielectric constant composite photoresist. The thicknesses of photopolymerized structure were then

measured by a profilometer (KLA-Tencor P15). The flow chart of microfabrication process is shown in Figure 4.3.

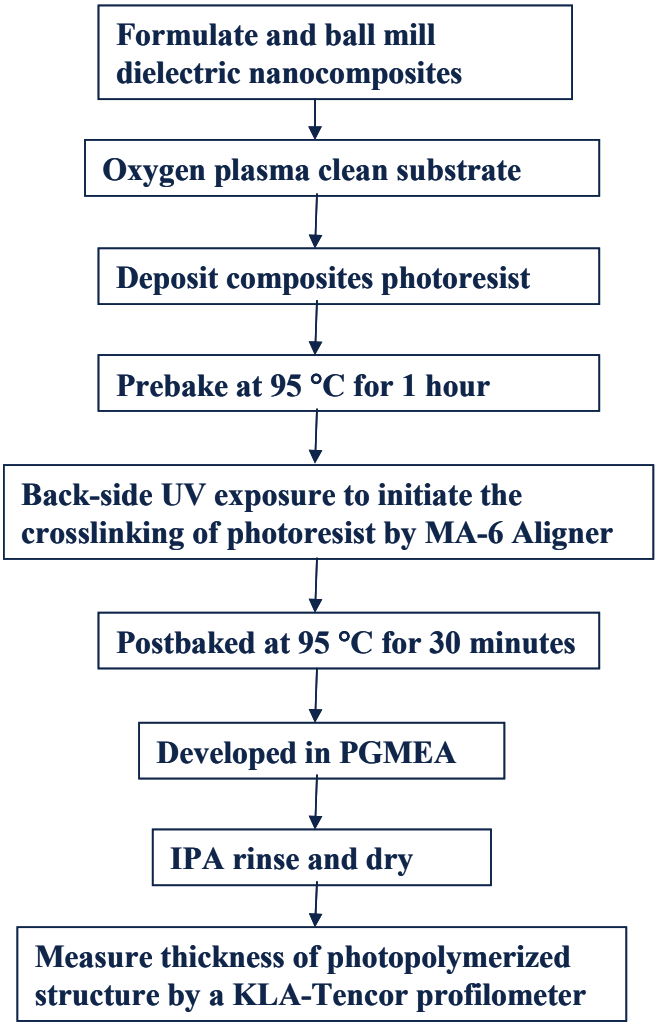

Figure 4.3 Flow chart of microfabrication process.

Figure 4.4 shows the photodefined pattern of SU8 composite photoresist containing 40 vol% small BT nanoparticles. The exposure dose was 1200 mJ/cm^{-2}, and the polymerized thickness was about 1.52 μm.

To measure the dielectric properties of composite photoresist, parallel plate capacitors were fabricated on Cu-coated glass substrates. First, a thin layer of titanium (200 Å) and copper (3000 Å) was deposited on the glass substrate as the bottom electrode

of capacitors by a DC sputterer (from CVC Products). Then, the SU8 composite photoresist was spin coated onto the Cu-coated glass substrate. The next processing steps were similar to the previously described method for processing SU8. The only difference is that the sample was exposed to 365 nm UV light in the front-side mode. Finally, the DC sputterer was used to deposit another layer of copper (3000 Å) as top electrode onto the material through a shadow mask. The capacitance and dissipation factor of the capacitor were then measured with an HP 4263A LCR meter, at the frequency from 10 KHz to 10 MHz. Figure 4.5 shows an example of parallel plate capacitors fabricated with SU8 composite photoresist containing 40 vol% small BT nanoparticles.

Embedded capacitors were demonstrated on a flexible polyimide substrate. Interdigitated electrodes were pre-fabricated on the flexible polyimide film. Then the high dielectric constant composite photoresist was spin coated on the substrate and patterned with the same processing method as described above for SU8.

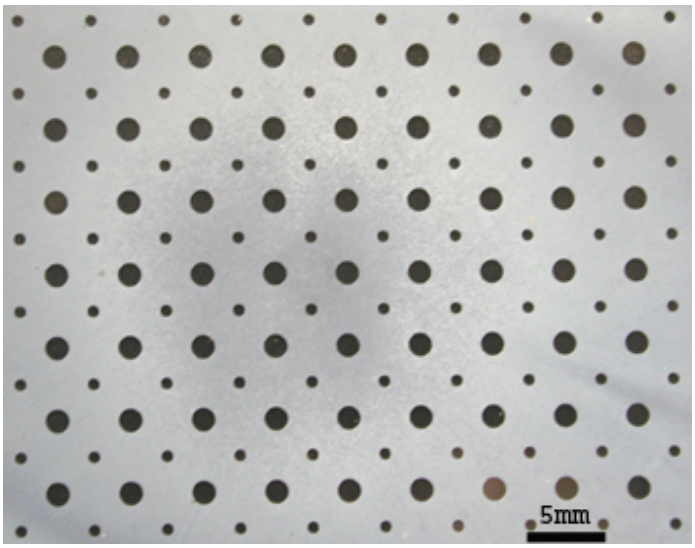

Figure 4.4 Photodefined pattern of SU8 composite photoresist containing 40 vol% small BT nanoparticles. The exposure dose was 1200 mJ/cm^{-2}, and the polymerized thickness about 1.52 μm.

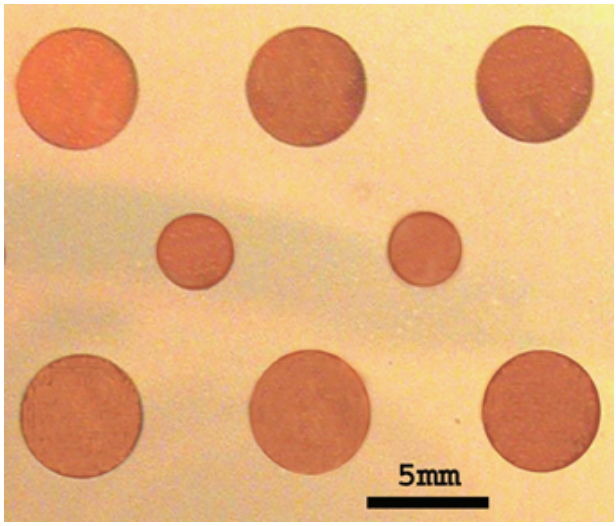

Figure 4.5 Parallel plate capacitor fabricated with SU8 composite photoresist containing 40 vol% small BT nanoparticles.

4.3 Results and Discussions

In polymer-ceramic high-κ composites, polymer matrices are used to provide the low temperature processing compatibility in line with the organic PCB (mostly epoxy-based) manufacturing processes. Epoxy has often been used as the polymer matrix in conventional high-κ polymer-ceramic composites. Because SU8 is a high functionality epoxy, using SU8 as the matrix for high-κ composite photoresist can ensure the good compatibility with the PCB manufacturing.

SU8 photoepoxy can be polymerized by cationic photopolymerization, which is typically induced by Lewis acid. In our system, the Lewis acid was generated by exposing triarylsulfonium salt to UV source, as shown in Figure 4.6. The photogenerated acid can catalyze epoxy ring opening reaction, and thereby initiate the cationic crosslinking of SU8.

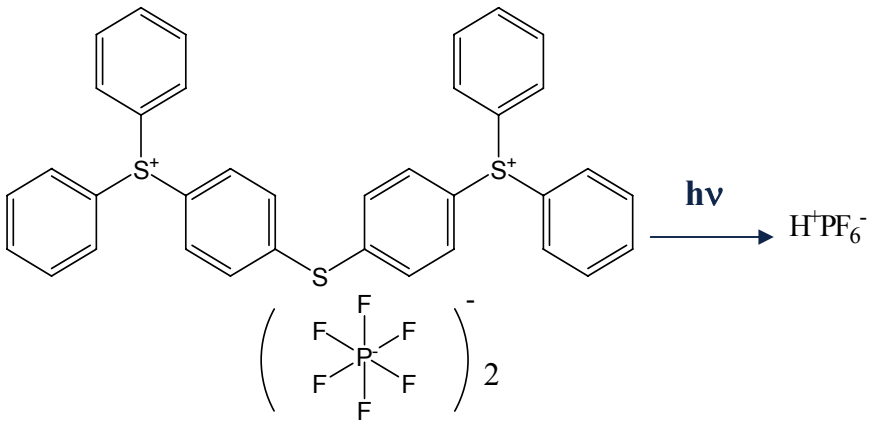

Figure 4.6 Photogeneration of Lewis acid.

4.3.1 UV Characteristics of BT Nanoparticles

BT nanoparticles are used to provide high dielectric constant in the nanocomposites. However, BT nanoparticles can absorb UV light, which have strong effect on the photopolymerization behavior of the SU8 composite photoresist. Figure 4.7 shows the UV-Vis spectroscopy of 0.01 wt% small (65nm) and large (590nm) BT nanoparticles in solvent γ-butyrolactone. γ-butyrolactone has very little UV absorption in the measurement wavelength range and was used as the reference. As shown in Figure 4.7, small and large BT nanoparticles show different UV-Vis absorption behavior. The large BT nanoparticles show a high and almost constant UV absorbance in the whole measurement wavelength range from 300 to 800 nm. On the other hand, the UV absorption intensity of small nanoparticles decreases dramatically as the UV wavelength increases. When the wavelength is above 441 nm, the large BT nanoparticles have stronger absorption than the small BT nanoparticles. In this wavelength range, the size of large BT particles is comparable to the UV wavelength. However, when the wavelength is below 441 nm, the small BT particles show stronger UV absorption. SU8 photoresist is typically exposed at 365 nm. At this wavelength, the UV absorbance of small BT particles is much stronger than the large BT particles. Overall the BT nanoparticles have

quite strong UV absorption, which can significantly hinder the generation of Lewis acid during UV exposure and thereby affect photopolymerization reaction of SU8 composite photoresist.

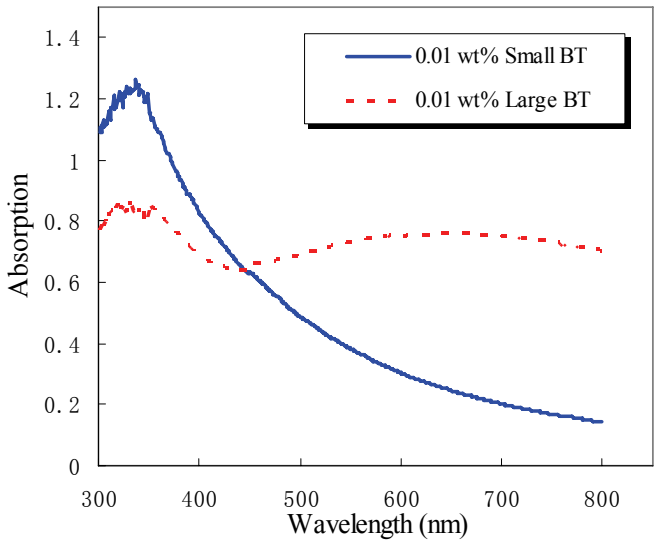

Figure 4.7 UV-Vis spectroscopy of small and large BT nanoparticles in solvent.

4.3.2 Photopolymerization of High-κ SU8 Composite Photoresist

In order to study the effect of BT nanoparticle inclusion on SU8 photopolymerization thicknesses, SU8 composite photoresist was deposited on glass substrates and then exposed in the back side mode. For neat SU8, an exposure dose of 300 mJ/cm^{-2} can polymerize SU8 of about 100 μm thick. However, even after 400 mJ/cm^{-2} irradiation the composite photoresist cannot be adequately polymerized to form dielectric film. Figure 4.8 shows the photopolymerized thickness after 1200mJ/cm^{-2} irradiation versus BT filler loading in the SU8 composite photoresist. The polymerized thicknesses decrease with the inclusion of more BT nanoparticles. The inclusion of small BT nanoparticles leads to a much smaller polymerized thickness when compared to the inclusion of large BT nanoparticles at the same filler loading. This change is associated with the UV absorbance of the BT nanoparticles. Small BT particles have stronger

absorbance at the 365 nm exposure wavelength, which reduces the depth that the UV light can penetrate through in the SU8 composite photoresist. Therefore, the polymerized thickness is smaller with the inclusion of small BT nanoparticles.

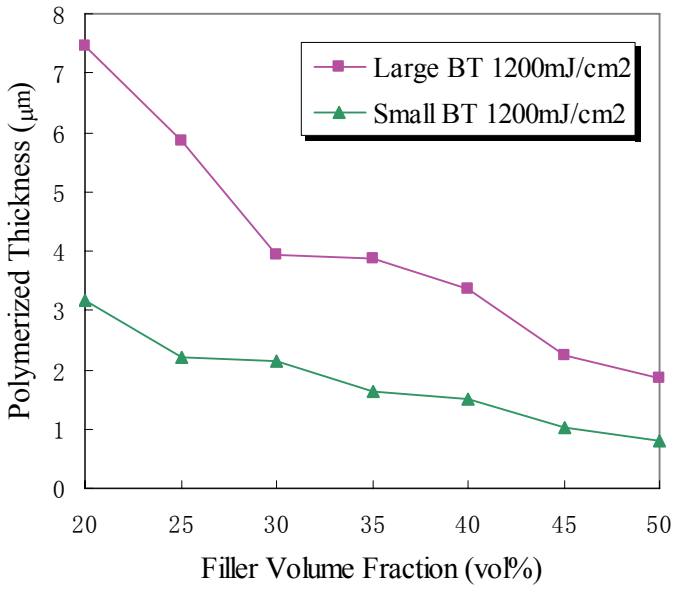

Figure 4.8 Photopolymerized thickness versus BT filler loading in the SU8 composite photoresist.

The photopolymerized thickness of composite photoresist also depends on the irradiation dose. A higher polymerized thickness can be obtained by increasing the exposure dose. As illustrated in Figure 4.9, for a composite containing 40 vol% large BT nanoparticles, the polymerized layer thickness increased from 3.35 μm to 5.08 μm when the exposure dose increases from 1200 to 1800 mJ/cm^{-2}. The dotted trend lines in Figure 4.9 indicate that the photopolymerization in composite photoresist follows logarithmic rule. Based on Beer-Lambert law, photopolymerization model predicts that the photopolymerized thickness (T_p) is proportional to the penetration depth (P_d) and logarithm of exposure dosage (D) [100, 101]:

$$T_p = P_d \ln(D / D_c) \qquad \text{Equation 4.1}$$

where D_c is the threshold dosage required to start the photopolymerization.

Table 4.1 shows a comparison of the penetration depth and threshold dosage calculated based on Equation 4.1. The penetration depth P_d is determined by the BT nanoparticle size as well as the filler loading. Large BT nanoparticles, which have less UV irradiation absorbance at 365 nm, result in a larger penetration depth. For the same size BT nanoparticles, a higher filer loading leads to a smaller penetration depth. Similarly, the threshold dosage D_c is also related to the BT nanoparticle size as well as the filler loading. However, the dependency is not as strong as for P_d, and all of the threshold dosage values are close to 400 mJ/cm^{-2}. The threshold dosage is slightly larger for composite photoresist filled with small BT nanoparticles because of the stronger UV absorbance of small BT nanoparticles at 365 nm. Table 4.1 also shows a higher threshold dosage is required at a higher BT loading.

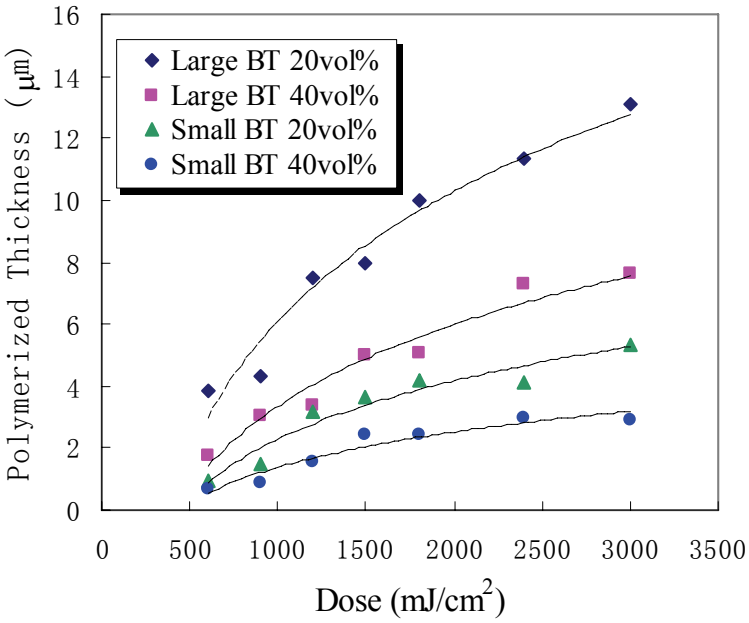

Figure 4.9 Photopolymerized thickness as a function of irradiation dose. The dotted trend lines are calculated according to logarithmic rule.

Table 4.1 Comparison of the penetration depth and threshold dosage of SU8 composite photoresist

BT Size	Vol. Fraciton (vol%)	P_d (μm)	D_c (mJ/cm^{-2})
Large	20	6.06	348
Large	40	3.81	416
Small	20	2.72	430
Small	40	1.64	432

4.3.3 Dielectric Properties of of High-κ SU8 Composite Photoresist

The dielectric constant of SU8 composite photoresist can be improved by the inclusion of BT nanoparticles. For neat SU8, the dielectric constant is about 3.5. With the addition of 50 vol% BT nanoparticles, the dielectric constant (@10 KHz) can be enhanced to 44 and 46 for small and large BT, respectively, as shown in Figure 4.10. The dielectric constant and dissipation factor of SU8 composite photoresist are almost same for large and small BT at the same filler loading. A modified Lichteneker equation is often used to predict the dielectric constant of composites that have high volume fraction of ceramic and also a larger difference in the value of relative permitivitty of ceramic and polymer [89].

$$\log \varepsilon = \log \varepsilon_1 + v_2(1-k)\log(\frac{\varepsilon_2}{\varepsilon_1}) \qquad \text{Equation 4.2}$$

where k is a fitting factor, which is typically 0.3 for well dispersed suspensions; ε_1 is the dielectric constant of the polymer matrix; ε_2 is the dielectric constant of the filler. According to the above equation, the dielectric constant of composite is dependent on the dielectric constant of ceramic phase as well as on the polymer phase. It is reported that the dielectric properties of BT nanoparticles have very strong size dependency. The dielectric constant of 590 nm BT nanoparticles is above 3000, however, it is less than 1000 for 65 nm particles [78]. From our results, such a difference in the dielectric

constant of BT nanoparticles does not yield significant differences in the dielectric properties of the SU8-BT nanocomposites. This suggests that as long as the dielectric constant of the filler is high enough, there will not be dramatic differences in the dielectric constant of its composites even if the dielectric constant of filler is quite different. Because by using smaller particles one can obtain thinner layer of dielectric coating and thereby higher capacitance density, smaller particles are recommended for embedded capacitors when applicable.

The frequency responses of the dielectric constant of SU8 composites photoresist are shown in Figure 4.11. The dielectric constant of SU8 composite photoresist decreases slightly when the frequency increases.

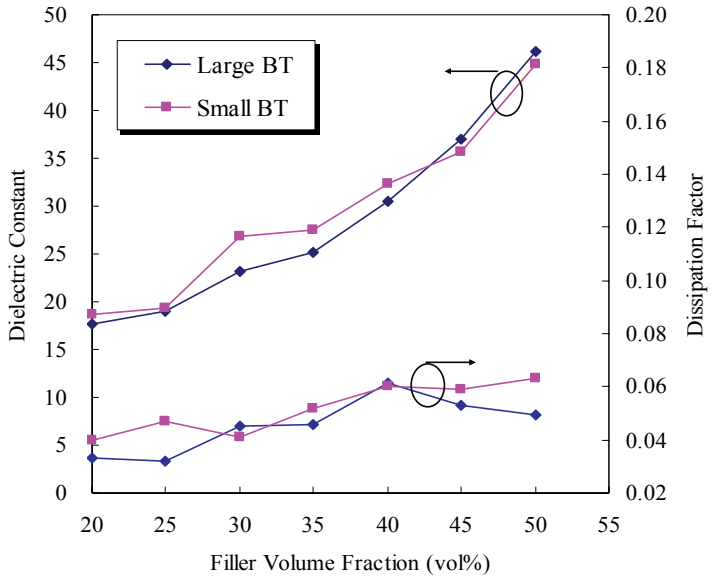

Figure 4.10 Dielectric constant and dissipation factor of SU8 composite photoresist versus the BT nanoparticles volume fraction.

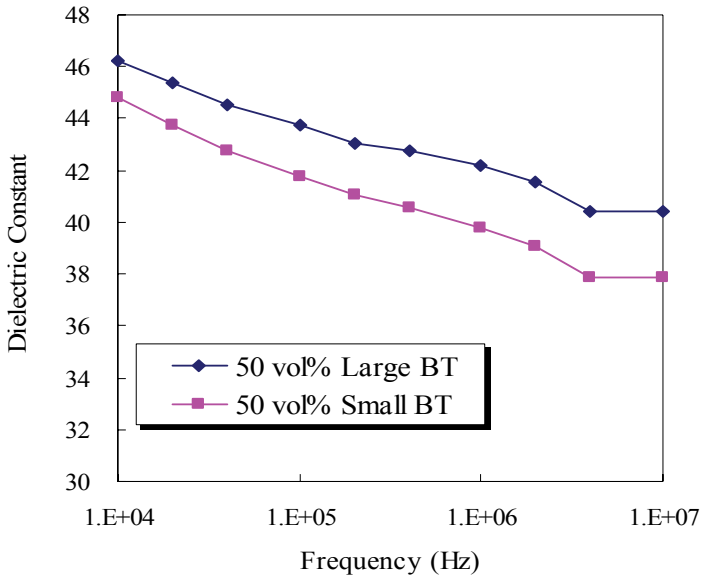

Figure 4.11 Frequency responses of the dielectric constant of SU8 composites photoresist.

4.3.4 Embedded Capacitors Fabricated on a Flexible Polyimide Substrate with High-κ SU8 Composite Photoresist

The SU8 composite photoresist shows a high dielectric constant at high filler loadings, and it can be processed by the straightforward photolithography method. Therefore, SU8 composite photoresist is suitable for embedded capacitors on organic substrates. Figure 4.12 shows the image of a test coupon with interdigitated capacitor electrodes fabricated on a flexible polyimide substrate. The inset shows the detailed structure of electrodes. The thickness of Cu electrodes is 12 μm. Figure 4.13 shows the embedded capacitors fabricated on the flexible polyimide substrate by the photolithography method. The dielectric is SU8 composite photoresist filled with 40 vol% large BT nanoparticles. Because the electrode thickness is large (12 μm), a dose of 4500 mJ/cm^{-2} was used to ensure complete polymerization of the composite photoresist that covered the whole depth of the electrodes. The dielectric constant was measured to be about 31, which is similar to the value from parallel plate capacitor measurement.

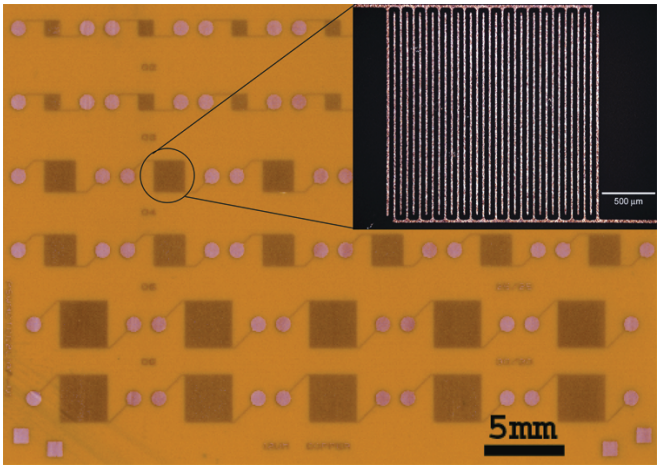

Figure 4.12 Image of a test coupon with interdigitated capacitor electrodes on a flexible polyimide substrate and the inset shows the detailed structure of interdigitated electrodes.

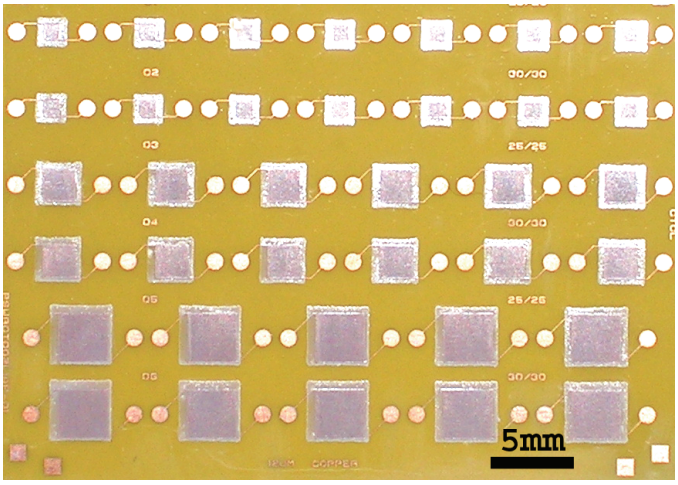

Figure 4.13 Image of embedded capacitors fabricated on the flexible polyimide substrate.

4.4. Conclusions

A novel, photodefinable, high dielectric constant composite material was developed. It consisted of SU8 as the polymer matrix and barium titanate (BT)

nanoparticles as the filler. It was found that the smaller BT nanoparticles had stronger UV absorbance at the exposure wavelength, and thereby led to smaller photopolymerization thicknesses in the composite photoresist. As the BT filler loading increased, the photopolymerization thickness decreased as well because of the absorption of BT nanoparticles. The SU8 composite photoresist showed a high dielectric constant at high BT filler loadings. The BT nanoparticle size does not have significant effect on the dielectric properties of composite photoresist. Embedded capacitors using the novel high dielectric constant SU8 composite photoresist were demonstrated on a flexible polyimide substrate by the conventional UV lithography method.

CHAPTER 5

ULTRAHIGH DIELECTRIC CONSTANT POLYMER-CARBON BLACK NANOCOMPOSITES FOR EMBEDDED CAPACITORS

5.1 Introduction

Integration of passives components requires the development of new high dielectric constant materials, due to the limited space in the PCB structure. In order to realize embedded capacitors, many approaches have been investigated, such as thin film CVD deposition, anodization, sputtering, and sol-gel process [16-30]. Each of these techniques has its advantages, nevertheless has its own disadvantages as well, e.g. requiring a high processing temperature, requiring expensive equipment, difficult to implement into large-area MCM-L substrates, and etc [77]. As an alternative approach, polymer-ceramic composites have been systematically evaluated as a candidate for embedded capacitors, because the combination of polymer and filler may give the composites advantages from both sides by a careful design and choice of components. The polymer-ceramic composites, however, have only had limited success. Commercially available polymer-ceramic composites only have a dielectric constant of up to 30, which is not sufficient for many applications for the next generation electronics. Therefore, a dielectric material that satisfies all of the requirements needed for embedded capacitors, especially in the cases that require high capacitance density, e.g. decoupling capacitors, has not been developed yet. This poses challenges as well as opportunities for the development of novel embedded capacitor dielectrics.

Another type of high-κ dielectric nanocomposite that can be used for embedded capacitors is the dielectric composite based on percolation mechanism. Percolation transition is a critical phenomenon. The dielectric properties of high-κ polymer-metal

composites near percolation threshold can be predicted by scaling theory [102-108]. According to scaling theory, the properties of physical quantities such as the dc electrical conductivity and dc dielectric constant of a percolation system should exhibit a power-law behavior. The effective dielectric constant can thus be described by the following equation [102-104]:

$$\overline{\sigma} = \sigma_D (f_c - f)^{-s} \qquad f < f_c \qquad \text{Equation 5.1}$$

$$\overline{\sigma} = \sigma_M (f - f_c)^{t} \qquad f > f_c \qquad \text{Equation 5.2}$$

$$\overline{\varepsilon} = \varepsilon_D \left| f - f_c \right|^{-q} \qquad \text{Equation 5.3}$$

where σ_M and σ_D are the dc electrical conductivity of metal and dielectric material, respectively; f_c is the percolation threshold concentration of metal at which the conductivity of conductor-insulator composite increases dramatically when f approaches f_c from below the percolation threshold; ε_D is the dielectric constant of the dielectric material; q , s and t are scaling constants, which are related to the material properties, microstructure, and connectivity of the metal-insulator composite.

Physically, this phenomenon can be explained as: when the concentration of the metal is close to the percolation threshold, large amount of metal clusters but no percolated cluster will be formed. These metal clusters will act as the electrodes of capacitors when they are loaded in an external electrical potential. Now, the composite can be regarded as a "super capacitor network" with very large area and small thickness. Therefore, the effective dielectric constant of the metal-insulator composite could be three or four orders higher than the dielectric constant of the insulating material.

Pecharroman etc. [104] first experimentally observed ultrahigh dielectric constant of 500,000 in molybdenum-filled mullite composites (cermets). Due to the narrow processing window of the composite near percolation threshold window, a functionally graded material (FGM) was prepared instead of homogeneous monolithic insulator-

conductor composites. The FGM was then cut through and polished down to 1 μm. With this method, the composition could be accurately controlled in the specimen, and thus the ultrahigh dielectric constant near the percolation threshold can be obtained.

Rao et al. [109] demonstrated that silver-epoxy composite materials have high dielectric constant (>1,000) and high reliability performance suitable for embedded passive application. It was found that the percolation threshold of the epoxy silver composite is around 11.5vol%. At silver flake concentration of 11.23 vol%, dielectric constant of 1000 was achieved. The die shear strength of epoxy silver composite (with 11.23 vol% silver flake) on polyimide substrate is around 28 Mpa, which suggests that the composite has superior dielectric properties and good processibility. However, the dielectric properties of epoxy-silver composite materials are very difficult to reproduce, because a small change of filler loading at the percolation region will dramatically change the electric and dielectric properties of the composites.

To obtain a reproducible high dielectric constant material compatible with the low temperature manufacturing process of printed circuit board (PCB), in this work, we present a study on epoxy-carbon black composites as the embedded capacitor dielectrics. Six different types of carbon blacks were evaluated. With a proper filler loading level and good dispersion, high dielectric constants over 1000 were observed for four out of the six carbon blacks. The dispersion of carbon black is critical to obtain high dielectric constant carbon black composites. Transmission electron microscope (TEM) and scanning electron microscope (SEM) were used to characterize the structure of carbon and their composites, respectively, in order to correlate the structure of carbon black and morphology of their composites with the corresponding material dielectric properties.

5.2 Experimental

5.2.1 Materials and Formulation

A bisphenol-A type epoxy resin (from Aldrich Chemical Company), an anhydride hardener (MHHPA, from Lindau Chemical Company), and an imidazole catalyst (2E4MZ-CN, from Shikoku Ltd.) were used as the polymer matrix in this study. For comparison, silicone (HIPEC® Q1-4939, from Dow Corning Incorporation) was also used as the polymer matrix for the dielectric composites because of its extremely low dissipation factor. The carbon blacks studied were CBC1, CBC2, CBD3, CBD4, CBM5, and CBM6.

The bisphenol-A resin was mixed with the hardener first, and then carbon black was added into the formulation. The mixture was premixed in an ultrasonicator for 1 hour, and then processed in a three-roll mill for 1 hour. The actual filler loading of composites after processing was determined by a thermogravimetric analysis (TGA), which was conducted with a TGA 2050 (from Thermal Advantages Inc.) under a nitrogen atmosphere at a heating rate of 10 ºC/min. Next, the catalyst was added into the formulation, and the mixture was dispersed in the ultrsonicator for 30 minutes.

5.2.2 Sample Preparation and Characterization

5.2.2.1 DSC Characterization

The curing conditions for bisphenol-A epoxy and silicone were determined by a modulated differential scanning calorimeter (DSC, Model 2920, from TA Instruments), at a heating rate of 5 ºC/min under a nitrogen atmosphere. Figure 5.1 shows the DSC thermograph of bisphenol-A epoxy and silicone. According to the curing peak temperature, the curing condition for both polymers and their composites was set to be 150 ºC for 1 hour.

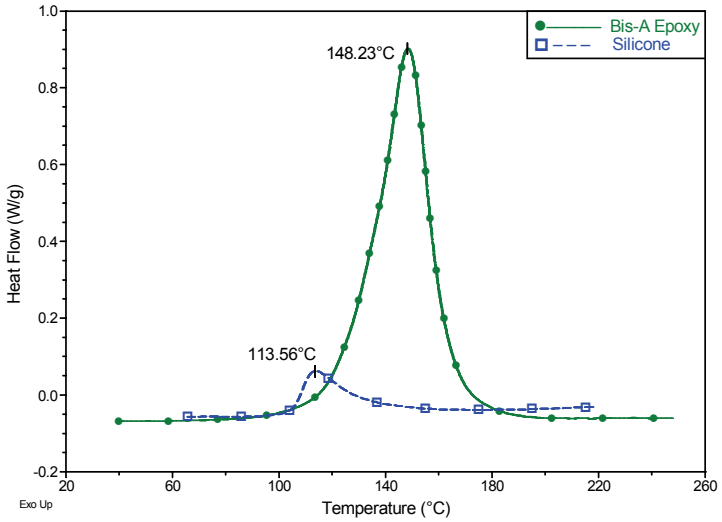

Figure 5.1 DSC curing profile of bisphenol-A epoxy and silicone.

5.2.2.2 Dielectric Properties Characterization

For dielectric properties measurements, parallel plate capacitors were fabricated on a silicon wafer with the formulated high dielectric constant composites. First, a thin layer of titanium (200 Å) and copper (3000 Å) were deposited on the wafer as the bottom electrode of capacitors by a DC sputterer (from CVC Products Incorporation). Then, the dielectric composite was spin coated onto the wafer. Next, the sample was cured with an optimized curing procedure in a Lindberg furnace under a nitrogen atmosphere. Finally, the DC sputterer was used to deposit another layer of copper (3000 Å) as the top electrode onto the material through a shadow mask. The capacitance and dissipation factor of the capacitor were then measured with an HP 4263A LCR meter, at frequencies from 10 KHz to 10 MHz.

5.2.2.3 Microscopy Observation

A JOEL 100C Transmission Electron Microscope (TEM), operating at 100 KV, was used to analyze the particle sizes and morphologies of carbon black powders. For

carbon black composites, the morphology studies were conducted by a field emission scanning electron microscopy (FESEM) (Model S-800, from Hitachi Company). Cross sections of the samples were polished before observation.

5.2.2.4 Thermomechanical Analysis

The coefficients of thermal expansion (CTE) of the cured dielectric composites were characterized using a thermomechanical analyzer (TMA, Model 290, from TA Instruments). The dimension of the sample was about 4×4×3 mm. The sample was heated from room temperature to 200 ºC at a rate of 5 ºC/min under a nitrogen atmosphere.

5.2.2.5 Dynamic Mechanical Analysis

A dynamic mechanical analyzer (DMA) by TA Instruments, Model 2980 was used to study the dynamic moduli of the cured dielectric composites. The measurement was conducted in a single cantilever mode at 1 Hz sinusoidal strain loading. The sample was heated from room temperature to 250 ºC at a rate of 3 ºC/min in the DMA furnace.

5.3 Results and Discussions

5.3.1 Characteristics of Carbon Blacks

Carbon black was selected as the filler for high dielectric constant composites due to its large surface area and its wide range of electrical properties based on it surface chemistry, particle size and aggregate structure. Table 5.1 shows the characteristics of carbon black used in this study. Since carbon blacks have a large surface area, chemical species are readily adsorbed or chemically bonded to the carbon surfaces, and the surface chemistry of carbon blacks appreciably affects the physicochemical properties of their composites. The information about carbon surfaces can be obtained by thermal degradation studies on carbon blacks. The dominant gases produced during thermal

degradation are CO and CO_2, which are from the desorption of surface oxide groups such as carboxyl, aldehyde, lactone, ether, and quinine, etc [110, 111]. Figure 5.2 shows TGA studies of carbon blacks under a nitrogen atmosphere. Carbon black CBD4, CBD3 and CBC1 have more weight loss than other carbon blacks, which indicates more oxide groups present in these carbon blacks.

Table 5.1 Characteristics of carbon black used in this study

	Average Particle Diameter (nm)	BET Surface Area (m^2/gram)	DBP Absorption (cc/100gram)
CBC1	**12**	**635**	**330**
CBC2	**50**	**35**	**90**
CBD3	**30**	**950**	**380**
CBD4	**18**	**410**	**120**
CBM5	**45**	**50**	**165**
CBM6	**30**	**65**	**190**

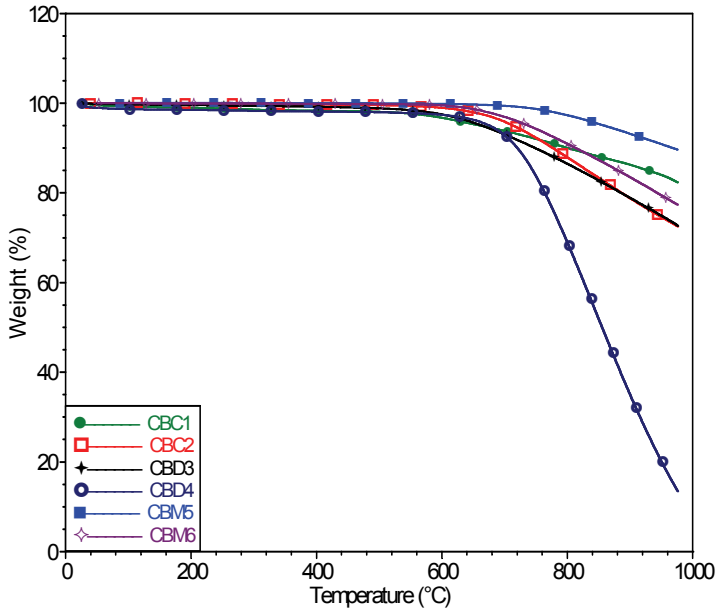

Figure 5.2 TGA studies of carbon blacks.

However, carbon blacks generally have much smaller weight loss than polymer matrices when heated. Figure 5.3 shows the TGA studies of bisphenol-A epoxy. At a temperature above 500 ºC, the epoxy was almost completely degraded, whereas the carbon blacks only lost a small percentage of their weight. Such a difference was utilized to accurately calculate the actual carbon black loading after three-roll mill processing, because the actual filler loading level may change during the processing, especially in our case in which a three-roll mill was used to disperse carbon blacks in the composites.

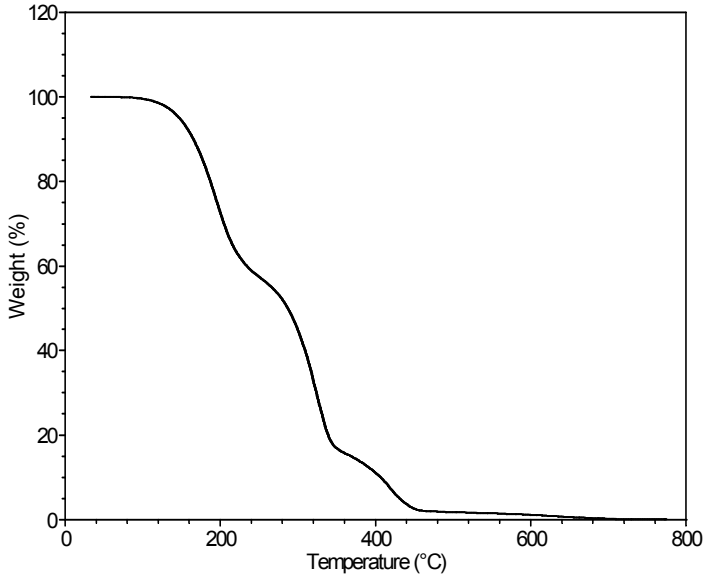

Figure 5.3 TGA studies of bisphenol-A epoxy.

5.3.2 Dielectric Properties of Carbon Black Composites

Figure 5.4 shows the dielectric constant of carbon black composites as a function of filler loading. Six different types of carbon blacks were evaluated; four of them show dielectric constants higher than 1000 (@ 10 kHz), and they were CBC1, CBC2, CBD3, and CBD4. An extremely high dielectric constant of 13,305 (@10 kHz) was achieved for an extra conductive carbon black CBD3. The highest dielectric constant obtained for CBC1, CBC2, and CBD4 composites were 1656, 2304, and 1315, respectively. The dielectric properties of carbon black composites are strongly dependent on the particle size and aggregate structure of the carbon blacks.

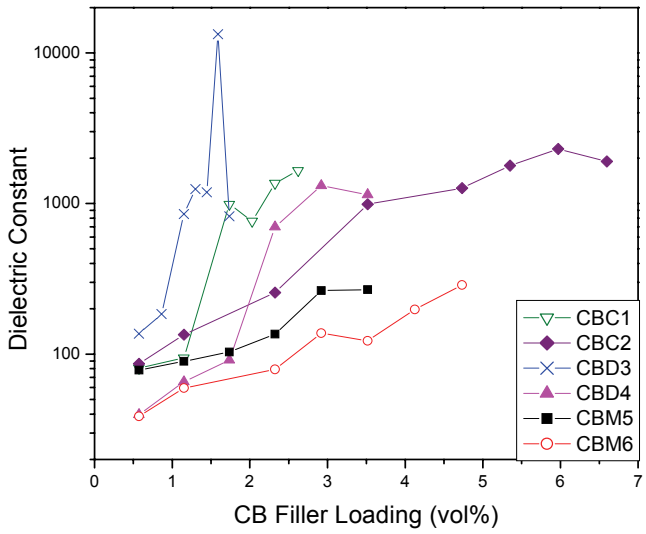

Figure 5.4 Dielectric constants of carbon black composites as a function of filler loading (@ 10 KHz).

Figure 5.5 shows the TEM micrographs of carbon black powders. The figure illustrates that the extra conductive carbon black CBD3 has a very small particle size, and an extremely high structure and surface area; thereby, the filler loading needed to obtain high dielectric constant composites is very small, only about 1 to 2 vol%. Carbon black CBC1 has a very high structure and a high conductivity, too, and the filler loading needed to reach high dielectric constants is low as well. However, for a relatively low conductivity carbon black CBC2, it has a large primary particle size of about 70 nm, and the particles are not highly aggregated. Therefore, the CBC2 filler loading corresponding to high dielectric constants is much higher than that of the CBD3 composites. A higher conductivity carbon black usually results in a higher dielectric constant in its composites; however, the composites are more difficult to process since the composites have a narrower composition window near the percolation threshold due to its high structure and large surface area.

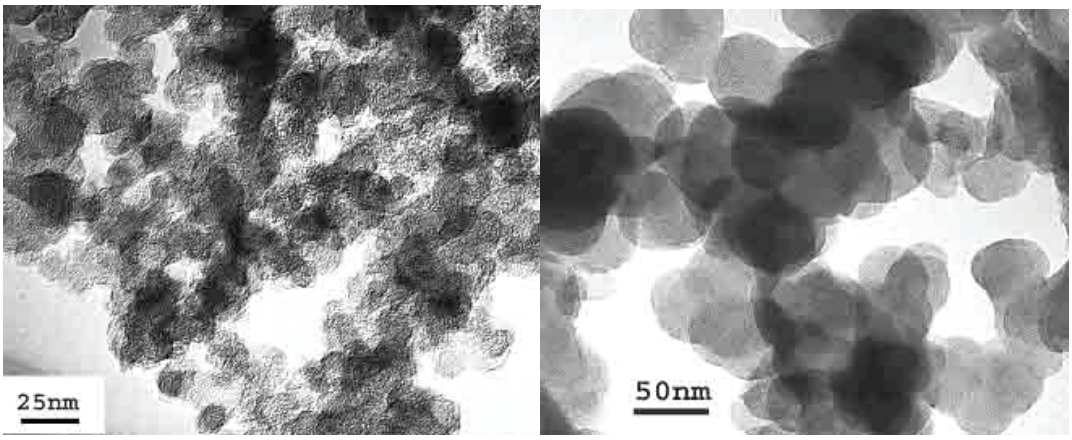

(a) CBC1 (b) CBC2

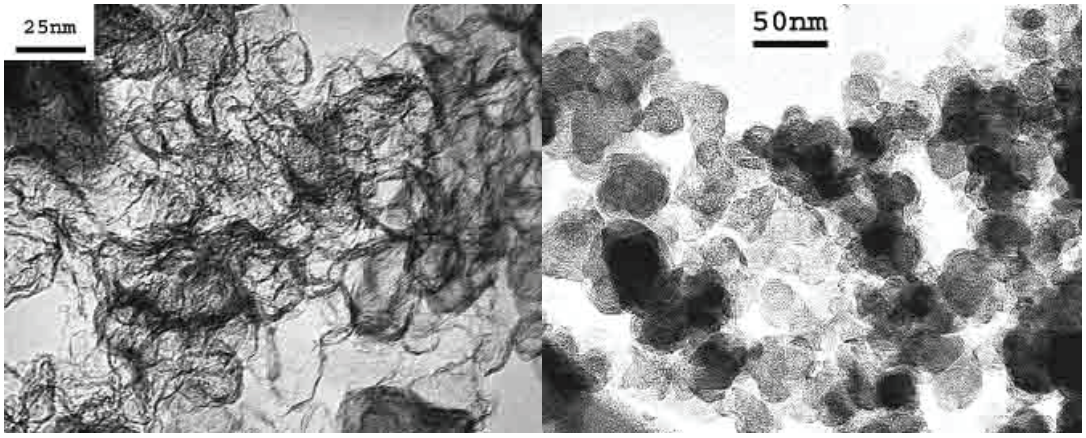

(c)CBD3 (d) CBD4

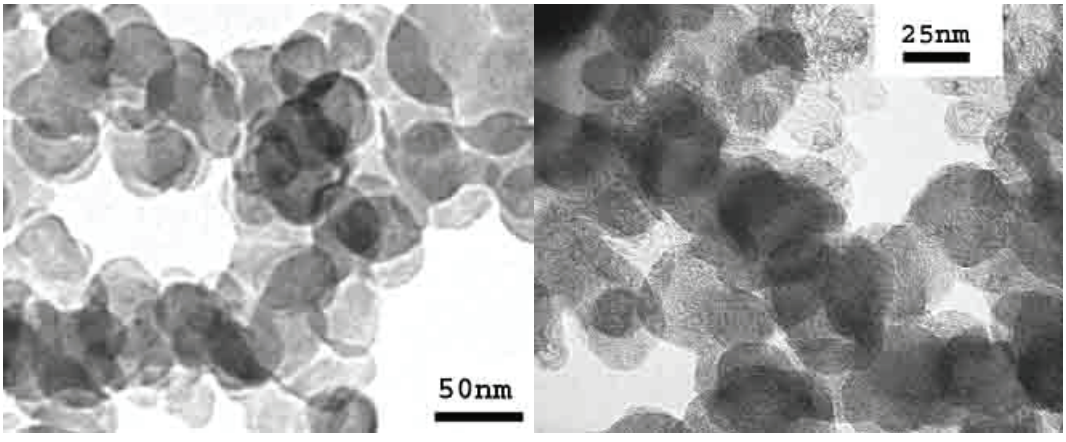

(e) CBM6 (f) CBM5

Figure 5.5 TEM micrographs of carbon blacks.

The extremely high dielectric constant of carbon black composites can be interpreted by the percolation theory, and the most commonly used model is the Kirkpatrick and Zallen [102, 103] statistical percolation model, which is used to predict the electrical properties of a percolation system with non-interacting randomly dispersed fillers. Close to the transition region, this statistical model predicts power-law behavior for the measurable quantities with the volume fraction of fillers. The dielectric constant exhibits a power-law dependence below percolation threshold as shown in the Equation 5.3. The characterizing exponent s is assumed to be universal for a fixed system dimensionality, i.e., $s = 0.7$ for a three-dimensional system.

According to percolation theory, high dielectric constant can only be obtained at filler loadings very close to the threshold. However, the high dielectric constants of carbon black composites were found over a relatively wide filler loading range, in particular for the CBC2 composites, which cannot be explained by the classical percolation theory. The reason for this occurrence is that the percolation theory is not adequate when the filler loading is outside of the percolation transition region, as the assumption of non-interacting fillers may no longer be valid at high filler loadings.

Figure 5.6 shows the dissipation factors of carbon black composites as a function of filler loading. The dissipation factors of high dielectric constant carbon black composites are high, i.e. always above 0.1. Dissipation factors of carbon black composites usually increases with carbon black filler loading, which is at least partly due to the increase of DC conductivity with the increase of filler loading, and higher DC conductivity can lead to higher rates of decay of stored charges. Because of its low structure, carbon black CBC2 leads to a relatively stable dissipation factor versus filler loading in its polymer composites.

Figure 5.7 illustrates the frequency dependence of the dielectric constant of carbon black composites. Carbon black composites, generally speaking, show high frequency dependence. The frequency dependence of the dielectric constant of carbon

black composites comes from three effects, i.e. the dispersion of carbon blacks, the polarization effects between isolated carbon black aggregates, and the anomalous diffusion within aggregates [108]. When in the presence of an electrical field, the charges move inside the carbon black aggregates according to the direction of the electrical field in each half cycle. Charges accumulate in the interfacial boundaries between carbon black aggregates and epoxy, and a dipole moment is imparted to a whole cluster for an isolated aggregate. The interfacial polarization in composites usually has a high frequency dependence, which accounts for the high frequency dependence of the dielectric properties of carbon black composites.

However, it was found that the dielectric constants of CBC2 composites were stable as a function of frequency, as shown in Figure 5.7. A more detailed study of the frequency response of CBC2 composites in Figure 5.8 shows that the frequency dependence is also dependent on the filler loading level. That is, at 6.0 vol% CBC2, the frequency dependence is low, whereas, at 2.3 vol%, there is strong frequency dependence.

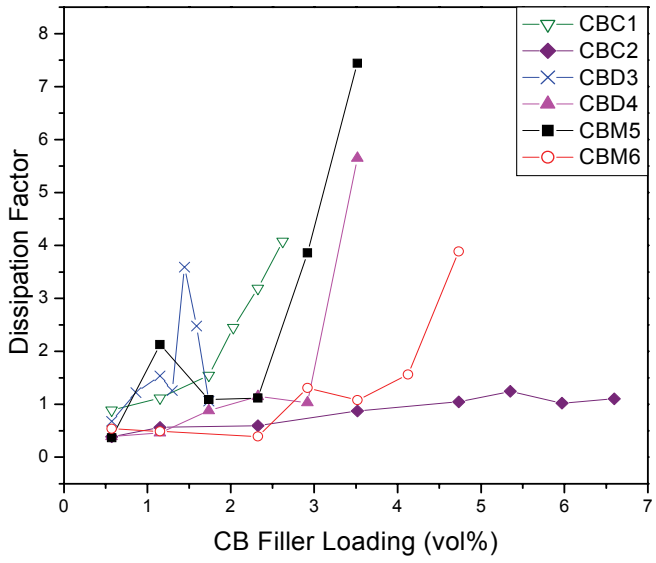

Figure 5.6 Dissipation factors of carbon black composites as a function of filler loading (@ 10 KHz).

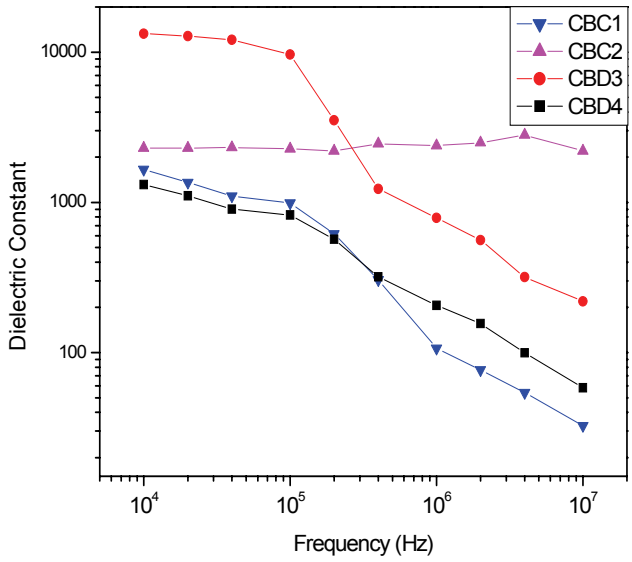

Figure 5.7 Frequency dependence of the dielectric constant of carbon black composites (@ 10 KHz).

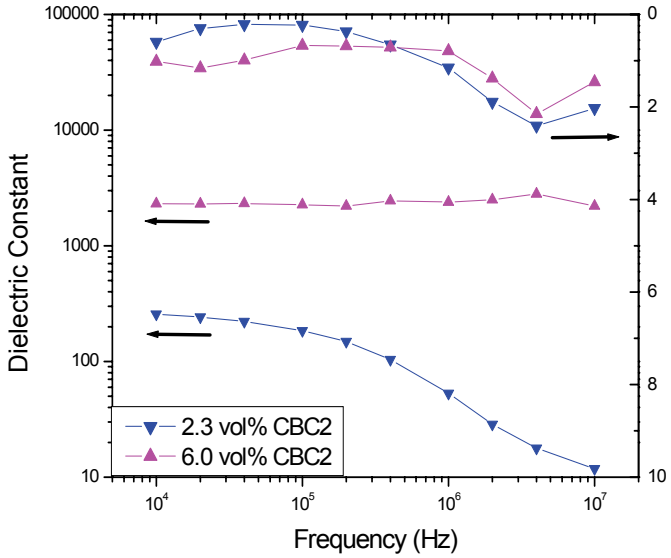

Figure 5.8 Frequency dependence of the dielectric constant of CBC2 composites (@ 10 KHz).

Figure 5.9 shows the SEM micrographs of 6 vol% CBC2 composites, and from top to bottom are 3K and 10K magnifications, respectively. The CBC2 aggregates are uniformly dispersed in the composites, with an average aggregate size about 1 μm.

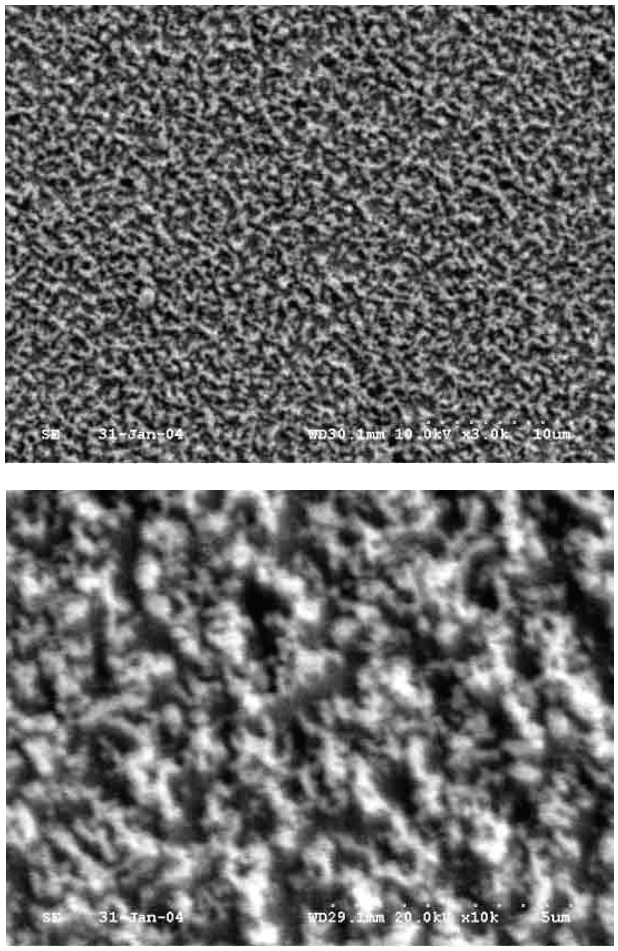

Figure 5.9 SEM micrographs of 6.0 vol% CBC2 composites. From top to bottom are 3K and 10K magnifications, respectively.

5.3.3 Mechanical Properties of Carbon Black Composites

The coefficient of thermal expansion (CTE) of carbon black composites was also studied. Figure 5.10 shows the TMA data for epoxy, 2.3 vol% CBC2-epoxy composite, and 6.0 vol% CBC2-epoxy composite. The CTE of CBC2 composites decreases with the increase of filler loading. However, the reduction in CTE of CBC2 composite is not very significant since the volume loading level of carbon black is low. Figure 5.11 illustrates the DMA data for epoxy, 2.3 vol% CBC2-epoxy composite, and 6.0 vol% CBC2-epoxy composite. The storage moduli are 3109 MPa and 6553 MPa for 2.3 vol% CBC2-epoxy composite and 6.0 vol% CBC2-epoxy composite, respectively, which are higher than

2475 MPa for neat epoxy. Carbon black composites show very good mechanical properties when compared to ceramic composites.

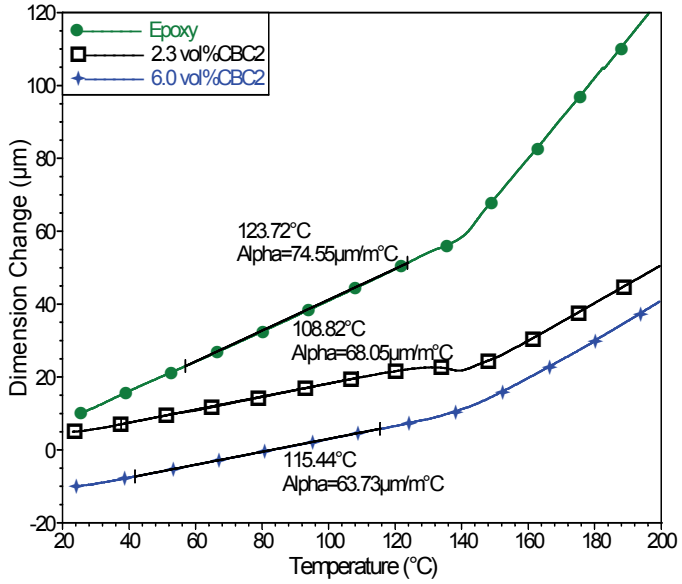

Figure 5.10 TMA data for epoxy, 2.3 vol% CBC2-epoxycomposite, and 6.0 vol% CBC2-epoxy composite.

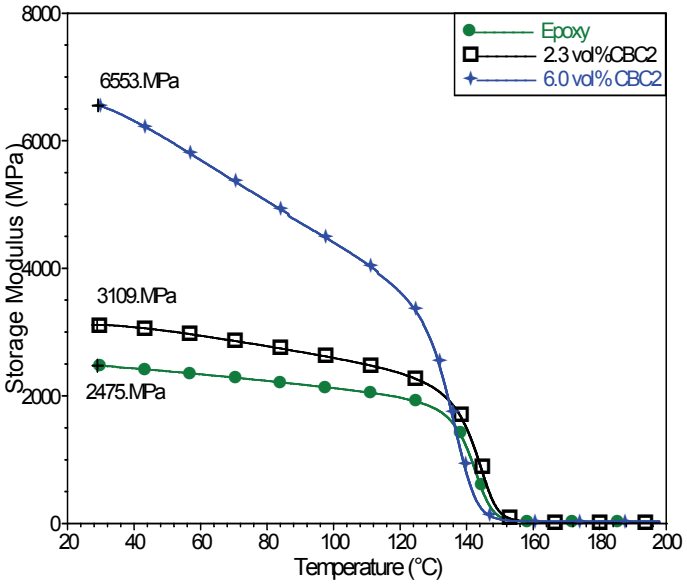

Figure 5.11 DMA data for epoxy, 2.3 vol% CBC2-epoxy composite, and 6.0 vol% CBC2-epoxy composite.

5.3.4 Effect of Polymer Matrices on the Dielectric Properties

Figure 5.12 shows the effects of low loss polymer matrices on the dielectric properties of CBC2-filled composites. Interestingly, the change of polymer matrix from bisphenol-A epoxy to silicone does not result in significant changes in the dielectric constants and dissipation factors. In carbon black composites, the charge transfer between aggregates causes high loss, and the carbon black dominates the dielectric properties of composites, therefore, changing the polymer matrices does not have a very significant influence on the dielectric properties of their composites.

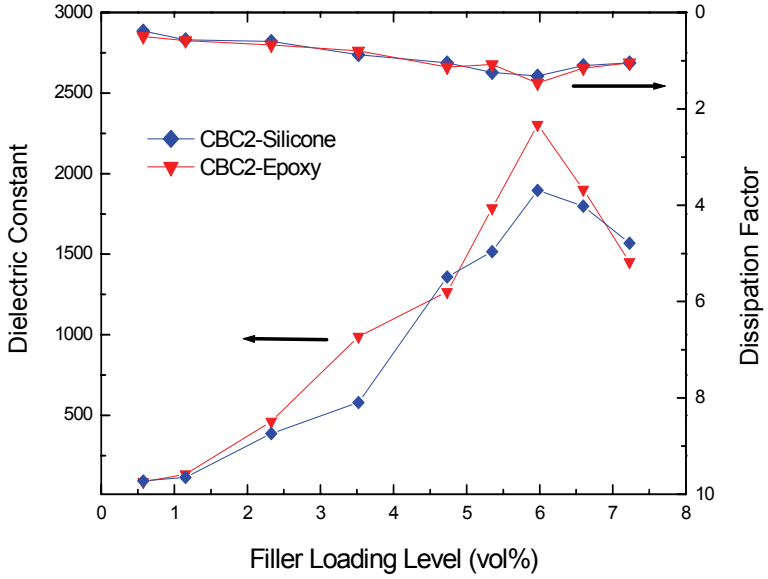

Figure 5.12 Effects of low loss polymer matrices on the dielectric properties of carbon black CBC2-filled composites (@ 10 KHz).

5.4 Conclusions

Carbon black-filled high dielectric constant composites were evaluated as the candidate materials for embedded capacitors. Six different types of carbon blacks were investigated. With proper filler loading level and good dispersion, high dielectric constants over 1000 were observed for four out of the six types of carbon black. For a

highly conductive carbon black CBD3, a high dielectric constant over 13,300 (@10 kHz) was achieved, and for a relatively low conductivity carbon black CBC2, a dielectric constant of about 2,300 (@10 kHz) was obtained. The filler loading level required to reach high dielectric constant in carbon black composites is much lower than that of ceramic composites, which enables the carbon black composites to possess good mechanical properties. Carbon black composites show a high frequency dependence, and the interfacial polarization in carbon black composites, which usually has a high frequency dependence, contributes significantly to the high dielectric constant of the composites.

CHAPTER 6

SHEAR MODULATED PERCOLATION IN CARBON NANOTUBE DIELECTRIC COMPOSITES

6.1 Introduction

Since their discovery by Iijima in 1991 [112], carbon nanotubes (CNTs) have been of great interest in scientific and engineering communities because of their superior physical properties. Viewed as one-dimensional cylindrical nanostructure rolled from a certain size of grapheme sheets, CNTs exhibit a high Young's modulus of 1TPa [113], and a high thermal conductivities of more than 3000 W/K·m for a multi-walled carbon nanotube (MWNT) [114] and of 6000 W/K·m for a single-walled carbon nanotube (SWNT) [115]. CNTs can be either semi-conducting or metallic, depending on their chirality and resulting band structure. Metallic SWNTs are ballistic conductors that exhibit two units of quantum conductance $4e^2/h$ [116-118], and the mobility in semiconducting SWNTs could be ballistic [119] or as high as 100,000 $cm^2/V{\cdot}s$ [120]. The ON/OFF current ratios in SWNTs are as large as 1,000,000 [119] and current carrying capacities can be up to 10^9 A/cm^2 [121].

The combination of excellent mechanical, thermal and electrical properties makes CNTs a promising building block for manufacturing low-cost high-performance nanostructured composite materials. Polyacrylonitrile (PAN) composite containing 10 wt% SWNTs exhibits a 100% improvement in tensile modulus and a 40 °C increase in glass transition temperature as compared to the control PAN fiber [122]. A similar observation was found in poly(p-phenylene benzobisoxazole) (PBO)/SWNT composites [123] and polystyrene/MWNT composites [124]. Thermal conductivity can be enhanced 125% by including 1.0 wt% SWNTs in an epoxy matrix [125] and 160% by including 1.0

vol% CNT in liquid α-olefin oil [126]. Aligned CNT composites are more advantageous for thermal management, e.g., 0.4 vol% loading of aligned MWNTs in silicone elastomer leads to a dramatic increase in thermal conductivities from 0.23 W/K·m to 1.21 W/K·m, which is a large increase of about 280% [127]. Of particular interest are the electrical and dielectric properties of CNT composites. Because of their high aspect ratio one-dimension structure and extraordinary carrier mobilities, a small loading of CNTs can make an insulating matrix conductive, and the resulting composites can be used for antistatic, electromagnetic interference shielding (EMI) applications [128], electrically conductive composites [129], and dielectric applications [130, 131]. As dielectric nanocomposites, it is reported [130] that towards low frequencies, the dielectric constant of a composite with about 2.0 vol % of MWNT increases rapidly and the value of the dielectric constant is as high as 300. The percolation threshold of the MWNT/PVDF composites is only 1.61 vol % of MWNT, and for the percolation composite, the dielectric loss value is always less than 0.4, irrespective of the frequency. Another study [131] shows that the MWNT composites exhibit high real and imaginary relative permittivities over broad bandwidth, showing strong dependence on the MWNT loading. It is observed that distinct resonance takes place at about 1.5 GHz, with the corresponding resonant frequency shifts downward as the MWNT concentration increases. Carbon nanotube (CNT)-epoxy composites with mass concentration of 25.9% can have a higher resonant frequency, and a dielectric constant above 50 was observed at the frequency up to about 1.5 GHz.

Despite of many promising properties, CNT composites are far from being well understood. The microstructure and corresponding properties of a CNT composite are affected by many factors, e.g. CNT aspect ratio, concentration, dispersion, surface chemistry, CNT-CNT interaction, CNT-polymer interaction, and etc. Particularly, the electrical and dielectric properties of a CNT composite, which are related to percolation behavior, are very sensitive to the above factors, hindering its applications in the cases

where electrical conductivity and chare storage are sought. Percolation is driven by thermodynamics and is a statistical concept that describes the formation of an infinite network of connected particles [132], where the electrical conductivities can increase 6-8 orders of magnitude by a small increase of filler loading [133]. The percolation threshold can be as low as 0.06 vol% in SWNT/water system stabilized by 2.8 wt% sodium dodecyl sulfate surfactant [128]. In MWNT composites, the percolation threshold could be below 0.15 wt% [133], less than 1.5 wt% [134], or about 1.61 wt% [130], depending on the dispersion status and characterisitics of the composites. CNT composites are usually processed in suspensions or melts, therefore the major factor that determines the dispersion state of CNTs is the shear force that CNTs have encountered during the processing. In light of this consideration, we have focused our studies on the effect of shear flow processing on the microstructure and properties of CNT composites. In this work, we report for the first time the evolution of anisotropic electrical conductivities and dielectric properties and the observation of anisotropic percolation in shear flow aligned CNT nanocomposites. Our results suggest the great importance of understanding the response of CNT dispersion states to the processing conditions.

6.2 Experimental Section

6.2.1 Sample Preparation

The MWNTs grown via chemical vapor deposition (CVD) method were obtained commercially. According to scanning electron microscope (SEM) characterization, the diameter of as-received MWNTs was about 50 nm and the length was in the range from 1 to 10 μm, with the mean length about 5 μm. A liquid diglycidyl ether of bishpenol A-type (DGEBA) epoxy resin and a tetraethylenepentaamine (TEPA) hardener were used as the polymer matrix for CNT composites. These formulations can be cured at room

temperature because of the exothermic curing reaction of DGEBA with TEPA. Amines, such as TEPA, are well known to have strong interaction with CNTs via π-π stacking and physisorption on the CNT sidewalls [135-139]. To utilize this high affinity of TEPA with CNTs and enhance the dispersion uniformity of CNT composites, MWNTs were first dispersed in the liquid TEPA hardener by ultrasonication for 2 hours, and then DGEBA epoxy resin was mixed with the dispersed MWNT/TEPA mixture. Subsequently, the whole formulation of MWNT/epoxy was transferred into the shear flow setup, which follows the structure of a coaxial cylinder viscometer consisting of two coaxial cylinders with different diameters, as shown in Figure 6.1. The liquid CNT/epoxy composites were sheared in the gap by rotating the inner cylinder at a constant angular velocity of about 34 rad/s. The shear rate can be calculated from Equation 6.1.

$$\gamma_x = 2\omega R_1^2 R_2^2 / R_x^2 (R_2^2 - R_1^2) \qquad \text{Equation 6.1}$$

where R_1, R_2 is the radius of inner and outer cylinder, respectively, and R_x is the arbitrary radius between R_1 and R_2. Nearly constant shear rate throughout the entire volume of fluid can be obtained if the space between cylinders is small [140]. In our setup, the shear rate was estimated to be about 50 s^{-1}. At this high shear rate, the viscosities of CNT composites with various CNT loadings were already leveled off and very close according to our rheology measurement (shown in Figure 6.2). As such, at this shear rate one may expect the dispersion state of CNTs is similar for composites with different CNT loadings. Because of the high reactivity of aliphatic amine and the exothermic curing reaction of DGEBA with TEPA, the CNT composite formulations can be cured at room temperature. Figure 6.3 shows the DSC thermograph of pure epoxy (DGEBA/TEPA) and 2.78 vol% MWNT/epoxy composite. Room temperature curing can prevent the perturbation of the microstructure of the shear processed CNT composites, because when elevated curing temperatures are used the reduction of viscosity can change the orientation state of CNTs. After being sheared for a specific period of time and cured at room temperature for 12

hours, the CNT/epoxy composites, together with the whole setup were cut accordingly in three directions. The sheared composites were cut into rectangular shape, about 1 mm thick, 10 mm long and wide with the thickness directions along the *X*, *Y*, and *Z* axes, respectively. *X* axis is the shear flow direction, *Y* axis is the velocity gradient direction, and *Z* axis is the vorticity direction, as shown in Figure 6.1. We measured the electrical conductivities along *X*, *Y*, and *Z* axes, respectively, and found the electrical conductivities along *Y* and *Z* axes were almost same but different from along *X* axis. Therefore, we denote the conductivities along *X* axis as σ_X and the average of conductivities along *Y* (σ_Y) and *Z* (σ_Z) axes σ_{YZ}.

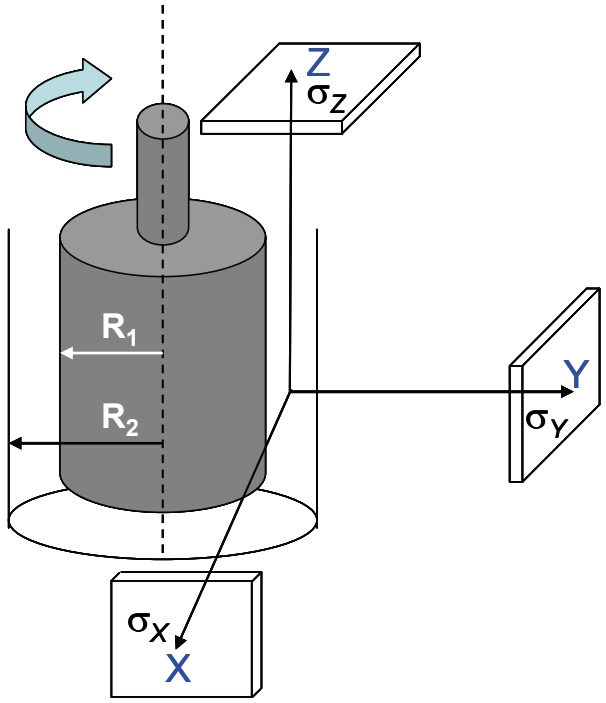

Figure 6.1 Schematic showing a disposable shear flow setup consisting of two coaxial cylinders. In the coordinate, *X* axis is the shear flow direction, *Y* axis is the velocity gradient direction, and *Z* axis is the vorticity direction. The sheared composites were cut into rectangular shape, about 10 mm long, 10 mm wide and 1 mm thick, with the thickness directions along the *X*, *Y*, and *Z* axes, respectively. R_1 and R_2 are the radii of inner and outer cylinder, respectively.

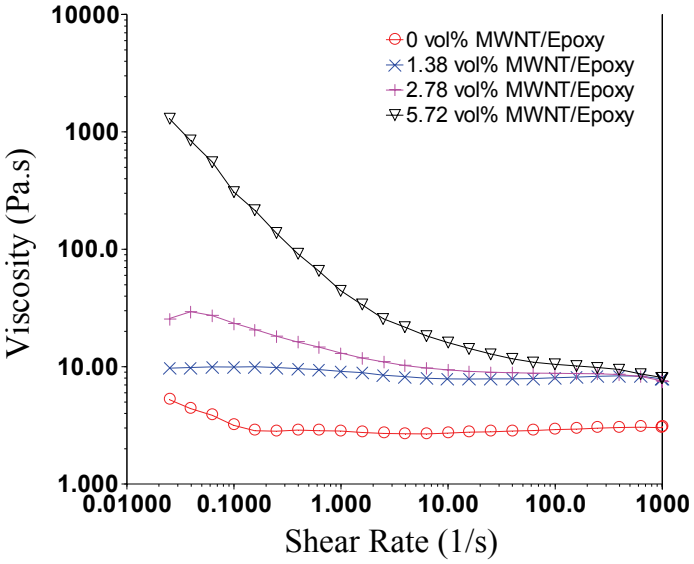

Figure 6.2 Shear viscosity vs. shear rate of the pure epoxy (DGEBA/TEPA) and CNT/epoxy composites.

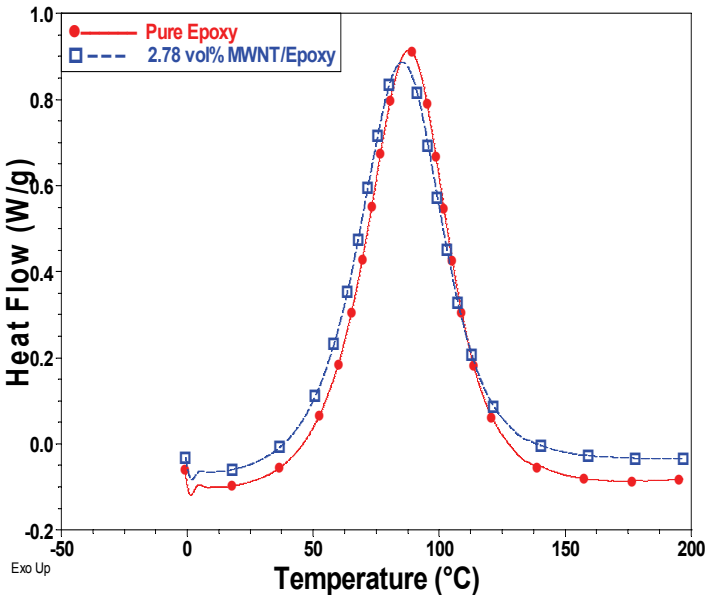

Figure 6.3 DSC thermograph of pure epoxy (DGEBA/TEPA) and 2.78 vol% MWNT/epoxy composite.

6.2.2 Characterization

The viscosity of epoxy and its CNT composites were investigated by an AR Rheometer (Model AR1000-N, from TA Instruments), under steady state flow procedure with parallel plate geometry at room temperature of 25 °C. The curing profile of pure epoxy (DGEBA/TEPA) and 2.78 vol% MWNT/epoxy composite was characterized by a modulated Differential Scanning Calorimeter (DSC, Model 2920, from TA Instruments), with a heating rate of 5 °C/min under nitrogen atmosphere. A LEO thermally-assisted field emission (TFE) scanning electron microscope (SEM) was used to study the dispersion state of CNTs in the composites. A relatively low voltage of 1.5 kV was used in the observations and no gold coating was applied on the top of observation plane. The volume condcutivities of unsheared and sheared MWNT/epoxy composites were characterized by a Keithley High Resistance Electrometer (Model 6517), which is capable of measuring high resistance up to $10^{17}\Omega$. Both sides of the samples were coated with a 300 nm thick gold layer, acting as the electrodes. For samples with resistance above 200 GΩ, a high voltage of 400 V was used in the resistivity measurement, otherwise, a low voltage of 40 V was used to prevent electric short of the low resistivity samples. The capacitance and dissipation factor of the sampels were then measured with an HP 4263A LCR meter, at the frequency from 10 KHz to 10 MHz.

6.3 Results and Discussion

6.3.1 Time Dependent Anisotropic Properties of Sheared CNT/epoxy Composites

The 1.38 vol% CNT/epoxy composites were sheared in the coaxial cylinder setup for various durations of time, in order to study the effect of processing time on the dispersion state of CNTs. Figure 6.4 shows the shear time dependent transition and anisotropic electrical conductivities of shear processed CNT/epoxy composites.

We observed very interesting behaviors in the sheared CNT composites. First, we found that 3 minutes of shear flow processing at the shear rate of 50 s^{-1} leads to the increase of electrical conductivities, as shown in Figure 6.4. This increase is not in line with the overall decreasing trend of the sheared composites, but this discrepancy is attributable to the hydrodynamic tube-tube interactions. Due to the high specific surface area of CNTs, hydrodynamic tube-tube interactions are significant [141]. Application of suitable shear force could lower the repulsive barrier between conductive particles and lead to agglomeration and formation of a conductive network at lower filler loadings [141]. Moreover, the CNTs are flexible enough to deform in modest flows and they can readily form interlocked coherent structures under suitable shear forces [142]. Therefore, a proper shear flow for short time resulted in the agglomeration of CNTs and thereby the increase of conductivities in the CNT/epoxy composites. Second, we found a distinctive transition behavior in the sheared composites with a filler loading of 1.38 vol%. Longer than 3 minutes of shear flow time results in the decrease of electrical conductivities，and specifically from 9 to 12 minutes, the electrical conductivities drops dramatically. Overall in the whole period of shear time up to 18 minutes, the electrical conductivities change as many as 8 orders of magnitude. This transition behavior is similar to the typical percolation transition, although here the transition is a function of shear time instead of a function of CNT filler loading as in a typical percolation transition. The third interesting finding is the anisotropic properties of the shear processed composites. After 18 minutes of shear flow, the electrical conductivity along *X* axis (σ_X) is almost 5 times higher than along *Y* or *Z* axis (σ_{YZ}). Both the time dependent transition and the anisotropic properties of the shear processed CNT composites suggest that the shear flow processing has significantly changed the dispersion state of the CNTs.

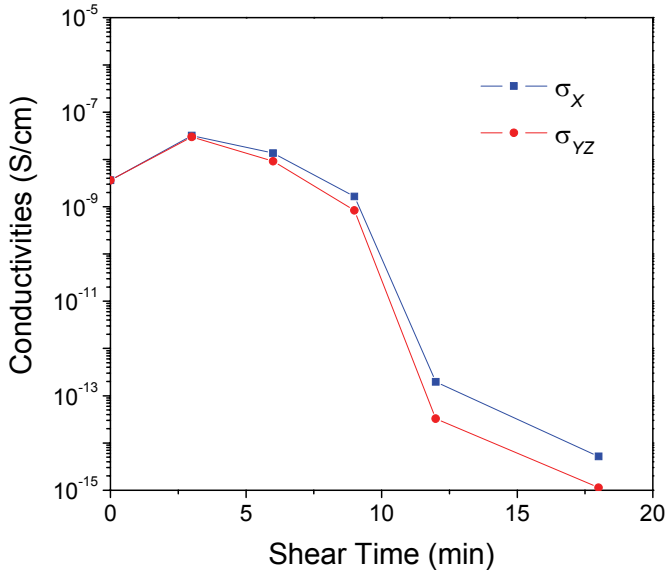

Figure 6.4 Shear time dependent transition and anisotropic electrical conductivities of shear processed CNT/epoxy composites.

6.3.2 Dispersion State of Unsheared and Sheared CNT/epoxy Composites

To study the dispersion state of the CNTs in the shear processed composites, the shear processed samples were examined by a scanning electron microscope (SEM). Because low filler loading samples are easier to observe in term of the CNT orientation state, 0.17 wt% MWNT/epoxy composites were studied. At this filler loading, $nL^3 = 15$ and $nL^2d = 0.15$, correspond to semidilute regime which is defined by $nL^3>1$ and $nL^2d<1$ (where n is the number of CNTs per unit volume, L is the CNT length, and d is the CNT diameter). Semidilute region is the region of the most scientific interests. Both the unsheared and sheared composites (at the rate of 50 s^{-1} for 18 minutes) were studied. As can be seen in Figure 6.5, in the unsheared sample the CNTs were coiled and randomly dispersed.

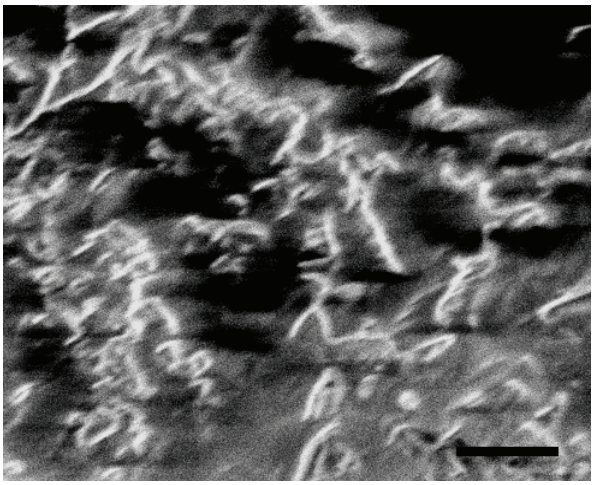

Figure 6.5 SEM images of unsheared 0.17 vol% CNT/epoxy composites. Scale bar, 1 μm.

Figure 6.6 SEM images of sheared 0.17 vol% CNT/epoxy composites. The SEM observation on the *YZ* plane (see the coordinate in Figure 6.1) of sheared CNT/epoxy composite sample reveals that the CNTs were much shorter than the full length of CNTs, indicating the CNTs on this plane were heads/tails of shear aligned CNTs, as shown in Figure 6.6a. On contrast, the SEM images on the *XZ* or *XY* planes of sheared CNT/epoxy composite samples show that CNTs were extended and aligned along a specific direction, as shown in Figure 6.6b. And a schematic showing the alignment of CNTs along the *X* axis (shear flow direction) is given in Figure 6.7. A comparison of the schematic and its projections on *YZ*, *XZ*, and *XY* planes (not shown) with the SEM images in Figure 6.6a and 6.6b suggests that CNTs in the sheared composites were aligned along the shear flow direction.

Now the novel and interesting behavior found in Figure 6.4 can be explained by the microstructures in Figure 6.6. Due to the alignment of the CNTs with shear flow, after a specific period of shear processing time the conductive CNT network was broken down and thus aligned CNTs were formed in the CNT/epoxy composites. The electrical

conductivities of CNT/epoxy composites thus dramatically decrease, showing the abrupt time dependent transition. Also because of the alignment of the CNTs along the shear flow direction, the electrical conductivities along the *X* axis are always higher than along the *Y* or *Z* axis, as conductive paths can be more easily formed along the CNT length direction. Because the shear flow can affect the formation and breakdown of percolative network, the percolation transition (as a function of filler loading) should be affected by the processing conditions such as the shear flow time.

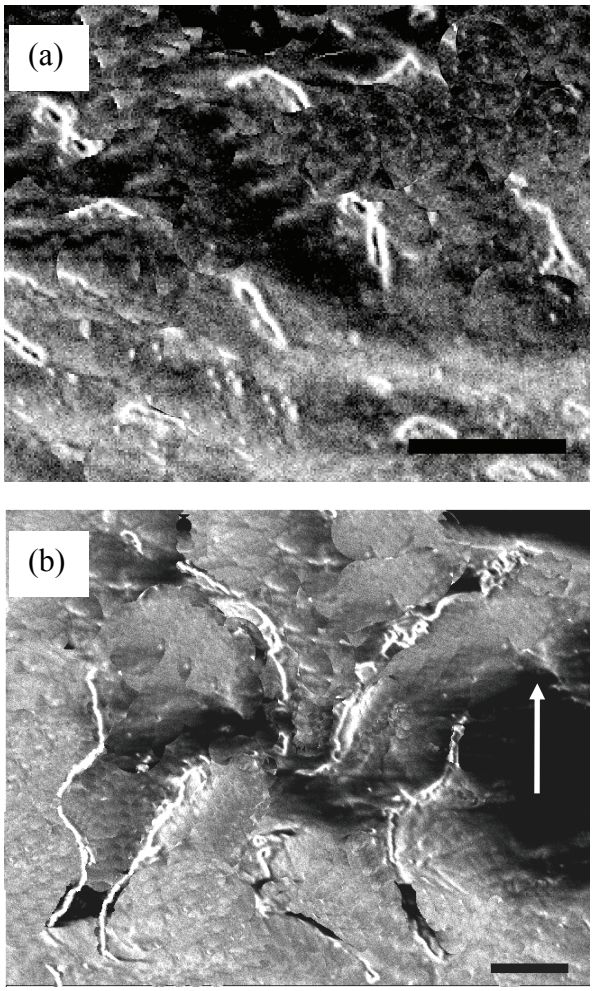

Figure 6.6 SEM images of sheared 0.17 vol% CNT/epoxy composites. (a) SEM image on the *YZ* plane of sheared CNT/epoxy composite. (b) SEM image on the *XZ* or *XY* plane of sheared CNT/epoxy composite. CNTs on these planes were aligned along a specific direction. The white arrow shows shear flow direction. Scale bar, 1 μm.

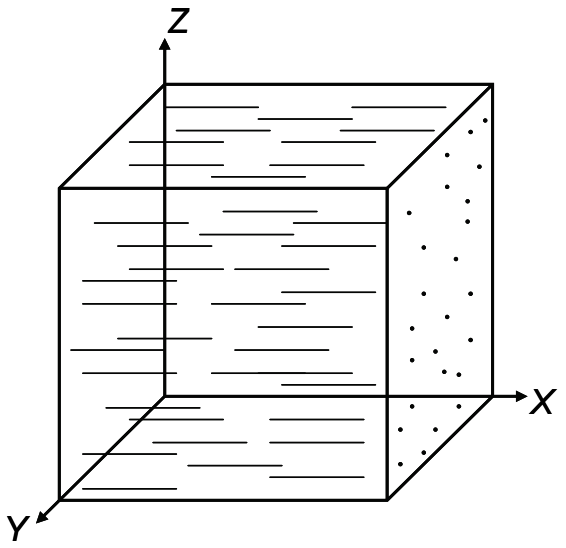

Figure 6.7 Schematic showing the alignment of CNTs along *X* direction (shear flow direction). A comparison of the schematic and its projection on *YZ*, *XZ*, and *XY* planes (not shown) with the SEM observations in Figure 6.6 suggests that MWNTs in the sheared composites were aligned along the shear direction.

6.3.3 Percolation of Unsheared CNT/epoxy Composites

The unsheared CNT/epoxy composites show a sharp transition in the percolation region, as illustrated in Figure 6.8a. The electrical conductivities dramatically increase about 10 orders of magnitude when the CNT concentration increases in the percolation region. According to scaling theory, the effective conductivities ($\overline{\sigma}$) of insulator-conductor composites near the percolation threshold f_c can be predicted by power laws [102-104]:

$$\overline{\sigma} = \sigma_m (f_c - f)^{-s} \quad \text{for } f < f_c \qquad \text{Equation 6.2}$$

$$\overline{\sigma} = \sigma_f (f - f_c)^{t} \quad \text{for } f > f_c \qquad \text{Equation 6.3}$$

where σ_m and σ_f are the electrical conductivities of insulating matrix and conductive filler, respectively; f is the concentration of the conductive filler within the insulating matrix; and s and t are scaling constants. The electrical conductivity data of unsheared

CNT/epoxy composites were fitted to Equation 6.2 for $f < f_c$, as shown in Figure 6.8b. The best fit gives a percolation threshold of 1.05 vol%. The scaling component of unsheared CNT composites is 0.89 ± 0.04, which is slightly larger than the theoretic value of $s \approx 0.7$ for three-dimensional percolation network formed by complex resistors [143].

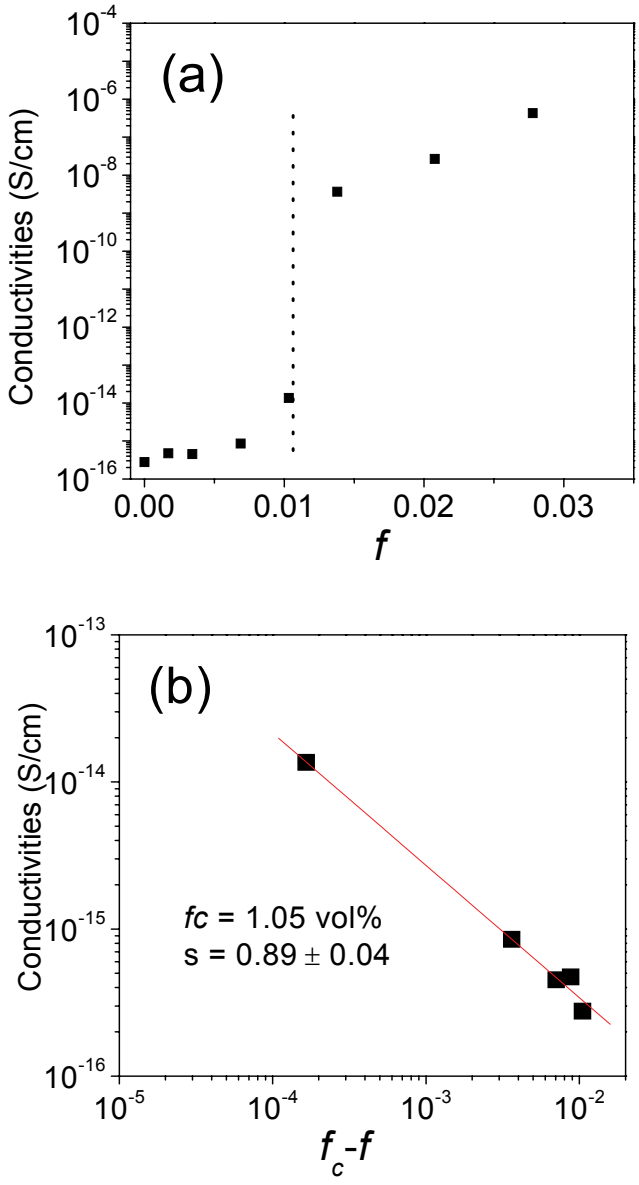

Figure 6.8 (a) Electrical conductivities vs. CNT volume fraction of unsheared CNT/epoxy composites. (b) The best fit of the electrical conductivities to the percolation theory when $f < f_c$, which gives f_c = 1.05% and s = 0.89 ± 0.04.

The dielectric properties of unsheared CNT/epoxy composites are shown in Figure 6.9. The dielectric constant first increases slightly with the CNT volume fraction. Then around the percolation threshold, the dielectric constant increases quickly to about 29. The dielectric loss shows a similar trend as the dielectric constant, increasing dramatically around percolation threshold region.

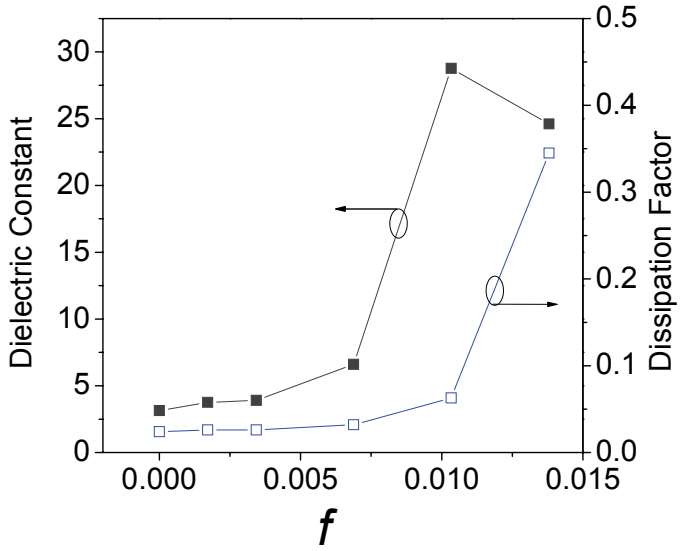

Figure 6.9 Dielectric properties vs. CNT volume fraction of unsheared CNT/epoxy composites.

6.3.4 Anisotropic Percolation of Sheared CNT/epoxy Composites

To study the effect of shear flow processing on the percolation transition, we used a fixed shear time of 18 minutes for preparing shear-aligned CNT/epoxy composites at all filler loadings. Figure 6.10 and Figure 6.11 show the electrical conductivities vs. CNT volume fraction of shear flow processed CNT/epoxy composites with thickness directions along *X* axis and *Y/Z* axes, respectively. For the same sheared composites, the electrical conductivities along the shear direction (σ_X) are higher than along the other two directions (σ_{YZ}) (Figure 6.10a and Figure 6.11a). By fitting the experimental conductivity

data into Equation 6.2, we obtained an isotropic percolation threshold f_c = 2.08 vol% for shear flow aligned CNT composites along all three (*X*, *Y*, and *Z*) directions (Figure 6.10b and 6.11b). Due to the alignment of CNTs along the shear flow direction, the percolation transitions of sheared composites take place at a much higher filler loading than unsheared composites, and the percolation threshold increases as much as 98%, from 1.05 vol% to 2.08 vol%. The dramatic increase of percolation threshold makes the originally conductive composites insulating, which explains the dramatic change of electrical conductivities of sheared composites in Figure 6.4.

We obtained the scaling components s = 1.51 ± 0.06 and s = 1.26 ± 0.04 along the *X* axis and *Y/Z* axes, respectively (Figure 6.10b and 6.11b). The scaling components of shear processed CNT composites are higher than the unsheared composites and close to the theoretic value of $s \approx 1.43$ for two-dimensional percolation network formed by resistors [144, 145]. The scaling component along the *Y*/*Z* axes is lower than that along the *X* axis. Therefore, in the sheared CNT/epoxy composites, the anisotropic electrical conductivities along different directions come from the anisotropy of the scaling component rather than the anisotropy of the percolation threshold, because the percolation threshold is isotropic.

It is worthwhile to mention that the anisotropic electrical properties of sheared CNT composites depend on the filler loading. Table 6.1 shows that in sheared composites σ_X are always higher than σ_{YZ}, because of the alignment of CNTs along the shear flow direction. The ratio of σ_X/σ_{YZ} is related to the percolation threshold. When the filler loading is below the percolation threshold, σ_X/σ_{YZ} is small, however, the ratio can be more than 2 orders of magnitude at high filler loadings above percolation threshold, as shown in Table 6.1.

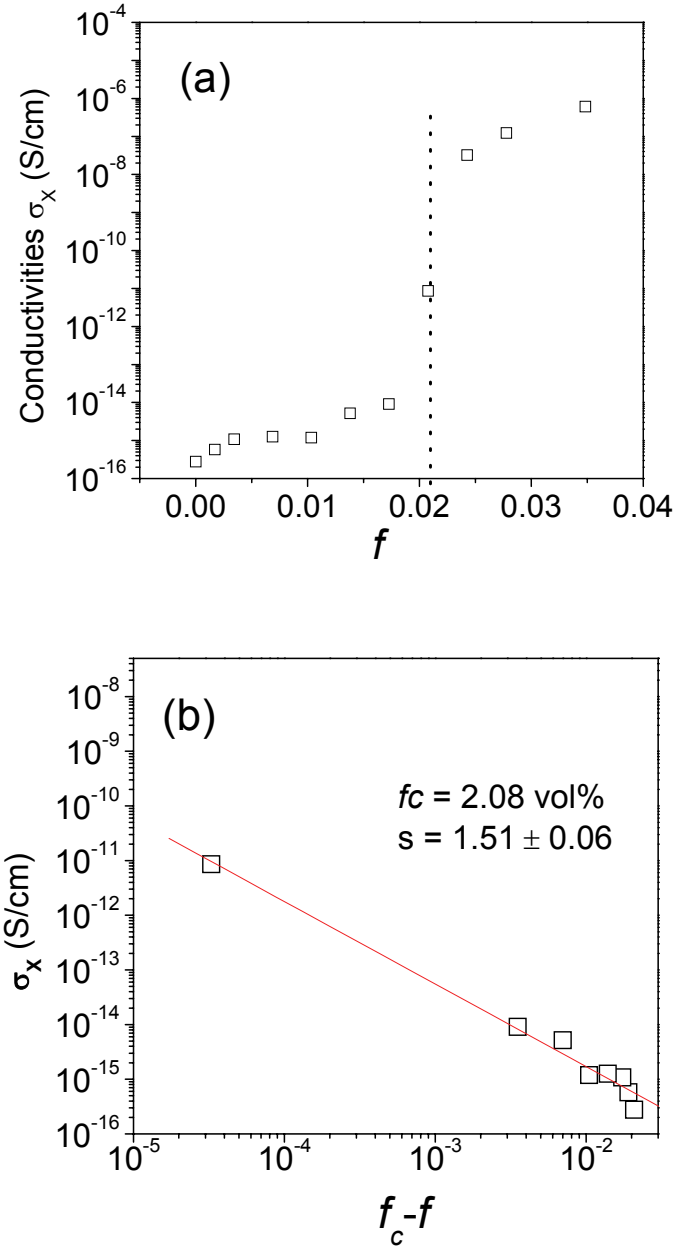

Figure 6.10 (a) Electrical conductivities vs. CNT volume fraction of shear flow processed CNT/epoxy composites with thickness directions along *X* axis. (b) The best fit of the electrical conductivities to the percolation theory when $f < f_c$, which gives f_c = 2.08% and $s = 1.51 \pm 0.06$.

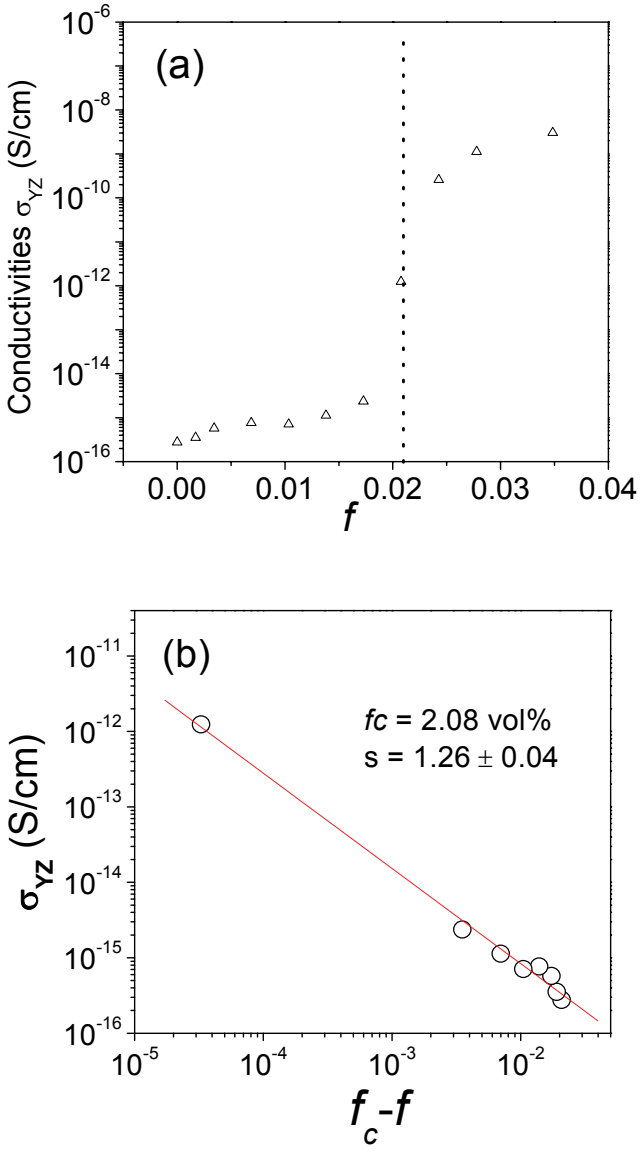

Figure 6.11 (a) Electrical conductivities vs. CNT volume fraction of shear flow processed CNT/epoxy composites with thickness directions along *Y*/*Z* axes. (b) The best fit of the electrical conductivities to the percolation theory when $f < f_c$, which give f_c = 2.08% and s = 1.26 ± 0.04.

Figure 6.12 shows the dielectric constant vs. CNT volume fraction of shear flow processed CNT/epoxy composites with thickness directions along *X* axis and along *Y*/*Z* axes. Below percolation threshold, the dielectric constant for samples along different

directions is small and similar. At the region around the percolation threshold, the dielectric constant along *X* axis is higher than along *Y/Z* axes. The maximum dielectric constant obtained is 67.5 and 37.8 for CNT composites along *X* axis and along *Y/Z* axes, respectively. Because of the shift of percolation threshold in the sheared CNT composites, the dielectric constant changes significantly for sheared CNT composites with CNT volume fraction between 1.0 vol% and 2.0 vol%, as compared to the unsheared CNT composites. For example, at 1.03 vol% CNT volume fraction, the dielectric constant is 28.8 for the unsheared CNT composite, whereas it is only 4.5 for shear processed CNT composite.

Table 6.1 Anisotropic electrical properties of sheared CNT composites

Filler loading (vol%)	σ_X (S/cm)	σ_{YZ} (S/cm)	σ_X/σ_{YZ}
0.17	5.75×10^{-16}	3.53×10^{-16}	1.6
1.38	5.17×10^{-15}	1.13×10^{-15}	4.5
2.43	3.23×10^{-8}	2.59×10^{-10}	124
3.48	6.1×10^{-7}	3.05×10^{-9}	200

Figure 6.13 shows the dissipation factor vs. CNT volume fraction of shear flow processed CNT/epoxy composites with thickness directions along *X* axis and along *Y/Z* axes. When CNT volume fraction is above percolation threshold, the dissipation factor of sheared CNT composites along all directions increases dramatically, because of the formation of conductive network. Because of the shift of percolation threshold in the sheared CNT composites, the dissipation factor also changes significantly for sheared CNT composites with CNT volume fraction between 1.0 vol% and 2.0 vol%, as compared to the unsheared CNT composites.

Figure 6.14 shows the frequency responses of shear flow processed 2.07 vol% CNT/epoxy composites with thickness directions along *X* axis and along *Y/Z* axes. The dielectric constant decreases with the increase of frequency.

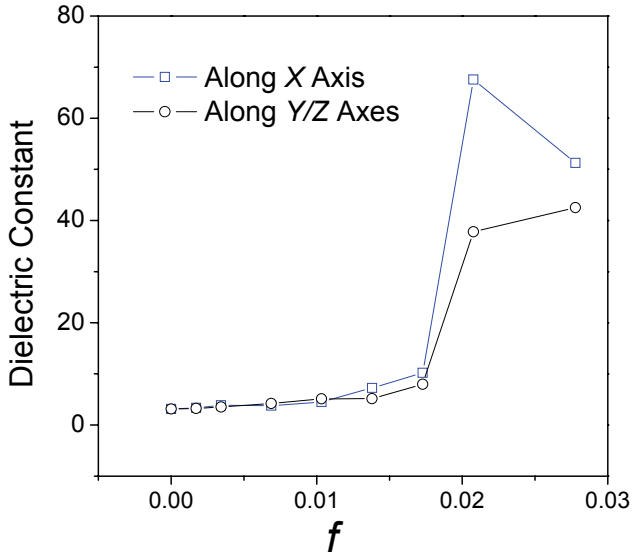

Figure 6.12 Dielectric constant vs. CNT volume fraction of shear flow processed CNT/epoxy composites with thickness directions along *X* axis and along *Y*/*Z* axes.

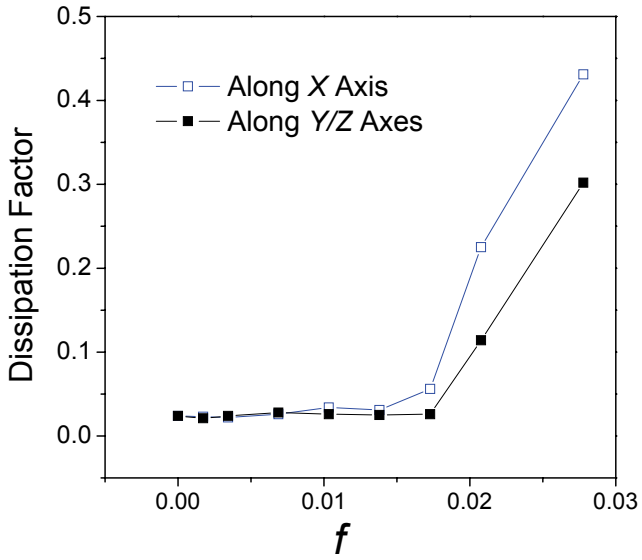

Figure 6.13 Dissipation factor vs. CNT volume fraction of shear flow processed CNT/epoxy composites with thickness directions along *X* axis and along *Y*/*Z* axes.

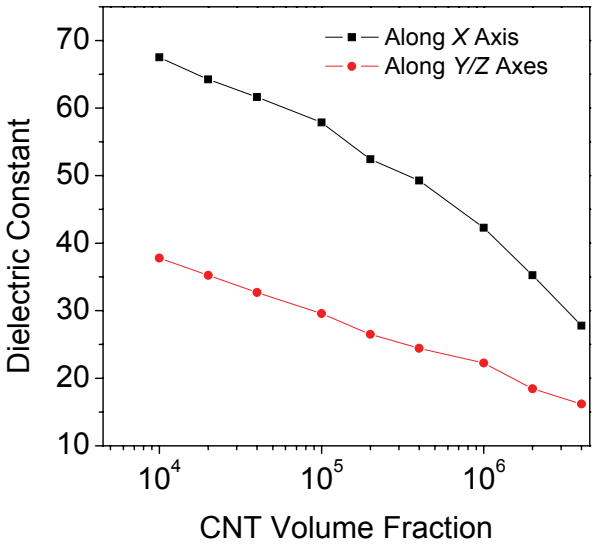

Figure 6.14 Frequency responses of shear flow processed 2.07 vol% CNT/epoxy composites with thickness directions along *X* axis and along *Y*/*Z* axes.

6.3.5 CNT Orientation Degree in Sheared CNT/epoxy Composites

Compared to unsheared MWNT/epoxy composites, the percolation threshold f_c of shear aligned composites is almost doubled. These higher percolation thresholds in shear flow aligned MWNT composites can be explained by the excluded volume theory with high aspect ratio filler [146-149]. The excluded volume is defined as the volume around an object in which the center of another similarly shaped object cannot penetrate. In continuum, the total excluded volume $<V_{ex}>$ is defined by the following equation [149]:

$$< V_{ex} >= N_c < V_e > \qquad \text{Equation 6.4}$$

where N_c is the critical number density of objects in the system and $<V_e>$ is the excluded volume of an object averaged over the orientational distribution in the system.

Figure 6.15 shows the configuration showing two sticks/nanotubes (*i* and *j*) of length *L*, diameter *W*, and the angle between is γ. For sticks with diameter *W* and length *L*

capped with a half sphere of radius $W/2$, the averaged excluded volume $<V_e>$ of the oriented system is as follows [149]:

$$< V_e >= (4\pi / 3)W^3 + 2\pi W^2 L + 2WL^2 < \sin\gamma >_\mu \quad \text{Equation 6.5}$$

where γ is the angle between any two sticks in contact and $<\sin\gamma>_\mu$ is the average of sin γ when sticks are confined to an angle of $2\theta_\mu$ (maximum disorientation angle) around the alignment direction of the system. It is apparent that the smaller the value of θ_μ, the better orientation the sample will have.

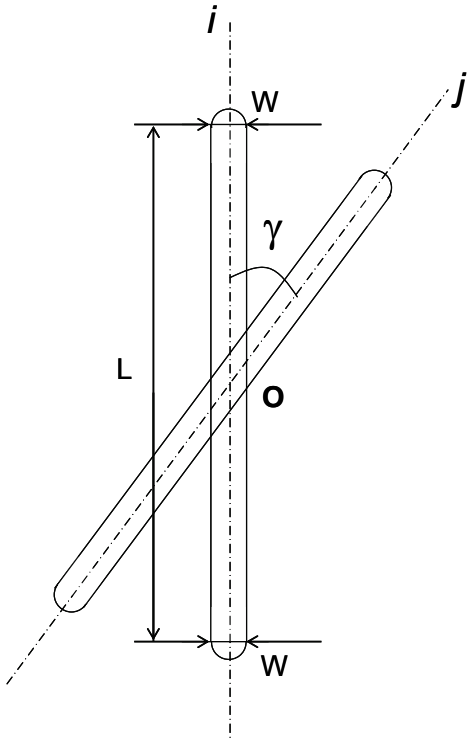

Figure 6.15 Configuration showing two sticks/nanotubes (*i* and *j*) of length *L*, diameter *W*, and the angle between is γ.

In three dimensions, the percolation threshold is linked to $<V_e>$ and $<V_{ex}>$ through the following equation [148]:

$$f_c = 1 - \exp(-N_c V) = 1 - \exp(-< V_{ex} > V / < V_e >) \quad \text{Equation 6.6}$$

where V is the true volume of each particle and equals:

$$V = (\pi/4)W^2L + (\pi/6)W^3 \qquad \text{Equation 6.7}$$

For each type of system, $<V_{ex}>$ is not invariant and falls within a range of values, with one extreme value 1.4 corresponding to randomly oriented thin rods [148], and the other 2.8 corresponding to parallel objects [147]. Substitution of the above values into Equation 6.6 leads to the double inequality [146]:

$$1-\exp(-1.4V/<V_e>) \le f_c \le 1-\exp(-2.8V/<V_e>) \qquad \text{Equation 6.8}$$

By substituting Equation 6.5 and 6.7 into Equation 6.8 and using $<\sin\gamma>_\mu$ given in literature [149], we calculated the percolation threshold at each orientation angle for our particular system with MWNTs of 50 nm in diameter and about 5 μm in length, as listed in Table 6.2. When θ_μ = 90°, the system is completely random in orientation, and the percolation threshold is between 0.68 and 1.35. For our unsheared MWNT/epoxy composites, the percolation threshold was found to be 1.05 vol%, which falls inside this range. When θ_μ = 0°, the system is perfectly parallel in orientation, and the percolation threshold is between 16.05 and 29.53. Our shear flow aligned MWNT/epoxy composites show an isotropic percolation threshold of 2.08 vol%, which is lower than the calculated value in the perfectly oriented case. However, our experimental threshold value fits into the case with maximum disorientation angle of 30°, indicating the CNTs in our sheared composites have less than perfect - but still good alignment.

Table 6.2 Calculated percolation threshold of MWNT/epoxy composites as a function of the maximum disorientation angle θ_μ.

θ_μ	$<\sin\gamma>_\mu$	$<V_e>$	Calc. f_c (vol%)
90°	0.78	2.03	$0.68 \le f_c \le 1.35$
45°	0.60	1.58	$0.87 \le f_c \le 1.74$
30°	0.44	1.18	$1.16 \le f_c \le 2.32$
0°	0.00	0.08	$16.05 \le f_c \le 29.53$

6.4 Conclusions

Shear flow processing has been shown to have significant effect on the dispersion state of CNTs in epoxy composites. SEM observations show that the CNTs were aligned along the shear flow direction. Evolution of electrical conductivities with shear time suggests that the alignment of CNTs in epoxy composites was time dependent. The shear flow processed CNTs/epoxy composites showed a higher percolation threshold, and the scaling components were non-universal along different directions, which results in the anisotropic conductivities and dielectric properties in shear processed CNT/epoxy composites. The understanding of the effect of shear flow processing on the CNT dispersion state and the correlation of CNT orientation with anisotropic percolation behavior may help the development of CNT composites for applications where electrical and dielectric properties are desired.

CHAPTER 7

HIGH-K LOW-LOSS PERCOLATIVE COMPOSITES FOR HIGH PERFORMANCE EMBEDDED CAPACITORS

7.1 Introduction

High dielectric constant (high-κ) composites have attracted great attention in recent years because they can be widely used as the high-κ gate dielectrics [150-152], embedded capacitor dielectrics [45, 63, 64], electroactive materials [153-156], and etc. A high-κ composite of great scientific and engineering importance is the percolative dielectric composite, i.e., an insulator/conductor system. All polymer percolative composites [153-157] and ceramic/metal composites (cermets) [104-106] are two extensively studied percolative systems with high dielectric constant. The studies in Chapter 5 and Chapter 6 also show that polymer-carbon black composites and polymer-carbon nanotube composites have very high dielectric constant up to 13,000. In the percolative composite, a low filler loading close to but not exceeding the percolation threshold is used to obtain a high dielectric constant, whereas, for polymer-ceramic composites a high filler loading is used because a higher filler loading will generally lead to a higher dielectric constant. Because the material processibility and adhesion strength deteriorate when the filler loading increases, the lower filler loading used in the percolative composites leads to a better material processibility and adhesion strength when compared to the epoxy-ceramic composites.

The electric and dielectric properties of a percolative composite can be predicted by the scaling (or percolation) theory. According to the scaling theory [102-105], the effective conductivity ($\bar{\sigma}$) and effective dielectric constant ($\bar{\varepsilon}$) of a percolative system should exhibit a power-law behavior, which can be expressed as follows:

$$\overline{\sigma} = \sigma_M (f - f_c)^t \qquad \text{for } f > f_c \qquad \text{Equation 7.1}$$

$$\overline{\sigma} = \sigma_D (f_c - f)^{-s} \qquad \text{for } f < f_c \qquad \text{Equation 7.2}$$

$$\overline{\varepsilon} = \varepsilon_D \left| f - f_c \right|^{-q} \qquad \text{Equation 7.3}$$

where σ_M and σ_D are the electrical conductivity of conductive filler and insulating dielectric matrix, respectively; f and f_c are the concentration and the percolation threshold concentration of the conductive filler within the dielectric matrix, respectively; ε_D is the dielectric constant of the dielectric matrix; and q, s and t are scaling constants related to the material property, microstructure and connectivity of the insulator-conductive filler interface. According to Equation 7.3, the effective dielectric constant of a percolative composite is inversely related to the difference between actual volume fraction filler loading f and the critical filler loading f_c. As such, a high dielectric constant can only be obtained when the volume fraction of the conductive filler is very close to but does not exceed the percolation threshold. At the proper filler loading, percolative composites can exhibit very high dielectric constants. In an all-polymer percolative composite consisting of poly(vinylidene fluoride-trifluoroethylene-chlorotrifluoroethylene) terpolymer matrix and polyaniline conductive particles, high dielectric constants of 1925 and 151were observed at 100 Hz and 1 MHz, respectively, for a 23% polyaniline composite [157]. Mullite/Mo cermets prepared by functionally graded material method can even reach a dielectric constant of 500000 without significant frequency dependence of their dielectric behavior [104]. However, due to its percolation nature, the electric and dielectric properties of a percolative composite are very sensitive to the composition. A slight change in the composition will lead to a significant change of materials properties, which impose serious challenge of producing materials with reproducible properties. Practically, it's impossible to fulfill demanding uniform distribution over a large substrate area at all. Moreover, the dielectric loss (tan δ) of a percolative composite usually is high, e.g. the dielectric loss is about 1.0 at 1 MHz

for a 23% polyaniline composite [157]. The energy loss due to consumption of a dielectric material can be determined by the following equation:

$$W \approx \pi\varepsilon\xi^2 f \tan\delta \qquad \text{Equation 7.4}$$

where ξ is the electric field strength and f is the frequency. Therefore, the energy loss is positively related to the dielectric loss. As such, a low dielectric loss is preferred in order to reduce the energy loss from a dielectric material, particularly for high frequency applications.

The composition window of a typical high dielectric constant percolative composite is too narrow for industry manufacturing; moreover, the dielectric loss of a percolative composite is too high for high frequency applications. In this work, to achieve a reproducible low-loss percolative composite we have discovered and developed a novel low-cost core-shell particle (self-passivated aluminum) filled high dielectric constant percolative composite. The polymer-aluminum percolative polymer composite shows a low dielectric loss, a high dielectric constant and a low frequency dependence. Influences of aluminum particle size and filler loading on the dielectric properties of composites were studied. Dielectric property measurements demonstrated that, for composites containing 80 wt% 3.0 μm aluminum, a dielectric constant of 109 and a low dissipation factor of about 0.02 (@10 KHz) can be achieved. At such loading level, materials showed good processability and good adhesion to the substrate. Bulk resistivity measurement, high resolution transmission electron microscope (HRTEM) observation, and thermogravimetric analysis (TGA) were conducted to characterize the aluminum powders, in order to understand the dielectric behavior of aluminum-filled composites. To further increase the dielectric constant, bimodal aluminum-filled composites were also systematically studied. A high dielectric constant of 160 (@10 KHz) with a low dissipation factor of less than 0.025 was achieved with the optimized bimodal aluminum composites. Because the filer-polymer interaction is important for a composite, an

aluminum particle surface treatment was performed with an epoxide-functionalized silane coupling agent to further enhance the dielectric properties and processibility of polymer/aluminum composites. To further understand the dielectric behavior of aluminum composites, low loss polymers such as silicone, polyimide (PI), polynorbornene (PNB), and benzocyclobutene (BCB), were explored as matrices for the aluminum composites. It is found that the polymer matrices can significantly change the dielectric properties of the aluminum composites, and the polymer-aluminum composites also show a characteristic of polymer-ceramic composites.

7.2 Experimental

7.2.1 Materials and Sample Preparation

7.2.1.1 Materials

Epoxy resin was chosen as the polymer matrix because of its ease of processing and its good compatibility with printed cuicuit board (PCB) manufacturing. The bisphenol-A type resin Epon828 was from Shell Chemicals Company. MHHPA (methylhexahydrophthalic anhydride), from Lindau Chemicals, Inc., and 2E4MZ-CN (1-cyanoethyle-2-ethyl-4-methylimidazole), from Shikoku Ltd., were used as the hardener and curing catalyst, respectively. The equivalent ratio of epoxide to anhydride was set to be 1:0.85. A cured bisphenol-A epoxy has a dielectric constant of about 3.5 and a dielectric loss of about 0.015. Silicone, polyimide, polynorbornene (PNB), and benzocyclobutene (BCB) were selected as the polymer matrices for the dielectric composites due to their low dissipation factors. Silicone (HIPEC® Q1-4939) was from Dow Corning Incorporation, polyimide (PI2729) was from HD Microsystems, PNB (Avatrel 2090P) was from Promerus Electronic Materials, and BCB (Cyclotene 4024) was from Dow Chemical Company. The mixing ratio of part A (resin) to part B (hardener

and curing catalyst) was 1:1 for silicone, and all other polymers (polyimide, PNB, and BCB) were one part and used as received. Self-passivated aluminum (Al) particles with particle sizes of 100 nm, 3 μm, and 10 μm, respectively, and 40 nm Al_2O_3 coated 3 μm Al particles were used in this high-κ polymer hybrid. The aluminum oxide powder, with average particle size of about 42 nm, was supplied from Nanophase Technologies Incorporation. The silane coupling agent (CA) γ-glycidoxypropyl-trimethoxysilane was used to improve the filler-polymer interaction. The CA had an epoxide as one of its end groups.

7.2.1.2 Formulations

The 2E4MZ-CN was first dissolved in the MHHPA and then the Epon828 was added into the solution. The epoxy system was carefully mixed in a centrifugal machine (from Glas-Col Company) for 2 hours. To achieve uniform distribution of metal powders inside the epoxy system, a 3-step mixing procedure were taken. First, the composites were hand-stirred for 15 minutes as a premixing step. Second, the paste from the first step is further dispersed in an ultrasonic chamber (Sonicator 3000, from Misonix Inc.) for 30 minutes. Finally, a high shear blender (from Eberbach Corporation) was used in order to break down the agglomeration of fine filler powders.

7.2.1.3 Aluminum Particle Surface Treatment

0.5 g silane coupling agent was mixed with 5.0 g distilled water and 95.0 g absolute ethanol, and then 10.0 g aluminum powder (3 μm and 100 nm, respectively) was added into the solvent mixture. The suspension was dispersed in an ultrasonicator (Sonicator 3000, from Misonix Inc.) for 1 hour. Formic acid was used to adjust the pH value to about 4, where the aluminum oxide (the ceramic shell) had the highest zeta potential and agglomeration of particles could be more easily broken down. The suspension was

refluxed at 120ºC for 24 hours. After surface treatment, the aluminum particles were rinsed with ethanol three times in order to remove any unreacted silane coupling agent.

7.2.2 Characterization

7.2.2.1 Dielectric Measurement

Silicon wafer served as the bottom electrode of capacitors after being deposited with a thin layer of titanium and copper by a DC sputterer (from CVC Products Incorporation). The composite material was coated onto the wafer with a bar coating method. Next, the whole sample was cured with an optimized step-curing procedure in an oven. Finally, the DC sputterer was used to deposit another layer of copper onto the material through a mask, to serve as top electrodes. Figure 7.1 shows the embedded capacitor test vehicle fabricated on a silicon substrate.

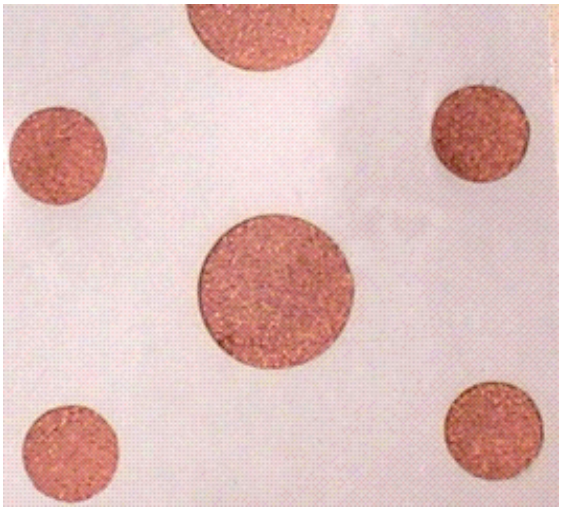

Figure 7.1 Embedded capacitors fabricated on a silicon substrate.

Dielectric measurement was conducted with an HP 4263A LCR meter, at the frequencies of 10 KHz to 10 MHz. And an RF Impedance and Dielectric Analyzer (Agilent, model E4991A) was used for the characterization of the frequency responses of dielectric properties up to the Giga Hertz range (≤ 1.5 GHz). For RF Impedance and

Dielectric Analyzer measurement, the sample preparation method was different from the above mentioned method; there was no need of DC sputtering for electrodes and the samples used were thicker than those measured by the LCR meter.

Dielectric constant was calculated from the measured capacitance data, according to the following equation:

$$C = \frac{\varepsilon_0 \varepsilon_r A}{t} \qquad \text{Equation 7.5}$$

where ε_0 is the permittivity of the free space (8.854×10^{-12} F/m), A is the area of capacitor electrode, and t is the thickness of dielectric layer. ε_r is the dielectric constant of measured composite material.

7.2.2.2 DSC Measurement

The curing profile of bisphenol-A epoxy system was studied by a modulated differential scanning calorimeter (DSC, Model 2920, from TA Instruments). Based on the curing profile of bisphenol-A epoxy system, as shown in Figure 7.2, three different step-curing profiles were investigated in order to determine the best curing procedure for aluminum filled composites. Three curing profiles were as follows: (1) 120 °C for 15 minutes, then 140 °C for 1 hour; (2) 120 °C for 15 minutes, then 145 °C for 1 hour; (3) 120 °C for 15 minutes, then 150 °C for 1 hour. All dynamic scans were performed at heating rate of 5 °C/min under N_2 purge.

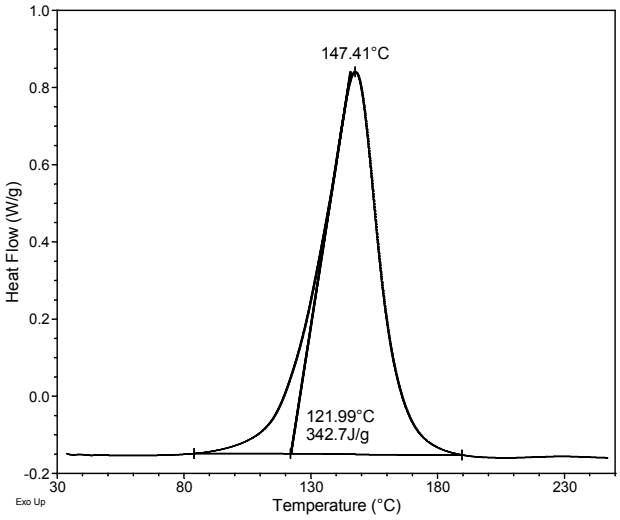

Figure 7.2 Curing profile of a bisphenol-A epoxy system.

The curing procedure was optimized based on three criteria. First, it should have a soft baking step to evaporate the solvent, because at high aluminum loading level, solvent must be used in order to achieve good dispersion of aluminum particle into the matrix. According to the curing profile of epoxy system, shown in Figure 7.2, the onset temperature of curing was around 122 °C. Therefore, 120 °C was selected to be the soft baking temperature, in that the curing process of epoxy is very slow at this temperature thus the solvent has enough time to vaporize without voiding. Second, the final curing temperature should be high enough to guarantee complete curing of epoxy, otherwise, the uncured part will cause the properties of the ultimate composite to change gradually in the long run of service. Third, the curing temperature should not be too high, since high curing temperature not only leads to evaporation of hardener HMPA, but also causes the precipitation of filler particle as the viscosity decrease with the increase of curing temperature. High curing temperature also induces thermo-mechanical stresses on the PCB substrate. The peak curing temperature of epoxy system is 147 °C; based on this, three final curing temperatures, 140 °C, 145 °C, and 150 °C were investigated.

Figure 7.3 showed the heat flow as a function of temperature of 60 wt% aluminum-filled composites cured under three different step-curing profiles. Nonreversible heat flow as a function of temperature is given in Figure 7.4. Under curing temperature 140 °C and 145 °C, the aluminum filled composites were not completely cured. Their curing degrees were 98.4% at 140 °C, and 99.5% at 145 °C, respectively. However, the curing of aluminum composites was complete under a curing temperature of 150 °C, which was then chosen as the curing temperature of aluminum composites.

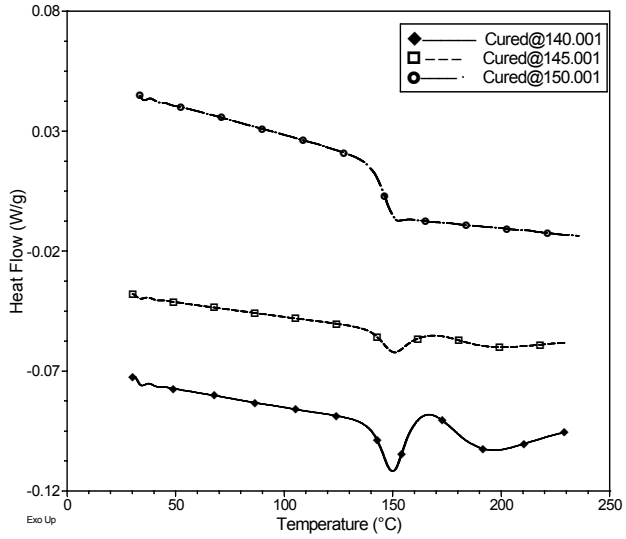

Figure 7.3 Heat flow as a function of temperature of 60 wt% aluminum filled composites cured under three different step-curing profiles. (1) 120 °C for 15 minutes, then 140 °C for 1 hour; (2) 120 °C for 15 minutes, then 145 °C for 1 hour; (3) 120 °C for 15 minutes, then 150 °C for 1 hour.

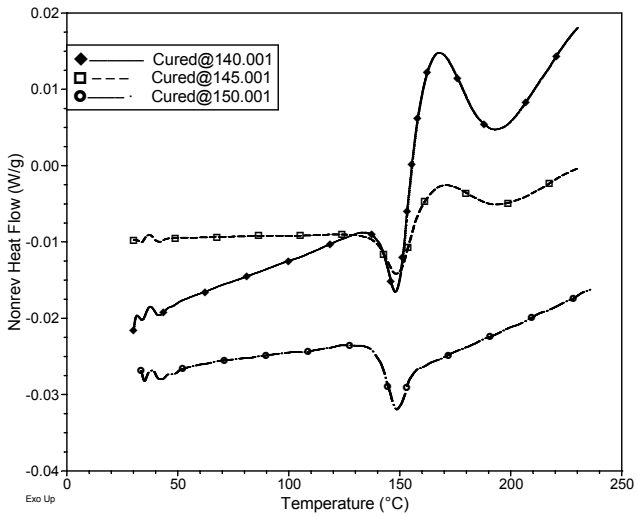

Figure 7.4 Nonreversible heat flow as a function of temperature of 60 wt% aluminum filled composites cured under three different step-curing profiles. (1) 120 °C for 15 minutes, then 140 °C for 1 hour; (2) 120 °C for 15 minutes, then 145 °C for 1 hour; (3) 120 °C for 15 minutes, then 150 °C for 1 hour.

7.2.2.3 Microscopy Observation

A JOEL 4000EX high-resolution Transmission Electron Microscope (HRTEM), operating at 400 KV, was used to analyze the particle size of aluminum powder and the thickness of its oxide layer. Morphologies of aluminum-filled composites were observed by an optical microscopy (Type 020-520-007 DMLP, Leico Microsystems, Germany). Crossection of samples was polished with grinding papers before observation. The microstructure of aluminum composites was also observed by a thermally-assisted field emission scanning electron microscopy (FESEM) (Model JOEL 1530).

7.2.2.4 Rheology Studies

Viscosity of aluminum-filled composites was investigated by a stress rheometer (Model AR1000-N, from TA Instruments). The experiments were performed under steady state flow procedure with parallel plate geometry at 25 °C.

7.2.2.5 Bulk Resistivity Measurement

Bulk resistivity of aluminum powder was measured by an in-house made device, using a polymethyl methacrylate (PMMA) pipe with metal electrodes placed on each end after it had been filled with sample powder. Load was applied on the electrodes by a hydraulic unit (from Carver Inc.). Resistance of the powder under selected load was then measured by a multimeter (from Keithley Inc.).

7.2.2.6 Thermogravimetric Analysis (TGA)

Thermogravimetric analysis was conducted with a TGA from TA Instruments (Model 2050). The heating rate was 10 °C/min. Air was used as the purge environment.

7.2.2.7 Adhesion Measurement

Adhesion strength of the aluminum composites toward Cu surface was characterized by the die shear measurement. Copper laminated FR-4 board was cut into both small (4 × 4 mm) and large (20 ×20 mm) dies. The dies were cleaned in isopropyl alcohol in ultrasonic chamber for 5 minutes, and then rinsed with water. Glass beads (0.5 wt%, diameter 75 μm) were used as spacers to control the distance between upper and lower dies. The small die was placed onto a thin film of composite material to form a layer of tested material, and then put onto the large die. Die shear tests were performed on a bond tester (Model 550-100K, Rouce Instruments), with a blade speed of 100 μm/sec.

The adhesion strength of epoxy resin and its aluminum composites to the copper surface was also determined by lap shear tests using an Instron 5548 Micro Tester. The copper-clad FR-4 substrate was cut into 6×30 mm strips, and then a 6×6 mm joint was formed by applying the resin or its composites between the overlapping areas of two FR-4 strips. Spacers, i.e., 0.5 wt% glass beads of 75 μm diameter were added into the

formulations to control the joint thickness. The lap shear assemblies were then cured in an oven.

7.2.2.8 Fourier Transformed Infrared (FTIR) Spectroscopy

The surface chemistry of the aluminum particles was characterized by an FTIR (Magna IR 560, from Nicolet Inc.). The aluminum particles were first dried in an oven at 120ºC for 12 hours, and then KBr pellets were prepared with the dried aluminum particles. The spectrum was collected in the range from 4000 to 400 cm^{-1}.

7.2.2.9 Dielectric Analyzer (DEA)

The frequency responses and temperature coefficient of capacitance (TCC) of the aluminum composites from 0.001 Hz to 100 KHz were studied by a dielectric analyzer (DEA 2970, from Thermal Advantages Inc.), using an interdigitated test coupon.

7.2.2.10 Thermomechanical Analyzer

The coefficient of thermal expansion (CTE) and the glass transition temperature (Tg) of the cured dielectric composites were characterized using a Thermomechanical Analyzer (TMA, Model 290, from TA Instruments). The sample was heated from room temperature to 200 ºC at a rate of 5 ºC/min under a nitrogen atmosphere.

7.3 Results and Discussion

7.3.1 Novel Dielectric Behavior of Polymer Composites Filled with Core-Shell Structured Particles

7.3.1.1 Core-Shell Structure of Self-Passivated Al Particles

Aluminum is a self-passivation metal. The self-passivated amorphous oxide layer forms an insulating boundary layer outside of the metallic core. Figure 7.5 shows the

micrograph of 100 nm aluminum powder from the high resolution TEM observation. Figure 7.6 shows the high resolution TEM micrograph of a single 100 nm Al particle. The dark area in the center is the metallic Al core, and the light grey layer surrounding the core is an insulating Al_2O_3 shell. The self-passivated oxide layer on the Al particle is dense and very uniform. The oxide thickness of a 100 nm particle is about 2.8 nm, as can be measured from the high resolution TEM micrograph.

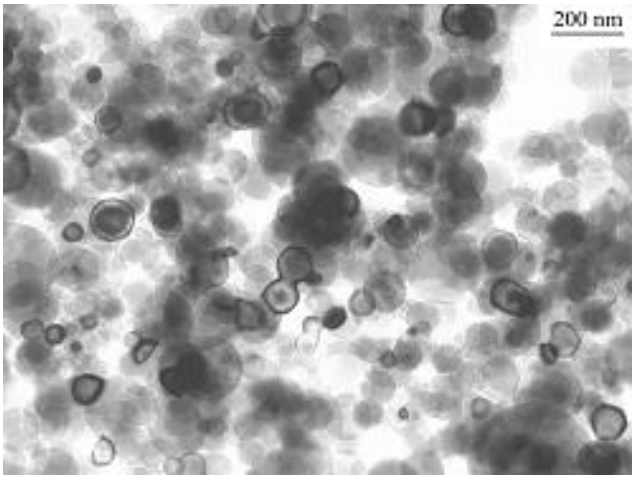

Figure 7.5 High resolution TEM micrograph of 100 nm aluminum powder.

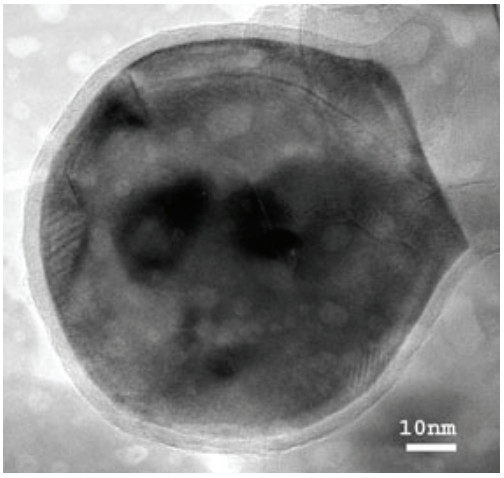

Figure 7.6 High resolution TEM micrograph of a single 100 nm aluminum particle. The particle shows an oxide thickness of about 2.8 nm.

7.3.1.2 Characteristics of Core-Shell Structured Al Particles

The thin passivation oxide layer forms a nanoscale insulating boundary layer outside of the metallic Al spheres, which has dramatic effects on the electrical, mechanical, and chemical behaviors of the resulting composites. As shown in Figure 7.7, bulk resistivities of all three aluminum powders are in the magnitude of 10^7 ohm.cm, which corresponds to semiconducting materials, completely different from electrically conductive aluminum metal. The resistivities of Al powders are related to the size of aluminum particles. They decrease monotonically with the decrease of Al particle sizes.

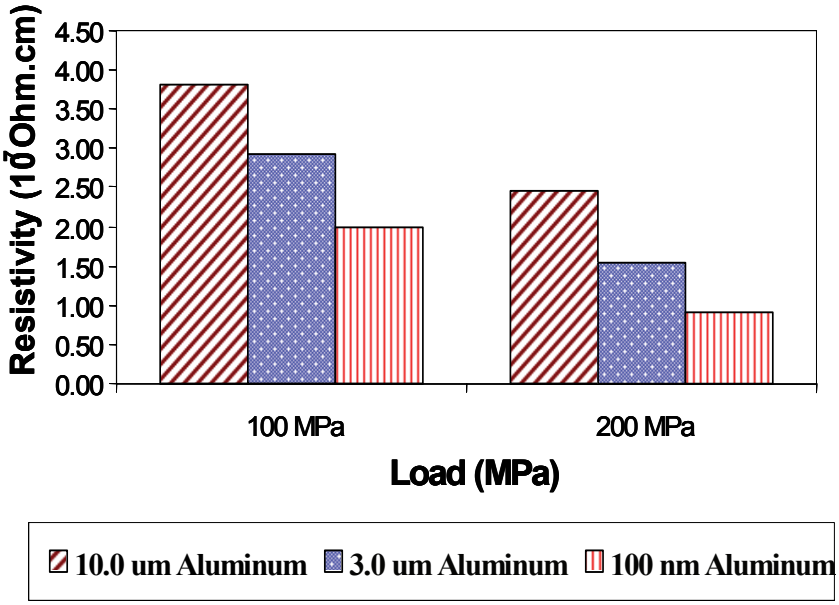

Figure 7.7 Bulk resistivity of aluminum powders.

After surface passivation when exposed in the ambient condition, aluminum particles become very stable, as can be seen from thermogravimetric analysis in Figure 7.8. The weight gain of aluminum from 25 °C to 400 °C is only about 0.07% for 3.0 μm and 10.0 μm aluminum powders, and about 0.30% for nanoaluminum powder. As temperature further increases to around the melting point of aluminum powder, the weight gain of aluminum powders increases dramatically due to the damage of protective

aluminum oxide layer. The smaller Al particles generally have larger weight gain, indicating that they are more reactive at elevated temperatures.

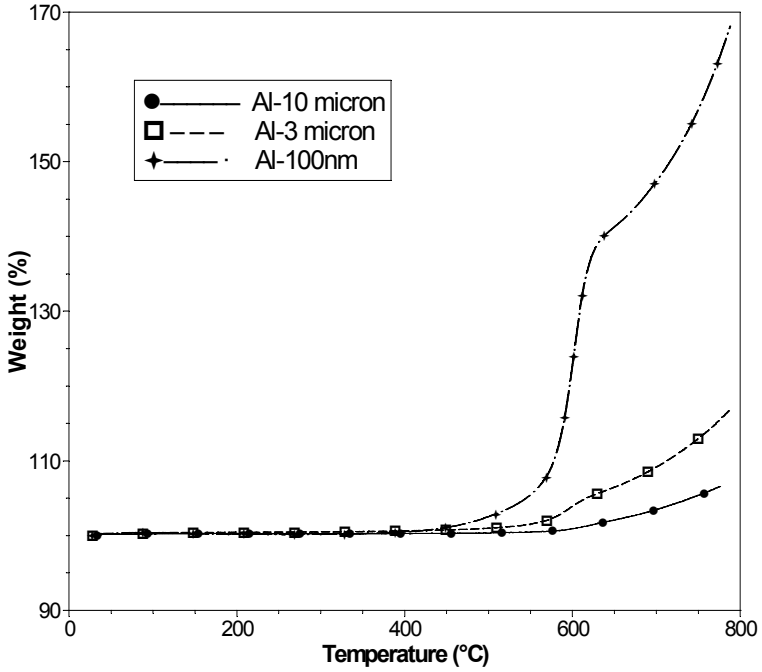

Figure 7.8 TGA analysis of aluminum powder.

7.3.1.3 Dielectric Properties of Self-Passivated Al Composites

Figure 7.9 shows the dielectric constant of Al filled composites as a function of filler loading. The 3.0 μm Al particles and 10.0 μm Al particles can be easily loaded up to 85 wt% in a bisphenol-A epoxy. However, for 100 nm Al filler, it's difficult to uniformly disperse Al particles when filler loading is higher than 50 wt%. Generally speaking, the dielectric constant of Al filled composites increases with the filler loading level, however, at high filler loading, the dielectric constant of composites may decrease due to voiding from imperfect filler packing and solvent evaporation, because solvent is required to disperse filler at loading level higher than 70 wt%. Due to the self-passivation nature of Al particles, the Al composites continued to be insulating even at high filler loading of 85 wt%. The presence of passivated insulating Al_2O_3 layer on the Al particles

makes the polymer/Al composites no longer a typical percolative composite. The 3.0 μm Al composites show higher dielectric constant than that of the 10.0 μm Al composites, and the maximum dielectric constant achieved is 109 for the former and 70 for the latter. At the same filler loading, 100 nm Al composites have higher dielectric constant than the other two sized Al composites. The highest dielectric constant is 60 at 50 wt% loading for 100 nm Al composites.

Figure 7.10 shows the dissipation factor of Al filled composites as a function of filler loading. A low dissipation factor of about 0.02 was observed for all Al composites, which is in the same magnitude as a neat bisphenol-A epoxy system (0.01-0.02).

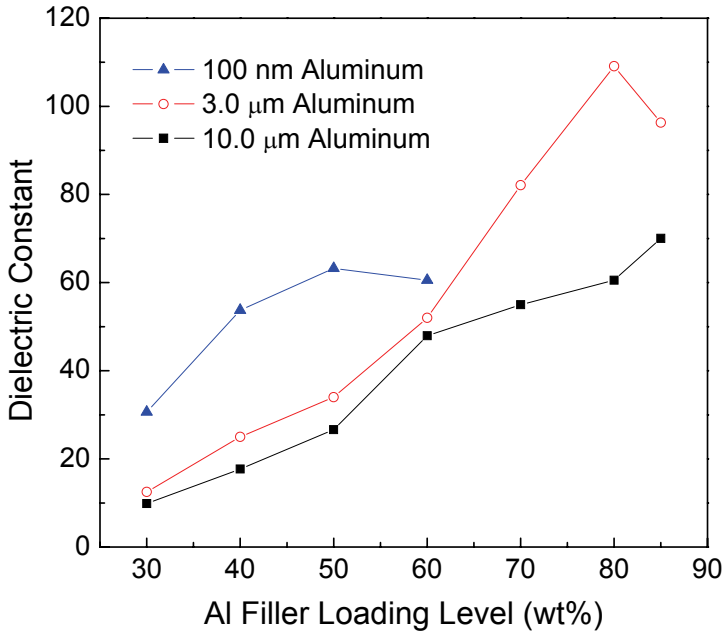

Figure 7.9 Dielectric constant of aluminum filled composites as a function of filler loading (@ 10 KHz).

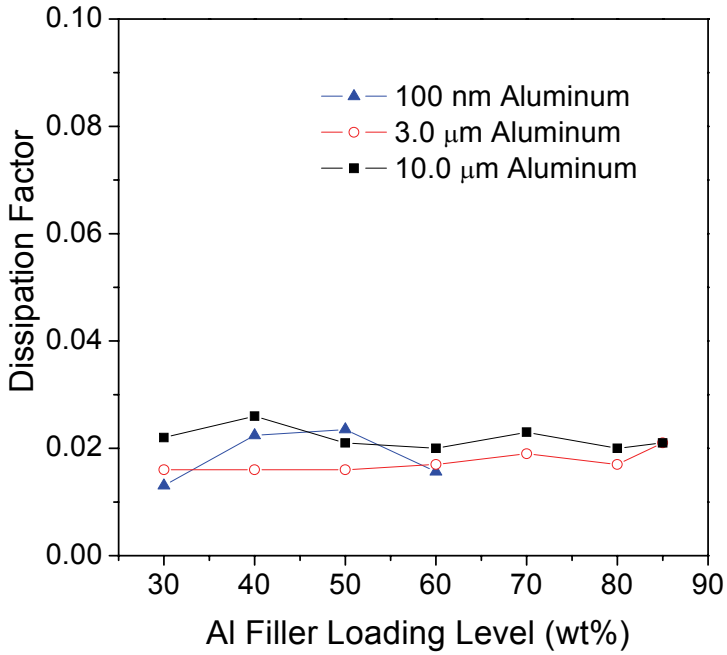

Figure 7.10 Dissipation factor of aluminum-filled composites as a function of filler loading (@ 10 KHz).

The filler size dependence of the dielectric properties of Al composites may be explained by the filler oxide shell thickness. The insulating oxide layer is very dense and uniform, as indicated by the very small weight gain in the TGA analysis. As shown in Figure 7.6, an oxide thickness of 2.8 nm was observed for the 100 nm aluminum powder used in this work. And the self-passivated oxide thickness is about 1 nm for a 10 nm aluminum particle. For bulk aluminum, the thickness of self-passivated insulating oxide is 4~5 nm at room temperature [158]. Table 7.1 lists the self-passivated oxide thickness as a function of Al filler particle size. It can be seen that the thickness of oxide layer is dependent on the aluminum particle size and it becomes thinner as the aluminum particle size decreases. The thinner insulating oxide thickness makes the smaller aluminum particle more conductive, which agrees well with the experimental data in bulk resistivity measurement, as shown in Figure 7.7. The thickness of the aluminum particles also plays

an important role in determining the dielectric behavior of epoxy-aluminum composites. At the same filler loading, the epoxy-aluminum composites filled with smaller particles show a higher effective dielectric constant than with the bigger particles, because the thinner oxide layer of a smaller aluminum particle may make its composites closer to a typical insulator-metal percolative composite without self-passivated insulating oxide on the metal core.

Table 7.1 Self-passivated oxide thickness vs. filler particle size

Filler Particle Size (nm)	**10**	**100**	**Bulk**
Oxide Thickness (nm)	**1.0**	**2.8**	**4 ~ 5**

Frequency dependence of 70 wt% 3 μm aluminum filled composites is shown in Figure 7.11. The dielectric constant of aluminum filled composites is stable in terms of frequencies, and there is only a slight decrease of the dielectric constant when the test frequency increases from 10 KHz to 1.5 GHz, which is in sharp contrast with the dielectric behavior of all polymer percolative composite [156]. However, Such a frequency independence behavior is consistent with the dielectric behavior of polymer-ceramic composites [45] as well as ceramic/metal (cermets) percolative composites [104].

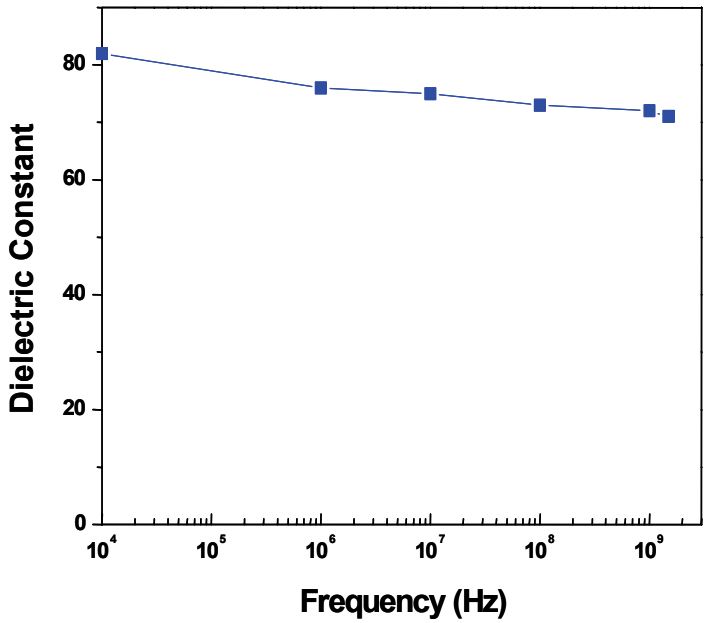

Figure 7.11 Frequency dependence of aluminum-filled composites.

7.3.1.4 Comparison of the Dielectric Properties of Al Composites, Al_2O_3 Composites and Al_2O_3-Coated Al Composites

To better understand the effect of the Al core and Al oxide thickness on the dielectric properties of Al composites , the properties of composites filled with 42 nm bulk Al_2O_3 particles and 40 nm Al_2O_3 coated 3 μm spherical Al particles were investigated. Figure 7.12 shows the micrograph of the cross section of a 40 nm Al_2O_3 coated 3 μm spherical Al particle by a field emission SEM. The coated oxide layer is not as uniform as self-passivated oxide layer, with a distribution of thickness from 27 to 52 Å. There are no clear distinction between self-passivated oxide and coated oxide from the FESEM image.

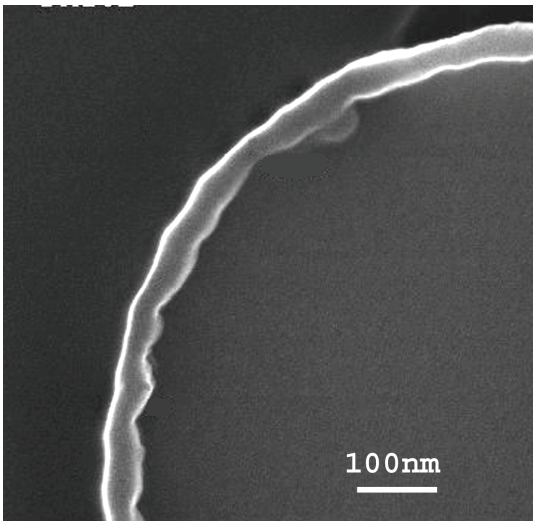

Figure 7.12 Micrograph of the cross section of a 40 nm Al_2O_3 coated 3 μm spherical aluminum particle by a FESEM.

Figure 7.13 illustrates the dielectric constant versus filler loading of composites filled with 42 nm bulk Al_2O_3 particles and 40 nm Al_2O_3 coated 3 μm Al particles. The maximum dielectric constants of 40 nm Al_2O_3 coated Al composites is about 45, which is much lower than 109 of their self-passivated counterpart. Therefore, the thickness of Al_2O_3 layer has significant influence on the dielectric behavior of the Al composites. In contrast, the 42 nm bulk Al_2O_3 composites show a very low dielectric constant, as shown in Figure 7.13, which indicates the importance of the metallic core for Al composites. Figure 7.14 shows the dissipation factor versus filler loading of composites filled with 42 nm bulk Al_2O_3, 40 nm Al_2O_3 coated 3 μm Al, and self-passivated 3 μm Al. The dissipation factor is low for all composites, which is desirable for embedded passive applications. The dissipation factors of Al_2O_3 coated Al composites, i.e. about 0.015, are slightly lower than self-passivated Al composites.

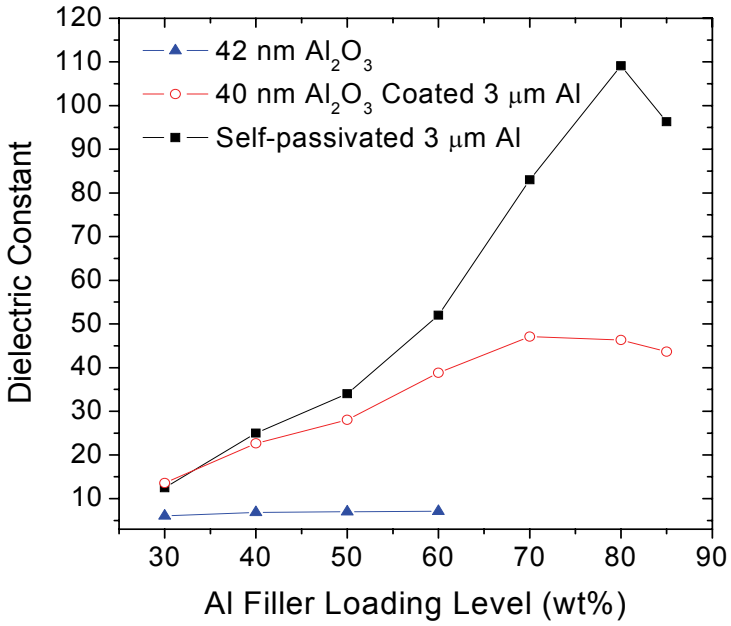

Figure 7.13 Dielectric constant versus filler loading of composites filled with 42 nm bulk Al_2O_3, 40 nm Al_2O_3 coated 3 μm Al, and self-passivated 3 μm Al.

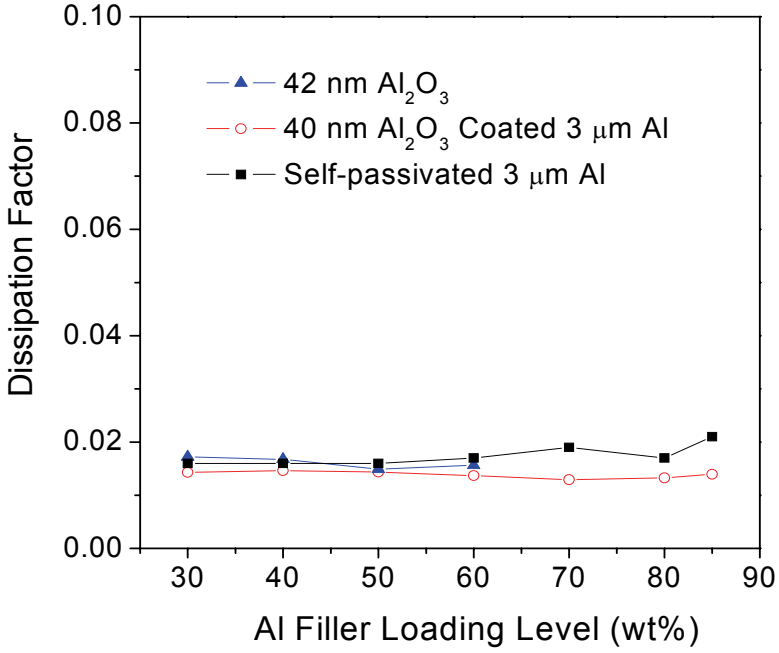

Figure 7.14 Dissipation factor versus filler loading of composites filled with 42 nm bulk Al_2O_3, 40 nm Al_2O_3 coated 3 μm Al, and self-passivated 3 μm Al.

7.3.1.5 Dielectric Mechanism of Composites Filled with Core-Shell Structured Fillers

Polymer-Al composites show a high dielectric constant and a low dielectric loss. The high dielectric constant of aluminum composites can be explained by the percolation behavior of insulator-conductor composites, even though the aluminum particles were measured to be semiconducting because of an insulating self-passivated oxide layer coated on the aluminum metallic core. For a typical insulator-metal composite system, the electric and dielectric properties near percolation threshold can be predicted by the percolation theory, as shown in Equation 7.1 to 7.3. In the above equations, the effective dielectric constant of a percolative composite is proportional to the dielectric constant of the insulator, which indicates the insulator is the "true" dielectric material, whereas the metal particles in the percolative composites can greatly reduce the effective dielectric thickness. The insulator-conductive filler composite could be considered as a super capacitor network, with a very large electrode area and small dielectric thickness, because each metal particle can act as an electrode of each tiny capacitor in the composite. Therefore, the effective dielectric constant of the insulator-conductive filler composite could be three or four orders of magnitude higher than the dielectric constant of the insulating matrix when the filler loading is close to the percolation threshold [104].

Because of the self-passivated insulating oxide layer on the aluminum particle surface, the epoxy-aluminum composites continued to be insulating even at high filler loading levels. However, the existence of aluminum metallic core can still dramatically reduce the effective dielectric thickness. But different from a typical percolation system, the dielectric layers, i.e. the thin layers of insulator between the metal cores, include two materials, i.e. the epoxy matrix and the unique nanoscale self-passivated insulating aluminum oxide. Because the dielectric layers are very thin and become thinner as a greater fraction of metallic spheres have been added in, a large capacitance can be observed in the aluminum composites. The oxide layer thicknesses of Al particles decrease with the decrease of particle sizes. A thinner Al_2O_3 layer on an Al particle leads

to a higher dielectric constant because the composite systems are closer to typical percolation system. Since the pure nanoaluminum oxide filler has no such metallic core as in an aluminum particle, the nanoaluminum oxide-filled composites do not show any percolation-related behavior and a much lower dielectric constant was observed, as can be seen in Figure 7.13. A unique characteristic of epoxy-aluminum composites is that the self-passivated insulating oxide layer of an aluminum particle is very uniform and dense and thereby can effectively control the dielectric loss of the epoxy-aluminum composites. As such, a low dissipation factor comparable to that of a neat epoxy is observed in the composites, because the epoxy matrix is the "true" dielectric material in the composites.

7.3.1.6 Reliability of Embedded Capacitors with Polymer-Al Composites

Figure 7.15 shows the leakage current versus electric field of 70 wt% 3.0 μm aluminum-filled composite. Leakage current is low and increases slightly when the electric field is below 4.7 MV/m, but increases quickly when voltage further increases. The breakdown field of aluminum composites is much lower than that of polymer-ceramic composites, which is usually above 10 MV/m.

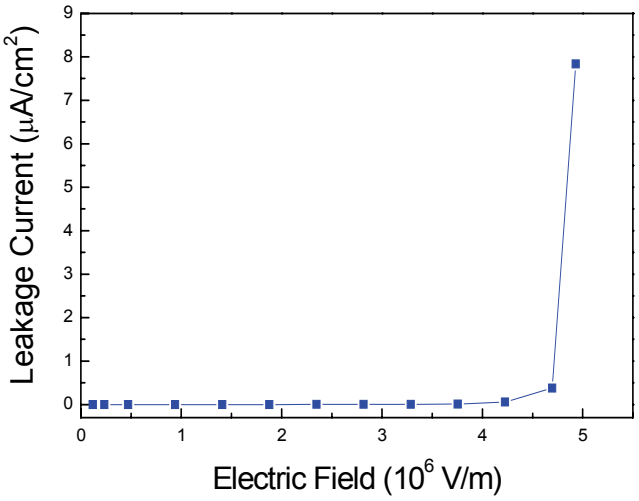

Figure 7.15 Leakage current of aluminum filled composites as a function of electric field.

Figure 7.16 shows the dielectric constant of aluminum-filled composites as a function of 85 °C/85% relative humidity aging time. Samples used were 80 wt% 3.0 μm aluminum-filled composite, 80 wt% 10.0 μm aluminum-filled composite, and 50 wt% nanoaluminum-filled composite. For all samples, the dielectric constant decreases with the aging time in the first 20 hours. After that, the dielectric constant exhibits almost no change with time. Smaller particle filler leads to a greater change in dielectric constant of composite materials than larger particle filler does. The change of dielectric constant is related to moisture absorption. Figure 7.17 shows the weight gain of aluminum composites during 85/85 aging. Moisture absorption is evident in the first 20 hours, as the weight gain is around 1.7 wt% during this period, however, there is almost no difference in weight gain between different-sized aluminum-filled composites. Further oxidation of aluminum filler may account for the difference in dielectric constant change of different-sized aluminum-filled composites. Smaller particles are more active, as found in TGA analysis, therefore, they are more readily further oxidized in 85/85 thermal humidity conditions. Larger particles have less further-oxidation during aging, therefore less change of dielectric constant was found.

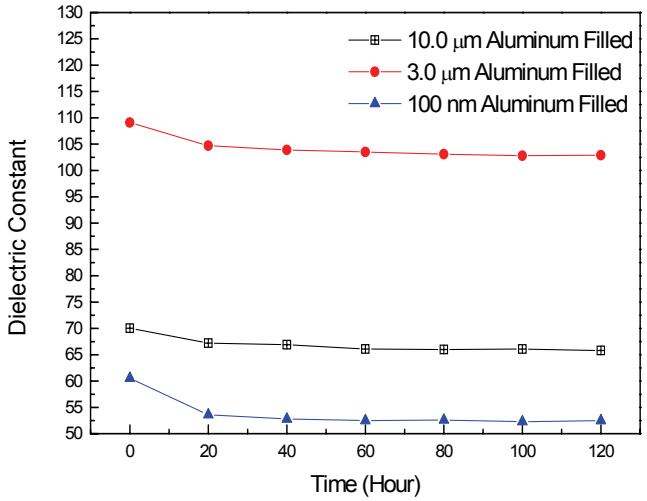

Figure 7.16 Influence of 85 °C/85% relative humidity aging on the dielectric constant of aluminum-filled composites.

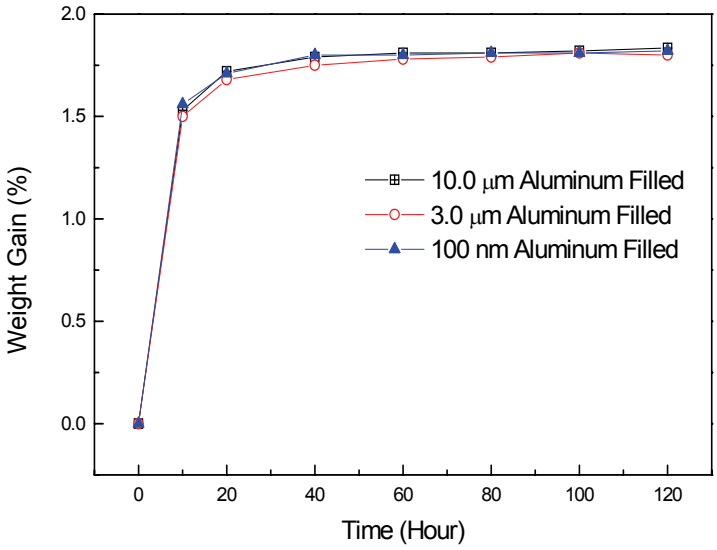

Figure 7.17 Weight gain of aluminum composites during 85 °C/85% relative humidity aging.

7.3.1.7 Mechanical Properties of Embedded Capacitors with Polymer-Al Composites

Mechanical properties such as the adhesion strength of a dielectric material to the substrate are important parameters for embedded capacitor applications. In this work,

adhesion strength of the aluminum composites toward Cu surface was characterized by the die shear measurement. Figure 7.18 shows die shear strength of 3.0 μm aluminum-filled composites, 10.0 μm aluminum-filled composites, and nanoaluminum-filled composites. The die shear strength decreases with the increase of filler loading as the amount of epoxy resin is reduced. Particularly, there is a dramatic decrease when the loading increases from 80 wt% to 85 wt% for 3.0 μm aluminum-filled composites and 10.0 μm aluminum-filled composites, and from 50 wt% to 60 wt% for nanoaluminum-filled composites. In aluminum-filled composites, epoxy resin serves as the adhesive binding the filler together. At high filler loading level, there is not enough epoxy to bind the filler, which results in the dramatic decrease of adhesion strength. However, at 80 wt% aluminum filler loading, the die shear strength is still 17.13 MPa and 17.58 MPa for 3.0 μm aluminum and 10.0 μm aluminum, respectively, which indicates the aluminum filled composites will have good adhesion to the copper layer when incorporated into the substrate structure.

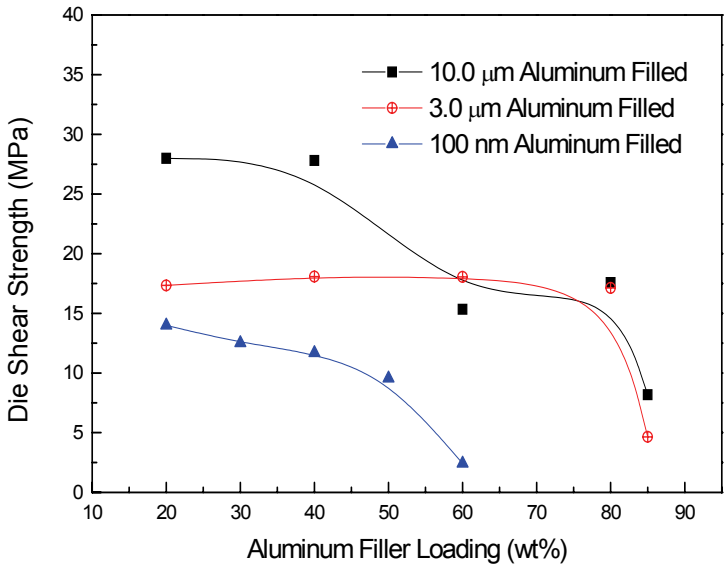

Figure 7.18 Die shear strength of aluminum filled composites.

7.3.2 High Dielectric Constant Bimodal Polymer-Aluminum Composites

7.3.2.1 Theoretical Maximum Packing Fractions of Bimodal Systems

From Figure 7.9, it was found that the dielectric constant of an aluminum-filled composite increases with the filler loading level, except at high filler loading levels where voiding (porosity) may occur due to the imperfect packing of filler particles or the solvent evaporation. To achieve the highest dielectric constant for aluminum-filled composites, the packing efficiency in the composites should be maximized in order to reduce the porosity. The filler packing efficiency of a given system is related to the viscosity of entire system. The viscosity of composites controls the dispersibility of filler in the system. It's well known that polydispersity of filler size can reduce the viscosity of a filled system, in particular, at high filler loading level the viscosity can be dramatically reduced by the increased particle size modality. Poslinski [159] found that a minimum viscosity of the composites could be achieved when the bimodal filler ratio is near the theoretical maximum packing fraction (MPF), which in turn indicates higher filler loading can be used with such bimodal combination for the composites.

Gupta and Seshadriz [92] developed an equation, based on Ouchiyama and Tanaka's model [90, 91, 160], to calculate the theoretical maximum packing fraction of a polydisperse system of spheres by taking into consideration particle size, size distribution and modality. The equation is given as follows:

$$\phi_m = \frac{\sum D_i^3 f_i}{\sum (D_i - \overline{D})^3 + \frac{1}{\overline{n}} \sum \left\{ (D_i - \overline{D})^3 - (D_i \sim \overline{D})^3 \right\} f_i} \qquad \text{Equation 7.6}$$

$$\text{where } \overline{n} = 1 + \frac{4}{13}(8\phi_m^0 - 1)\overline{D} \frac{\sum (D_i + \overline{D})^2 \left\{ 1 - \frac{3}{8}\left(\frac{\overline{D}}{D_i + \overline{D}} \right) \right\} f_i}{\sum \left\{ D_i^3 - (D_i - \overline{D})^3 \right\} f_i} \qquad \text{Equation 7.7}$$

$$\text{and } \overline{D} = \sum D_i f_i \qquad \text{Equation 7.8}$$

Here D_i is the diameter of the i-th component, f_i is the number fraction of i-th component, and ϕ_m^0 is the maximum packing of spheres of uniform size. And the abbreviation $(D_i - \overline{D})$ is defined as:

$$(D_i - \overline{D}) = 0 \text{ for } D_i \le \overline{D} \qquad \text{Equation 7.9}$$

$$(D_i - \overline{D}) = D_i - \overline{D} \text{ for } D_i \ge \overline{D} \qquad \text{Equation 7.10}$$

In addition, the number fraction f_i can be calculated from:

$$f_i = \frac{\nu_i / D_i^3}{\sum \nu_i / D_i^3} \qquad \text{Equation 7.11}$$

where ν_i is the volume fraction of i-th component.

Theoretical maximum packing fractions can be obtained from calculations of the above equations. Table 7.2 lists the theoretical maximum packing fractions and the corresponding bimodal filler ratios for each specific system.

Table 7.2 Theoretical maximum packing fractions of bimodal systems

Filler Combination		MPF	Volume fraction of Large Particle	Volume fraction of Small Particle
Large Particle	Small Particle			
10.0 μm	3.0 μm	0.735	0.75-0.82	0.25-0.18
10.0 μm	100 nm	0.891	0.76	0.24
3.0 μm	100 nm	0.876	0.77	0.23

7.3.2.2 Rheology Properties of Bimodal Systems

According to Table 7.2, 10.0 μm plus 100 nm filler combination has the largest theoretical maximum packing fraction of 0.891, and for all bimodal systems, the maximum packing fractions occur when the volume fraction of large particle to small

particle is in the range of 4:1 to 3:1. A set of bimodal filler volume fraction ratios (large particle/small particle), i.e., 70/30, 75/25, 76/24, 77/23, 78/22, 79/21, 80/20, and 85/15 were then chosen to perform rheology studies, in order to find the bimodal filler volume fraction ratio that gives the minimum viscosity in the bimodal composites when they are filled with the same filler loading level. All composite materials were prepared with the same filler loading of 60 wt%. The experiments were performed under steady state flow procedure with parallel plate geometry. Figure 7.19 shows plots of shear viscosity as a function of shear rate of bimodal aluminum filled systems: (a) 10 μm plus 3.0 μm aluminum, (b) 10 μm plus 100 nm aluminum, and (c) 3.0 μm plus 100 nm aluminum. All materials show shear thinning behavior. At a low shear rate, the viscosity of different systems is quite different, however, at high shear rates, the viscosity becomes leveled.

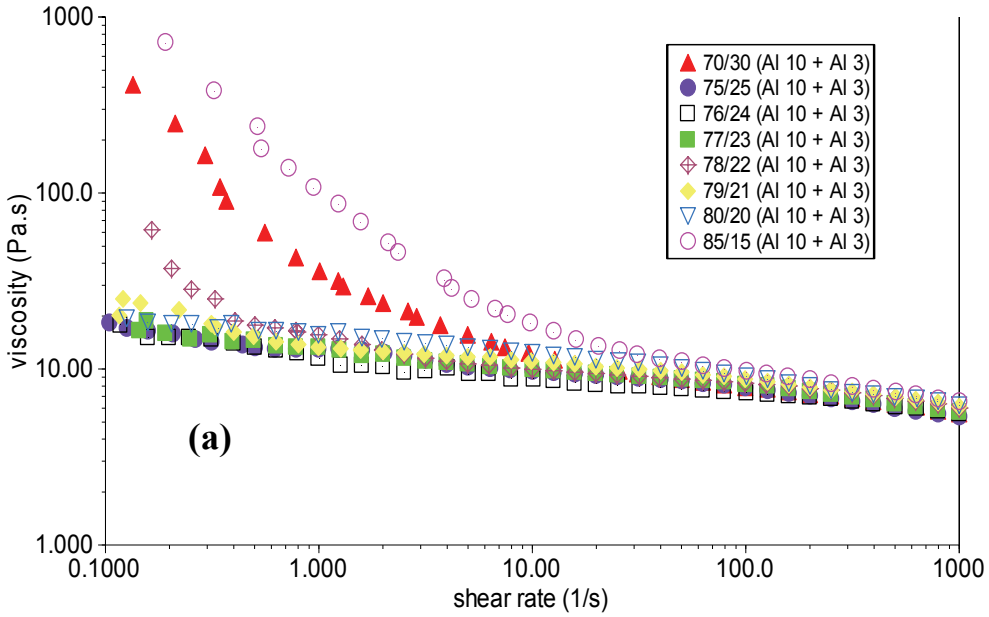

Figure 7.19 Shear viscosity as a function of shear rate of bimodal aluminum-filled composites. (a) 10 μm plus 3.0 μm aluminum, (b) 10 μm plus 100 nm aluminum, and (c) 3.0 μm plus 100 nm aluminum. In the legend, Al3, Al10, and Al0.1 denote 3.0 μm, 10.0 μm, and 100 nm aluminum, respectively.

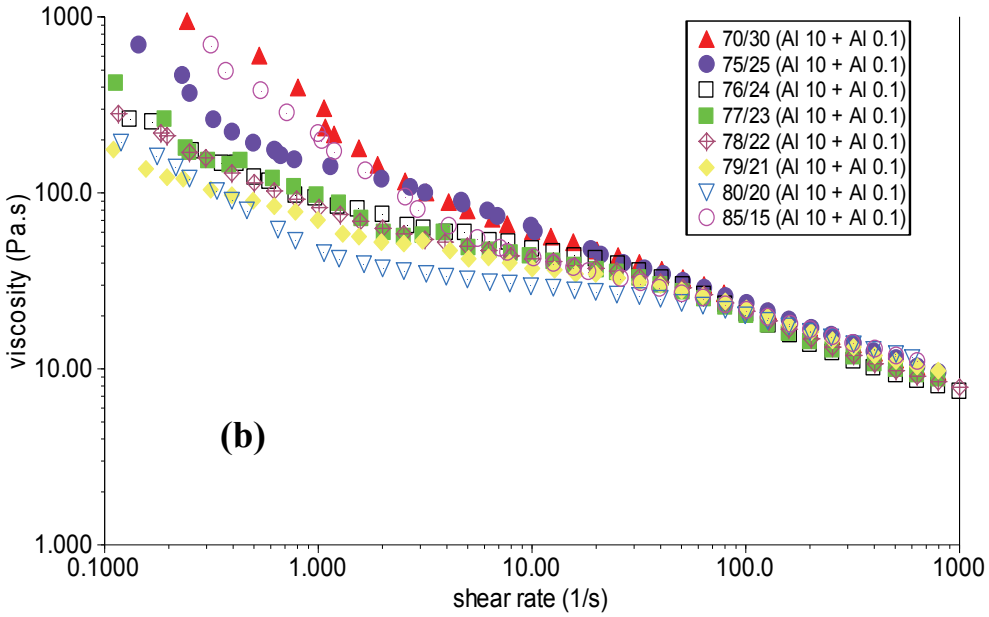

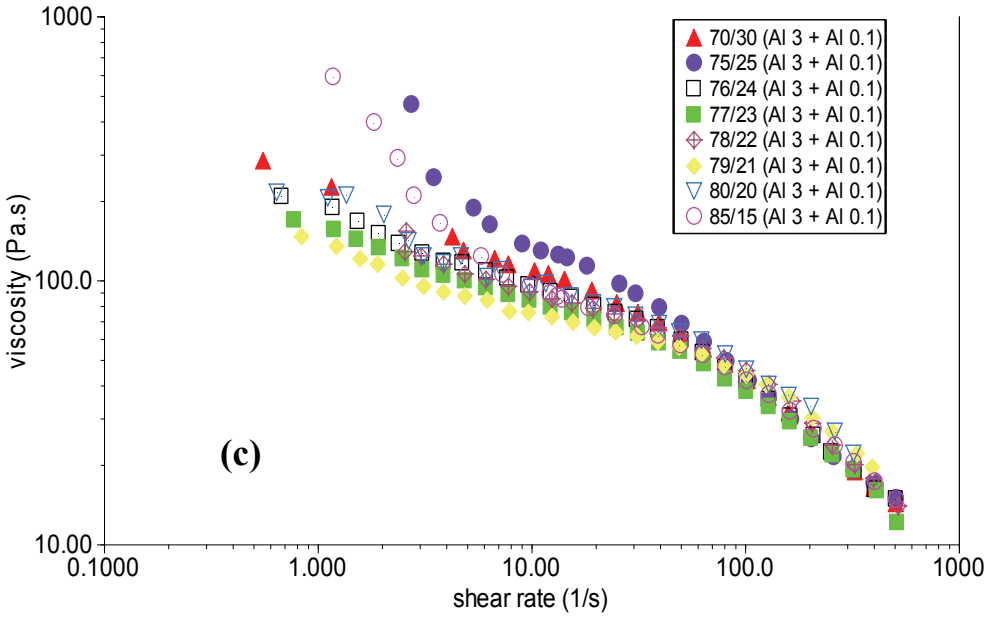

Figure 7.19 Continued.

The comparison of shear viscosity of three bimodal aluminum-filled systems (10.0 μm + 3.0 μm aluminum, 10.0 μm + 100 nm aluminum, and 3.0 μm + 100 nm

aluminum) at fixed bimodal filler volume fraction ratios (large particle/small particle) is given in Figure 7.20. For all bimodal filler ratios, 3.0 μm plus 100 nm aluminum-filled system has the highest viscosity, and 10.0 μm + 3.0 μm aluminum-filled system has the lowest viscosity. Viscosity of filled composites is determined by the volume filler loading level and the interfacial area between filler particles and the epoxy matrix of the composites. Higher filler loading leads to higher viscosity, which makes it more difficult to uniformly disperse the filler in the composites. At fixed filler loading, the viscosity of composites depends on the interfacial area between the filler particles and the epoxy. Because smaller particles overall have larger surface area, which induces more friction during shearing measurement, the combination of smallest bimodal fillers, i.e. 3.0 μm plus 100 nm aluminum, has the highest viscosity.

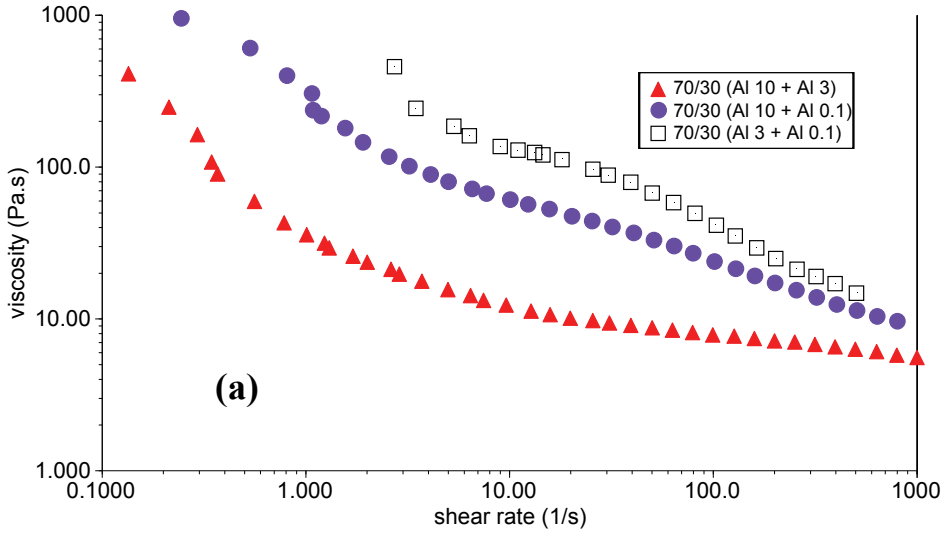

Figure 7.20 Comparison of shear viscosity of three bimodal aluminum-filled systems (10.0 μm + 3.0 μm aluminum, 10.0 μm + 100 nm aluminum, and 3.0 μm + 100 nm aluminum) at fixed bimodal filler ratio (a) 70/30, (b) 75/25, and (c) 85/15. In the legend, Al3, Al10, and Al0.1 denote 3.0 μm, 10.0 μm, and 100 nm aluminum, respectively.

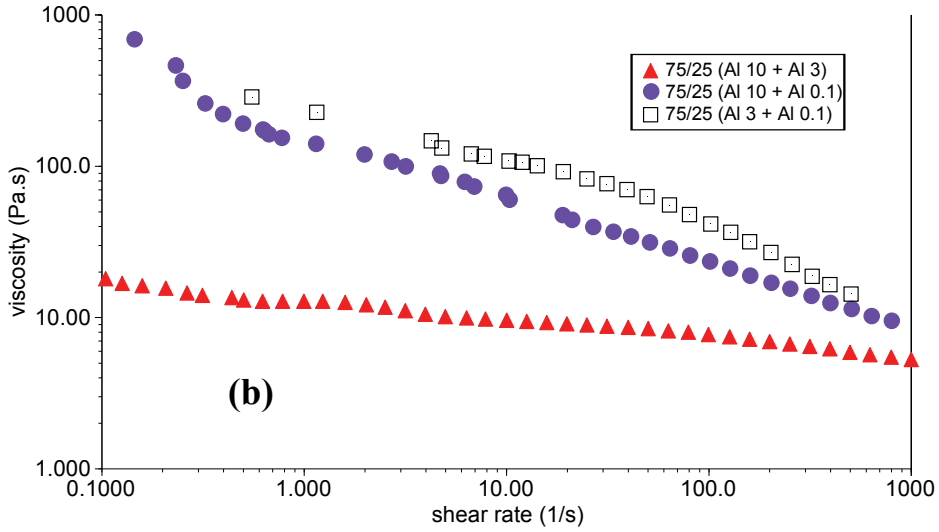

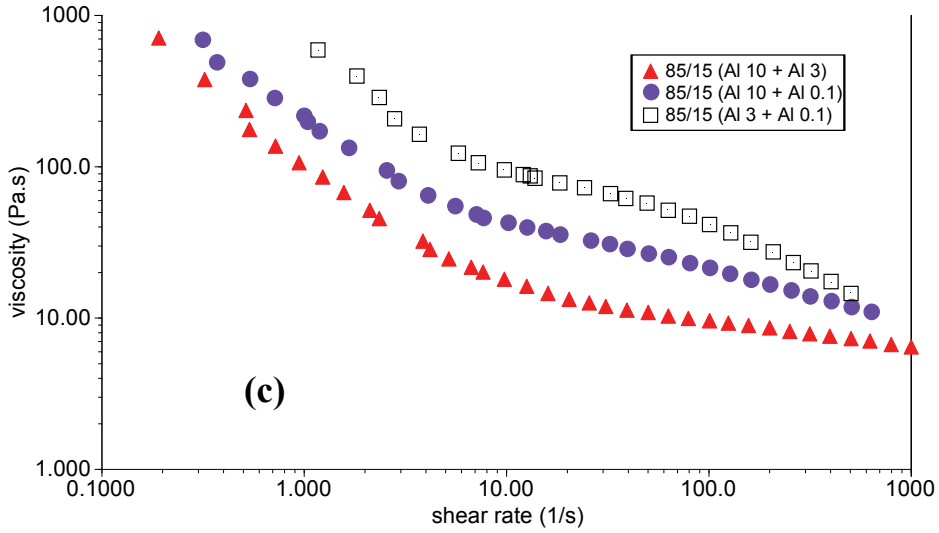

Figure 7.20 Continued

Figure 7.21 shows the viscosity of bimodal aluminum composites at shear rate 10 s^{-1} as a function of bimodal filler volume fraction ratio (large particle/small particle). At the fixed shear rate of 10 s^{-1}, for all three systems, the bimodal filler volume fraction ratio of 70/30 or 85/15 has a higher shear viscosity than other combinations. Minimum shear viscosity is found at bimodal filler volume fraction ratio 76/24 for system with 10.0 μm plus 3.0 μm aluminum, at bimodal ratio 80/20 for system with 10.0 μm plus 100 nm

aluminum, and at bimodal ratio 79/21 for system with 3.0 μm plus 100 nm aluminum. The bimodal ratio showing the lowest viscosity at the same filler loading level indicates that such filler combination has the best packing efficiency, and thus the highest filler loading can be obtained at such ratio for the system. These combinations of bimodal filler volume fraction ratio, as listed in Table 7.3, were then selected for further dielectric studies.

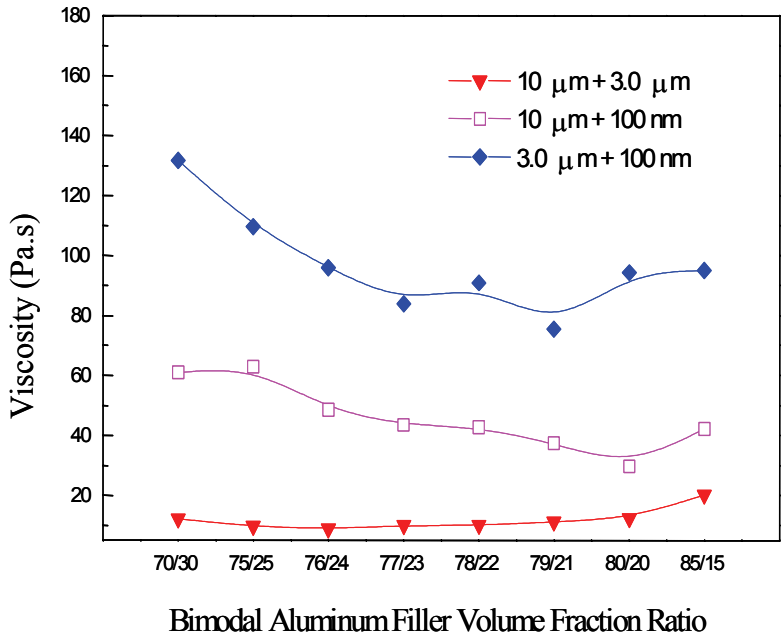

Figure 7.21 Viscosity of bimodal aluminum composites as a function of bimodal filler volume fraction ratio at shear rate 10 s^{-1}.

Table 7.3 Filler volume fraction ratios (large particle/small particle) corresponding to minimum viscosity of bimodal aluminum-filled systems

Filler Combination	Bimodal Filler Volume Fraction Ratio at Minimum Viscosity
10 μm + 3.0 μm	76/24
10 μm + 100 nm	80/20
3.0 μm + 100 nm	79/21

7.3.2.3 Dielectric Properties of Bimodal Systems

Figure 7.22 shows the dielectric constant and dissipation factor of bimodal aluminum-filled composites at 10 KHz, respectively. The dielectric constant of aluminum-filled composites increases with the filler loading level. With the optimized bimodal filler volume fraction ratio, the highest dielectric constant obtained is 88 for 10.0 μm plus 3.0 μm aluminum-filled system, 136 for 10.0 μm plus 100 nm aluminum-filled system, and 160 for 3.0 μm plus 100 nm aluminum-filled system. Dissipation factors of all composites are around or below 0.025, which is desirable for embedded passive application.

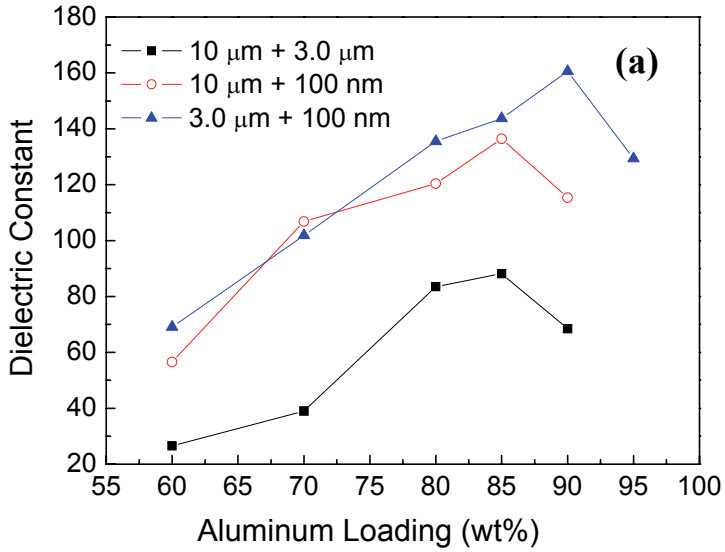

Figure 7.22 (a) Dielectric constant and (b) dissipation factor of bimodal aluminum filled composites as a function of aluminum loading level (@ 10 KHz).

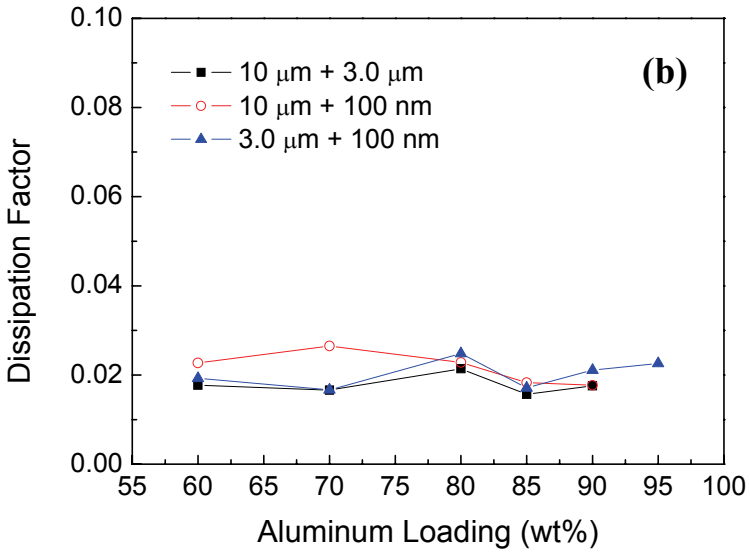

Figure 7.22 Continued.

7.3.2.4 Microstructures of Bimodal Systems

Figure 7.23 shows the optical microscope pictures of aluminum-filled composites. Pictures (d), (f), and (h) are morphologies of 60 wt% 10.0 μm plus 3.0 μm aluminum-filled composite, 60 wt% 10.0 μm plus 100 nm aluminum-filled composite, and 60 wt% 3.0 μm plus 100 nm aluminum-filled composite, respectively. The fillers at the loading of 60 wt% are not as tightly packed as those in pictures (e), (g), and (i), which are morphologies of 85 wt% 10.0 μm plus 3.0 μm aluminum-filled composite, 85 wt% 10.0 μm plus 100 nm aluminum-filled composite, and 90 wt% 3.0 μm plus 100 nm aluminum-filled composite, respectively. The tightly packed filler particles at high filler loading in (e), (g), and (i) lead to the maximum dielectric constant of each system. The bimodal composites in (e), (g), and (i) show much higher maximum dielectric constants than unimodal composites in (a) and (b), which is simply due to the higher packing efficiency in the bimodal system. In unimodal composites, only epoxy matrix surrounds the filler particles, however, in bimodal systems, some smaller second filler particles are filled in the gap of bigger primary particles.

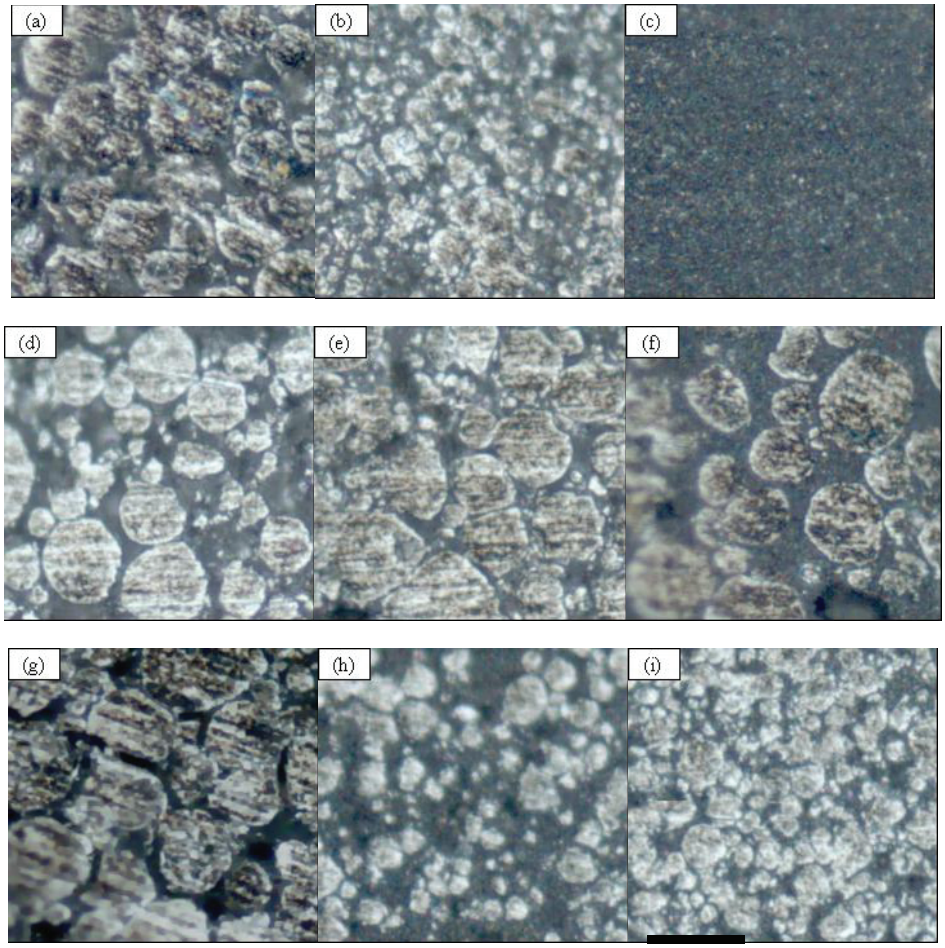

Figure 7.23 Optical microscope pictures of aluminum-filled composites. (a) 10.0 μm aluminum at 85 wt%, (b) 3.0 μm aluminum at 80 wt%, (c) 100 nm aluminum at 60 wt%, (d) 10.0 μm + 3.0 μm aluminum at 60 wt%, (e) 10.0 μm + 3.0 μm aluminum at 85 wt%, (f) 10.0 μm + 100 nm aluminum at 60 wt%, (g) 10.0 μm + 100 nm aluminum at 85 wt%, (h) 3.0 μm + 100 nm aluminum at 60 wt%, and (i) 3.0 μm + 100 nm aluminum at 90 wt%. (a), (b), (c), (e), (g), and (i) are loaded at the filler loading corresponding to the maximum dielectric constant for the filler combination.

7.3.3 Surface Functionalization of Aluminum Particles for Enhanced Dielectric Properties and Processibility of Polymer-Aluminum Composites

Because of the core-shell structure of aluminum particles, polymer-aluminum nanocomposite has the combined advantages of a percolative composite and a polymer-ceramic system, showing a high dielectric constant and a low dielectric loss. Therefore, polymer-aluminum nanocomposite was promising for embedded decoupling applications. Because filler surface treatment is a vital factor to obtain high dielectric constant in polymer nanocomposites [63, 64], in this work, an aluminum particle surface functionalization was performed with an epoxide-functionalized silane coupling agent to further enhance the dielectric properties and processibility of polymer/aluminum composites.

7.3.3.1 Surface Chemistry of Untreated and Treated Aluminum Particles

Figure 7.24 shows the FTIR spectra of both untreated and silane coupling agent treated nanoaluminum particles. For untreated nanoaluminum particle, there is an absorption band at 3422 cm^{-1}, which corresponds to the hydrogen-bonded –OH group. The FTIR spectrum of untreated particles indicates that as with the bulk aluminum oxide particles, there are hydroxyl groups (Al-OH) on the surface of the insulating oxide shell of the untreated aluminum particles. The –OH functional groups on the aluminum oxide shell of an aluminum particle are reactive and can be utilized to functionalize the particle. To further enhance the dielectric properties and processibility of polymer/aluminum composites, in this study the aluminum particle surface was chemically modified with an epoxide-functionalized silane coupling agent, by taking advantage of these –OH groups. Such filler surface treatment is known to be a vital factor to obtain a high dielectric constant in polymer/ceramic nanocomposites, e.g., the surface treatment of lead magnesium niobate-lead titanate (PMN-PT) prior to the mixing of ceramic filler with

epoxy could dramatically increase the dielectric constant of polymer ceramic composites [63, 64]. Figure 7.25 is a schematic showing the reaction mechanisms of silane coupling agent with the –OH groups on the oxide shell of an aluminum particle surface. The alkoxy (-OR) groups of silane coupling agent were first hydrolyzed with water to form silanol (Si-OH) groups. And then the silanol groups were condensed with the hydroxyl groups on the aluminum oxide shell of aluminum particles, via acid-catalyzed reactions. The condensation reaction has a relatively high activation energy, therefore an elevated temperature (120 ºC) was used during refluxing to facilitate the reaction. After surface treatment, the peak corresponding to –OH group at the region of 3300-3500 cm^{-1} disappears, as shown in Figure 7.24. This indicates a rather complete reaction of silane coupling agent with the –OH functional groups on an aluminum particle surface. Two new absorption bands can be observed in Figure 7.24 in the frequency above 3500 cm^{-1}, one at 3676 cm^{-1} and another at 3748 cm^{-1}. These absorption peaks are due to the Si-OH vibration. After hydrolyzation, the trimethoxysilane formed three Si-OH groups on each coupling agent (shown in Figure 7.25). Because the reaction temperature was moderate, not all three Si-OH groups were condensed to form Si-O-Al or Si-O-Si. As such, the unreated Si-OH on the coupling agent results in the absorption bands at the frequency 3500 cm^{-1}. The absorption bands of treated particles at 2969 cm^{-1} and 2867 cm^{-1} is caused by the stretching of the C-H bond of coupling agent; another new band at 1246 cm^{-1} can be assigned to the C-O bond of three-membered epoxy ring. Therefore, the FTIR characterization suggests that the silane coupling agent be successfully grafted on the aluminum particle surfaces.

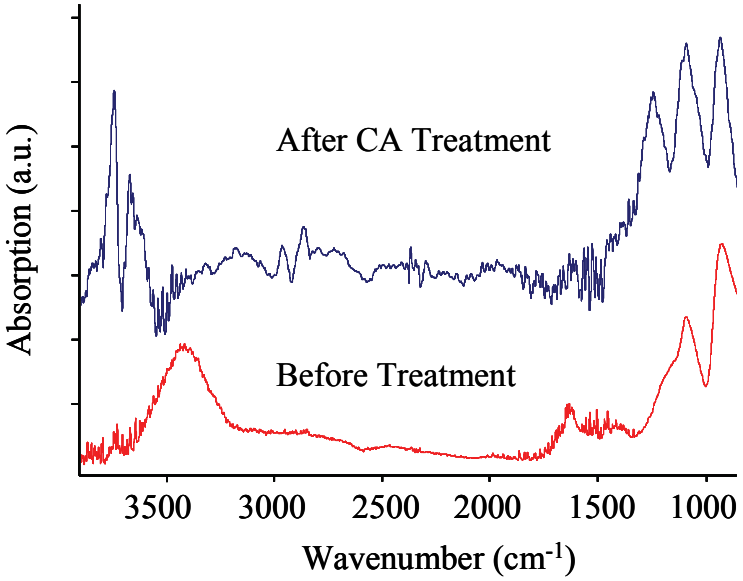

Figure 7.24 FTIR spectra of untreated and silane coupling agent treated nanoaluminum particles.

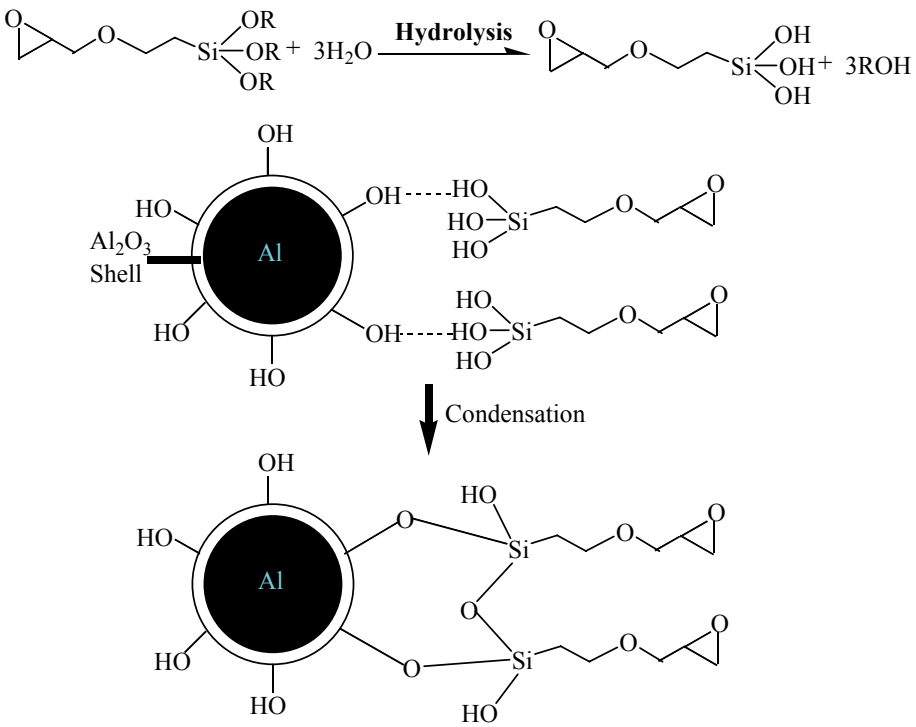

Figure 7.25 Schematic showing the reactions of silane coupling agent with aluminum particle surface.

The thermal degradation behaviors of untreated and silane coupling agent treated aluminum particles were studied by TGA. Figure 7.26 (a) shows the effect of coupling agent treatment on the degradation behavior of aluminum particles. The insulating aluminum oxide shell of aluminum particles is very dense and stable. As can be seen in Figure 7.26(a), there is almost no weight change from room temperature up to 450 ºC for untreated aluminum particles. However, at temperature close to the melting point of aluminum (about 660 °C), aluminum particles get enough energy to react with O_2 in the air and form thicker aluminum oxide. Figure 7.26(a) shows at temperature around 600 °C, the weight of aluminum particles dramatically increases. Compared to untreated aluminum particles, the coupling agent treated aluminum particles shows a different degradation behavior. For both 3 μm and 100 nm sizes, the coupling agent treated aluminum particles shows significant weight loss at temperatures below 450 ºC, in contrast to the nearly zero weigh change for untreated particles. The silane coupling agent grafted on the particle surface has an organic chain, which could degrade at elevated temperatures, and thereby weight loss was observed with treated aluminum particles. The degraded silane coupling agent forms silica on the aluminum particles surface and could significantly reduce the oxidation rate of aluminum at the temperature above 600 ºC, therefore the weight gain at high temperature is lower for particles after surface modification. Compared to coupling agent treated 3 μm particles, the treated nanoaluminum particles initially have more weight loss, as illustrated in Figure 7.26(b), which indicates more silane coupling agent was absorbed and reacted on the nanoaluminum oxide shell, because of the relatively larger specific surface area of smaller particles. Therefore, both TGA results and FTIR analysis confirmed that the silane coupling agent was successfully grafted on the aluminum particle surface.

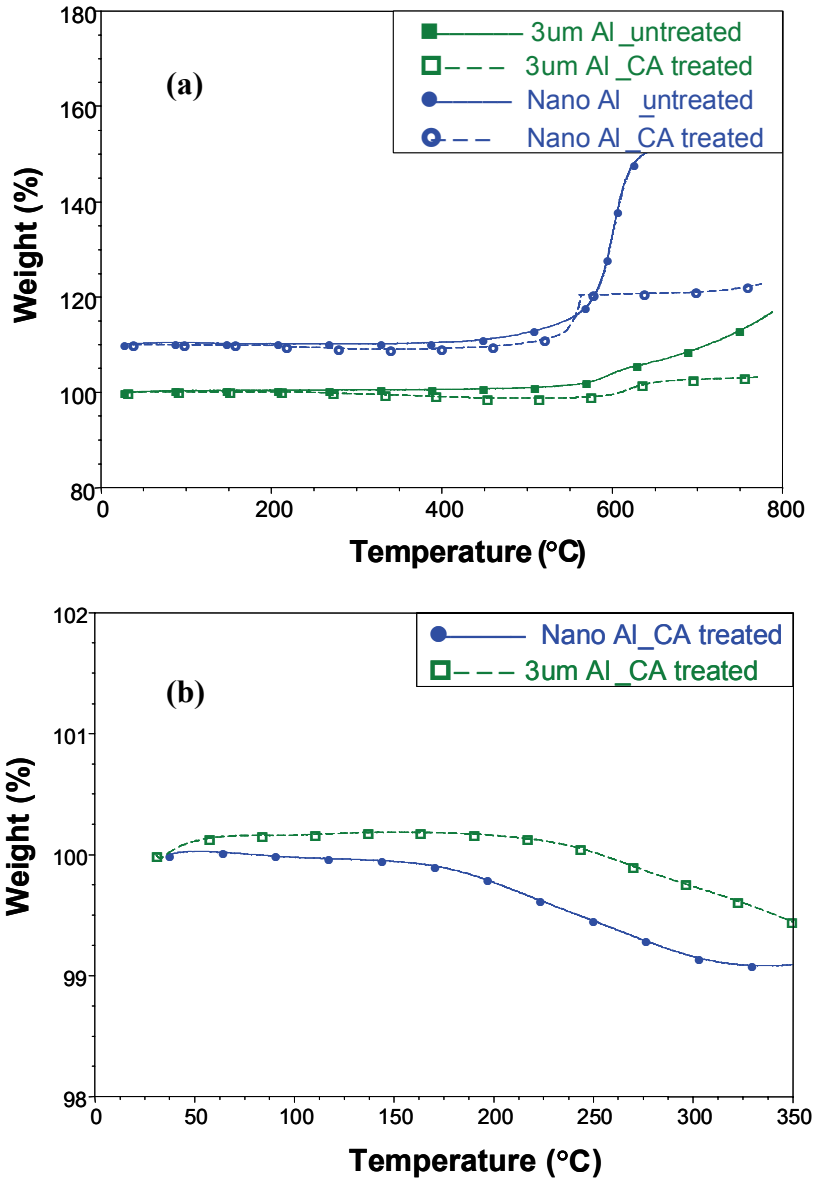

Figure 7.26 TGA studies of aluminum powders. (a) Effect of coupling agent treatment on the degradation behavior of aluminum particles. (b) Effect of particle sizes on the degradation behavior of coupling agent treated particles.

7.3.3.2 Effect of Particle Surface Functionalization on the Rheology Properties of Aluminum Composites

To investigate the viscosity and dispersability of coupling agent treated aluminum particles, 70 wt% 3.0 μm aluminum/epoxy composites and 40 wt% nanoaluminum/epoxy composites were formulated. Up to these filler loadings, no solvent is required for dispersing the aluminum particles in the composites, which makes it easier to compare the properties between untreated and treated composite systems. Rheology properties of these aluminum composites were studied with a stress rheometer under steady state flow procedure with parallel plate geometry. Figure 7.27(a) shows the rheology properties of a neat epoxy resin and its 3.0 μm aluminum composites. The neat epoxy resin shows a low viscosity and a Newtonian behavior, whereas the untreated 3.0 μm aluminum/epoxy composites has a much higher viscosity and a significant shear rate dependence. In the case of untreated aluminum composites, many aluminum particles were in agglomerated status, with some epoxy liquid trapped inside the agglomerates, which could significantly increase the effective solid content of particles and thereby increasing the viscosity. The shear thinning behavior of untreated 3.0 μm aluminum composites is due to the breakdown of agglomerates as the shear rate increases. After the coupling agent surface modification, the viscosity of 3.0 μm epoxy/aluminum composite was dramatically reduced, because the aluminum agglomerates were broken down into primary particles during treatment and then better dispersed, which explains the reduced shear thinning behavior of the coupling agent treated aluminum composites as well. Figure 7.27(b) illustrates the rheology properties of neat epoxy resin and its nanoaluminum composites. The same effect of coupling agent treatment on viscosity was found in the 100 nm nanoaluminum composites.

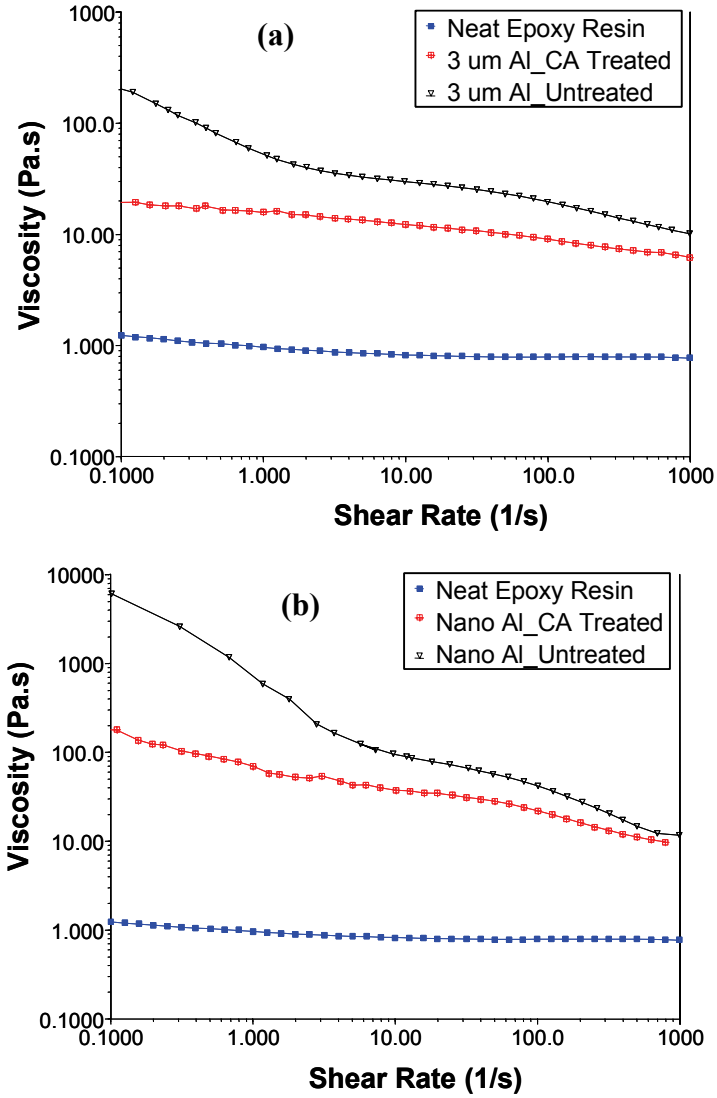

Figure 7.27 Rheology properties of untreated and coupling agent treated aluminum composites. (a) 3 μm aluminum composites. (b) Nanoaluminum composites.

7.3.3.3 Effect of Particle Surface Functionalization on the Dielectric Properties of Aluminum Composites

The dielectric properties of both untreated and treated 70 wt% 3.0 μm aluminum/epoxy composites and 40 wt% nanoaluminum/epoxy composites were studied. As shown in Figure 7.28, the dielectric constant (@10 KHz) of untreated 3.0 μm aluminum/epoxy composite and nanoaluminum/epoxy composite were 82.1 and 52.3,

respectively, which are tens of times higher than that of the polymer matrix (about 3.5). The dissipation factor was low, about 0.02, for both untreated aluminum composites, due to the insulating ceramic shell. After the coupling agent treatment, the dielectric constant of 3.0 μm aluminum/epoxy composites was increased about 17%, up to 96, and the dielectric constant of nanoaluminum/epoxy composites was increased about 26%, up to 66.1. After coupling agent treatment, the dissipation factor was still low and no clear changing trend was found between the untreated and coupling agent treated nanocomposites. The improvement of dielectric constant comes from the better dispersion of coupling agent treated aluminum particles in the polymer matrix. Figure 7.29 shows the SEM micrographs of (a) 40 wt% untreated nanoaluminum composites and (b) silane coupling agent treated nanoaluminum composites. The untreated aluminum particles have a much larger agglomerate size than the coupling agent treated aluminum particles in their epoxy composites. The breakdown of big filler agglomerates may help reduce the voids in the nanocomposites, which could significantly increase the effective dielectric constant of the composites, as found with polymer/ceramic nanocomposites [63, 64].

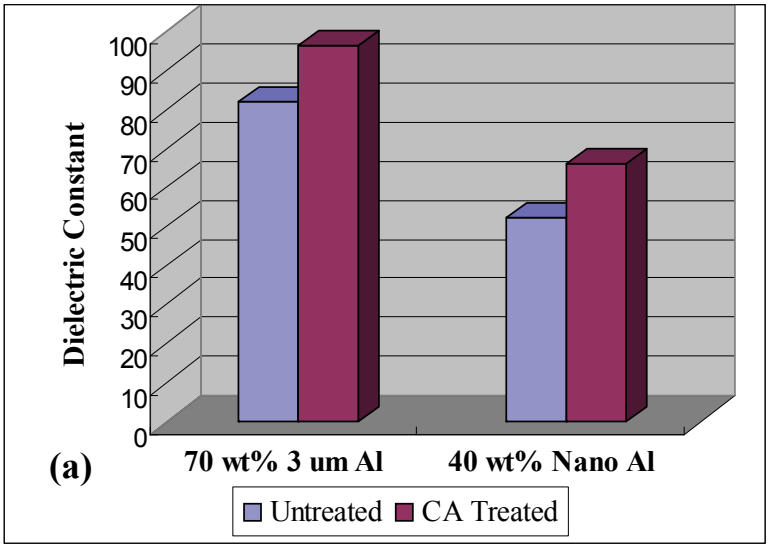

Figure 7.28 Comparison of the (a) dielectric constant and (b) dissipation factor (@10 KHz) of aluminum composites.

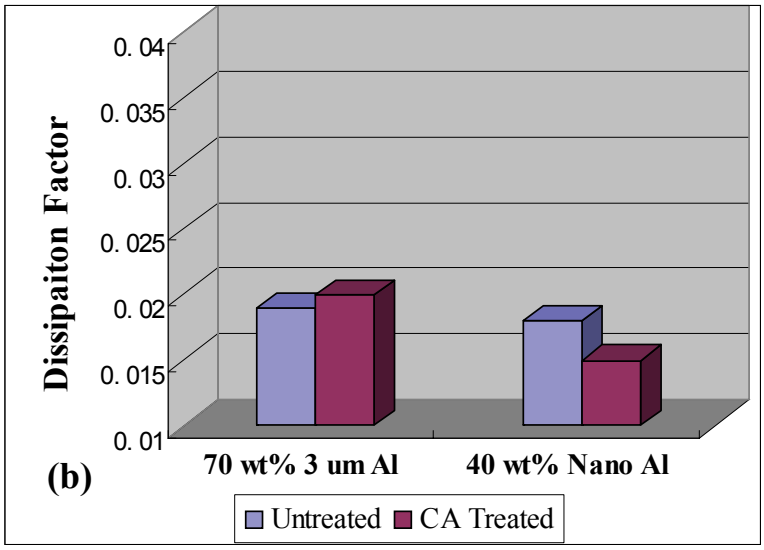

Figure 7.28 Continued.

(a)

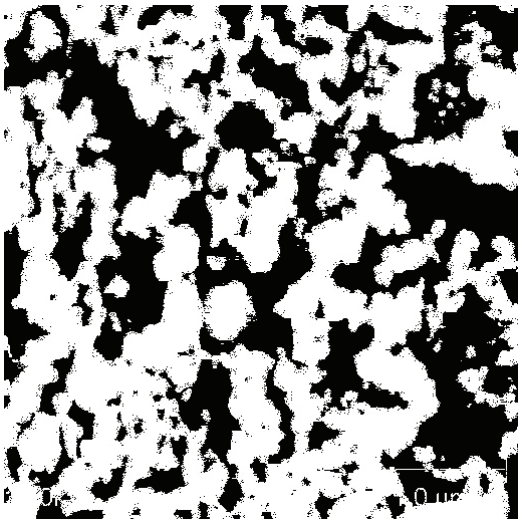

Figure 7.29 SEM micrographs of (a) untreated nanoaluminum composites and (b) silane coupling agent treated 100 nm nanoaluminum composites.

(b)

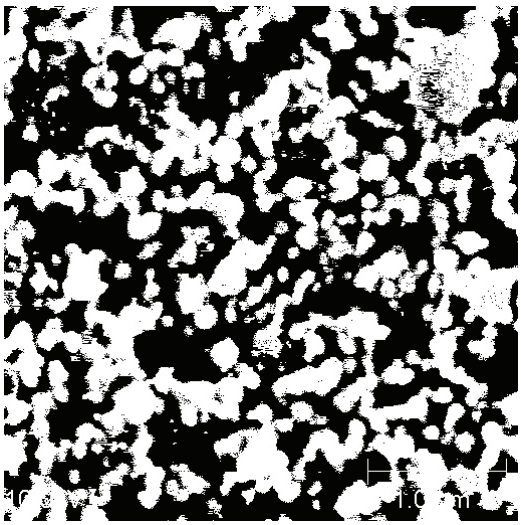

Figure 7.29 Continued.

7.3.3.4 Frequency and Temperature Responses of Aluminum Composites

The frequency responses of aluminum composites were studied by a dielectric analyzer (DEA). Frequency responses of the 40 wt% coupling agent treated nanoaluminum composites is shown in Figure 7.30. The dielectric constant data from 0.001 Hz to 100 KHz were taken from the DEA test, and the 1 MHz and 10 MHz data were from LCR meter measurement. The dielectric constant at 10 kHz is about 66, and it increases to about 81 as the frequency decreases 7-order of magnitude to 0.001 Hz. In general, the dielectric constant only slightly decreases with the increase of frequency. Such a frequency independence behavior is consistent with the dielectric properties of cermets [104]. The frequency response of a dielectric material is determined by its polarizabilities. There are four major types of polarization with their polarization relaxations occurring at specific frequencies: electronic polarization (10^{15} Hz), ionic polarization (10^{12} Hz to 10^{13} Hz), molecular or dipolar polarization (10^{11} Hz to 10^{12} Hz), and interfacial polarization (around 10^{3} Hz). When the frequency of applied electric field is above the relaxation frequency of a polarization mechanism, the contribution from this polarization mechanism will be dramatically reduced because this polarization is too slow

to completely follow the oscillation of the applied electric field. The frequency independence behavior of aluminum composites indicates the major polarization mechanism contributing to the high dielectric constant doesn't change over the measurement frequency range. However, the dissipation factor of nanolauminum composite increases dramatically as the frequency decreases below 1 Hz. In this low frequency range, electrode polarization may be the major reason, which may affect the dissipation factor much more than the dielectric constant.

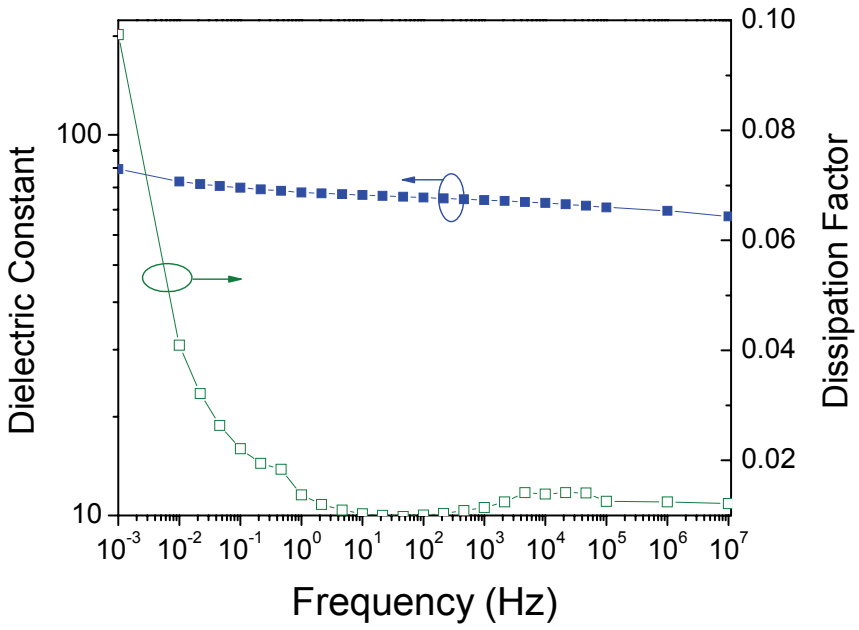

Figure 7.30 Frequency responses of aluminum composites.

The temperature coefficient of capacitance (TCC) of aluminum composites from room temperature up to 200 ºC were studied by the DEA as well. Figure 7.31 shows the effect of temperature on the dielectric properties of 40 wt% coupling agent treated 100 nm nanoaluminum composites. The dielectric constant of aluminum composites generally increases with the temperature. This trend is consistent with the frequency responses, according to the time-temperature superposition rule of polymeric materials. The

temperature shows a more complicated effect on the dissipation factor of aluminum composites, but in general, the dissipation factor in all temperature ranges is low, comparable with that of a neat epoxy resin.

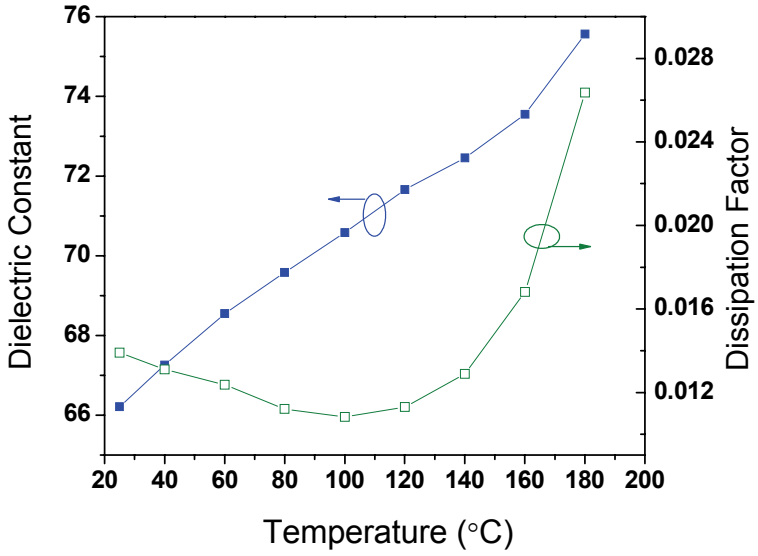

Figure 7.31 Effect of temperature on the dielectric properties (@10 KHz) of aluminum composites.

7.3.3.5 Mechanical Properties of Untreated and Treated Aluminum Composites

Mechanical properties such as the adhesion strength to the substrate are important materials parameters for embedded capacitor applications. In this work, lap shear tests were used to characterize the adhesion strength of aluminum/epoxy nanocomposites to the copper surface. Figure 7.32 shows the lap shear adhesion strength of a neat epoxy and its aluminum composites. The lap shear strength of the neat epoxy resin is about 3.9 MPa. The inclusion of aluminum particles will significantly reduce the lap shear adhesion strength; in particular for 40 wt% untreated nanoaluminum composites, the lap shear adhesion strength is only about 1.4 MPa, less than 35% of that of neat epoxy resin. For both 3.0 μm aluminum and nanoaluminum particles, the coupling agent treated aluminum

composites showed higher lap shear strength. The epoxide functional group of grafted silane coupling agent on the aluminum oxide shell may react with the copper surface of a lap shear test coupon and thereby increasing the lap shear strength of aluminum composites.

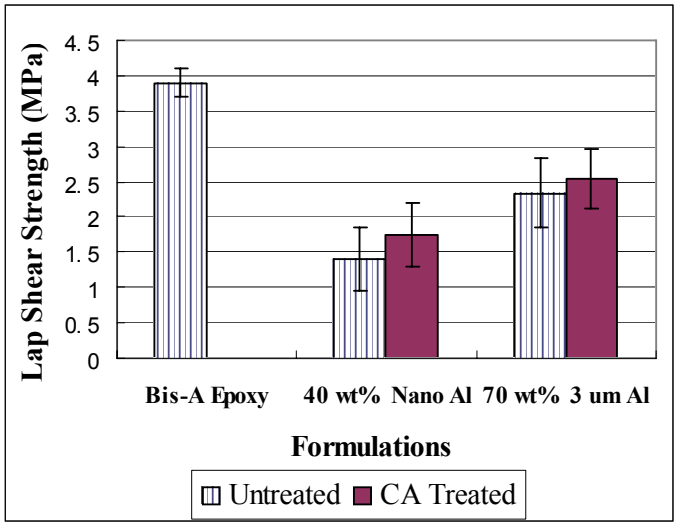

Figure 7.32 Lap shear adhesion strength of a neat epoxy resin and its aluminum composites.

7.3.4 Effect of Low-Loss Polymer Matrices on the Dielectric Properties of Aluminum Composites

The dielectric properties of a composite are not only determined by the filler, but also by the polymer matrix. It is interesting to know the effects of the polymer matrix on the dielectric behavior of polymer-aluminum composites. Besides bisphenol-A epoxy, another four polymer materials were selected for this study on the basis of their good electrical characteristics and mechanical properties. These four polymers are silicone, polyimide, polynorbornene, and BCB. When compared to bisphenol-A epoxy, these polymers have very low dissipation factors. Figure 7.33 shows the DSC thermograph of

silicone, polyimide, polynorbornene, BCB, and epoxy. The curing conditions for these polymers will be selected based on this thermograph.

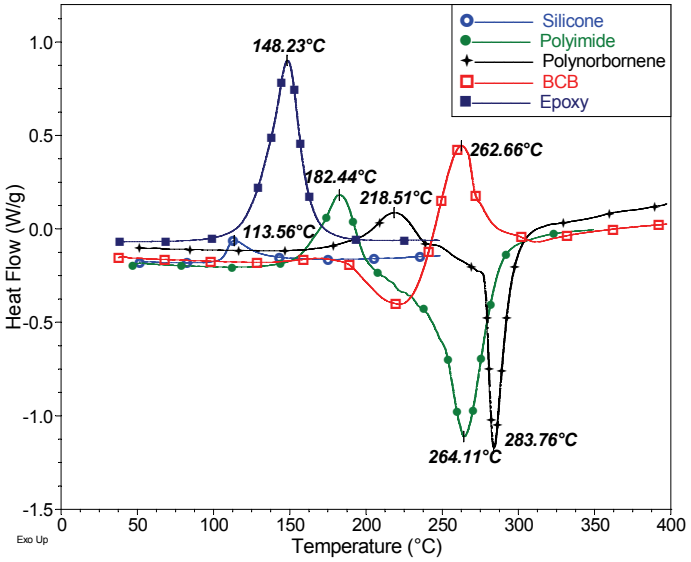

Figure 7.33 DSC thermograph of silicone, polyimide, polynorbornene, BCB, and epoxy.

7.3.4.1 Silicone/Aluminum Composites

Silicone as a low loss dielectric material has been widely used in the electronic industry because of its good compatibility with most device surfaces. Cured silicone has a dielectric constant of about 2.72 and a dissipation factor of about 0.0007, which is much lower than 0.02 for an epoxy. As shown in Figure 7.33, this two-part silicone material has a curing peak at 112 ºC. The onset curing temperature is about 100 ºC, and curing finishes at about 150 ºC. Based on this, 150 ºC for 1 hour was selected as the curing condition for silicone and its composites.

Figure 7.34 shows the dielectric properties of aluminum-silicone composites as a function of filler loading. The dissipation factor of silicone-based composites is less than 0.01, which is lower than that of epoxy-based composites, i.e. about 0.02. Therefore, the lower loss polymer matrix plays an important role in reducing the dissipation factor of aluminum composites. A lower dielectric loss is important for many applications, in

particular for high frequency such as radio frequency (RF) applications, because the energy consumed by a dielectric is proportional to both the dielectric loss and the frequency. On the other hand, the dielectric constant of silicone composite is also lower than that of epoxy-based composites. As can be seen in Figure 7.34, the maximum dielectric constants obtained are 42 and 23 for 3 μm and 10 μm aluminum-filled silicone composites, respectively, which are much lower than their epoxy-based counterparts. The dielectric constant of 3 μm aluminum filled silicone composites is higher than that of 10 μm Al composites, which is the same as in epoxy-based composites shown in Section 7.3.1. The lower dielectric constant of silicone-based composites is due to the lower dielectric constant of silicone matrix. The dielectric constant of silicone is about 2.71, whereas it is 3.5 for an epoxy. The dependence of the dielectric constant of an aluminum composite on the polymer matrix is consistent with the dielectric behavior of polymer-ceramic composites. It was found that a higher κ polymer matrix generally leads to a higher κ of its ceramic composites [63, 77, 88].

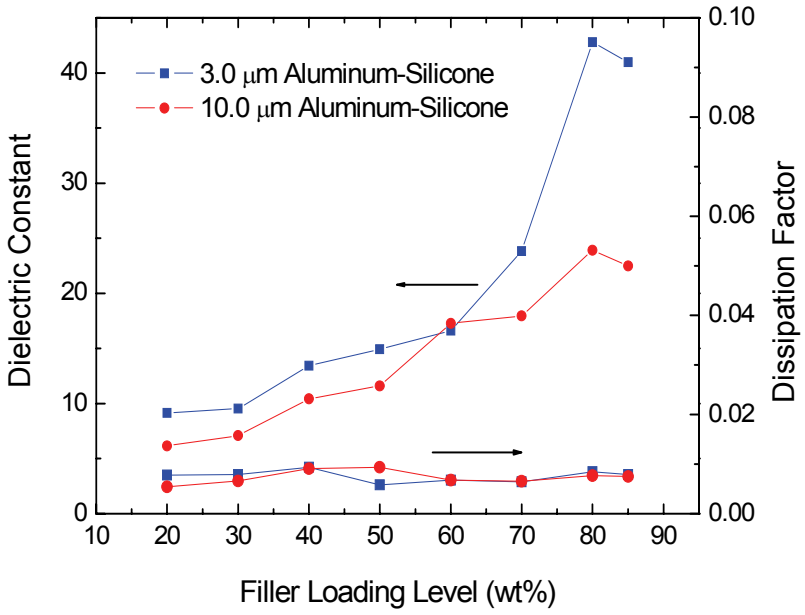

Figure 7.34 Dielectric properties of silicone-aluminum composites as a function of filler loading.

7.3.4.2 Polyimide (PI)/Aluminum Composites

Polyimide is a high temperature engineering polymer with excellent mechanical, thermal, and electrical properties. It has been widely used as a stress buffer, passivation layer, chip bonding, and interlayer dielectric in the microelectronic industry. Polyimide has excellent dielectric properties, with a dielectric constant of about 3.5 and a dissipation factor of about 0.002. The curing profile in Figure 7.33 shows two peaks, one exothermic peak at 182 ºC, and one endothermic peak at 264 ºC. The exothermic reaction ends at about 220 ºC. As such, to ensure complete curing of the samples, a multi-step curing procedure, including 300 ºC for 1 hour as the last step was selected as the curing condition for polyimide-aluminum composites.

The dielectric properties of polyimide-aluminum composites as a function of filler loading are shown in Figure 7.35. The dielectric constants of polyimide-aluminum composites are much higher than that of silicone composites due to the higher dielectric constant of the polyimide matrix. The maximum dielectric constants obtained are 84 and 58 for 3 μm and 10 μm aluminum-filled polyimide composites, respectively. Even though the dielectric constant of polyimide and bisphenol-A is the same, i.e. 3.5, the dielectric constant of their composites is quite different. At the same filler loading, the polyimide-aluminum composites show a lower dielectric constant as well as a lower dissipation factor (~0.01) when compared to the epoxy-aluminum composites. The difference in the dielectric constant of polyimide composites and epoxy composites may be explained by the presence of an interphase layer between the polymer matrix and the aluminum particles. For a polymer-ceramic system, Vo et al. [161] found that its dielectric properties can not simply be predicted by the dielectric mixture laws, instead, should be determined by the polymer phase, filler phase, and an interphase region. This interphase region, where polymer chains surround and bond to each filler particle, shows unique electric and dielectric properties other than that of the polymer matrix and filler particles. For aluminum composites, the interaction of a polymer matrix with the aluminum

particles is dependent on the chemistry of the polymer backbone. Epoxy usually has strong interaction and adhesion with inorganic particles because of its epoxide functional groups, and polyimide has reasonably strong interaction with the inorganic particles as well, however its rigid backbone due to the existence of aromatic rings makes its adhesion to filler worse than epoxy. And the difference in the polymer-aluminum interaction may result in the change of the characteristics and thickness of the interphase layer in the polymer composites. Therefore, the dielectric behavior of composites based on two different polymer matrices can be different even though the dielectric constant of these two polymer matrices is the same.

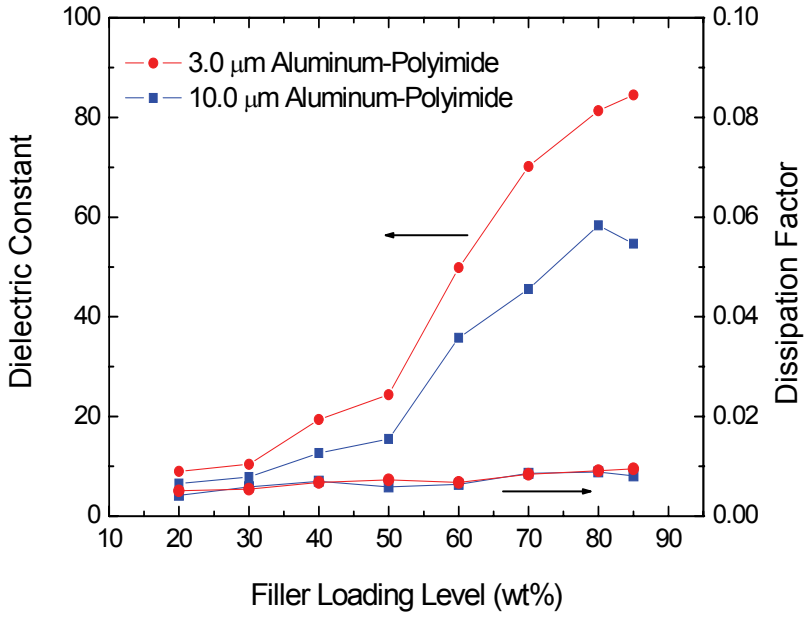

Figure 7.35 Dielectric properties of polyimide-aluminum composites as a function of filler loading.

7.3.4.3 Polynorbornene (PNB)/Aluminum Composites

Polynorbornene is produced through tightly controlled polymerization of bulky and cyclic monomers to form the saturated polymers by a transition metal catalyst. The chemical structure of polynorborne is shown in Figure 7.36 Because of its saturated

hydrocarbon non-polar chemical structure, this polymer has a low moisture absorption (<0.1%), a good thermal stability (Tg ~380ºC), a very low dissipation factor of about 0.0008, and a low dielectric constant of about 2.6. The DSC thermograph of polynorbornene in Fig.4 shows an exothermic peak at 218 ºC and an endothermic peak at 283 ºC, and the curing finishes at about 250 ºC. A multi-step curing procedure, including 250 ºC for 1 hour as the last step was then selected as the curing condition to ensure complete curing of the polynorbornene-aluminum composites.

Figure 7.37 illustrates the dielectric properties of polynorbornene-aluminum composites as a function of filler loading. The maximum dielectric constants obtained are 32 and 21 for 3 μm and 10 μm aluminum-filled polynorbornene composites, respectively. The dissipation factor of polynorbornene-aluminum is very low too, i.e. less than 0.01.

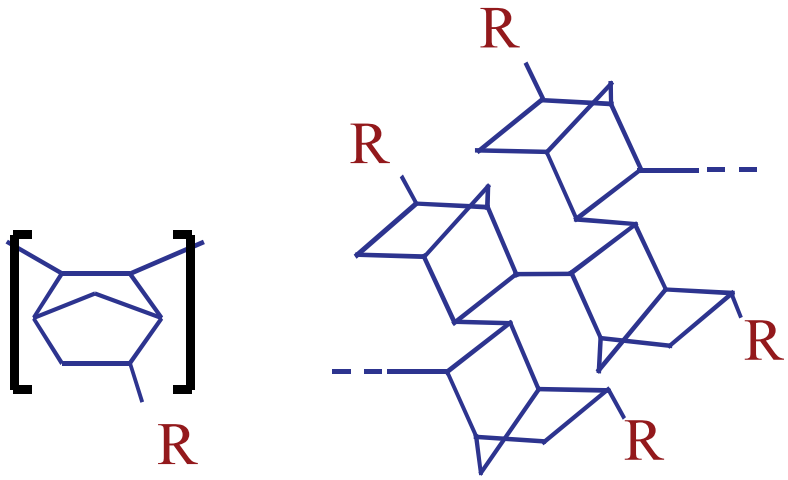

Figure 7.36 Chemical structure of polynorbornene.

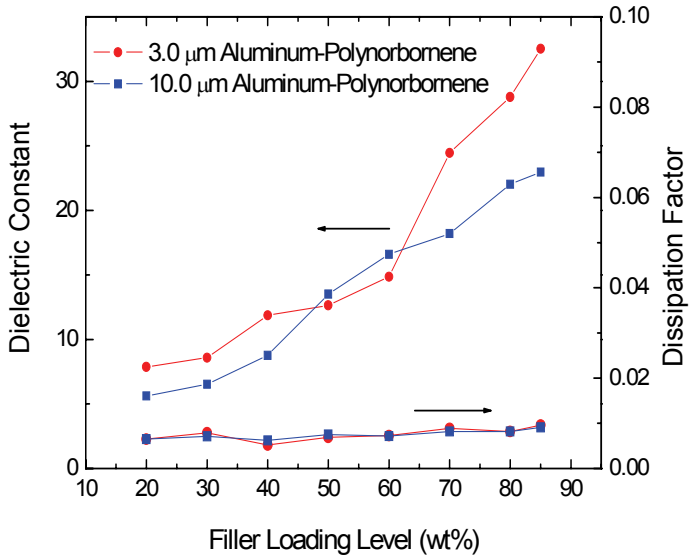

Figure 7.37 Dielectric properties of polynorbornene-aluminum composites as a function of filler loading.

7.3.4.4 Benzocyclobutene (BCB)/Aluminum Composites

Photosensitive BCB has been developed as a thin film dielectric for microelectronics applications. It has a low dissipation factor of 0.0007 and a low dielectric constant of about 2.72. The DSC thermograph of BCB in Figure 7.33 shows a curing peak at 262 ºC. The thermal curing of BCB includes two steps. The first step involves thermally activated ring opening of BCB to form an *o*-quinodimethane, which then reacts with residue alkene in the polymer to form tri-substituted tetrahydronaphthalene. Since both *o*-quinodimethane and tetrahydronaphthalene can easily be oxidized by oxygen, a relatively low curing temperature of 260 ºC (less than the curing peak temperature in DSC thermograph) for 1 hour was selected as the curing condition for BCB-aluminum composites. The composites were cured under nitrogen purging in a Lindberg furnace. However, the aluminum filler particles seemed incompatible with BCB, because the coated composite thin films were often found to

flake-off during processing, even if an adhesion promoter (AP3000) was used as the primer for the films.

Figure 7.38 shows the dielectric properties of BCB-aluminum composites as a function of filler loading. The maximum dielectric constants obtained are 42 and 29 for 3 μm and 10 μm aluminum-filled BCB composites, respectively, which is higher than that of silicone-aluminum composites. However, the dissipation factor of BCB composites (~0.02) is also much higher than that of silicone composites, although these two polymers themselves have similar dissipation factors. This is probably due to the oxidation of the BCB reactant group by a small amount of oxygen present in the curing tube, and the increased polarity from oxidized groups may lead to the relatively higher dissipation factor of BCB composites.

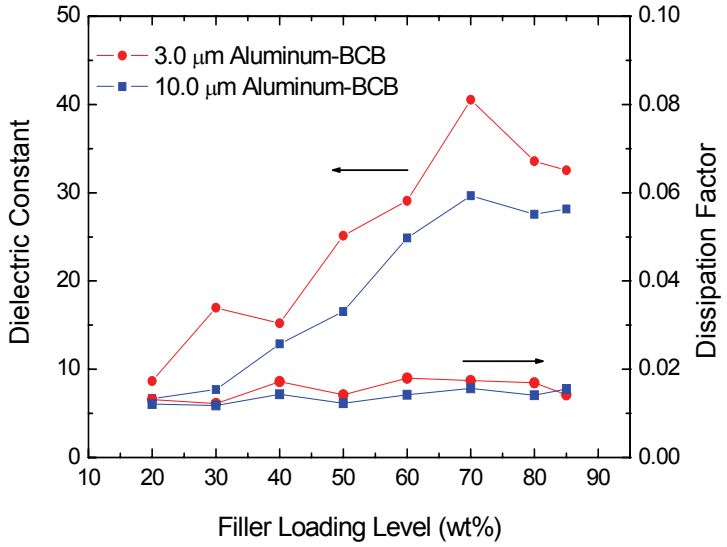

Figure 7.38 Dielectric properties of BCB-aluminum composites as a function of filler loading.

7.3.4.5 Frequency Dependence of the Dielectric Behavior

Study of the frequency response of a dielectric material can facilitate the understanding and application of this material. In this work, the frequency responses of

aluminum composites based on silicone, polyimide, polynorbornene, and BCB were characterized and compared with that of the epoxy-based composites, as epoxy-based composites such as epoxy-ceramic composites are the most commonly used dielectric materials for embedded capacitors in the printed circuit board industry. Figure 7.39 shows the frequency dependence of the dielectric constant of 3.0 μm aluminum composites based on epoxy, silicone, polyimide, polynorbornene, and BCB. All of the composites have the same filler loading of 80 wt%. At the same filler loading of 80%, a higher dielectric constant can be obtained with epoxy as the matrix than with other polymer matrices. And the decrease of the dielectric constant as frequency increases is more significant in epoxy-based composite than in other polymer-based composites, too. However, in general the dielectric constant of all aluminum composites only slightly decreases with the increase of frequency. Such a frequency independence behavior is consistent with the dielectric properties of percolative ceramic-metal composites [104].

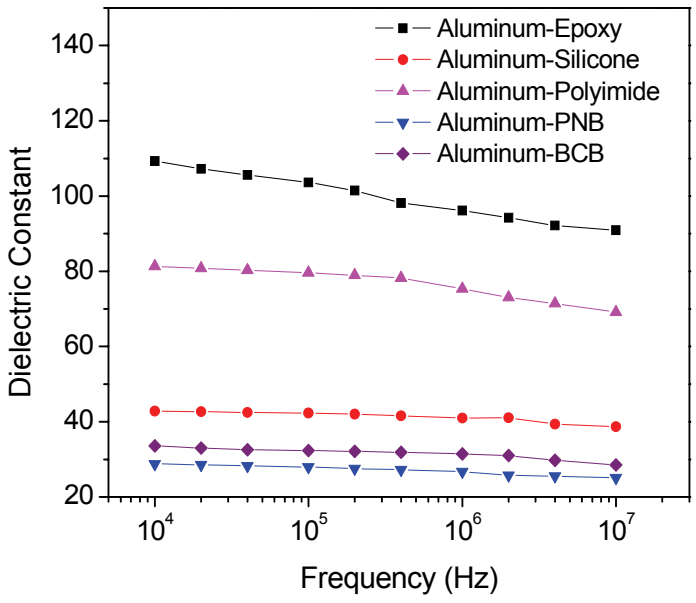

Figure 7.39 Frequency dependence of the dielectric constant of aluminum composites based on epoxy, silicone, polyimide, polynorbornene, and BCB.

7.3.4.6 Thermo-Mechanical Properties of Aluminum Composites

Reliability of a component is always a big concern when one applies it to an electronic system. For embedded passives, the coefficient of thermal expansion (CTE) of the materials is particularly important, because the passives are usually laminated as a thin/thick film inside of a board. The CTE mismatch between neighboring layers can easily cause delamination and thus lead to the system failure. Because the printed circuit boards are often processed at temperature up to around 200 ºC, in this work the thermo-mechanical properties of aluminum composites were characterized by a TMA at temperature up to 200 ºC. From the studies in previous sections, it was found that the epoxy-based and polyimide-based composites can have much higher dielectric constant than the composites based on other polymer matrices. Moreover, the majority of printed circuit board is based on epoxy or polyimide (e.g. high power RF application due to its lower dissipation factor). As such, in this work the TMA studies were focused on materials with epoxy and polyimide as the matrices. Figure 7.40 illustrates the TMA characterization of the thermomechanical properties of bis-phenol A epoxy, polyimide, 80 wt% 3 μm aluminum-epoxy composite, and 80 wt% 3 μm aluminum-polyimide composite. Table 7.4 lists the coefficients of thermal expansion and glass transition temperatures of all four formulations according to Figure 7.40. In the table, α_1 is commonly called CTE of a material, which is the coefficient of thermal expansion below the glass transition temperature; α_2 is the coefficient of thermal expansion above the glass transition temperature. The aluminum-filled composites have much lower CTEs than their corresponding polymer matrices. At 80 wt% filler loading, the CTEs of the epoxy-based composite and polyimide-based composite are about 29.94 μm/mºC and 28.95 μm/mºC, respectively, which are desirable for embedded passive applications, because these numbers are very close to the CTE of a PCB board, i.e. 16-24 μm/mºC. The α_2 and Tg of polyimide and its composites are not available because the measurement

temperatures (up to 200ºC) are much lower than the glass transition temperature of polymide, which is typically around 350 ºC.

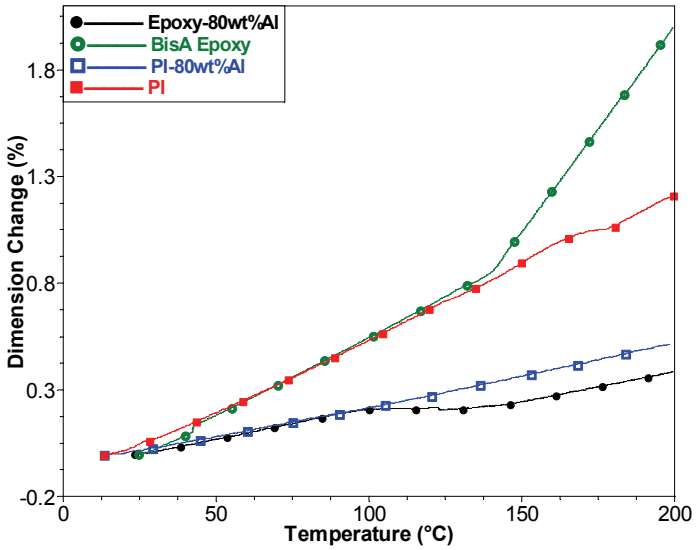

Figure 7.40 TMA characterization of the thermomechanical properties of bisphenol-A epoxy, polyimide, 80 wt% 3 μm aluminum-epoxy composite, and 80 wt% 3 μm aluminum-polyimide composite.

Table 7.4 Coefficients of thermal expansion and glass transition temperatures of Bisphenol-A epoxy, polyimide, and their aluminum composites.

	α_1 (μm/m °C)	α_2 (μm/m °C)	Tg (°C)
Epoxy	74.15	192.5	139.75
80wt%Al-Epoxy	29.94	28.27	132.74
PI	69.66	N/A	N/A
80wt%Al-PI	28.95	N/A	N/A

7.4 Conclusions

A novel high dielectric constant composite material was developed by using self-passivation aluminum as the filler. The self-passivated insulating aluminum oxide layer on the aluminum metallic core showed significant effects on the electric and dielectric properties of the corresponding aluminum composites. With the insulating aluminum oxide layer, a high loading level of aluminum can be used while the composite materials continued to be insulating. For composites containing 80 wt% 3.0 μm aluminum, a dielectric constant of 109 and a low dissipation factor of about 0.02 (@10 KHz) were achieved. Aluminum composites had good reliability as shown in the 85/85 aging test, and good adhesion towards copper laminated substrate as shown in the die shear measurement. Ouchiyama and Tanaka's model was used to calculate the theoretical maximum packing fraction of bimodal system of spheres. Based on this calculation, rheology studies were performed to find the optimum bimodal filler volume fraction ratio that leads to the best packing efficiency of bimodal fillers. It was found that the viscosity of polymer composites showed a minimum at optimum bimodal filler ratio. The minimum shear viscosity occurred at a bimodal filler volume fraction ratio 76/24 for system with 10.0 μm plus 3.0 μm aluminum, at a bimodal filler ratio 80/20 for system with 10.0 μm plus 100nm aluminum, and at a bimodal filler ratio 79/21 for system with 3.0 μm plus 100nm aluminum. Such bimodal filler volume fraction ratios can provide the highest filler loading for the specific systems. Using the optimized bimodal filler volume fraction ratio from rheology study, the highest dielectric constant obtained at 10 KHz was 88 for the system filled with 10.0 μm plus 3.0 μm aluminum, 136 for system filled with 10.0 μm plus 100 nm aluminum, and 160 for system filled with 3.0 μm plus100 nm aluminum. To enhance the dielectric properties and processibility of polymer/aluminum composites, the aluminum particle surface was modified with an epoxide-functionalized silane coupling agent. FTIR and TGA characterization showed that the silane coupling

agent was successfully grafted on the aluminum particle surface. Rheology properties of polymer/aluminum composites were studied with a stress rheometer. It was found that the coupling agent treatment can significantly reduce the viscosity of the aluminum composites, which indicates coupling agent treatment can improve the processibility of aluminum composites at high filler loading levels. At the same filler loading level, composites with the coupling agent-treated aluminum particles showed a higher dielectric constant. The microstructures of aluminum composites showed that a coupling agent treatment can improve the aluminum particle distribution and thereby enhancing the dielectric constant of aluminum composites. Study of frequency responses showed that the dielectric constant of aluminum composites is almost independent of the measurement frequencies, whereas the dissipation factor can increase dramatically as the frequency decreases below 1 Hz, due to the effect of electrode polarization. The dielectric constant of aluminum composites increases with the temperature. Low loss polymers such as silicone, polyimide, polynorbornene, and benzocyclobutene (BCB), were explored as the matrices for the aluminum composites. It is found that the polymer matrices can significantly change the dielectric properties of the aluminum composites. A polymer matrix with a lower dielectric constant generally results in a lower dielectric constant of its aluminum composites. In this regard, polymer-aluminum composites have a similar dielectric characteristic as polymer-ceramic composites. The dielectric loss of aluminum composites can also be slightly reduced with these lower loss polymers. Because of the core-shell structure of the self-passivated aluminum filler, the electrical behavior of its composites is highly dependent on the polymer matrices, which accounts for the reduced dissipation factor with lower loss polymers. Aluminum-filled composites also have a low coefficient of thermal expansion, which is desirable for embedded capacitor applications.

CHAPTER 8

CONCLUSIONS AND FUTURE WORK RECOMMENDATION

8.1 Conclusions

This work focuses on the materials design, development and processing of polymer-based dielectric nanocomposites for high performance embedded capacitor applications. The methodology of this approach is to combine the advantages of the polymer and the filler to satisfy the fabrication (low-temperature processability), dielectric (high dielectric constant), electrical (low leakage and high breakdown), and mechanical (good adhesion and thermal stress reliability) requirements for embedded capacitors.

Polymer-ceramic high-κ nanocomposite formulations were systematically investigated in order to obtain high dielectric constant ($\kappa>50$) nanocomposites at the lowest filler loading for embedded capacitor applications. It was found that material design and processing were critical. The addition of chelating agent can effectively improve the dielectric constant of the epoxy varnish, which resulted in the enhancement of the dielectric constant of its BT nanocomposites. Bimodal fillers can increase the dielectric constant of BT nanocomposites by enhancing the packing efficiency of BT nanoparticles. A proper amount of dispersing agent was essential in order to obtain high dielectric constant nanocomposites. With 5 wt% phosphate dispersing agent, a high dielectric constant of about 58 was obtained in the 50 vol% bimodal BT nanocomposite. Acidic phosphate ester dispersing agent can effectively improve the dispersion and dielectric constant of epoxy-barium titanate nanocomposites, however, the incorporation of phosphate ester led to the reduction of adhesion of nanocomposites to Cu substrate.

To improve the adhesion of epoxy-BT nanocomposites whist keeping the high dielectric constant of BT nanocomposites provided by the dispersing agent, the BT nanoparticles were refluxed and functionalized with acidic phosphate ester before being formulated in the epoxy matrix. Thermogravimetric Analyzer (TGA) and Fourier Transformed Infrared Spectroscopy (FTIR) showed that the phosphate ester was chemically bonded on the particle surface. It was found the filler surface functionalization can significantly improve the adhesion of nanocomposites to Cu substrate. The nanocomposites with functionalized filler showed a high dielectric constant of 45.6, and successfully passed the high temperature thermal stress reliability test.

To further improve the reliability of polymer-ceramic nanocomposites at high filler loadings, the epoxy matrix was modified with a secondary rubberized epoxy, which formed isolated flexible domains (island) in the continuous primary epoxy phase (sea). The effects of sea-island structure on the thermal mechanical properties, adhesion, and thermal stress reliability of embedded capacitors were systematically evaluated. The optimized, rubberized nanocomposite formulations had a high dielectric constant above 50 and successfully passed the stringent thermal stress reliability test. A high breakdown voltage of 89 MV/m and a low leakage current of 1.9×10^{-11}A/cm^2 were measured in the large area thin film capacitors.

A novel, photodefinable, high dielectric constant composite material was developed. It consisted of SU8 as the polymer matrix and barium titanate (BT) nanoparticles as the filler. It was found that the smaller BT nanoparticles had stronger UV absorbance at the exposure wavelength, and thereby led to smaller photopolymerization thicknesses in the composite photoresist. As the BT filler loading increased, the photopolymerization thickness decreased as well because of the absorption of BT nanoparticles. The SU8 composite photoresist showed a high dielectric constant at high BT filler loadings. The BT nanoparticle size does not have significant effect on the

dielectric properties of composite photoresist. Embedded capacitors using the novel high dielectric constant SU8 composite photoresist were demonstrated on a flexible polyimide substrate by UV lithography method.

Carbon black-filled high dielectric constant composites were investigated as the candidate materials for embedded capacitors. Six different types of carbon blacks were investigated. With proper filler loading level and good dispersion, high dielectric constants over 1000 were observed for four out of the six types of carbon black. For a highly conductive carbon black CBD3, a high dielectric constant over 13,300 (@10 kHz) was achieved, and for a relatively low conductivity carbon black CBC2, a dielectric constant of about 2,300 (@10 kHz) was obtained. The filler loading level required to reach high dielectric constant in carbon black composites is much lower than that of ceramic composites, which enables the carbon black composites to posses good mechanical properties. Carbon black composites show a high frequency dependence, and the interfacial polarization in carbon black composites, which usually has a high frequency dependence, contributes significantly to the high dielectric constant of the composites.

Shear flow processing has been shown to have significant effect on the dispersion state of CNTs in epoxy composites. SEM observations show that the CNTs were aligned along the shear flow direction. Evolution of electrical conductivities with shear time suggests that the alignment of CNTs in epoxy composites was time dependent. The shear flow processed CNTs/epoxy composites showed a higher percolation threshold, and the scaling components were non-universal along different directions, which results in the anisotropic conductivities and dielectric properties in shear processed CNT/epoxy composites. The understanding of the effect of shear flow processing on the CNT dispersion state and the correlation of CNT orientation with anisotropic percolation behavior may help the development of CNT composites for applications where electrical and dielectric properties are desired.

An innovative low-cost high dielectric constant polymer-based composite that combines the advantages of polymer-ceramic and polymer-metal systems was developed for embedded capacitor application. This novel material uses low-cost self-passivated aluminum particles as the filler for the polymer composites. The thin self-passivated oxide layer forms a nanoscale insulating boundary outside of the metallic spheres, which has a dramatic influence on the electrical behavior of the resulting composites. The nanoscale insulating oxide layer allows the aluminum composites to have a high dielectric constant as a percolation system; on the other hand, the insulating oxide layer confines the electrons within an aluminum particle, thus keeping a very low loss of the composites. For composites containing 80 wt% 3.0 μm aluminum, a dielectric constant of 109 and a low dissipation factor of about 0.02 (@10 KHz) were achieved. Aluminum composites had good reliability as shown in the 85/85 aging test, and good adhesion towards copper laminated substrate as shown in the die shear measurement.

Ouchiyama and Tanaka's model was used to calculate the theoretical maximum packing fraction of bimodal system of spheres. Based on this calculation, rheology studies were performed to find the optimum bimodal filler volume fraction ratio that leads to the best packing efficiency of bimodal fillers. It was found that the viscosity of polymer composites showed a minimum at optimum bimodal filler ratio. The minimum shear viscosity occurred at a bimodal filler volume fraction ratio 76/24 for system with 10.0 μm plus 3.0 μm aluminum, at a bimodal filler ratio 80/20 for system with 10.0 μm plus 100nm aluminum, and at a bimodal filler ratio 79/21 for system with 3.0 μm plus 100nm aluminum. Such bimodal filler volume fraction ratios can provide the highest filler loading for the specific systems. Using the optimized bimodal filler volume fraction ratio from rheology study, the highest dielectric constant obtained at 10 KHz was 88 for the system filled with 10.0 μm plus 3.0 μm aluminum, 136 for system filled with 10.0 μm plus 100 nm aluminum, and 160 for system filled with 3.0 μm plus100 nm aluminum.

To enhance the dielectric properties and processibility of polymer/aluminum composites, the aluminum particle surface was modified with an epoxide-functionalized silane coupling agent. FTIR and TGA characterization showed that the silane coupling agent was successfully grafted on the aluminum particle surface. Rheology properties of polymer/aluminum composites were studied with a stress rheometer. It was found that the coupling agent treatment can significantly reduce the viscosity of the aluminum composites, which indicates coupling agent treatment can improve the processibility of aluminum composites at high filler loading levels. At the same filler loading level, composites with the coupling agent-treated aluminum particles showed a higher dielectric constant. The microstructures of aluminum composites showed that a coupling agent treatment can improve the aluminum particle distribution and thereby enhancing the dielectric constant of aluminum composites. Study of frequency responses showed that the dielectric constant of aluminum composites is almost independent of the measurement frequencies, whereas the dissipation factor can increase dramatically as the frequency decreases below 1 Hz, due to the effect of electrode polarization. The dielectric constant of aluminum composites increases with the temperature.

Low loss polymers such as silicone, polyimide, polynorbornene, and benzocyclobutene (BCB), were explored as the matrices for the aluminum composites. It is found that the polymer matrices can significantly change the dielectric properties of the aluminum composites. A polymer matrix with a lower dielectric constant generally results in a lower dielectric constant of its aluminum composites. In this regard, polymer-aluminum composites have a similar dielectric characteristic as polymer-ceramic composites. The dielectric loss of aluminum composites can also be slightly reduced with these lower loss polymers. Because of the core-shell structure of the self-passivated aluminum filler, the electrical behavior of its composites is highly dependent on the polymer matrices, which accounts for the reduced dissipation factor with lower loss

polymers. Aluminum-filled composites also have a low coefficient of thermal expansion, which is desirable for embedded capacitor applications.

8.2 Future Work Recommendation

8.2.1 Synthesis of Core-Shell Structured Nanoparticles for Ultrahigh-κ Nanocomposites

The dielectric composite filled with self-passivated aluminum particles is a remarkable high-κ material for embedded capacitor application, which has a high dielectric constant about 50 times higher than that of the polymer binder. To mimic the self-passivation nature of an aluminum particle for high-κ application, one may artificially passivate the nano metal particles to form a core-shell structure with a sol-gel or a hydrothermal coating method. The core and shell materials can be varied. With tailored nature and thicknesses of the insulating shell layer, one may adjust the dielectric constant, dissipation factor, and other electrical properties of the nano metal particles-filled composites. Increased dielectric constant could thus be achieved when compared to self-passivating aluminum composites, because the nature and thickness of the oxide layer may have dominant influence on the dielectric properties.

Core-shell structured nano particles can be synthesized via one-step or two-step synthetic route. Two-step synthetic route, where nano metal particles are synthesized first and subsequently transferred into another pot for growth of insulating shell layer, is a relatively easier approach to prepare core-shell nanoparticles. However, this multistep method is rather complicated and scale-up for mass production is difficult. As such, a one-step method, i.e. reducing noble metals in the presence of oxide-forming precursors, can be utilized to synthesize core-shell nanoparticles in a one-step process.

To minimize the equivalent series resistance (ESR) of embedded capacitors made of core-shell particle-filled nanocomposites, highly electrically conductive metal, such as silver, gold, and copper, can be chosen as core materials, which can be coated with various metal oxide shell materials. Insulating shell materials could be silicon dioxide, zirconium dioxide, and titanium dioxide, because of their easiness of shell formation via hydrolysis of the metal oxide precursors. Compared with aluminum nanoparticles whose native oxide has a dielectric constants of about 9, SiO_2 shell has a lower dielectric constant about 3.7-3.9 (κ of PECVD SiO_2 could be larger than 5.0), whereas ZrO_2 shell and TiO_2 shell have much higher dielectric constant about 12.5 and 110, respectively. It is interesting to know whether the dielectric constant of the oxide shell will significantly influence the dielectric constant of the nanocomposites, provided that all the other conditions are the same. Apart from oxide shell, ferroelectric ceramics such as barium titanate, strontium titanate, barium strontium titanate, etc. could be synthesized and deposited on nano metal particle surfaces to prepare core-shell nanoparticles. Depending on its crystallite size and crystal structure, $BaTiO_3$ has a high dielectric constant up to 5,000. To prepare $BaTiO_3$ shell for core-shell structure nanoparticles, sol-gel and hydrothermal method are preferred due to their low equipment cost and ease of producing uniform coverage on the nano metal particle surfaces. The dielectric behavior of barium titanate is strongly dependent on its grain size, because the grain size has a significant effect on the tetragonality of ceramic crystal structure. Therefore, various $BaTiO_3$ shell thicknesses can be deposited on the nano metal particles to study such effects.

Besides metal core, other core materials such as carbon black can be investigated as well. Carbon black composites have high dielectric constant but also high dielectric loss. By forming insulating oxide shell layer out of carbon black core, it is expected that the dielectric loss of its composite will be reduced.

8.2.2 Passivating Conductive Core with Self Assembled Monolayers (SAMs) and High-κ Ceramic Nano Clusters

Another approach to mimic self-passivation nature of an aluminum particle is to form a core-shell structure with a self assembled monolayer (SAM) coating. Organic mono-functional SAM compounds coating on metal particles and ceramic layer formation on the SAM-coated metal particles are recommended.

Mono-functional SAM compounds can be used to form a passivated layer. Thiol, carboxylate, cyanide and cyanate groups are candidates for the functional end group; and the other end could be a non-functional hydrophobic group such as methyl or benzene. Table 8.1 gives some examples of mono-functional SAM compounds that can be studied.

Table 8.1 Mono-functional SAM compound candidates

	Type	Chemical Name and Structure
1.	Perfluorothiols with various molecular chain lengths	Perfluorohexanethiol $C_6H_5F_9S$
		Perfluorooctanethiol $C_8H_5F_{13}S$
		Perfluorodecanethiol $C_{10}H_5F_{17}S$
2.	Fluorinated carboxylic acids	Trifluoropropioni acid CF_3CH_2COOH
		Trifluorobutyric acid $CF_3CH_2CH_2COOH$
3.	Thiolphenol	Fluorothiophenol C_6H_4FSH

Di-functional SAM compounds wcan be used as well. One functional end group can be a silane functional group that forms a strong covalent bond to a hydroxyl group on a ceramic nano cluster surface and on the other end can be thiol, carboxylate, cyanide or cyanate that possesses high affinity to the metals such as Ag, Cu, Pt, Pd or Au. Therefore, di-functional SAM compounds not only can be as a passivation layer but also can be used as a coupling agent to bridge metal particles to ceramic particles. The ceramic particles can be in situ synthesized, with a smaller size than the nano metal particles so that they can assemble on SAM-coated nano metal particle surfaces, or these nano ceramic

particles can be separately synthesized and then transferred to react with the SAM-coated nano metal particles. Table 8.2 shows a list of some di-functional SAM compounds that can be used for high K nano ceramic cluster coating.

Table 8.2 Bi-functional SAM compound candidates

Name	Chemical Structure
(3-mercaptopropyl)trimethoxysilane	$HSCH_2CH_2CH_2Si(OCH_3)_3$
3-mercaptopropylmethyldimethoxysilane	$HSCH_2CH_2CH_2Si(OCH_3)_2CH_3$
(3-mercaptopropyl)trimethoxysilane	$HSCH_2CH_2CH_2Si(OCH_2CH_3)_3$
(mercaptomethyl)methyldiethoxysilane	$HSCH_2Si\ CH_3(OCH_2CH_3)_2$
(mercaptomethyl)dimethylethoxysilane	$HSCH_2Si(CH_3)_2(OCH_2CH_3)$
3-isocyanatopropyltriethoxysilane	$OCNCH_2CH_2CH_2$-$Si(O\ CH_2CH_3)_3$
2-(diphenylphosphino)ethyltriethoxysilane	$[Ph]_2$-$PCH_2CH_2Si(OCH_2CH_3)_3$
2-cyanoethyltriethoxysilane	$N{\equiv}C$-$CH_2CH_2Si(OC_2H_5)_3$
3-cyanopropyltrichlorosilane	$N{\equiv}C$-$CH_2CH_2CH_2SiCl_3$

8.2.3 Ternary High-κ Dielectric Composites for Embedded Capacitors

Polymer-ceramic composite has a low dielectric loss, but its dielectric constant is not as high as percolative composite and its adhesion to the substrate is not very good, either. On the other hand, a percolative composite has a high dielectric constant and a good adhesion to the substrates, but its dielectric loss is too high for high frequency applications.

To obtain high dielectric constant, low dielectric loss, and good adhesion in a dielectric composite, ternary high-κ dielectric composite filled with a non-conductive and a conductive filler is recommended. For example, ceramic filler can be used as the primary filler particles in the polymer dielectric composite; to enhance the dielectric constant and adhesion of the composite, a second-type of filler can be added to the formulation. The second-type filler is conductive and can be carbon black, conductive

polymer (e.g. polyaniline), nano metal particles (Ag, Au, Cu, and etc.). Only a small amount of the second-type filler will be used in the formulation in order to obtain low dielectric loss. By a careful design of the ternary dielectric systems, two types of fillers may provide a synergetic effect, leading to high-κ composites with a high dielectric constant, a low dielectric loss, and a good adhesion to the substrates.

APPENDIX A

AUTHOR'S AWARDS, PATENTS, AND PUBLICATIONS

A.1 Awards

[1] 12th Motorola-IEEE/CPMT Society Fellowship for Research on Electronic Packaging at the 54th Electronic Component & Technology Conference (ECTC),, IEEE Society and Motorola Inc., 2004.

[2] Applied Materials Fellowship, Applied Materials Foundation, 2004-2005.

[3] Finalist for the 13th Motorola-IEEE/CPMT Fellowship at the 55th Electronic Component & Technology Conference (ECTC), 2005.

[4] Outstanding Paper Award for "High-Performance Low Cost Metal-Filled Composite for Embedded Passive Applications", Jianwen Xu and C.P. Wong, 5th Electronics Packaging Technology Conference (EPTC), Singapore, December 2003.

A.2 Patents

[1] Yang Rao, C. P. Wong, Jianwen Xu, "High Dielectric Constant Polymer Composites and Methods of Preparation Thereof", US Patent 6,864,306, 2005.

[2] Jianwen Xu, C. P. Wong, "High Dielectric Constant and Low Loss Self-Passivation Metal-Filled Polymer Composites for Embedded Passive Applications" (US Patent Pending).

[3] Zhuqing Zhang, Lingbo Zhu, Yangyang Sun, Jianwen Xu, Hongjin Jiang, C.P. Wong, "Aligned Carbon Nanotube for Electrical and Thermal Interconnect" (US Patent Pending).

A.3 Publications

[1] C.P. Wong, Jianwen Xu, "Embedding", *Kirk-Othmer Encyclopedia of Chemical Technology*, 5th Edition, vol. 10, pp 1-29, John Wiley and Sons, New York, 2005.

[2] Jianwen Xu, C.P. Wong, "Low-loss Percolative Dielectric Composite", *Applied Physics Letters*, 87(8), 082907, 2005.

[3] Jianwen Xu, William Florkowski, Rosario A. Gerhardt, Kyoung-sik Moon, and C. P. Wong, "Shear Modulated Percolation in Carbon Nanotube Composites", *Journal of Physics Chemistry, B,* 110, 12289, 2006.

[4] Jianwen Xu, Christopher Tison, Kyoung-sik Moon and C.P. Wong, "A Novel Aluminum-Filled Composite for Embedded Passive Applications", *IEEE Transaction on Advanced Packaging*, 29(2), 295, 2006.

[5] Lingbo Zhu, Jianwen Xu, Yonghao Xiu, Yangyang Sun, Dennis W. Hess, and C. P. Wong, "Growth and Electrical Characterization of High-aspect-ratio Carbon Nanotube Arrays", *Carbon*, 44, 253, 2006.

[6] Jianwen Xu, C. P. Wong, "Effect of the Polymer Matrices on the Dielectric Behavior of a Percolative High-k Polymer Composite for Embedded Capacitor Applications", *Journal of Electronic Materials*, 35(5), 1087, 2006.

[7] Lingbo Zhu, Yonghao Xiu, Jianwen Xu, Prabhakar A. Tamirisa, Dennis W. Hess, and C. P. Wong, "Superhydrophobicity on Two-tier Rough Surfaces Fabricated by Controlled Growth of Aligned Carbon Nanotube Arrays Coated with Fluorocarbon", *Langmuir*, 21, 11208, 2005.

[8] Jianwen Xu, C.P. Wong, "Ultra High-k Polymers for Embedded Passive Applications", *Encyclopedia of Smart Materials*, John Wiley and Sons, New York, in press, 2005.

[9] Jianwen Xu, C. P. Wong, "Characterization and Properties of an Organic-Inorganic Dielectric Nanocomposite for Embedded Decoupling Capacitor Applications", *Composites, Part A*, in press (published online on March 10), 2006.

[10] Jianwen Xu, Swapan Bhattacharya, Pranabes Pramanik, and C.P. Wong, "High Dielectric Constant Polymer-Ceramic Nanocomposites at Moderate Filler Loadings for Embedded Capacitors", *Journal of Electronic Materials*, in press, 2006.

[11] Lingbo Zhu, Jianwen Xu, Yonghao Xiu, Dennis W. Hess, and C. P. Wong, "A Rapid Growth of Aligned Carbon Nanotube Films and High-Aspect-Ratio Arrays", *Journal of Electronic Materials*, 35, 195, 2006.

[12] Jianwen Xu, C.P. Wong, “High Dielectric Constant SU8 Composite Photoresist for Embedded Capacitors”, *Journal of Applied Polymer Science,* in press, 2006.

[13] Jianwen Xu, Kyoung-sik Moon, Swapan Bhattacharya, Pranabes Pramanik, and C.P. Wong, “Optimization of Epoxy-Barium Titanate Nanocomposites for High Performance Embedded Capacitor Components”, *IEEE Transactions on Component Packaging Technologies*, submitted, 2006.

[14] Jianwen Xu, C.P. Wong, “Effect of Filler Surface Functionalization on the Properties of High Dielectric Constant Epoxy-Barium Titanate Nanocomposites”, *Materials Chemistry and Physics,* submitted, 2005.

[15] Jianwen Xu, Michelle Wong, and C.P. Wong, “Super High Dielectric Constant Carbon Black-Filled Polymer Composites as Integral Capacitor Dielectrics”, *IEEE Transactions on Component Packaging Technologies*, submitted, 2004.

[16] Jun Li, Zhuqing Zhang, Jianwen Xu, CP Wong, “Smart Self-Cleaning Materials-Lotus Effect Surfaces”, *Encyclopedia of Smart Materials*, John Wiley and Sons, New York, in press, 2005.

[17] Jiongxin Lu, Kyoung-sik Moon, Jianwen Xu, and C. P. Wong, “Synthesis and Ddielectric Properties of Novel High-K Polymer Composites Containing In-situ Formed Silver Nanoparticles for Embedded Capacitor Applications," *Journal of Materials Chemistry*, 16, 1543, 2006.

[18] Lingbo Zhu, Jianwen Xu, Dennis W. Hess, and C. P. Wong, “Electrowetting of Aligned Carbon Nanotube Films”, *Journal of Physical Chemistry*, *B*, submitted, 2006.

[19] Lingbo Zhu, Jianwen Xu, Fei Xiao, Dennis. W. Hess, and C. P. Wong, “The Growth of Carbon Nanotube Stacks in the Kinetics-Controlled Regions”, *Carbon*, submitted, 2006.

[20] Kyoung-sik Moon, Yi Li, Jianwen Xu and C.P Wong, “Lead-Free Interconnect Technique by Using Variable Frequency Microwave”, *Journal of Electronic Materials*, 34(7), 1081, 2005.

[21] Brian C. Englert, Jianwen Xu and C. P. Wong, “Micro and Nanostructuring Through Templating and Plasma Etching Techniques to Produce Hydrophobic PDMS Materials”, *Langmuir*, submitted, 2006.

[22] Jun Li, Jianwen Xu, CP Wong, "Superhydrophobicity on Low Frequency Oxygen Plasma Treated Poly(tetrafluoroethylene)", submitted, *Surface and Interface Analysis*, 2004.

[23] Jun Li, Jianwen Xu, CP Wong, "Lotus Effect Thin Films as Anti-Stiction Coatings for MEMS", submitted, *IEEE Transactions on Component Packaging Technologies*, 2004.

[24] Jianwen Xu, Swapan Bhattacharya, Kyoung-sik Moon, Jiongxin Lu, Brian Englert and C.P. Wong, "Large-Area Processable High k Nanocomposite-Based Embedded Capacitors", *Proceedings of the 56th IEEE Electronic Components and Technology Conference*, pp 1520-1532, May 2006, San Diego, California.

[25] Lingbo Zhu,Yonghao Xiu, Jianwen Xu, Dennis W. Hess, and C.P. Wong, "Optimizing Geometrical Design of Superhydrophobic Surfaces for Prevention of Microelectromechanical System (MEMS) Stiction", *Proceedings of the 56th IEEE Electronic Components and Technology Conference*, pp 1129-1135, May 2006, San Diego, California.

[26] Jianwen Xu and C. P. Wong, "Photodefinable High-k SU8 Nanocomposite for Embedded Capacitors", *11th International Symposium on Advanced Packaging Materials: Processes, Properties and Interfaces*, March 2006, Atlanta, GA.

[27] Brian C. Englert, Jianwen Xu and C. P. Wong, "Microstructured and Plasma Etched PDMS Materials as Hydrophobic Materials", *11th International Symposium on Advanced Packaging Materials: Processes, Properties and Interfaces*, March 2006, Atlanta, GA.

[28] Jianwen Xu, C.P Wong, "High-K Nanocomposites with Core-Shell Structured Nanoparticles for Decoupling Applications", *Proceedings of the 55th IEEE Electronic Components and Technology Conference*, pp1234 - 1240, May 2005, Lake Buena Vista, Florida.

[29] Jianwen Xu, C.P Wong, "Dielectric Behavior of Ultrahigh-k Carbon Black Composites for Embedded Capacitor Applications", *Proceedings of the 55th IEEE Electronic Components and Technology Conference*, pp 1864 - 1869, May 2005, Lake Buena Vista, Florida.

[30] C.P. Wong, J. Xu, L. Zhu, Y. Li, H. Jiang, Y. Sun, J. Lu, H. Dong, "Recent Advances on Polymers and Polymer Nanocomposites for Advanced Electronic Packaging Applications", Proceedings of the 7th International IEEE Symposium on

High Density Packaging and Component Failure Analysis in Electronics Manufacturing (HDP'05), June 27-30, 2005, Shanghai, China.

[31] Lingbo Zhu, Jianwen Xu, Zhuqing Zhang, Dennis Hess, and C. P. Wong, "Lotus Effect Surface for Prevention of Microelectromechanical System (MEMS) Stiction", *Proceedings of the 55th IEEE Electronic Components and Technology Conference*, pp 1798 - 1801, May 2005, Lake Buena Vista, Florida.

[32] Lingbo Zhu, Yangyang Sun, Jianwen Xu, Zhuqing Zhang, Dennis Hess, and C. P.Wong, "Aligned Carbon Nanotubes for Electrical Interconnect and Thermal Management", *Proceedings of the 55th IEEE Electronic Components and Technology Conference*, pp 44 - 50, May 2005, Lake Buena Vista, Florida.

[33] Jianwen Xu, Fei Xiao, Jiongxin Lu and C.P Wong, "Study of Core-Shell Structured Nanoparticles for High-k Embedded Capacitor Dielectrics", *2nd International Workshop in Nano Bio-Packaging,* March 2005, Atlanta, GA.

[34] Jiongxin Lu, Kyoung-Sik Moon, Jianwen Xu and C. P. Wong, "Dielectric Loss Control of High-K Polymer Composites by Coulomb Blockade Effects of Metal Nanoparticles for Embedded Capacitor Applications", *10th International Symposium on Advanced Packaging Materials: Processes, Properties and Interfaces*, pp 237-242, March 2005, Irvine, CA.

[35] Jianwen Xu, C.P Wong, "Control of the Loss Factor of High-K Nano-composites with Low Loss Polymers", *Proceedings of the 54th IEEE Electronic Components and Technology Conference*, Vol. 1, pp496-506, June 2004, Las Vegas, NV.

[36] Jianwen Xu, C.P Wong, "Super High Dielectric Constant Carbon Black-Filled Polymer Composites as Integral Capacitor Dielectrics", *Proceedings of the 54th IEEE Electronic Components and Technology Conference*, Vol. 1, pp536-541, June 2004, Las Vegas, NV.

[37] Jianwen Xu and C.P. Wong, "Low Loss High-K Nano Composites as Integral Capacitor Dielectrics", *9th International Symposium on Advanced Packaging Materials: Processes, Properties and Interfaces*, pp158-170, March 2004, Atlanta, GA.

[38] Jun Li,; Jianwen Xu, Lianhua Fan, C.P, Wong, "Lotus Effect Coating and Its Application for Microelectromechanical Systems Stiction Prevention", *Proceedings of the 54thIEEE Electronic Components and Technology Conference*, Vol. 1, pp943-947, June 2004, Las Vegas, NV.

[39] Jianwen Xu and C.P Wong, "High Dielectric Constant Polymer Composites Filled with Nanostructured Carbon Black", *1st International Workshop in Nano Bio-Packaging,* March 2004, Atlanta, GA.

[40] Kyoung-sik Moon, Yi Li, Jianwen Xu and C.P Wong, "Lead-Free Solder Interconnect by Variable Frequency Microwave (VFM)", *Proceedings of the 54th IEEE Electronic Components and Technology Conference*, Vol. 2, pp1989-1995, June 2004, Las Vegas, NV.

[41] Haiying Li, Kyoung-Sik Moon, Yi Li, Lianhua Fan, Jianwen Xu, C.P Wong, "Reliability Enhancement of Electrically Conductive Adhesives in Thermal Shock Environment", *Proceedings of the 54th IEEE Electronic Components and Technology Conference*, Vol. 1, pp165-169, June 2004, Las Vegas, NV.

[42] Kyoung-sik Moon, Yi Li, Jianwen Xu and C.P Wong, "A Novel Technique for Lead-Free Soldering Process Using Variable Frequency Microwave (VFM)", *9th International Symposium on Advanced Packaging Materials: Processes, Properties and Interfaces*, pp 118-125, March 2004, Atlanta, GA.

[43] Haiying Li, Kyoung-Sik Moon, Yi Li, Lianhua Fan, Jianwen Xu, C.P Wong, "Physical Properties and Thermocycling Performance of Electrically Conductive Adhesives (ECAs) Modified by Flexible Molecules", *9th International Symposium on Advanced Packaging Materials: Processes, Properties and Interfaces*, pp 45-50, March 2004, Atlanta, GA.

[44] Jianwen Xu, C.P. Wong, "Development of a Novel Aluminum-filled Composite for Embedded Passive Applications", *Proceedings of 53rd Electronic Components & Technology Conference*, pp 173-181, May 2003, New Orleans, LA.

[45] Jianwen Xu, C.P. Wong, "High Performance and Low Cost Nano-composite for Decoupling Capacitor Applications", *Proceedings of 3rd International IEEE Conference on Polymers and Adhesives in Microelectronics and Photonics*, pp 337-344, October 2003, Montreux, Switzerland.

[46] Jianwen Xu, C.P. Wong, "High Performance Low cost Metal-Filled Composites for Embedded Passive Applications", *Proceedings of 5th Electronics Packaging Technology Conference*, pp544-550, December 2003, Singapore.

[47] Kyoung-sik Moon, Suresh Pothukuchi, Jianwen Xu, C.P Wong, "Dielectric Properties of Polymer Composite as Integral Capacitor", *Proceedings of 52nd*

Electronic Components & Technology Conference, pp 1748-1752, May 2002, San Diego, CA.

[48] Kyoung-sik Moon, Suresh Pothukuchi, Jianwen Xu, C.P Wong, "Study of Dielectric Properties of Polymer Composite as Integral Capacitor", 8th *International Symposium on Advanced Packaging Materials: Processes, Properties and Interfaces*, pp238-242, March 2002, Atlanta, GA.

REFERENCES

[1] R. R. Tummala, E. J. Rymaszewski, and A. G. Klopfenstein, "Microelectronics Packaging Handbook," 2nd Edition ed. Massachusetts: Kluwer Academic Publishers, 1999.

[2] J. H. Lau, *Chip on Board Technologies for Multichip Modules*. New York: Van Nostrand Reinhold, 1994.

[3] M. T. Bohr, "Interconnect scaling - The real limiter to high performance ULSI," *Solid State Technology*, vol. 39, pp. 105, 1996.

[4] B. Schwartz, "Microelectronics Packaging .2.," *American Ceramic Society Bulletin*, vol. 63, pp. 577-581, 1984.

[5] Prismark, "The Electronic Industry Report," New York 2004.

[6] R. Ladew and A. Makl, "Integrating Passvie Components," presented at ISHM, 1995.

[7] "2004 International Electronics Manufacturing Initiative (iNEMI) Roadmap."

[8] H. Kapdia, "Evaluating the Need for Integrated Passive Substrates," *Advancing Microelectronics*, vol. 26, pp. 12, 1999.

[9] R. K. Ulrich and L. W. Schaper, "Integrated Passive Component Technology." New Jersey: John Wiley & Sons, 2003.

[10] P. Chahal, R. R. Tummala, M. G. Allen, and M. Swaminathan, "A novel integrated decoupling capacitor for MCM-L technology," *IEEE Transactions on Components Packaging and Manufacturing Technology Part B-Advanced Packaging*, vol. 21, pp. 184-193, 1998.

[11] J. P. Shaffer, A. Saxena, S. D. Antolovich, T. H. J. Sanders, and S. B. Warner, *The Science and Design of Engineering Materials*. Boston: McGraw-Hill, 1999.

[12]R. J. Jensen, in *Microelectronic Processing: Chemical Engineering Aspects*, *Chap. 9*, D. W. Hess and K. F. Jensen, Eds. Washington, DC: American Chemical Society, 1989.

[13] W. D. Kingery, H. K. Bowen, and D. R. Uhlmann, *Introduction to Ceramics*. New York: Wiley, 1976.

[14] M. A. Omar, in *Elementary Solid State Physics*, *Chap. 8*. Reading, MA: Addision-Wesley, 1975.

[15] L. L. Hench and J. K. West, in *Principles of Electronic Ceramics*, *Chap. 8*. New York: Wiley, 1990.

[16] R. Kambe, R. Imai, T. Takada, M. Arakawa, and M. Kuroda, "MCM Substrate with High Capacitance," *IEEE Transactions on Components Packaging and Manufacturing Technology Part B-Advanced Packaging*, vol. 18, pp. 23-27, 1995.

[17] G. B. Alers, R. B. van Dover, L. F. Schneemeyer, L. Stirling, C. Y. Sung, P. W. Diodato, R. Liu, Y. H. Wong, R. M. Fleming, D. V. Lang, and J. P. Chang, "Advanced amorphous dielectrics for embedded capacitors," presented at *IEEE International Electron Devices Meeting (IEDM)*, Washington, DC, 1999.

[18] M. Tsukada, J. Cross, M. Nishizawa, K. K., and N. Kamehara, "Preparation and Characterization of Dielectric Thin Films for Decoupling Capacitors," presented at ICEMCM, 1995.

[19] T. Takken and D. Tckerman, "Integral Decoupling Capacitance Reduces Multichip Module Ground Bounce," presented at IEEE Multi-Chip Module Conference, 1993.

[20] H. M. Clearfield, S. Wijeyesekera, E. Logan, A. Luu, D. Gieser, C. Lin, and J. Jing, "Integrated passive devices using Al/BCB thin films," presented at IMAPS Multichip Module, 1998.

[21] S. Yamamichi, P. Y. Lesaicherre, H. Yamaguchi, K. Takemura, S. Sone, H. Yabuta, K. Sato, T. Tamura, K. Nakajima, S. Ohnishi, K. Tokashiki, Y. Hayashi, Y. Kato, Y. Miyasaka, M. Yoshida, and H. Ono, "An ECR MOCVD (Ba,Sr)TiO3 based stacked capacitor technology with RuO2/Ru/TiN/TiSix storage nodes for Gbit-scale DRAMs," presented at International Electron Devices Meeting (IEDM), Washington, DC, 1995.

[22] S. Dey, "IMAPS Advanced Passive Technology Workshop," Braselton, GA, 1997.

[23] Z. Nami, O. Misman, A. Erbil, and G. S. May, "Effect of growth parameters on TiO2 thin films deposited using MOCVD," *Journal of Crystal Growth*, vol. 179, pp. 522-538, 1997.

[24] O. Misman, S. K. Bhattacharya, A. Erbil, and R. R. Tummala, "PWB compatible high value integral capacitors by MOCVD," *Journal of Materials Science-Materials in Electronics*, vol. 11, pp. 657-660, 2000.

[25] Y. B. Park, X. D. Li, G. J. Nam, and S. W. Rhee, "Effects of annealing in O2 and N2 on the microstructure of metal organic chemical vapor deposition Ta2O5 film and the interfacial SiO2 layer," *Journal of Materials Science-Materials in Electronics*, vol. 10, pp. 113-119, 1999.

[26] M. Nielsen and H. Cole, "Demonstration of Integral Passives on Double Sided Polyimide Flex," presented at International Conference on High-Density Interconnect and Systems Packaging, 2000.

[27] B. Hendrix and B. Stauf, "Low Temperature Process for High Density Thin Film Integrated Capacitors," presented at International Conference on High-Density Interconnect and Systems Packaging, 2000.

[28] D. Dimos, S. J. Lockwood, R. W. Schwartz, and M. S. Rodgers, "Thin-Film Decoupling Capacitors for Multichip Modules," *Ieee Transactions on Components Packaging and Manufacturing Technology Part A*, vol. 18, pp. 174-179, 1995.

[29] R. Heistand, "Solutions for passive integration," presented at IMAPS Advanced TechnologyWorkshop in Integrated Passives, Denver, CO, 1998.

[30] H. Kumazawa, S. Annen, and E. Sada, "Hydrothermal Synthesis of Barium-Titanate Fine Particles from Amorphous and Crystalline Titania," *Journal of Materials Science*, vol. 30, pp. 4740-4744, 1995.

[31] H. Kumazawa, T. Kagimoto, and A. Kawabata, "Preparation of barium titanate ultrafine particles from amorphous titania by a hydrothermal method and specific dielectric constants of sintered discs of the prepared particles," *Journal of Materials Science*, vol. 31, pp. 2599-2602, 1996.

[32] E. W. Shi, C. T. Xia, W. Z. Zhong, B. G. Wang, and C. D. Feng, "Crystallographic properties of hydrothermal barium titanate crystallites," *Journal of the American Ceramic Society*, vol. 80, pp. 1567-1572, 1997.

[33] S. Wada, T. Suzuki, and T. Noma, "Preparation of barium titanate fine particles by hydrothermal method and their characterization," *Journal of the Ceramic Society of Japan*, vol. 103, pp. 1220-1227, 1995.

[34] T. R. N. Kutty and P. Padmini, "Synthesis of polytitanates from Ba(OH)(2)-TiO2-H2O system through gel to crystallite conversion," *Journal of Materials Science Letters*, vol. 15, pp. 1973-1975, 1996.

[35] T. R. N. Kutty and P. Padmini, "Mechanism of Batio3 Formation through Gel-to-Crystallite Conversions," *Materials Chemistry and Physics*, vol. 39, pp. 200-208, 1995.

[36] K. Fukai, K. Hidaka, M. Aoki, and K. Abe, "Preparation and Properties of Uniform Fine Perovskite Powders by Hydrothermal Synthesis," *Ceramics International*, vol. 16, pp. 285-290, 1990.

[37] D. Balaraman, C. Jinwoo, V. Patel, P. M. Raj, I. R. Abothu, S. Bhattacharya, W. Lixi, M. Swaminathan, and R. Tummala, "Simultaneous switching noise suppression using hydrothermal barium titanate thin film capacitors," presented at 54th Electronic Components and Technology Conference, 2004.

[38] D. Balaraman, P. Markondeya Raj, S. Bhattacharya, and R. R. Tummala, "Novel hydrothermal processing of ceramic-polymer composites for integral capacitor applications," presented at 52nd Electronic Components and Technology Conference, 2002.

[39]R. Berry, P. Hall, and M. Harris, "Thin Film Technology." New Nork: Van Nostrand, 1968, pp. 271-288.

[40] D. Vermilyea, "Electronic Conduction in Anodic Films - Role of Forming Solution," *Journal of the Electrochemical Society*, vol. 112, pp. 1232-&, 1965.

[41] F. J. Burger, Cheseldi.Dm, and J. A. Moresi, "New High Performance Aluminum Electrolytic Capacitors," *Ieee Transactions on Parts Materials and Packaging*, vol. Pmp1, pp. S210-&, 1965.

[42] S. G. Byeon and Y. Tzeng, "Improved Oxide Properties by Anodization of Aluminum Films with Thin Sputtered Aluminum-Oxide Overlays," *Journal of the Electrochemical Society*, vol. 135, pp. 2452-2458, 1988.

[43] V. Surganov, "Planarized Thin-Film Inductors and Capacitors for Hybrid Integrated-Circuits Made of Aluminum and Anodic Alumina," *IEEE Transactions on Components Packaging and Manufacturing Technology Part B-Advanced Packaging*, vol. 17, pp. 197-200, 1994.

[44] H. Kapadia, H. Cole, M. Nielsen, and N. Krishnamurthy, "Necessary characterization of integral passives for high performance applications," presented at IMAPS Advanced Technology Workshop in Integrated Passives, Denver , CO, 1998.

[45] Y. Rao and C. P. Wong, "Material characterization of a high-dielectric-constant polymer-ceramic composite for embedded capacitor for RF applications," *Journal of Applied Polymer Science*, vol. 92, pp. 2228-2231, 2004.

[46] S. Yano, "Dielectric Relaxation and Molecular Motion in Poly(Vinylidene Fluoride)," *Journal of Polymer Science Part a-2-Polymer Physics*, vol. 8, pp. 1057-&, 1970.

[47] H. Kakutani, "Dielectric Absorption in Oriented Poly(Vinylidene Fluoride)," *Journal of Polymer Science Part a-2-Polymer Physics*, vol. 8, pp. 1177-&, 1970.

[48] P. Vasudevan, H. S. Nalwa, K. L. Taneja, and U. S. Tewari, "Pyroelectricity in Thiourea Formaldehyde Polymer," *Journal of Applied Physics*, vol. 50, pp. 4324-4326, 1979.

[49] Q. M. Zhang, V. Bharti, and X. Zhao, "Giant electrostriction and relaxor ferroelectric behavior in electron-irradiated poly(vinylidene fluoride-trifluoroethylene) copolymer," *Science*, vol. 280, pp. 2101-2104, 1998.

[50] T. C. Chung and A. Petchsuk, "Synthesis and properties of ferroelectric fluoroterpolymers with Curie transition at ambient temperature," *Macromolecules*, vol. 35, pp. 7678-7684, 2002.

[51] Z. Yu, C. Ang, L. E. Cross, A. Petchsuk, and T. C. Chung, "Dielectric and electroactive strain properties of poly(vinylidene fluoride-trifluoroethylene-chlorotrifluoroethylene) terpolymers," *Applied Physics Letters*, vol. 84, pp. 1737-1739, 2004.

[52] H. S. Nalwa, J. M. Sinha, and P. Vasudevan, "Synthesis and Electrical-Properties of Monomeric and Polymeric Iron-Phthalocyanines," *Makromolekulare Chemie-Macromolecular Chemistry and Physics*, vol. 182, pp. 811-816, 1981.

[53] H. S. Nalwa, L. R. Dalton, and P. Vasudevan, "Dielectric-Properties of Copper-Phthalocyanine Polymer," *European Polymer Journal*, vol. 21, pp. 943-947, 1985.

[54] N. Phougat and P. Vasudevan, "Electrocatalytic activity of some metal phthalocyanine compounds for oxygen reduction in phosphoric acid," *Journal of Power Sources*, vol. 69, pp. 161-163, 1997.

[55] N. Phougat, P. Vasudevan, Santosh, and A. K. Shukla, "Nafion(R)-Bound Carbon Electrodes Containing Transition-Metal Phthalocyanines for Oxygen Reduction in Solid-Polymer-Electrolyte Fuel-Cells," *Journal of Power Sources*, vol. 46, pp. 61-64, 1993.

[56] P. Vasudevan, N. Mann, Santosh, A. M. Kannan, and A. K. Shukla, "Electroreduction of Oxygen on Some Novel Cobalt Phthalocyanine Complexes," *Journal of Power Sources*, vol. 28, pp. 317-320, 1989.

[57] P. Vasudevan, N. Phougat, and A. K. Shukla, "Metal phthalocyanines as electrocatalysts for redox reactions," *Applied Organometallic Chemistry*, vol. 10, pp. 591-604, 1996.

[58] D. K. Das-Gupta and K. Doughty, "Polymer Ceramic Composite-Materials with High Dielectric-Constants," *Thin Solid Films*, vol. 158, pp. 93-105, 1988.

[59] D. Sinha and P. K. C. Pillai, "Hysteresis Behavior in Lead Zirconate Titanate Polyvinylidene Fluoride Composites," *Ferroelectrics*, vol. 76, pp. 459-467, 1987.

[60] D. Sinha and P. K. C. Pillai, "Ceramic-Polymer Composites as Potential Capacitor Material," *Journal of Materials Science Letters*, vol. 8, pp. 673-674, 1989.

[61] S. Ogitani, S. A. Bidstrup-Allen, and P. A. Kohl, "Factors influencing the permittivity of polymer/ceramic composites for embedded capacitors," *IEEE Transactions on Advanced Packaging*, vol. 23, pp. 313-322, 2000.

[62] V. Agarwal, P. Chahal, R. R. Tummala, and M. G. Allen, "Improvements and Recent Advances in Nanocomposite Capacitors Using a Colloidal Technique," presented at 48th Electronic Components & Technology Conference, 1998.

[63] Y. Rao, S. Ogitani, P. Kohl, and C. P. Wong, "Novel polymer-ceramic nanocomposite based on high dielectric constant epoxy formula for embedded capacitor application," *Journal of Applied Polymer Science*, vol. 83, pp. 1084-1090, 2002.

[64] H. Windlass, P. M. Raj, D. Balaraman, S. K. Bhattacharya, and R. R. Tummala, "Colloidal processing of polymer ceramic nanocomposite integral capacitors," *IEEE Transactions on Electronics Packaging Manufacturing*, vol. 26, pp. 100-105, 2003.

[65] R. E. Newnham, D. P. Skinner, and L. E. Cross, "Connectivity and Piezoelectric-Pyroelectric Composites," *Materials Research Bulletin*, vol. 13, pp. 525-536, 1978.

[66] L. E. Cross, R. E. Newnham, T. Gururaja, and W. Schulze, "Composite Piezoelectric Transducers," *American Ceramic Society Bulletin*, vol. 60, pp. 357-357, 1981.

[67] B. Tareev, *Physics of Dielectric Materials*. Moscow: Mir Publishers, 1979.

[68] G. Goodman, "*Ceramic Materials for Electronics*," R. Buchanan, Ed. New York: Marcel Dekker, 1986.

[69] W. R. Tinga, W. A. G. Voss, and D. F. Blossey, "Generalized Approach to Multiphase Dielectric Mixture Theory," *Journal of Applied Physics*, vol. 44, pp. 3897-3902, 1973.

[70] I. Krakovsky and V. Myroshnychenko, "Modeling dielectric properties of composites by finite-element method," *Journal of Applied Physics*, vol. 92, pp. 6743-6748, 2002.

[71] E. H. Kerner, "The Electrical Conductivity of Composite Media," *Proceedings of the Physical Society of London Section B*, vol. 69, pp. 802-807, 1956.

[72] R. Landauer, "The Electrical Resistance of Binary Metallic Mixtures," *Journal of Applied Physics*, vol. 23, pp. 779-784, 1952.

[73] R. D. Stoy, "Solution Procedure for the Laplace Equation in Bispherical Coordinates for 2 Spheres in a Uniform External-Field - Perpendicular Orientation," *Journal of Applied Physics*, vol. 66, pp. 5093-5095, 1989.

[74] R. D. Stoy, "Solution Procedure for the Laplace Equation in Bispherical Coordinates for 2 Spheres in a Uniform External-Field - Parallel Orientation," *Journal of Applied Physics*, vol. 65, pp. 2611-2615, 1989.

[75] P. Hedvig, "Ferroelectric Polymers," H. Nawla, Ed. New York: Marcel Dekker,, 1995.

[76] N. Jayasundere and B. V. Smith, "Dielectric-Constant for Binary Piezoelectric 0-3 Composites," *Journal of Applied Physics*, vol. 73, pp. 2462-2466, 1993.

[77] S. K. Bhattacharya and R. R. Tummala, "Next generation integral passives: materials, processes, and integration of resistors and capacitors on PWB substrates," *Journal of Materials Science-Materials in Electronics*, vol. 11, pp. 253-268, 2000.

[78] M. R. Leonard and A. Safari, "Crystallite and Grain Size Effects in BaTiO3," *Proceedings of the Tenth IEEE International Symposium on Applications of Ferroelectrics*, vol. vol.2, pp. 1003 - 1005 1996.

[79] M. P. McNeal, S. J. Jang, and R. E. Newnham, "The effect of grain and particle size on the microwave properties of barium titanate (BaTiO3)," *Journal of Applied Physics*, vol. 83, pp. 3288-3297, 1998.

[80] G. Arlt, D. Hennings, and G. Dewith, "Dielectric-Properties of Fine-Grained Barium-Titanate Ceramics," *Journal of Applied Physics*, vol. 58, pp. 1619-1625, 1985.

[81] P. Papet, J. P. Dougherty, and T. R. Shrout, "Particle and Grain-Size Effects on the Dielectric Behavior of the Relaxor Ferroelectric Pb(Mg1/3Nb2/3)O3," *Journal of Materials Research*, vol. 5, pp. 2902-2909, 1990.

[82] Y. Rao, A. Takahashi, and C. P. Wong, "Di-block copolymer surfactant study to optimize filler dispersion in high dielectric constant polymer-ceramic composite," *Composites Part a-Applied Science and Manufacturing*, vol. 34, pp. 1113-1116, 2003.

[83] B. Ellis, "Chemistry and Technology of Epoxy Resins." Glasgow: Blackie Academic & Professional, 1993.

[84] C. A. May, "Epoxy Resins: Chemistry and Technology," 2nd ed. New York: Marcel Dekker, Inc., 1988.

[85] L. Matejka, J. Lovy, S. Pokorny, K. Bouchal, and K. Dusek, "Curing Epoxy-Resins with Anhydrides - Model Reactions and Reaction-Mechanism," *Journal of Polymer Science Part a-Polymer Chemistry*, vol. 21, pp. 2873-2885, 1983.

[86] Z. Q. Zhang and C. P. Wong, "Study on metal chelates as catalysts of epoxy and anhydride cure reactions for no-flow underfill applications," *Polymers for Microelectronics and Nanoelectronics*, vol. 874, pp. 264-278, 2004.

[87] E. P. Plueddemann, *Silane Coupling Agents*. New York: Plenum Press, 1982.

[88] S. K. Bhattacharya and R. R. Tummala, "Integral passives for next generation of electronic packaging: application of epoxy/ceramic nanocomposites as integral capacitors," *Microelectronics Journal*, vol. 32, pp. 11-19, 2001.

[89] Y. Rao, J. M. Qu, T. Marinis, and C. P. Wong, "A precise numerical prediction of effective dielectric constant for polymer-ceramic composite based on effective-medium theory," *IEEE Transactions on Components and Packaging Technologies*, vol. 23, pp. 680-683, 2000.

[90] N. Ouchiyama and T. Tanaka, "Porosity Estimation for Random Packings of Spherical-Particles," *Industrial & Engineering Chemistry Fundamentals*, vol. 23, pp. 490-493, 1984.

[91] N. Ouchiyama and T. Tanaka, "Estimation of the Average Number of Contacts between Randomly Mixed Solid Particles," *Industrial & Engineering Chemistry Fundamentals*, vol. 19, pp. 338-340, 1980.

[92] R. K. Gupta and S. G. Seshadri, "Maximum Loading Levels in Filled Liquid-Systems," *Journal of Rheology*, vol. 30, pp. 503-508, 1986.

[93] J. G. Kloosterboer, "Network Formation by Chain Crosslinking Photopolymerization and Its Applications in Electronics," *Advances in Polymer Science*, vol. 84, pp. 1-61, 1988.

[94] F. Boey, S. K. Rath, A. K. Ng, and M. J. M. Abadie, "Cationic UV cure kinetics for multifunctional epoxies," *Journal of Applied Polymer Science*, vol. 86, pp. 518-525, 2002.

[95] C. G. K. Malek, "SU8 resist for low-cost X-ray patterning of high-resolution, high-aspect-ratio MEMS," *Microelectronics Journal*, vol. 33, pp. 101-105, 2002.

[96] M. McNie, D. King, C. Vizard, A. Holmes, and K. W. Lee, "High aspect ratio micromachining (HARM) technologies for microinertial devices," *Microsystem Technologies*, vol. 6, pp. 184-188, 2000.

[97] V. Seidemann, S. Butefisch, and S. Buttgenbach, "Fabrication and investigation of in-plane compliant SU8 structures for MEMS and their application to micro valves and micro grippers," *Sensors and Actuators a-Physical*, vol. 97-8, pp. 457-461, 2002.

[98] R. Guerre, C. Hibert, Y. Burri, P. Fluckiger, and P. Renaud, "Fabrication of vertical digital silicon optical micromirrors on suspended electrode for guided-wave optical switching applications," *Sensors and Actuators a-Physical*, vol. 123-24, pp. 570-583, 2005.

[99] N. Damean, B. A. Parviz, J. N. Lee, T. Odom, and G. M. Whitesides, "Composite ferromagnetic photoresist for the fabrication of microelectromechanical systems," *Journal of Micromechanics and Microengineering*, vol. 15, pp. 29-34, 2005.

[100] P. F. Jacobs, "Rapid prototyping & manufacturing : fundamentals of stereolithography ", 1992.

[101] S. Jiguet, A. Bertsch, H. Hofmann, and P. Renaud, "Conductive SU8 photoresist for microfabrication," *Advanced Functional Materials*, vol. 15, pp. 1511-1516, 2005.

[102] Kirkpatr.S, "Nature of Percolation Channels," *Solid State Communications*, vol. 12, pp. 1279-1283, 1973.

[103] R. Zallen, *The Physics of Amorphous Solids*. New York: Wiley, 1983.

[104] C. Pecharroman and J. S. Moya, "Experimental evidence of a giant capacitance in insulator-conductor composites at the percolation threshold," *Advanced Materials*, vol. 12, pp. 294-297, 2000.

[105] D. M. Grannan, J. C. Garland, and D. B. Tanner, "Critical-Behavior of the Dielectric-Constant of a Random Composite near the Percolation-Threshold," *Physical Review Letters*, vol. 46, pp. 375-378, 1981.

[106] D. S. Mclachlan, I. I. Oblakova, and A. B. Pakhomov, "The Complex Dielectric-Constant of a Metal (Superconductor)-Insulator System near the Percolation-Threshold," *Physica B*, vol. 194, pp. 2011-2012, 1994.

[107] D. J. Bergman and Y. Imry, "Critical Behavior of Complex Dielectric-Constant near Percolation Threshold of a Heterogeneous Material," *Physical Review Letters*, vol. 39, pp. 1222-1225, 1977.

[108] Y. Song, T. W. Noh, S. I. Lee, and J. R. Gaines, "Experimental-Study of the 3-Dimensional Ac Conductivity and Dielectric-Constant of a Conductor-Insulator Composite near the Percolation-Threshold," *Physical Review B*, vol. 33, pp. 904-908, 1986.

[109] Y. Rao and C. P. Wong, "Novel Ultra-high Dielectric Constant Polymer Based Composite for Embedded Capacitor Application," presented at Electronic Components & Technology Conference, San Diego, CA, 2002.

[110] S. S. Barton, G. L. Boulton, and B. H. Harrison, "Surface Studies on Graphite - Estimation of Average Polarity of Oxygen Complexes," *Carbon*, vol. 10, pp. 391-&, 1972.

[111] J. A. Ayala, W. M. Hess, A. O. Dotson, and G. A. Joyce, "New Studies on the Surface-Properties of Carbon-Blacks," *Rubber Chemistry and Technology*, vol. 63, pp. 747-778, 1990.

[112] S. Iijima, "Helical Microtubules of Graphitic Carbon," *Nature*, vol. 354, pp. 56-58, 1991.

[113] E. W. Wong, P. E. Sheehan, and C. M. Lieber, "Nanobeam mechanics: Elasticity, strength, and toughness of nanorods and nanotubes," *Science*, vol. 277, pp. 1971-1975, 1997.

[114] P. Kim, L. Shi, A. Majumdar, and P. L. McEuen, "Thermal transport measurements of individual multiwalled nanotubes," *Physical Review Letters*, vol. 8721, pp. -, 2001.

[115] S. Berber, Y. K. Kwon, and D. Tomanek, "Unusually high thermal conductivity of carbon nanotubes," *Physical Review Letters*, vol. 84, pp. 4613-4616, 2000.

[116] C. T. White and T. N. Todorov, "Carbon nanotubes as long ballistic conductors," *Nature*, vol. 393, pp. 240-242, 1998.

[117] W. J. Liang, M. Bockrath, D. Bozovic, J. H. Hafner, M. Tinkham, and H. Park, "Fabry-Perot interference in a nanotube electron waveguide," *Nature*, vol. 411, pp. 665-669, 2001.

[118] J. Kong, E. Yenilmez, T. W. Tombler, W. Kim, H. J. Dai, R. B. Laughlin, L. Liu, C. S. Jayanthi, and S. Y. Wu, "Quantum interference and ballistic transmission in nanotube electron waveguides," *Physical Review Letters*, vol. 8710, pp. art. no.-106801, 2001.

[119] A. Javey, J. Guo, Q. Wang, M. Lundstrom, and H. J. Dai, "Ballistic carbon nanotube field-effect transistors," *Nature*, vol. 424, pp. 654-657, 2003.

[120] T. Durkop, S. A. Getty, E. Cobas, and M. S. Fuhrer, "Extraordinary mobility in semiconducting carbon nanotubes," *Nano Letters*, vol. 4, pp. 35-39, 2004.

[121] Z. Yao, C. L. Kane, and C. Dekker, "High-field electrical transport in single-wall carbon nanotubes," *Physical Review Letters*, vol. 84, pp. 2941-2944, 2000.

[122] T. V. Sreekumar, T. Liu, B. G. Min, H. Guo, S. Kumar, R. H. Hauge, and R. E. Smalley, "Polyacrylonitrile single-walled carbon nanotube composite fibers," *Advanced Materials*, vol. 16, pp. 58-+, 2004.

[123] S. Kumar, T. D. Dang, F. E. Arnold, A. R. Bhattacharyya, B. G. Min, X. F. Zhang, R. A. Vaia, C. Park, W. W. Adams, R. H. Hauge, R. E. Smalley, S. Ramesh, and P. A. Willis, "Synthesis, structure, and properties of PBO/SWNT composites," *Macromolecules*, vol. 35, pp. 9039-9043, 2002.

[124] D. Qian, E. C. Dickey, R. Andrews, and T. Rantell, "Load transfer and deformation mechanisms in carbon nanotube-polystyrene composites," *Applied Physics Letters*, vol. 76, pp. 2868-2870, 2000.

[125] M. J. Biercuk, M. C. Llaguno, M. Radosavljevic, J. K. Hyun, A. T. Johnson, and J. E. Fischer, "Carbon nanotube composites for thermal management," *Applied Physics Letters*, vol. 80, pp. 2767-2769, 2002.

[126] S. U. S. Choi, Z. G. Zhang, W. Yu, F. E. Lockwood, and E. A. Grulke, "Anomalous thermal conductivity enhancement in nanotube suspensions," *Applied Physics Letters*, vol. 79, pp. 2252-2254, 2001.

[127] H. Huang, C. H. Liu, Y. Wu, and S. S. Fan, "Aligned carbon nanotube composite films for thermal management," *Advanced Materials*, vol. 17, pp. 1652-+, 2005.

[128] B. Vigolo, C. Coulon, M. Maugey, C. Zakri, and P. Poulin, "An experimental approach to the percolation of sticky nanotubes," *Science*, vol. 309, pp. 920-923, 2005.

[129] J. Sandler, M. S. P. Shaffer, T. Prasse, W. Bauhofer, K. Schulte, and A. H. Windle, "Development of a dispersion process for carbon nanotubes in an epoxy matrix and the resulting electrical properties," *Polymer*, vol. 40, pp. 5967-5971, 1999.

[130] L. Wang and Z. M. Dang, "Carbon nanotube composites with high dielectric constant at low percolation threshold," *Applied Physics Letters*, vol. 87, pp. -, 2005.

[131] J. H. Wu and L. B. Kong, "High microwave permittivity of multiwalled carbon nanotube composites," *Applied Physics Letters*, vol. 84, pp. 4956-4958, 2004.

[132] J. P. Clerc, G. Giraud, J. Roussenq, R. Blanc, J. P. Carton, E. Guyon, H. Ottavi, and D. Stauffer, "Percolation - Experimental Simulations, Analytical and Numerical-Models," *Annales De Physique*, vol. 8, pp. 5-105, 1983.

[133] S. A. Curran, P. M. Ajayan, W. J. Blau, D. L. Carroll, J. N. Coleman, A. B. Dalton, A. P. Davey, A. Drury, B. McCarthy, S. Maier, and A. Strevens, "A composite from poly(m-phenylenevinylene-co-2,5-dioctoxy-p-phenylenevinylene) and carbon nanotubes: A novel material for molecular optoelectronics," *Advanced Materials*, vol. 10, pp. 1091-+, 1998.

[134] Z. H. Fan and S. G. Advani, "Characterization of orientation state of carbon nanotubes in shear flow," *Polymer*, vol. 46, pp. 5232-5240, 2005.

[135] J. Kong, N. R. Franklin, C. W. Zhou, M. G. Chapline, S. Peng, K. J. Cho, and H. J. Dai, "Nanotube molecular wires as chemical sensors," *Science*, vol. 287, pp. 622-625, 2000.

[136] M. Shim, A. Javey, N. W. S. Kam, and H. J. Dai, "Polymer functionalization for air-stable n-type carbon nanotube field-effect transistors," *Journal of the American Chemical Society*, vol. 123, pp. 11512-11513, 2001.

[137] A. Star, J. C. P. Gabriel, K. Bradley, and G. Gruner, "Electronic detection of specific protein binding using nanotube FET devices," *Nano Letters*, vol. 3, pp. 459-463, 2003.

[138] D. Chattopadhyay, L. Galeska, and F. Papadimitrakopoulos, "A route for bulk separation of semiconducting from metallic single-wall carbon nanotubes," *Journal of the American Chemical Society*, vol. 125, pp. 3370-3375, 2003.

[139] A. A. Mamedov, N. A. Kotov, M. Prato, D. M. Guldi, J. P. Wicksted, and A. Hirsch, "Molecular design of strong single-wall carbon nanotube/polyelectrolyte multilayer composites," *Nature Materials*, vol. 1, pp. 190-194, 2002.

[140] F. Rodriguez, *Principles of Polymer Systems*. Washington, DC: Taylor & Francis, **1996**.

[141] R. Schueler, J. Petermann, K. Schulte, and H. P. Wentzel, "Agglomeration and electrical percolation behavior of carbon black dispersed in epoxy resin," *Journal of Applied Polymer Science*, vol. 63, pp. 1741-1746, 1997.

[142] S. Lin-Gibson, J. A. Pathak, E. A. Grulke, H. Wang, and E. K. Hobbie, "Elastic flow instability in nanotube suspensions," *Physical Review Letters*, vol. 92, pp. -, 2004.

[143] J. P. Straley, "Critical Exponents for Conductivity of Random Resistor Lattices," *Physical Review B*, vol. 15, pp. 5733-5737, 1977.

[144] R. Fisch, "Critical Behavior of Random Resistor Networks near Percolation Threshold," *Physical Review B*, vol. 18, pp. 416-420, 1978.

[145] L. Hu, D. S. Hecht, and G. Gruner, "Percolation in transparent and conducting carbon nanotube networks," *Nano Letters*, vol. 4, pp. 2513-2517, 2004.

[146] A. Celzard, E. McRae, C. Deleuze, M. Dufort, G. Furdin, and J. F. Mareche, "Critical concentration in percolating systems containing a high-aspect-ratio filler," *Physical Review B*, vol. 53, pp. 6209-6214, 1996.

[147] I. Balberg, "Universal Percolation-Threshold Limits in the Continuum," *Physical Review B*, vol. 31, pp. 4053-4055, 1985.

[148] I. Balberg, "Excluded-Volume Explanation of Archie Law," *Physical Review B*, vol. 33, pp. 3618-3620, 1986.

[149] I. Balberg, C. H. Anderson, S. Alexander, and N. Wagner, "Excluded Volume and Its Relation to the Onset of Percolation," *Physical Review B*, vol. 30, pp. 3933-3943, 1984.

[150] F. T. Chen, C. W. Chu, J. He, Y. Yang, and J. L. Lin, "Organic thin-film transistors with nanocomposite dielectric gate insulator," *Applied Physics Letters*, vol. 85, pp. 3295-3297, 2004.

[151] K. Dutta and S. K. De, "High dielectric permittivity in silica-polyaniline nanocomposites," *Journal of Nanoscience and Nanotechnology*, vol. 6, pp. 499-504, 2006.

[152] A. Maliakal, H. Katz, P. M. Cotts, S. Subramoney, and P. Mirau, "Inorganic oxide core, polymer shell nanocomposite as a high K gate dielectric for flexible electronics applications," *Journal of the American Chemical Society*, vol. 127, pp. 14655-14662, 2005.

[153] Z. M. Dang, L. Wang, H. Y. Wang, C. W. Nan, D. Xie, Y. Yin, and S. C. Tjong, "Rescaled temperature dependence of dielectric behavior of ferroelectric polymer composites," *Applied Physics Letters*, vol. 86, pp. -, 2005.

[154] C. Huang, Q. M. Zhang, J. Y. Li, and M. Rabeony, "Colossal dielectric and electromechanical responses in self-assembled polymeric nanocomposites," *Applied Physics Letters*, vol. 87, pp. -, 2005.

[155] H. S. Xu, Z. Y. Cheng, V. Bharti, S. X. Wang, and Q. M. Zhang, "All-polymer electromechanical systems consisting of electrostrictive poly(vinylidene fluoride-trifluoroethylene) and conductive polyaniline," *Journal of Applied Polymer Science*, vol. 75, pp. 945-951, 2000.

[156] Q. M. Zhang, H. F. Li, M. Poh, F. Xia, Z. Y. Cheng, H. S. Xu, and C. Huang, "An all-organic composite actuator material with a high dielectric constant," *Nature*, vol. 419, pp. 284-287, 2002.

[157] C. Huang, Q. M. Zhang, and J. Su, "High-dielectric-constant all-polymer percolative composites," *Applied Physics Letters*, vol. 82, pp. 3502-3504, 2003.

[158] N. F. Mott, "Oxidation of metals and the formation of protective films," *Nature*, vol. 145, pp. 996-1000, 1940.

[159] A. J. Poslinski, M. E. Ryan, R. K. Gupta, S. G. Seshadri, and F. J. Frechette, "Rheological Behavior of Filled Polymeric Systems .2. The Effect of a Bimodal Size Distribution of Particulates," *Journal of Rheology*, vol. 32, pp. 751-771, 1988.

[160] N. Ouchiyama and T. Tanaka, "Porosity of a Mass of Solid Particles Having a Range of Sizes," *Industrial & Engineering Chemistry Fundamentals*, vol. 20, pp. 66-71, 1981.

[161] H. T. Vo and F. G. Shi, "Towards model-based engineering of optoelectronic packaging materials: dielectric constant modeling," *Microelectronics Journal*, vol. 33, pp. 409-415, 2002.